Optical-radio-frequency double-resonance studies of two- and three-level systems

by

Changjiang Wei

A thesis submitted for the degree of
Doctor of Philosophy of
the Australian National University

June 1994

Declaration

The contents of this thesis, except where indicated, are entirely my own work. The work was conducted while I was a full time postgraduate student at the Australian National University.

This thesis has never been submitted to another university or similar institution.

Changjiang Wei

Changjiang Wei

Canberra, June, 1994

Acknowledgements

I sincerely thank my supervisor Dr. Neil B. Manson for his tireless supervision of all aspects of the work presented in this thesis. The three year experience working with Neil is and will always be a great treasure to me.

I wish to thank my joint supervisor Dr. John P. D. Martin for his advice and opinions on all aspects of the work presented in this thesis.

I also wish to thank Dr. Peter T. H. Fisk, Dr. X. F. He and Dr. Kenneth G. H. Baldwin for many stimulating discussions. I am grateful to Mrs. Dianne Hodges for her kindly help in many aspects. Thanks are also due to all other members of the Laser Physics Centre for making it such a pleasant place to work, particularly, to Professor Lewis T. Chadderton for many interesting conversations, and to my fellow graduate students Matthew Sellars and Tosporn Boonyarith with whom many things were shared: lasers, mirrors, ideas and happiness and Scott Holmstrom for his critical prove reading. The technical assistance from Mr. Ian McRae is gratefully acknowledged. Thanks are also due to Mr. Wolfgang Boehm for keeping the liquid helium supply always available.

The financial assistance of an ANU PhD scholarship from the Australian National University is gratefully acknowledged.

I am grateful to my parents for their encouragement and support. Finally, I would like to thank my wife Xueye for her support.

Abstract

This thesis studies the interaction between two- and three-level systems and strong, coherent radio-frequency (rf) electromagnetic fields. The investigations were carried out in both the frequency domain, where steady state properties are examined, and the time domain, where transient behaviours are studied. The two- and three-level systems studied arise from the nuclear spin I = 1 triplet within the ^3A ground state of the nitrogen-vacancy (N-V) centre in diamond. The nuclear magnetic resonance (NMR) is detected optically using a coherent optical-rf double resonance Raman heterodyne technique. Owing to the unique features of both the nuclear spin triplet and the detection technique, many interesting experimental results have been obtained.

The thesis is comprised of four parts. Part 1 includes Chapters 1 to 3, which provides introductory accounts. The two-level system concept and associated theoretical treatments in the density matrix formalism are introduced in Chapter 1. The theory is given in a very general form and is developed later in relevant chapters for specific situations. Chapter 2 gives an introduction to the N-V centre and its electronic and hyperfine energy levels. The Raman heterodyne technique and the experimental details are described in Chapter 3.

In Part 2, consisting of Chapters 4 and 5, the nuclear magnetic transition of interest is characterized. Chapter 4 describes various coherent transient observations including nutation, free-induction-decay (FID), spin echo, spin-locking, delayed FID, and rotary echo, from which important parameters such as the transition strength, population decay time T_1, and dephasing time T_2 can be deduced. The dependence of these parameters upon the wave function mixing due to the level anti-crossing is discussed in Chapter 5.

Part 3 is the most significant part of the thesis and consists of Chapters 6 to 9. In these chapters the interaction of a two- and three-level system with electromagnetic fields are studied in the frequency domain using pump-probe spectroscopy. This technique involves driving the systems with a strong (pump) field and monitoring it with a separate (probe) field. The absorption and dispersion profiles of a driven two-level system probed by a weak field are discussed in Chapter 6. Topics include the dynamic "Stark" effect and amplification without inversion. When the probe intensity is increased from weak to strong, multiphoton transitions and multiphoton gain without inversion are observed. These effects are described in Chapter 7. When the pump and probe fields interact separately with two transitions which share one common level the two-level system is extended to a three-level one. The power broadening of the Autler-Townes spectrum in such a three-level system is the topic presented in Chapter 8. Chapter 9 considers the case where there are two strong fields and a weak probe field. The discussion is in terms of the dressed state picture and it is shown that the dressed state can be also dressed.

Experimental results of the transient nutation in dressed states are presented in part 4 which consists of Chapter 10. The dressed states transition strength is determined for the first time experimentally.

Finally, Chapter 11 presents a summary of this thesis.

Contents

Chapter 1

Introduction

In this chapter the important concepts and formalisms are introduced including: (i) the two-level system model, (ii) the density matrix formalism, (iii) the rotating-wave-approximation, (iv) the vector model description of a two-level system interacting with electromagnetic field and (v) the dressed state formalism. The discussion presented here is kept in a general form. Detailed theoretical treatments for specific situations are presented later in the relevant chapters. As a consequence of the two-level system model being of such a fundamental importance, there are numerous publications on the subject. Rather than give extensive references only a few well-known text books are referred. More complete reference lists are included later in each relevant chapter. Finally a brief outline of this thesis is presented.

1.1 Two-Level System Model

It is very difficult if not impossible to discuss the matter-radiation interaction in exact terms. Fortunately, when the frequency of a radiation field is close to the resonant frequency of one of the many atomic transitions, the two-level model has been proved to be a surprisingly good approximation. Within this model, the far off-resonant interaction between the radiation field and the rest of the atomic transitions is neglected, thus, the whole atom can be treated as a quantum system with only two levels coupled by the radiation field.

More specifically, the radiation fields studied in this thesis are coherent, monochromatic electromagnetic fields and the two-level system provides the most important simplified quantum model for such a matter-radiation

interaction. It is not only physically realistic but also mathematically tractable as the Schrodinger equation can be solved analytically with the aid of the rotating-wave-approximation. Such a model has been extensively studied in the spectral range spanning from radio-frequency (rf), where it deals with the magnetic dipole interaction, to optical frequency, where the model is used to understand the electric dipole interaction. Many interesting phenomena associated with a two-level system responding to strong, near-resonant, coherent field have been explored such as Rabi nutation, power broadening, dynamic Stark effect, Mollow triplet and Autler-Townes doublet [1-9].

1.2 Theoretical Approach

1.2.1 Density Matrix Formalism of Quantum Mechanics

A quantum atomic system can be described in terms of the atomic wave function, $\Psi(\mathbf{r},t)$, which is the solution of the Schrodinger equation

$$i\hbar \frac{\partial \Psi}{\partial t} = \mathcal{H} \Psi = [\mathcal{H}_0 + V(t)]\Psi . \qquad (1.1)$$

Here $\mathcal{H}$ is the total Hamiltonian of the quantum atomic system and can be written as a sum of a time-independent Hamiltonian, $\mathcal{H}_0$, and a time-dependent interaction Hamiltonian, V(t). $\mathcal{H}_0$ describes the quantum system in the absence of external fields. The eigenvectors $|n\rangle$ and eigenvalues $E_n = \hbar\,\omega_n$ of $\mathcal{H}_0$ are known

$$\mathcal{H}_0 |n\rangle = E_n |n\rangle = \hbar\,\omega_n |n\rangle. \qquad (1.2)$$

For the purpose here, V(t) describes the magnetic dipole interaction of the quantum atomic system with the electromagnetic field and has the form,

$$V(t) = -\mu\,\mathbf{B}(t) . \qquad (1.3)$$

μ is the magnetic dipole moment and $\mathbf{B}(t)$ is the magnetic component of the applied field. In general the wavelength of the rf electromagnetic field is much larger than the quantum atomic system size, hence, the spatial dependence of the applied field is ignored.

The wave function, Ψ, can be written as a linear superposition of eigenvectors of $\mathcal{H}_0$,

$$\Psi = \sum_n c_n(t)\ |n\rangle . \tag{1.4}$$

Instead of using the wave function, Ψ, the density matrix, ρ, can be used to describe the quantum atomic system. The density matrix operator is defined by

$$\rho = |\Psi\rangle\langle\Psi| . \tag{1.5}$$

The density matrix equations of motion can be derived by substituting Eq.(1.5) into Eq.(1.1) and adding phenomenological damping terms

$$\dot{\rho} = \frac{1}{i\hbar}\left[\ \mathcal{H}, \rho\ \right] + (\text{damping terms}) , \tag{1.6}$$

or in the matrix element form

$$\dot{\rho}_{nm} = -i\,\omega_{nm}\,\rho_{nm} - \frac{i}{\hbar}\sum_k \left(V_{nk}\,\rho_{km} - \rho_{nk}\,V_{km} \right) + (\text{damping term})_{nm} . \tag{1.7}$$

The atomic transition frequency ω_{nm} is defined as

$$\omega_{nm} = \frac{E_n - E_m}{\hbar} = \omega_n - \omega_m . \tag{1.8}$$

In principle, if Eq.(1.7) could be solved, then, all of the properties of the quantum atomic system would have been able to be fully described. For example, the probability of the system being in level $|n\rangle$ is given by the diagonal element $\rho_{nn} = |c_n|^2$, the absorptive and dispersive response associated

with the $|n\rangle \Leftrightarrow |m\rangle$ transition is proportional to the imaginary and real parts of the off-diagonal element $\rho_{nm}=c_n c_m^*$, respectively. Unfortunately, the density matrix equations of motion, Eq (1.7), can not be solved directly for the general situation. The two-level model provides great simplification in calculations and more importantly gives a very good account to most problems. It is worthwhile to point out that even if a numerical solution of it is possible in this super computer era the important role of the two-level system model in providing a clear and simple physical picture will remain unrivalled.

1.2.2 Density Matrix Equations of Motion for a Closed Two-Level System

We consider a two-level system with a ground state, $|1\rangle$, and an excited state, $|2\rangle$, driven by a near-resonant coherent electromagnetic field at frequency ω as shown in Fig. 1-1.

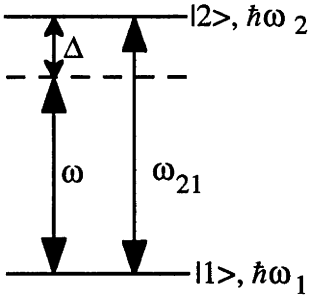

Figure 1-1. Near-resonant excitation of a two-level atom.

The Hamiltonian for this system is

$$\mathcal{H} = \mathcal{H}_0 + V(t)\,, \tag{1.9}$$

where $\mathcal{H}_0$ is the free atomic Hamiltonian whose eigenvectors and eigenvalues are given by

$$\mathcal{H}_0 \,|\, n\rangle = E_i \,|\, n\rangle = \hbar\, \omega_n \,|\, n\rangle \qquad n = 1, 2\,. \tag{1.10}$$

The interactions between the two-level system and an applied electromagnetic field are described by the interaction Hamiltonian, V(t). When the states |1> and |2> are coupled by a magnetic dipole transition, the interaction Hamiltonian, V(t) has the form,

$$V(t) = \begin{pmatrix} 0 & V_{12} \\ V_{21} & 0 \end{pmatrix} = \begin{pmatrix} 0 & -\mu_{12}\mathbf{B}(t) \\ -\mu_{12}\mathbf{B}^{*}(t) & 0 \end{pmatrix} \qquad (1.11)$$

The density matrix equations of motion for such a two-level system including phenomenological decay terms can be written as

$$\frac{\partial \rho_{11}}{\partial t} = -\frac{i}{\hbar}(V_{12}\rho_{21} - V_{21}\rho_{12}) - \frac{\rho_{11} - \rho_{11}^{eq}}{T_1}, \qquad (1.12a)$$

$$\frac{\partial \rho_{22}}{\partial t} = \frac{i}{\hbar}(V_{12}\rho_{21} - V_{21}\rho_{12}) - \frac{\rho_{22} - \rho_{22}^{eq}}{T_1}, \qquad (1.12b)$$

$$\frac{\partial \rho_{21}}{\partial t} = -i\omega_{21}\rho_{21} + \frac{i}{\hbar}V_{21}(\rho_{22} - \rho_{11}) - \frac{\rho_{21}}{T_2}. \qquad (1.12c)$$

Here $\omega_{21} = \omega_2 - \omega_1$ is the two-level system transition frequency. ρ_{11}^{eq} and ρ_{22}^{eq} are the equilibrium populations of levels |1> and |2> in the absence of the applied electromagnetic field, respectively. T_1 is the longitudinal relaxation time which describes the population decay and T_2 is the transverse relaxation time which describes the coherence dephasing that leads to a transition linewidth (for weak applied field) of homogeneous width $\Gamma_h = (\pi T_2)^{-1}$.

The closed system, which has the virtue of simplicity in mathematical treatment, is defined by

$$\rho_{11} + \rho_{22} = \rho_{11}^{eq} + \rho_{22}^{eq} = 1, \quad \text{and} \quad \dot{\rho}_{11} + \dot{\rho}_{22} = 0, \qquad (1.13)$$

that is, any population that leaves the excited (ground) state enters the ground (excited) state. The total population of the two-level system is a constant.

It is more precise to describe a two-level system abstracted from a real multi-level system as an open two-level system, where the two levels under consideration are allowed to exchange population with other levels which act as a population reservoir. However, an open two-level system needs more parameters to characterize than does a closed two-level system. This leads to more complexities in mathematical treatment. Furthermore these parameters are not always readily determined from experiment. More importantly the results of an open two-level system are qualitatively similar to those for a closed two-level system [see, for example, 7, 8]. In light of the above factors, throughout this thesis the experimental results obtained in the N-V centre NMR two-level system, which is without doubt an open two-level system, are compared to the theoretical calculations based on a closed two-level system model.

Eq.(1.12) describes the interaction between a two-level system and electromagnetic fields. The richness of interesting physical phenomena arising from the different interaction schemes is reflected in the form of the interaction Hamiltonian, V(t). For example, with a single monochromatic field Eq.(1.12) describes power broadening, saturation in the frequency domain and Rabi nutation in the time domain (see, Chapter 4), whereas with two monochromatic fields it predicts dynamic Stark splitting and amplification without inversion (see, Chapter 6). In general, Eq.(1.12) can be solved directly, however, its solution can be greatly simplified by introducing the rotating-wave-approximation described in the following section.

1.2.3 Rotating-Wave-Approximation

When a linear, monochromatic field with frequency ω is applied to a two-level system the interaction Hamiltonian that corresponds to the applied field

$$\mathbf{B}(t) = \mathbf{B}_0 \cos \omega t , \qquad (1.14)$$

is

$$V_{12} = V_{21} = -\mu_{12} \mathbf{B}_0 \cos \omega t = -\frac{\hbar \chi}{2} (e^{-i\omega t} + e^{i\omega t}) . \qquad (1.15)$$

Here $\chi = \mu_{12}\mathbf{B}_0/\hbar$ is the Rabi frequency of the applied field which characterizes the strength of the interaction between the two-level system and the field.

The two-level system density matrix equations of motion, Eq.(1.12), can be solved directly although not analytically for the V_{12} given by Eq.(1.15). However, a significant simplification and more physical insight can be achieved by adopting the well-known rotating-wave-approximation.

By inspecting Eq.(1.12c), it can be seen that in the absence of a driving field, ρ_{21} tends to evolve in time as $\exp(-i\omega_{21}t)$. For this reason, for a near-resonant field $\omega \approx \omega_{21}$, the part of V_{21} that oscillates as $\exp(-i\omega t)$ acts as a far more effective term in driving the system than does the part that oscillates as $\exp(i\omega t)$. It is thus a good approximation to take V_{21} not as Eq.(1.15) but instead as

$$V_{21} = V_{12}^{*} = -\frac{\hbar \chi}{2} e^{-i\omega t} . \qquad (1.16)$$

This approximation is called the rotating-wave-approximation. Within this approximation, the density matrix equations of motion, Eq.(1.12), become

$$\frac{\partial \rho_{11}}{\partial t} = i\frac{\chi}{2}(\tilde{\rho}_{21} - \tilde{\rho}_{12}) - \frac{\rho_{11} - \rho_{11}^{eq}}{T_1}, \qquad (1.17a)$$

$$\frac{\partial \rho_{22}}{\partial t} = -i\frac{\chi}{2}(\tilde{\rho}_{21} - \tilde{\rho}_{12}) - \frac{\rho_{22} - \rho_{22}^{eq}}{T_1}, \qquad (1.17b)$$

$$\frac{\partial \tilde{\rho}_{21}}{\partial t} = -(i\Delta + \frac{1}{T_2})\tilde{\rho}_{21} - i\frac{\chi}{2}(\rho_{22} - \rho_{11}). \qquad (1.17c)$$

The rapidly oscillating factor of the off-diagonal elements ρ_{21} has been removed by introducing the slowly varying quantity $\tilde{\rho}_{21}$

$$\tilde{\rho}_{21} = \rho_{21} e^{i\omega t} \quad \text{and} \quad \tilde{\rho}_{12} = \rho_{12} e^{-i\omega t}. \qquad (1.18)$$

and the detuning Δ is defined by

$$\Delta = \omega_{21} - \omega. \qquad (1.19)$$

1.2.4 Vector Model of the Density Matrix and Bloch Equation

From above discussions we have seen that the two-level quantum system can be described by either atomic wave functions or the density matrix. In what follows we will show that such a system can be also described in terms of a vector in the classical picture.

Equation (1.17), which describes quantum mechanically a two-level system interacting with field, can be cast into a simple but rigourous form which resembles the Bloch equation for a magnetic dipole undergoing classical precession in a magnetic field. The evolution of the density matrix elements can be represented by the motion of a fictitious vector **M** (Bloch vector). The z component of **M** is related to the population difference and the x, y components to the real, imaginary parts of the off-diagonal elements,respectively. The electromagnetic field is described by a field vector, **F**, which is defined by a

Rabi intensity, χ, and detuning, Δ, and lies in the x-z plane for an off resonant field and parallel to the x axis for a resonant field (Fig.1-2).

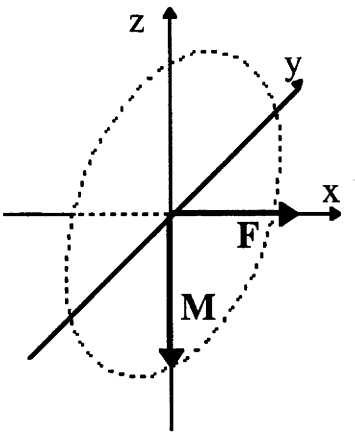

Figure 1-2. Vector model provides a simple geometrical representation of the time-dependence behaviour of the two-level system and electromagnetic field interaction, following directly from the Schrodinger equation. The figure shows the situation for a resonant field where the field vector **F** lies along the x axis and the Bloch vector **M** precesses in the y-z plane at Rabi frequency χ.

Introducing the Bloch vector **M** and the field vector **F**

$$\mathbf{M} = (u, v, w) = [\tilde{\rho}_{21} + \tilde{\rho}_{12}, i (\tilde{\rho}_{21} - \tilde{\rho}_{12}), \rho_{22} - \rho_{11}]$$

$$= (2 \, \mathrm{Re} \, \tilde{\rho}_{21} , - 2 \, \mathrm{Im} \, \tilde{\rho}_{21}, \rho_{22} - \rho_{11}) , \qquad (1.20a)$$

$$\mathbf{F} = (\chi, 0, - \Delta). \qquad (1.20b)$$

The Bloch equation can be derived by substituting Eqs.(1.20) into Eq.(1.17) and can be written as

$$\frac{d \mathbf{M}}{d t} = \mathbf{M} \times \mathbf{F} + (\text{relaxation terms}), \qquad (1.21)$$

or

$$\dot{u} = -\frac{1}{T_2} u - \Delta v , \qquad (1.22a)$$

$$\dot{v} = -\frac{1}{T_2} v + \Delta u + \chi w , \qquad (1.22b)$$

$$\dot{w} = -\chi v - \frac{w - w^{eq}}{T_1} . \qquad (1.22c)$$

Finally I would like to point out that in the above discussion the Bloch equation is derived implicitly in a rotating frame as the Bloch vector is defined using the slowly varying components $\tilde{\rho}_{21}$ and $\tilde{\rho}_{12}$. The vector model of the density matrix has value not only in solving the equations, but also in providing a physical picture of the density matrix in motion.

1.2.5 Concept of Dressed-State

In studying the strong interaction of a two-level system with an electromagnetic field, it is often convenient, both physically and mathematically, to introduce the dressed state picture which allows one to gain more physical insight into the problem. The dressed states are the eigenstates of the total atom + field system within the rotating-wave-approximation. A detailed description of dressed states can be found in the excellent book [9] written by Cohen-Tannoudji *et al.* For the purpose of this thesis, a brief discussion is adequate.

We consider a two-level system interacting with an electromagnetic field (dressing field) of frequency ω as shown in Fig. 1-1. The two-level system is characterized by the ground state, $|1\rangle$, and the excited state, $|2\rangle$, with energies $\hbar\omega_1$ and $\hbar\omega_2$, respectively. The dressing field has a detuning, $\Delta = \omega_{21} - \omega$. The Hamiltonian for the two-level system + dressing field is given by

$$\mathcal{H} = \mathcal{H}_A + \mathcal{H}_F + \mathcal{H}_{AF} , \qquad (1.23)$$

where the two-level system Hamiltonian $\mathcal{H}_A$ and the applied field Hamiltonian $\mathcal{H}_F$ can be written as

$$\mathcal{H}_A = \hbar\,\omega_1\,|1\rangle\langle 1| + \hbar\omega_2\,|2\rangle\langle 2|, \qquad (1.24)$$

$$\mathcal{H}_F = \hbar\,\omega\,a^+\,a\,. \qquad (1.25)$$

where a^+ and a are the photon annihilation and creation operators, respectively. Using the rotating-wave-approximation, the atom-field interaction Hamiltonian becomes

$$\mathcal{H}_{AF} = \frac{\hbar\,\chi}{2}\,(\,a^+\,|1\rangle\langle 2| + a\,|2\rangle\langle 1|\,)\,, \qquad (1.26)$$

where the first term describes the process in which a photon is created accompanied by the transition from the excited state, |2>, to the ground state, |1>, and the second term describes the opposite process where a photon is annihilated accompanied by the |1> to |2> transition. In Eq.(1.26), the dependence of the atom+field coupling on the photon number, n, has been ignored in the strong field limit. Without the atom-field interaction, the unperturbed dressed states are just products of atomic states with photon number states, they form a manifold of doublets: |1, n+1> and |2, n> separated by ω. The |1, n+1> and |2, n> doublet splitting is the detuning Δ. The dressed states (Fig. 1-3) are the eigenstates of the total Hamiltonian, Eq.(1.23), and can be written as

$$|A, n\rangle = \cos\theta\,|2, n\rangle + \sin\theta\,|1, n+1\rangle, \qquad (1.27a)$$

$$|B, n\rangle = -\sin\theta\,|2, n\rangle + \cos\theta\,|1, n+1\rangle, \qquad (1.27b)$$

where θ, given by $\tan 2\theta = \chi / \Delta$, describes the wave function mixing due to the interaction. The coefficients $\sin\theta$ and $\cos\theta$ are of the form

$$\sin\theta = \sqrt{\frac{\Omega - \Delta}{2\,\Omega}} \quad \text{and} \quad \cos\theta = \sqrt{\frac{\Omega + \Delta}{2\,\Omega}}\,. \qquad (1.28)$$

where Ω is the generalized Rabi frequency given by

$$\Omega = \sqrt{\Delta^2 + \chi^2} \quad . \tag{1.29}$$

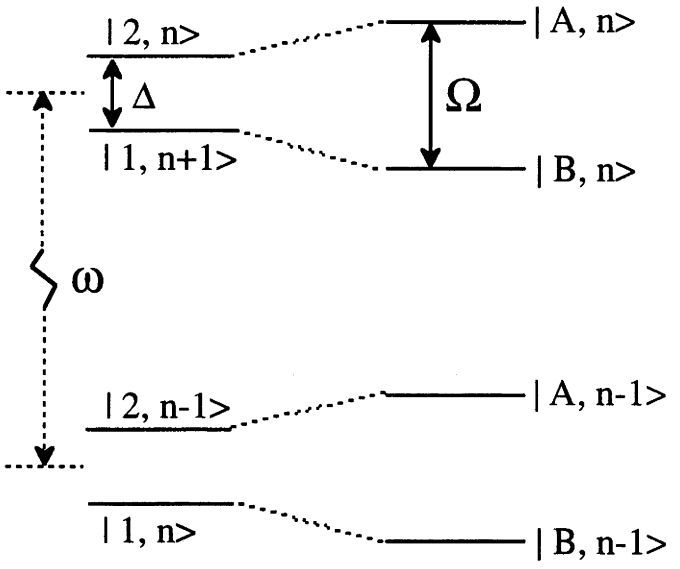

Figure 1-3. The energy levels in the dressed state picture.
Left, without interaction; right, with interaction.

In the dressed state picture the various spectral components can be viewed as arising from transitions between these dressed states. It is very convenient to establish the spectral positions and sometime the relative intensities for each components using the dressed state picture. However, as far as the spectral profile calculation is concerned the dressed state picture does not provide any mathematical simplification. In this thesis the calculation of spectral profiles are carried out using the density matrix formalism in the bare state picture as given in section 1.2.3, the dressed state picture however is often used to give an illuminating picture of the physical process.

1.3 Outline of the Thesis

Although, as mentioned earlier, the two-level system interacting with electromagnetic fields has been studied extensively both theoretically and

experimentally, it still remains a great challenge for experimentalists to adequately demonstrate the details of the theoretical treatments. This is not always an easy task due to experimental difficulties. The main goal of this thesis is to tackle this challenge by employing a sensitive Raman heterodyne detection technique to study a nearly ideal two-level system. The experimental results presented in this thesis are: (i) often better and more systematic in the cases where experimental observations have been reported previously, (ii) the first experimental investigations of theoretical predictions.

The main theme of the thesis is experimental investigations of the interaction of a two-level system (and its extension to a three-level system) with strong, coherent electromagnetic fields in both the frequency and time domain. The well-known pump-probe spectroscopy method, in which the interaction of two-level system with a strong, coherent electromagnetic field (pump field) is investigated by a separate field (probe field), is used. In the frequency domain measurements, the steady state absorption and dispersion profiles of the driven two-level system are measured. In the time domain measurements, the time evolution of the probe field response is studied. In this thesis the term "pump" field is used to refer to a field (usually strong) with a fixed frequency, the term "probe" field is used to refer to a weak field (unless otherwise specified to be strong) and, more importantly, whose interaction with the system is monitored either in the frequency or time domain. The significant features studied are the dynamic "Stark" splitting in the frequency domain and the quantum beats in the time domain.

As was mentioned, there are a few basic parameters used to describe a two-level system interacting with an electromagnetic field, namely, the longitudinal relaxation time, T_1, transverse relaxation time, T_2, Rabi intensity, χ , homogeneous linewidth, $\Gamma_h = (\pi T_2)^{-1}$ and inhomogeneous linewidth, Γ_{inh}.

Depending on the relative values of these parameters, different physical processes can be observed, all of which are interesting in their own right. These processes are schematically represented in Fig. 1-4.

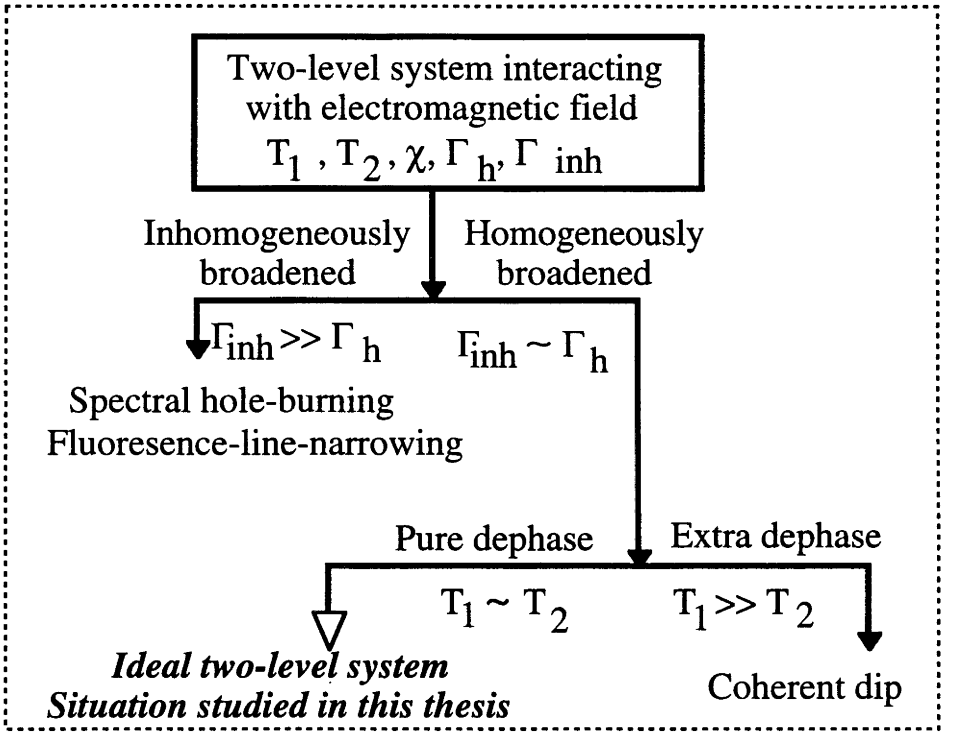

Figure 1-4. Schematic of the different physical processes.

The two-level system studied experimentally in this thesis is a NMR transition within the ^3A ground state hyperfine levels of the nitrogen-vacancy (N-V) centre in diamond. The transition is allowed due to magnetic dipole interactions. As will be shown in Chapters 4 and 5, this specific NMR two-level system is very close to an ideal two-level system. An ideal two-level system is one where the environmental perturbations are minimised such that the transition linewidth is close to homogeneously broadened and limited by longitudinal relaxation. As a result, in this thesis I will focus theoretical discussions on the interaction of an ideal two-level system with strong, coherent electromagnetic fields.

In this chapter, I have introduced some important concepts and formalisms. This will provide the foundation for all of the subsequent theoretical calculations presented in this thesis. In the following two chapters the N-V centre and Raman heterodyne technique will be described. In Chapters 4 and 5, the results of various coherent transient measurements are presented, by which the NMR transitions of interest are characterized. The main focus of these two chapters is to characterize the NMR system and to establish that the NMR system is indeed close to an ideal two-level system.

In Chapters 6 to 9, the steady state behaviour of the NMR two-level system interacting with electromagnetic fields are studied in the frequency domain. The results include weak (Chapter 6) and strong (Chapter 7) probe field in a two-level system, strong probe field in a three-level system (Chapter 8) and a two-level system driven by two strong monochromatic fields (Chapter 9). The most interesting results include: the observation of 11-th order multiphoton resonances and 3-photon gain without inversion (see, Chapter 7) and Autler-Townes splitting in the presence of two strong monochromatic fields (see, Chapter 9).

In Chapter 10, the transient behaviour of the NMR two-level system interacting with electromagnetic fields are studied in the time domain. From the coherent transient measurements we are able to determine experimentally, for the first time, the important parameters of dressed state such as transition strength, longitudinal relaxation time T_1 and transverse relaxation time T_2. The results presented here contain a number of first observations.

References:

[1] A. Abragam, *Principles of Nuclear Magnetism*
(Clarendon Press, Oxford, 1961)

[2] C. P. Slichter, *Principles of Magnetic Resonance*
(Springer-Verlag, Berlin, 1978)

[3] L. Allen and J.H.Eberly, *Optical Resonance and Two-Level Atoms*
(Wiley, New York, 1975)

[4] M.D.Levenson, *Introduction to Nonlinear Laser Spectroscopy*
(Academic, New York, 1982)

[5] J. I. Steinfeld (ed.), *Laser and Coherence Spectroscopy*
(Plenum, New York, 1978)

[6] B. W. Shore, *The Theory of Coherent Atomic Excitation* Vol. I & II
(Wiley, New York, 1990)

[7] P.Meystre and M.Sargent III, *Elements of Quantum Optics*
(Springer-Verlag, Berlin, 1991)

[8] R. W. Boyd, *Nonlinear Optics* (Academic, New York, 1992)

[9] C.Cohen-Tannoudji, J.Dupont-Roc and G.Grynberg,
Atom-Photon Interactions: Basic Processes and Applications.
(Wiley, New York, 1992)

Chapter 2

The Nitrogen-Vacancy Centre in Diamond

There are a few practical restrictions which make the experimental investigation of the interaction of a two-level system and strong, coherent electromagnetic fields difficult. Firstly, it is necessary to identify an ideal two-level system. Such systems are not common due to the presence of many environmental effects. For example, in solid state there is an inhomogeneous broadening of the transition because of crystal field or static magnetic field inhomogeneities, in atomic gases the transition is often broadened by the doppler effect . Even without this inhomogeneous broadening, there are extra dephasing processes such as phonon interaction and spin-flip in solids and collision broadening in gases which make T_2 much shorter than T_1. Secondly, it is necessary to obtain a Rabi intensity, χ, such that $\chi \gg 1/T_2$ [$\chi=\mu_{21}\mathbf{B}/\hbar$, for magnetic dipole interactions, or $\chi=\mu_{21}\mathbf{E}/\hbar$, for electric dipole interactions, where **B** (**E**) is the magnetic (electric) field strength]. This is nearly always difficult due to either a small transition moment, μ_{21}, or an insufficient field intensity, **B** (or **E**), or both. Finally, it is necessary to employ a very sensitive detection technique because in the strong field limit, the signal is usually very weak due to saturation.

In this chapter as well as in Chapters 3-5, I will demonstrate that the NMR transition in the ^{3}A ground state of the N-V centre is a close-to-ideal system with a large transition strength and the magnetic transition can be studied by the sensitive Raman heterodyne detection technique. The physical and electronic properties of the N-V centre are discussed in the remainder of this chapter.

2.1 Introduction

The ground state of the N-V centre is a ^3A electronic spin triplet state: $S_z = 0, \pm 1$. Each electronic spin level is a nuclear spin triplet: $I_z = 0, \pm 1$ associated with nuclear spin I=1 nitrogen nucleus ^{14}N. The transitions studied in this thesis are the $|0, 0\rangle \Leftrightarrow |0, -1\rangle$ and $|0, 0\rangle \Leftrightarrow |0, 1\rangle$ nuclear magnetic transitions in the $|S_z, I_z\rangle$ basis, which have transition frequencies of ~ 5.4 and ~ 4.7 MHz, respectively at a static magnetic field of ~ 0.106 Tesla applied along the [111] direction. The two-level system studied in this thesis consists of the $|0, 0\rangle$ and $|0, -1\rangle$ levels. If the $|0, 0\rangle \Leftrightarrow |0, 1\rangle$ transition is also driven the $|0, 0\rangle$, $|0,1\rangle$ and $|0, -1\rangle$levels form a three-level system. When a static magnetic field applied along the [111] direction has a strength close to 0.1028 Tesla there is a wave function mixing of the electronic spin levels $S_z = |0\rangle$ and $S_z = |-1\rangle$ because of level anti-crossing. This wave function mixing results in two effects which are vital for the present study. First, the nuclear magnetic transition strength of interest is enhanced by a factor of ~ 100. With this enhancement large Rabi intensities can be readily achieved with a non-resonant, home-made radio-frequency (rf) coil and a convenient rf source. Second, due to the wave function mixing, the optical transition between any of the nuclear spin levels to the common excited state ^3E becomes allowed. This is an important result because the sensitive Raman heterodyne technique can then be used to detect the NMR transitions (see chapter 3).

2.2 N-V Centre Configuration

The nitrogen-vacancy (N-V) centre in diamond can be formed in type Ib diamonds which contain nitrogen atoms on isolated substitutional lattice sites after electron or neutron irradiation and subsequent annealing at temperatures over 900 K [1]. Radiation with energy of ~ 1 MeV produces carbon vacancies

which, at temperature above 900 K, become mobile. The vacancies diffuse through the lattice and can be trapped by isolated substitutional nitrogen to form a defect called the N-V centre. Thus , the centre consists of a substitutional nitrogen atom and a vacancy at a nearest neighbour carbon site (see Fig.2-1). It has trigonal C_{3v} symmetry with the C_3 major principal axis along the nitrogen-vacancy pair, which is the crystallographic [111] directions [2-4]. There are four orientations of trigonal centres in the cubic lattice. When a static magnetic field, **B**, is applied along the [111] direction, the subgroup of the N-V centres whose C_3 axis lies along the field are aligned. *Only these aligned N-V centres are considered in this study.* In general, the static magnetic field direction is aligned with the [111] direction within a small angle θ ($|\theta| < 1^0$). This alignment can be achieved using the optical hole bleaching method [5].

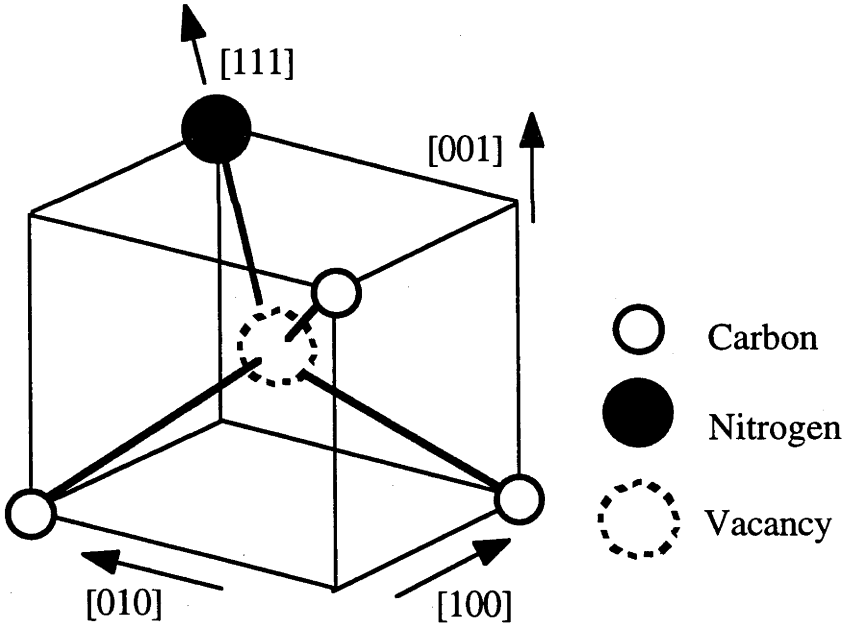

Figure 2-1. Nitrogen-Vacancy (N-V) centre in diamond crystal. The centre consists of a carbon vacancy and a substitutional nitrogen atom.

2.3 The ^3A ground State

The optical characteristic of the N-V centre is a strong zero-phonon line at 638 nm [2, 6] which originates from a ground to excited state, $^3A \Leftrightarrow {}^3E$ transition [5, 7-9]. Fig.2-2 shows the energy levels of the optical and magnetic transitions involved in this study.

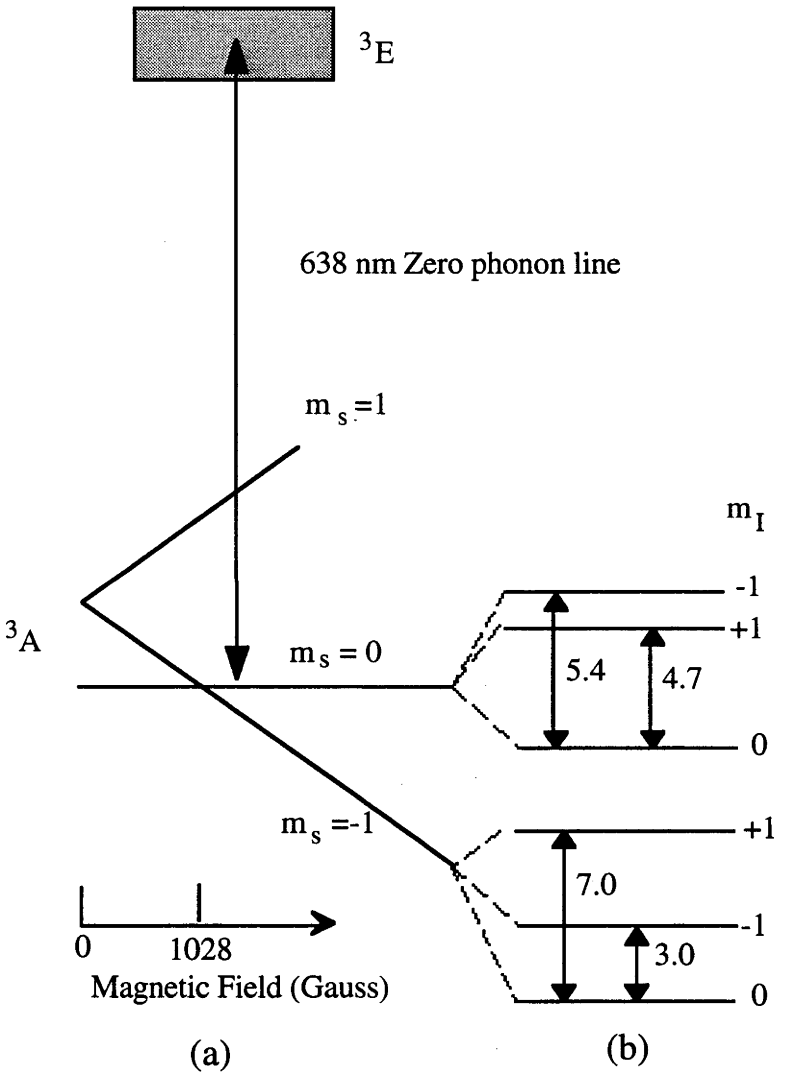

Figure 2-2. Energy level diagram for the N-V centre. (a) Energy level splitting of the ^3A ground state in a static magnetic field applied along the [111] axis, anticrossing occurs at 0.1028 Tesla. (b) The hyperfine splitting at magnetic field ~ 0.1060 Tesla.

At zero field the ^3A ground state is split by the crystal field interaction into an electronic spin doublet $S_z = |\pm 1\rangle$ and an electronic spin singlet $S_z = |0\rangle$ separated by 2.88 GHz [4,5,7]. When a static magnetic field is applied along the [111] direction it splits the ground state $S_z = |\pm 1\rangle$ spin doublet. At a field of 0.1028 Tesla the $S_z = |0\rangle$ and $S_z = |-1\rangle$ levels approach the same energy but do not cross due to the hyperfine interaction and the off diagonal crystal field interaction from any residual slight misalignment of the static magnetic field to the [111] axis [5]. The notional crossing is generally referred to as level anti-crossing (LAC). In this level anti-crossing region, the wave function is an mixture of the $S_z = |0\rangle$ and $S_z = |-1\rangle$ states [10,11]. *In this study the experiments were always carried out in the region close to the level anti-crossing.*

The only nuclear spin associated with the N-V centre is that of the nitrogen isotope ^{14}N, I=1, which gives rise to the hyperfine structure of interest in this study. The spin Hamiltonian of the electron spin triplet ground state, coupled to the nitrogen nuclear spin, in the presence of static magnetic field **B** is given by [10,12],

$$\begin{aligned}\mathcal{H} &= \mathcal{H}_Z + \mathcal{H}_{CF} + \mathcal{H}_{HF} + \mathcal{H}_{Zn} + \mathcal{H}_Q \\ &= \beta\, \mathbf{B.g.S} + \mathbf{S.D.S} + \mathbf{S.A.I} - \beta_n\, \mathbf{B.g_n.I} + \mathbf{I.P.I}.\end{aligned} \tag{2.1}$$

The terms on the right hand side of Eq.(2.1) give the electronic Zeeman, the second order crystal field, the magnetic hyperfine, the nuclear Zeeman and the nuclear quadrupole interaction, respectively. β = 1.40 MHz/Gauss and β_n = 0.762 kHz/Gauss are the electron and nuclear Bohr magnetons, respectively. g=2.0028 is the electronic g value and g_n=0.4036 is the ^{14}N nuclear g value. Eq.(2.1) can be expressed in terms of electron and nuclear spin operators in the principal coordinate system defined by

X-axis: [$\underline{1}\,\underline{1}\,2$], Y-axis: [$1\,\underline{1}\,0$], Z-axis: [1 1 1]. (2.2)

The static magnetic field **B** is applied in the X-Z plane at an angle θ from the Z-axis. The static magnetic field is then written as

$$\mathbf{B} = B\,(\sin\theta,\ 0,\ \cos\theta)\ . \tag{2.3}$$

When the static magnetic field strength is far away from the level anti-crossing region (0.1028 Tesla), the electronic and nuclear spin S, S_z, I, and I_z are good quantum numbers. The eigenstates of the Hamiltonian, Eq.(2.1), for the ^3A ground state can the be written as [10,11]

$$|S,\ S_z\rangle|I,\ I_z\rangle \equiv |S_z,\ I_z\rangle, \qquad S=1,\ S_z=0,\ \pm1,\ I=1,\ I_z=0,\ \pm1\ . \tag{2.4}$$

In the level anti-crossing region, the eigenstates are, in general, linear superposition of the $|S_z,\ I_z\rangle$ eigenvectors,

$$\begin{aligned} |\Psi\rangle &= \sum_{S_z\,I_z} |\,S_z,\ I_z\rangle\langle S_z,\ I_z\,|\Psi\rangle \\ &= \sum_{S_z\,I_z} a_n\,(S_z\,I_z)\,|\,S_z,\ I_z\rangle\ , \quad S_z=0,\ -1,\ I_z=0,\ \pm1\ . \end{aligned} \tag{2.5}$$

The $S_z=|1\rangle$ levels are not included in this study because they have a much greater energy than those of interest (~ 5.76 GHz near the level anti-crossing region).

In the $|S_z,\ I_z\rangle$ basis, the spin Hamiltonian is a 6 x 6 matrix [10,12],

$$
\begin{array}{c}
\quad |-1,-1\rangle \quad |-1,0\rangle \quad |-1,+1\rangle \quad |0,-1\rangle \quad |0,0\rangle \quad |0,+1\rangle \\
\mathcal{H} = \begin{bmatrix}
a_{11} & -\frac{k_n\zeta}{\sqrt{2}} & 0 & \frac{k\zeta}{\sqrt{2}} & 0 & 0 \\
-\frac{k_n\zeta}{\sqrt{2}} & a_{22} & -\frac{k_n\zeta}{\sqrt{2}} & A_\perp & \frac{k\zeta}{\sqrt{2}} & 0 \\
0 & -\frac{k_n\zeta}{\sqrt{2}} & a_{33} & 0 & A_\perp & \frac{k\zeta}{\sqrt{2}} \\
\frac{k\zeta}{\sqrt{2}} & A_\perp & 0 & a_{44} & -\frac{k_n\zeta}{\sqrt{2}} & 0 \\
0 & \frac{k\zeta}{\sqrt{2}} & A_\perp & -\frac{k_n\zeta}{\sqrt{2}} & a_{55} & -\frac{k_n\zeta}{\sqrt{2}} \\
0 & 0 & \frac{k\zeta}{\sqrt{2}} & 0 & -\frac{k_n\zeta}{\sqrt{2}} & a_{66}
\end{bmatrix}
\end{array}
\tag{2.6}
$$

where the diagonal matrix elements, a_{ii}, i = 1, ..., 6 are given by

$$a_{11} = (-k + k_n)\,\eta + \frac{D}{3} + A_{//} + \frac{P}{3}, \tag{2.7a}$$

$$a_{22} = -k\,\eta + \frac{D}{3} - \frac{2P}{3}, \tag{2.7b}$$

$$a_{33} = (-k - k_n)\,\eta + \frac{D}{3} - A_{//} + \frac{P}{3}, \tag{2.7c}$$

$$a_{44} = k_n\,\eta - \frac{2D}{3} + \frac{P}{3}, \tag{2.7d}$$

$$a_{55} = -\frac{2D}{3} - \frac{2P}{3}, \tag{2.7e}$$

$$a_{66} = -k_n\,\eta - \frac{2D}{3} + \frac{P}{3}. \tag{2.7f}$$

The parameters in Eq.(2.6) are, $\eta = \cos\theta$, $\zeta = \sin\theta$, $k = (\gamma/2\pi)B$ and $k_n = (\gamma_n/2\pi)B$, where $\gamma = g\beta/\hbar$ and $\gamma_n = g_n\beta_n/\hbar$ are the electron and nuclear gyromagnetic ratios, respectively. Their values are $\gamma/2\pi = 2.80$ MHz/G and $\gamma_n/2\pi = 0.307$ kHz/G [10].

Eq.(2.6) has been solved numerically and the wave functions, Ψ_n, and energy levels, E_n, have been obtained as a function of either magnetic field

strength, **B**, or misalignment angle, θ [10,11]. The NMR transitions have also been studied experimentally as a function of either magnetic field strength **B** or misalignment angle θ using the Raman heterodyne detection technique [10,11,13]. By fitting the experimental data with the theoretical calculations the parameters in the spin Hamiltonian have been determined to be [10,11,13]: electron g value $g = g_{//} = g_{\perp} = 2.0028$, the zero field splitting D = 2.88 GHz, the hyperfine coupling $A_{//} = 2.3$ MHz, $A_{\perp} = 2.1$ MHz, and the nuclear quadrupole parameter P = 5.1 MHz.

2.4 Wave Function Mixing

It is the wave function mixing occurring at the level anti-crossing region that makes the present study possible. It results in two effects which are vital for the present study: (i) the nuclear hyperfine transition strength is significantly enhanced, hence large Rabi frequencies can be readily achieved using conventional rf set-up, and (ii) the optical transition from the ground state hyperfine levels to a common excited level becomes allowed which is essential for using the Raman heterodyne detection. A thorough discussions of the wave function mixing can be found in Refs.[10,11,14] where the spin Hamiltonian, Eq.(2.6), is solved numerically. Due to its significance to this work, a brief discussion of the wave function mixing using perturbation theory is given below.

By inspecting the spin Hamiltonian, Eq.(2.6), it can be seen that the transverse component of the magnetic hyperfine interaction, $A_{\perp}$, and the static magnetic field component perpendicular to the [111] direction due to any residual misalignment, $\mathbf{B}\sin\theta$, give rise to wave function mixing of the hyperfine levels associated with the electron spin $S_Z = |0\rangle$ states with those of the electron spin $S_Z = |-1\rangle$ state. As an example, we consider the case where the

static magnetic field with a magnitude of ~ 0.1060 Tesla which gives a separation between the S_z = |0> and |-1> electronic spin levels $\Delta_{EPR} \approx 100$ MHz and the field is aligned to the [111] direction within 0.5°. In this case $\eta=\cos\theta \approx 1$ and $\zeta=\sin\theta \approx 0.01$. The off-diagonal terms in the spin Hamiltonian are much smaller than the diagonal terms, therefore, we can use perturbation theory to calculate the first order correction to the wave function. In the $|S_Z,I_Z>$ basis the zero order wave functions are,

$$\Psi^0_{-,-} = |-1, -1>, \quad \Psi^0_{-,0} = |-1, 0>, \quad \Psi^0_{-,+} = |-1, +1>, \tag{2.8a}$$

$$\Psi^0_{0,-} = |0, -1>, \quad \Psi^0_{0,0} = |0, 0>, \quad \Psi^0_{0,+} = |0, +1>. \tag{2.8b}$$

The wave functions with first order corrections can be calculated by

$$\Psi_k = \Psi^0_k + \sum_n \frac{\mathcal{H}_{nk}}{E^0_k - E^0_n} \Psi^0_n, \tag{2.9}$$

where E_k^0 is the zero order eigenenergy which is given by the diagonal terms, a_{kk} [see, Eqs.(2.7)] of the spin Hamiltonian. Using Eq.(2.9) the wavefunctions with first order corrections can be written as

$$\Psi_{-,-} = |-1,-1\rangle - \frac{k_n \zeta}{\sqrt{2}\,(k_n \eta + A_{//} + P)}\,|-1, 0\rangle + \frac{k \zeta}{\sqrt{2}\,(-k\eta + D + A_{//})}\,|0,-1\rangle,$$

(2.10a)

$$\Psi_{-,0} = |-1,0\rangle + \frac{k_n \zeta}{\sqrt{2}\,(k_n \eta + A_{//} + P)}\,|-1,-1\rangle - \frac{k_n \zeta}{\sqrt{2}\,(k_n\eta + A_{//} - P)}\,|-1,+1\rangle$$

$$- \frac{A_{\perp}}{(k + k_n) - D + P}\,|0, -1\rangle + \frac{k \zeta}{\sqrt{2}\,(-k \eta + D)}\,|0, 0\rangle,$$

(2.10b)

$$\Psi_{-,+} = |-1,+1\rangle + \frac{k_n \zeta}{\sqrt{2}\,(k_n \eta + A_{//} - P)}\,|-1,0\rangle$$

$$+ \frac{A_{\perp}}{\sqrt{2}\,(k_n\eta + A_{//} - P)}\,|0,0\rangle - \frac{k \zeta}{\sqrt{2}\,(k \eta - D + A_{//})}\,|0, +1\rangle,$$

(2.10c)

$$\Psi_{0,-} = |0,-1\rangle + \frac{k \zeta}{\sqrt{2}\,(k \eta - D - A_{//})}\,|-1,-1\rangle$$

$$+ \frac{A_{\perp}}{\sqrt{2}\,[(k + k_n)\eta - D + P)}\,|-1,0\rangle - \frac{k_n \zeta}{\sqrt{2}\,(k_n \eta + P)}\,|0,0\rangle,$$

(2.10d)

$$\Psi_{0,0} = |0,0\rangle + \frac{k \zeta}{\sqrt{2}\,(k \eta - D)}\,|-1,0\rangle + \frac{A_{\perp}}{\sqrt{2}\,[(k_n + k)\eta - D + A_{//} - P)}\,|-1,+1\rangle$$

$$+ \frac{k_n \zeta}{\sqrt{2}\,(k_n \eta + P)}\,|0, -1\rangle + \frac{k_n \zeta}{\sqrt{2}\,(-k_n \eta + P)}\,|0, +1\rangle,$$

(2.10e)

$$\Psi_{0,+} = |0,+1\rangle + \frac{k \zeta}{\sqrt{2}\,(k \eta - D + A_{//})}\,|-1,+1\rangle - \frac{k_n \zeta}{\sqrt{2}\,(-k_n \eta + P)}\,|0, 0\rangle.$$

(2.10f)

It can be seen that the due to the transverse component of the hyperfine interaction, $A_\perp$, the wave function between different electronic spin levels are mixed. Therefore, the nuclear spin transitions will have some contribution from the electronic spin transitions. When the magnitude of the applied static magnetic field is close to the level anti-crossing region in which the electron spin levels $S_z = |0\rangle$ and $|-1\rangle$ are separated by Δ_{EPR}~100 MHz, the mixing due to $A_\perp$ term ($A_\perp$ = 2.1 MHz) will be in the order of $A_\perp/\Delta_{EPR}$ ~ a few percent. This results in the NMR transition matrix element having a value of a few percent of that of an EPR transition and therefore a factor of ~100 stronger than the normal $\Delta I=\pm 1$ nuclear magnetic transition.

The $k\zeta$ and $k_n\zeta$ terms, arising from the misalignment of the static magnetic field, give rise to wave function mixing of the different electronic spin levels and of the different nuclear spin levels within the same electronic spin level, respectively. Due to the wave function mixing of the different nuclear spin levels the optical transitions from the ground state nuclear spin levels to a common excited state become allowed and significant which is a critical condition of using the Raman heterodyne technique for magnetic transition measurement.

Exactly at the level anti-crossing (0.1028 Tesla) the EPR transition also lies in the low (~10 MHz) frequency region. This causes a broadening of the hyperfine transitions and gives rise to a strong background signal. As a consequence, in this work it is desirable to work with static magnetic field values close to but not exactly at the level anti-crossing value. Typically a field of ~ 0.1050 - 0.1070 Tesla was used with the $I_Z = |0\rangle \Leftrightarrow |-1\rangle$ transition at ~ 5.4 MHz.

2.5 The ^3E Excited State and Optical Transition

The first excited state ^3E is 1.945 eV (~ 638 nm) above the ground state and has a radiative lifetime of 13 ns [15]. The homogeneous linewidth estimated from spectral hole burning measurements is on the order of ~100 MHz and the inhomogeneous linewidth is about 40 cm^{-1}. Further details of the ^3E excited state or precise knowledge of the energy levels within the ^3E excited state are not available. In the Raman heterodyne experiments, the $^3A \Leftrightarrow ^3E$ transition is driven by a single mode laser field with a linewidth of ~ 1 MHz. It can be treated as a selective excitation between the ground state and the excited state of a particular subgroup of N-V centres in the broad, inhomogeneous distribution.

2.6 Remarks

In the level anti-crossing region the wave function is a linear superposition of $|S_z, I_z\rangle$ basis vectors. However, it can be shown that one of the $|S_z, I_z\rangle$ components in Eq.(2.10) dominates in each eigenstates, Ψ_n, unless the static magnetic field is very close to the level anti-crossing region of ~ 0.1028±0.0005 Tesla [10]. As most measurements in this study were carried out at magnetic fields strength outside this region, we still use $|S_z, I_z\rangle$ to label the levels instead of using the symbol $|n\rangle$ and use $|I_z'\rangle \Leftrightarrow |I_z''\rangle$ to label NMR transitions instead of using $|n\rangle \Leftrightarrow |m\rangle$. The former is more convenient and also physically clear.

The transitions of interest in the thesis are the $|0,0\rangle \Leftrightarrow |0,-1\rangle$ transition at ~ 5.4 MHz and the $|0,0\rangle \Leftrightarrow |0,1\rangle$ transition at ~ 4.7 MHz. As mentioned above the eigenfunctions and eigenvalues are dependent upon the static magnetic field value and the misalignment angle which are not easily reproducible from day-to-day measurements. Hence, small movements of the sample and small

differences of the static magnetic field value lead to small changes in both the transition frequency and transition strength. However the particular magnitude of the transition frequency and the transition strength are not of concern in this study because it is the spectral profiles changes associated with specific Rabi frequencies that are of interest. The Rabi frequencies could be readily determined from the dynamic "Stark" splitting or the Rabi nutation frequency. For simplicity we will always simply refer the $|0,0\rangle \Leftrightarrow |0,-1\rangle$ transition as to $I_z=|0\rangle \Leftrightarrow |-1\rangle$ transition or the 5.4 MHz transition likewise the $|0,0\rangle \Leftrightarrow |0,1\rangle$ transition as to $I_z=|0\rangle \Leftrightarrow |1\rangle$ transition or the 4.7 MHz transition.

References

[1] L. du Preez, PhD Thesis, Witwatersrand University, Johnnnesburg, 1965

[2] G. Davies and M. F. Hamer, Proc. R. Soc. Lond. A. 348, 285, (1976)

" *Optical studies of the 1.945 eV vibronic band in diamond* "

[3] J. H. N. Loubser and J. A. van Wyk, Diamond Research (London: Industrial Diamond Information Bereau) pp11-4, 1977

[4] J. H. N. Loubser and J. A. van Wyk, Rep. Prog. Phys. 41, 1201, (1978)

" *Electron spin resonance in the study of diamond* "

[5] K. Holliday, N. B. Manson, M. Glasbeek and E. van Oort, J. Phys.:Condense.Matter 1, 7093, (1989)

" *Optical hole-bleaching by level anti-crossing and cross relaxation in the N-V centre in diamond* "

[6] J. Walker, Rep. Prog. Phys. 42, 1605, (1979)

" *Optical absorption and luminescence in diamond* "

[7] N. R. S. Reddy and N. B. Manson and E. R. Krausz, J. Lumin. 38, 46, (1987)

" *Two-laser spectral hole burning in a colour centre in diamond* "

[8] E van Oort, N. B. Manson and M. Glasbeek, J. Phys. C: Solid State Phys. 21, 4385, (1988)

" *Optically detected spin coherence of the diamond N-V centre in its triplet ground state* "

[9] K. Holliday, X.-F. He, P. T. H. Fisk and N. B. Manson, Opt. Lett. 15, 983, (1990)

" *Raman heterodyne detection of electron paramagnetic resonance* "

[10] X.-F. He, PhD. Thesis, The Australian National University, Canberra, 1992

" *Raman heterodyne detected magnetic resonance of the nitrogen-vacancy centre in diamond* "

[11] X.-F. He, N. B. Manson and P. T. H. Fisk, Phys. Rev.B. 47, 8816, (1993)

" *Paramagnetic resonance of photoexcited N-V defects in diamond. II. Hyperfine interaction with the* ^{14}N *nucleus* "

[12] C. P. Poole, Jr. and H. A. Farach, " *The theory of magnetic resonance* " (Wiley, NY. 1972)

[13] N. B. Manson, X.-F. He and P. T. H. Fisk, Opt. lett. 15, 1094, (1990)

"*Raman heterodyne detected electron-nuclear-double-resonance measurements of the nitrogen-vacancy centre in diamond* "

[14] N. B. Manson, X. F. He and P. T. H. Fisk, J. Lumin. 53, 49, (1992)

" Raman heterodyne studies of the nitrogen-vacancy centre in diamond "

[15] A. T. Collins, M. F. Thomaz and M. I. B. Jorge, J. Phys. C: Sol. St. Phys. 16, 2177, (1983)

" *Luminescence decay time of the 1.945 eV centre in type Ib diamond* "

Chapter 3

The Raman Heterodyne Detection of Magnetic Resonance and Experimental Details

This chapter describes the very sensitive Raman heterodyne detection technique which satisfies one of the requirements discussed in the previous chapter. The experimental details are also described.

3.1 Introduction

The Raman heterodyne technique is a coherent, optical-radio-frequency (rf) double resonance method for detecting magnetic transitions. It was first reported by Mlynek *et al.*[1] and since then has been successfully used for detecting nuclear magnetic resonance (NMR) and electron paramagnetic resonance (EPR) in rare earth ion systems [1-14], transition metal ion systems [15,16] and colour centres [17-21]. It can be used for both cw and transient measurements. Like other conventional optically detected magnetic resonance (ODMR) techniques where the optical photon is being detected rather than the rf photon, the Raman heterodyne technique improves the sensitivity for magnetic resonance spectroscopy. But what is more significant is that there is an important difference between the Raman heterodyne technique and other conventional ODMR techniques which makes the Raman heterodyne technique very suitable to the present study. With the conventional ODMR techniques only the changes in the populations of the levels coupled by the optical and rf fields could be detected. As a result, the coherent information contained in the off-diagonal density matrix terms could not, in general, be observed directly [22]. The Raman heterodyne technique directly probes the coherence between

the magnetic transition levels since it relies on a coherent Raman process being stimulated simultaneously by the coherent rf and the laser fields [1,2].

3.2 Raman Heterodyne Signal

The Raman heterodyne technique is an example of a three level optical-rf double resonance process (Fig.3-1). The electric dipole transition $|1\rangle \Leftrightarrow |3\rangle$ is driven coherently by an optical (laser) field at frequency $\omega_L = \omega_{31}$ and the magnetic dipole transition $|1\rangle \Leftrightarrow |2\rangle$ is driven coherently by an rf field at frequency $\omega_{rf} = \omega_{21}$. The resultant coherence between levels $|2\rangle$ and $|3\rangle$ produces a coherent (Stokes) Raman signal field E_s at frequency $\omega_s = \omega_{31} - \omega_{21} = \omega_{32}$ (see, Fig.3-1). In addition, due to the presence of a second subgroup of centres within the inhomogeneous line, the laser field can also be resonant with the $|2\rangle \Leftrightarrow |3\rangle$ transition, which along with the rf field, produces a coherent anti-Stokes Raman field at frequency $\omega_s = \omega_{32} + \omega_{21} = \omega_{31}$. The stimulated Raman signal fields beat with the laser at the rf frequency, ω_{rf}, and this is detected in the beam transmitted through the crystal using a photodiode. By sweeping the rf field frequency through the $|1\rangle \Leftrightarrow |2\rangle$ transition the profiles of this transition can be obtained.

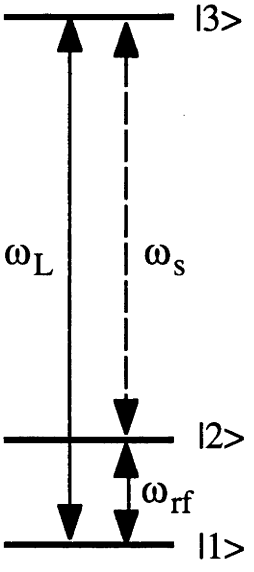

Figure 3-1. Energy-level diagram for the stimulated Raman process in a three-level system. An rf field excites $|1\rangle \Leftrightarrow |2\rangle$ magnetic transition and a laser field excites $|1\rangle \Leftrightarrow |3\rangle$ transition.

The Raman heterodyne technique applies to any three level system where all three transitions are dipole allowed [2]. For the N-V centre the nuclear magnetic transition $|1\rangle \Leftrightarrow |2\rangle$ is magnetic dipole allowed and the optical transitions $|1\rangle \Leftrightarrow |3\rangle$ and $|2\rangle \Leftrightarrow |3\rangle$, corresponding to the transitions between the hyperfine levels within the ^3A ground state to a common level in the ^3E excited state, are electric dipole allowed through the wave function mixing occurring in the level anti-crossing region (see, Chapter 2).

For an optical thin sample, the Raman signal polarization, $\tilde{P}_s(t)$, induced in the sample by the applied rf and laser fields [2,19] is given by

$$\tilde{P}_s(t) = N\left(\mu_{31}\langle\tilde{\rho}_{13}(t)\rangle + \mu_{32}\langle\tilde{\rho}_{23}\rangle\right). \qquad (3.1)$$

The tilde denotes the slowly varying part and the angular brackets denote the averaging over the optical and rf transition inhomogeneous distributions. This polarization is the origin of the Raman heterodyne signal field, $\tilde{E}_s$, at frequency ω_{32}. From Maxwell's equations

$$\frac{\partial \tilde{E}_s}{\partial z} = -2\pi i k_s \tilde{P}_s(t), \qquad (3.2)$$

μ_{31} and μ_{32} are the electric dipole moments of the $|1\rangle \Leftrightarrow |3\rangle$ and $|2\rangle \Leftrightarrow |3\rangle$ optical transitions, respectively. N is the number density of atoms in the sample. z is distance along the sample and k_s is the wave vector of the induced Raman field $\tilde{E}_s$.

The Raman signal field $\tilde{E}_s$ and the input laser field E_0 give rise the total field E_T[2] given by.

$$E_T = \frac{1}{2} E_0 + \tilde{E}_s. \qquad (3.3)$$

From the total intensity $I_T = |E_T|^2$, the observable heterodyne beat signal on the detector, varying at the rf frequency, is obtained [2],

$$I_s = \frac{1}{2}(E_0 \tilde{E}_s^* + E_0^* \tilde{E}_s) . \qquad (3.4)$$

The optical coherences $\tilde{\rho}_{13}$ and $\tilde{\rho}_{23}$ can be calculated by solving the density matrix equations of motion describing the Raman heterodyne detection and hence the Raman signal can be calculated. The density matrix equation of motion describing the Raman heterodyne detection consists of a set of 9×9 linear first order differential equations [2]. However, in the experiments the optical field was kept sufficiently weak so that it could be regarded as a weak perturbation and need only be treated to first order. The three-level system is reduced to a NMR two-level system with the laser field acting as a reliable probe of the coherence within the spin levels. This is a very significant point that was fully treated by Wong *et al.* [2] when the Raman heterodyne technique was first introduced. It has been shown that, to lowest order of optical field, the optical coherences $\tilde{\rho}_{13}$ and $\tilde{\rho}_{23}$ in Eq.(3.1) are proportional to the rf coherences ρ_{12} and ρ_{21} respectively. Therefore the electric field component of the induced Raman beam is given by [2,19]

$$\begin{aligned} \tilde{E}_s &= k \mu_{13} \mu_{23} E_0 \, \mathrm{Re} < \rho_{21}(t) > \\ &= k \mu_{13} \mu_{23} E_0 \, \mathrm{Re} < \tilde{\rho}_{21}(t) e^{-i \omega_{rf} t} > , \end{aligned} \qquad (3.5)$$

where k is a constant, ρ_{21} is the off-diagonal element of the density matrix which represents the coherence between nuclear hyperfine levels |1> and |2>. Substituting Eq.(3.5) into Eq.(3.4), the Raman heterodyne signal intensity becomes,

$$I_s = k \mu_{13} \mu_{23} |E_0|^2 \, \mathrm{Re} < \tilde{\rho}_{21}(t) e^{-i \omega_{rf} t} >, \qquad (3.6)$$

or

$$I_s = k \mu_{13} \mu_{23} |E_0|^2 (\mathrm{Re} < \tilde{\rho}_{21} > \cos \omega_{rf} t + \mathrm{Im} < \tilde{\rho}_{21} > \sin \omega_{rf} t). \quad (3.7)$$

It can then be seen from Eq.(3.7) that the Raman signal has a component in-phase with the applied rf field and one out-of-phase with the applied rf field. With rf phase sensitive detection, the in-phase dispersive signal I (0°) or the out-of-phase absorptive signal I(90°) can be selected [2,19]. Thus, the dispersion and absorption of the magnetic transition are directly related to the real and imaginary parts of the off-diagonal term of the density matrix.

$$\text{Dispersion} \propto I_s (0^\circ) \propto \mathrm{Re} < \tilde{\rho}_{21} > ,$$

$$\text{Absorption} \propto I_s (90^\circ) \propto \mathrm{Im} < \tilde{\rho}_{21} > .$$

The amplitude of the Raman heterodyne signal is given by

$$\text{Amplitude} \propto |< \tilde{\rho}_{21} >| = \sqrt{[\mathrm{Re} <\tilde{\rho}_{21}>]^2 + [\mathrm{Im}<\tilde{\rho}_{21}>]^2} .$$

In experiments, the oscillating electrical signal from the detector that is in-phase with the applied rf field is referred to as the dispersion signal and its magnitude is measured as a function of the applied rf frequency, ω_{rf}. The experimental traces obtained in this way are compared with theoretical calculations of the real part of the off-diagonal density matrix term of an ensemble of two-level atoms. Likewise the out-of-phase signal is termed the absorption and compared with the theoretical calculations of imaginary part of the off-diagonal density matrix term as a function of applied rf field frequency.

3.3 The Experimental Details

3.3.1 Sample and Equipment

An 1× 1× 1 mm^3 diamond cube was mounted in the centre of a six-turn rf coil such that the rf field would be aligned along the [1$\underline{1}$0] direction (Fig.3-2). The response of the rf coil was found to be linear in the frequency range of interest. This enables us to apply more than one rf field to the coil for the pump-probe spectroscopy measurements. The sample and coil were located within an *Oxford Instruments 3T* helium exchange gas cryostat and cooled to liquid helium temperature (~ 4.2K). The cryostat was equipped with a superconducting magnet whose field could be steadily varied from zero to 3 Tesla with an inhomogeneity less than 1 part in 10^5 in a volume of 3 mm^3. The static magnetic field was set to a magnitude close to the level anti-crossing region of the N-V centre (typically, ~ 0.1050 - 0.1070 Tesla in this study) and was at right angle to the coil axis.

The output of a *Coherent* CR599-21 cw, single mode dye laser was focused in the sample. The direction of propagation was along the axis of the rf field. The laser power was a few mW and the frequency coincided with the $^3A \Leftrightarrow {}^3E$ zero phonon optical transition of the N-V centre at 638 nm. The transmitted beam was detected by a *New Focus* model 1801 DC-125 MHz photodiode.

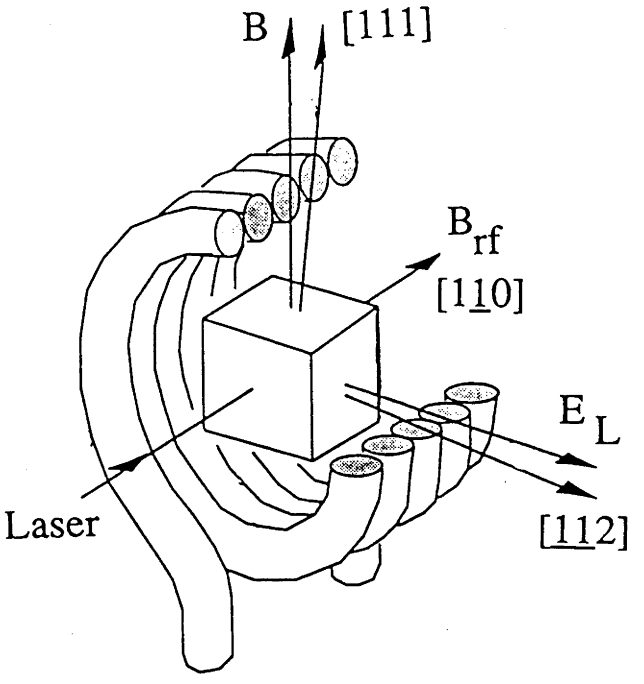

Figure 3-2. The experimental geometry and the directions of laser field, rf field and static magnetic field for Raman heterodyne measurements.

The crystal was rotated within the coil until the static magnetic field was within 1° of the crystallographic [111] direction. This alignment was achieved by recording the transmitted laser intensity at 638 nm as a function of the magnetic field for different crystal orientations while noting the optical spectral hole bleaching effect of the N-V centre [23]. As discussed in Chapter 2, there are four orientations of N-V centres in the crystal. When the magnetic field is aligned along the [111] axis, those N-V centres whose C_3 axis is along the [111] direction have a different electronic spin transition energy than the other three orientations which all have the same energy. At a magnetic field of ~ 600 Gauss the resonance frequencies of all four orientations become equal. This results in a decrease in the transmission due to cross relaxation which, in turn, prohibits spectral hole burning. If the crystal is not well aligned the degeneracy is lifted and three separate lines appear in the transmission vs magnetic field

magnitude. The alignment could be further improved by minimising the frequency of the Raman heterodyne EPR signal by further small changes of the crystal orientation [24] but the situation used in the present study only requires the crystal to be aligned within ~ ±1°.

The amplitude of the rf magnetic field at the rf coil centre is given by [25]

$$B_{rf} = \frac{4\pi N}{\sqrt{L^2 + 4a^2}} I_{rf} , \qquad (3.8)$$

where N is total turns of the coil, I_{rf} is the rf current in Amperes, L and a are the length and radius of the coil, respectively. For the particular rf coil used in the experiments reported here, N = 6, L = 7 mm and a = 8 mm, the rf magnetic field strength at the centre of the coil is

$$B_{rf}\,(\text{gauss}) \approx 7.09\, I_{rf}\,(\text{ampere}) . \qquad (3.9)$$

Therefore, by measuring the current in the rf coil, the rf field strength can be calculated. The dimensions of the diamond crystal (1 mm × 1 mm × 1 mm) may give rise to an inhomogeneity in the rf field strength inside the sample. This would cause N-V centres located at different parts of the sample to experience different rf magnetic field magnitudes. When the crystal is located in the coil centre, the rf field strength difference between the centre and the edges of the sample is estimated with the experimental geometry to be: $\Delta B_{rf} \approx 0.01\, B_{rf}$. This ~1% inhomogeneity is negligible in the low rf field regime. However, in the strong rf field regime this inhomogeneity may cause additional broadening of the magnetic transitions.

The rf magnetic field strength at the coil centre has been measured to have a maximum value of ~ 5 Gauss at a frequency between ~ 4-6 MHz.

However, when the experiments were conducted only relative rf power levels were recorded (labelled by dB) using an rf power attenuator, because it is the spectral changes associated with specific Rabi frequencies that are of interest. The Rabi frequencies of the applied rf field can be conveniently and accurately determined from the nutation frequency or the dynamic "Stark" splitting. It is not experimentally convenient to obtain the rf magnetic field strength by measuring the current in the rf coil from day-to-day experiments. It is however straightforward experimentally to record the Rabi frequencies which is the parameter used in the calculations. This is also more satisfactory in view of the fact that, as discussed in Chapter 2, the transition strength varies with the static magnetic field strength and the crystal alignment which are practically not reproducible from day-to-day measurements.

3.3.2 cw Phase Sensitive Detection

The experimental configuration for cw, phase sensitive Raman heterodyne measurements is shown in Fig.3-3. The laser beam had a diameter of ~ 0.1 mm and a typical power level used was 5 mW. The pump rf field was supplied by a *Hewlett Packard* HP 8601A rf generator and amplified by an *ENI* model 310L 10Watt rf power amplifier. The probe rf field was supplied by a *Hewlett Packard* HP 8443A tracking generator and amplified by an *Amplifier Research* model 5W1000 5Watt rf power amplifier. For ordinary cw profile measurements only one rf source was needed and the pump rf source was disconnected. For the pump-probe spectroscopy measurements the output from two power amplifiers were summed and applied to the rf coil. A 50Ω load was used in all the experiments in order to thermally dissipate the rf fields. The magnetic component of the rf field was perpendicular to the axis of the active centre and had a maximum strength of a few Gauss. The ac voltage generated at the photodiode was amplified and then applied to the rf port of a double balance

mixer. The probe frequency from the HP 8443A tracking generator was used as a local oscillator. The phase of the local oscillator can be adjusted by an *EG&G/ORTEC* model DB463 delay line to give the signal in-phase (dispersive) or out-of-phase (absorptive) with the probe frequency. The in-phase signal is referred to as dispersion and the out-of-phase signal as absorption, which are proportional to the real and imaginary part of the density matrix off-diagonal term, respectively [2]. The output signal from the mixer was amplified by a *Princeton Applied Research* model 113 pre-amplifier and then displayed on an oscilloscope and averaged by a *Princeton Applied Research* model 4202 signal averager or a *Philips* model 3320A digital storage oscilloscope.

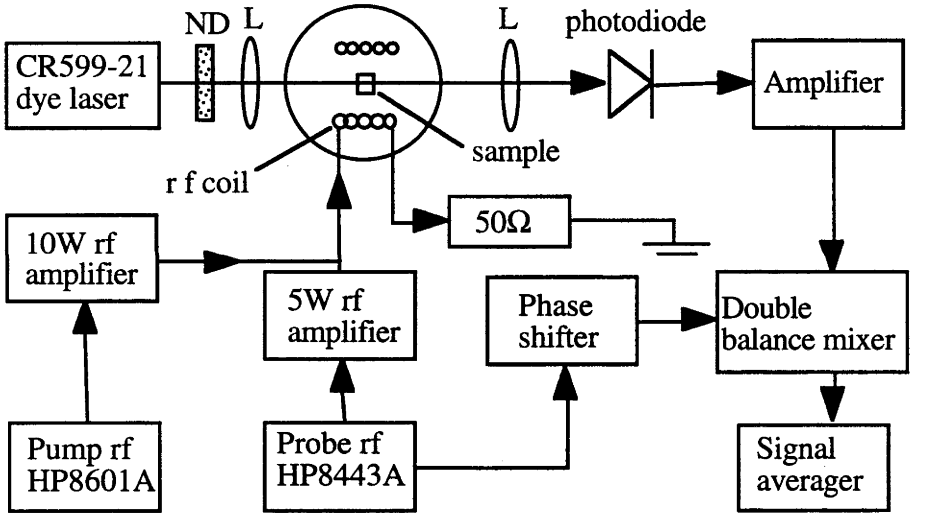

Figure 3-3. Schematic of experimental setup for cw phase sensitive Raman heterodyne measurements. ND: neutral density filter; L: lens.

3.3.3 cw Amplitude Detection

The experimental configuration for cw, amplitude Raman heterodyne measurements is shown in Fig.3-4. The rf equipment used for these experiments was similar to that used for phase sensitive detection. However, instead of using a double balanced mixer, the Raman signal was processed by a

Spectrum Analyzer consisting of a *Hewlett Packard* HP 8553B rf section and *Hewlett Packard* HP 8552B IF section which are swept synchronously with the tracking generator. The phase information is lost in amplitude detection and resultant signal is proportional to the modulus of the off-diagonal term of the density matrix [2,19]. The amplitude detection has the virtue of being more convenient experimentally since it uses a commercial spectrum analyzer rather than a double balanced mixer. For this reason, in routine operation the amplitude detection scheme is used to optimize the experimental parameters as a precursor to phase sensitive detection experiments.

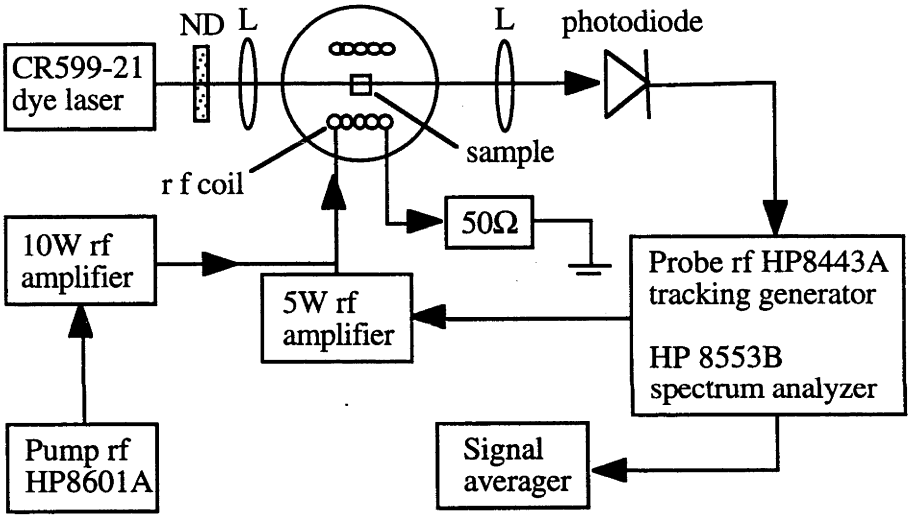

Figure 3-4. Schematic of experimental setup for cw amplitude detection Raman heterodyne measurements. ND: neutral density filter; L: lens.

3.3.4 Transient Measurements

The experimental configuration for transient Raman heterodyne measurements is shown in Fig.3-5. The main differences with these experiments, in comparison with the cw work, was the rf source system. Two rf switch units were used to pulse the cw fields produced by the rf generators. The trigger signal from a home-made pulse generator with adjustable pulse length and repetition rate was used to trigger, simultaneously, the rf switches

and the *Philips* model 3320A digital storage oscilloscope. The frequency of the rf field was held fixed and the time evolution of the Raman heterodyne signal was monitored. For experimental convenience the transient measurements were all carried out using amplitude detection.

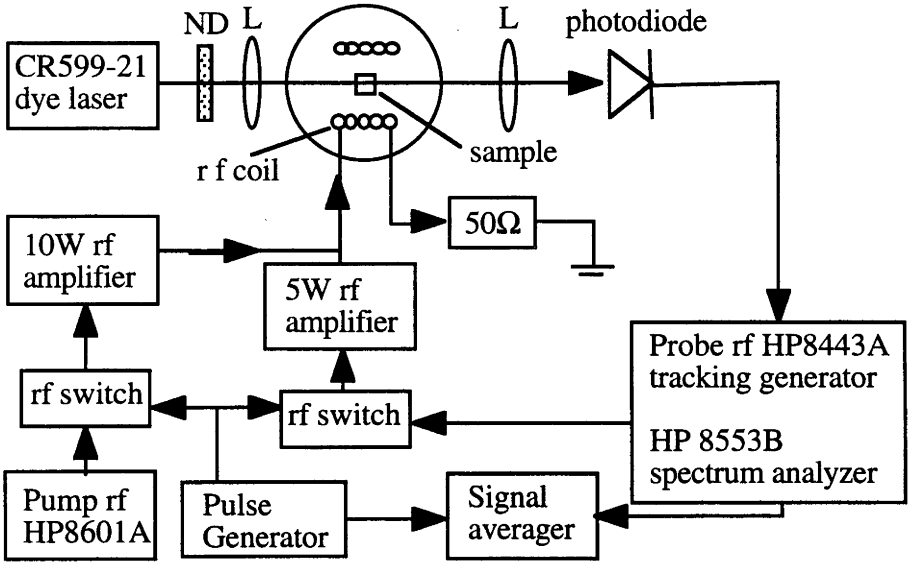

Figure 3-5. Schematic of experimental setup for transient Raman heterodyne measurements. ND: neutral density filter; L: lens.

References

[1] J. Mlynek, N. C. Wong, R. G. DeVoe, E. S. Kintzer and R. G. Brewer, Phys. Rev. Lett. 50, 993, (1983)

" *Raman heterodyne detection of nuclear magnetic resonance* "

[2] N. C. Wong, E. S. Kintzer, J. Mlynek, R. G. DeVoe and R. G. Brewer, Phys. Rev. B28, 4993, (1983)

" *Raman heterodyne detection of nuclear magnetic resonance* "

[3] M. Mitrunaga, E. S. Kintzer and R. G. Brewer, Phys. Rev. Lett. 52, 1484,(1984)

" *Raman heterodyne interference of inequivalent nuclear sites* "

[4] D. R. Taylor, Opt. Commun. 52, 204, (1984)

" *Symmetry analysis of Raman heterodyne interference* "

[5] M. Mitrunaga, E. S. Kintzer and R. G. Brewer, Phys. Rev. B31, 6947,(1985)

" *Raman heterodyne interference: observation and analytic theory* "

[6] E. S. Kintzer, M. Mitrunaga and R. G. Brewer, Phys. Rev. B31, 6958,(1985)

" *Raman heterodyne interference: symmetry analysis* "

[7] L. E. Erickson, Phys. Rev. B32, 1, (1985)

" *NMR measurement of an ion in an excited state by indirect optical detection: A* $^1G_4$ *level of* $LiYF_4:Pr^{3+}$ "

[8] P. D. Bloch, W. S. Brocklesby, R. T. Harley and D. R. Taylor, J. Physique, C7, 523, (1985)

"*Symmetry selection rules in Raman heterodyne detection of nuclear resonance*"

[9] Y. Takahashi, T. Tanake, H. Hatanaka, H. Fukuda and T. Hashi, J.Lumin. 38, 261, (1987)

" *Optical effects in Raman-heterodyne-detected NMR in* $Pr^{3+}:LaF_3$ "

[10] L. E. Erickson, J. Phys. C: Solid State Phys. 20, 291, (1987)

"*A low-magnetic field Raman heterodyne study of the Van Vleck paramagnet* $YAlO_3:Eu^{3+}$ "

[11] N. B. Manson and A. J. Silversmith, J. Phys. C: Solid State Phys. 20, 1507, (1987)

" *RF hole-burning within inhomogeneously broadened Raman heterodyne NMR signals* "

[12] Y. Takahashi, K. Ishikawa, T. Tanake, H. Fukuda. H. Hatanaka and T. Hashi, Phys. Rev. B 38, 7121, (1988)

" *Observation of crystal twinning of* LaF_3 *with Raman heterodyne detection of NMR in* $Pr^{3+}:LaF_3$ "

[13] L. E. Erickson, Phys. Rev. B39, 6342, (1989)

" *Optically detected multipulse nuclear-quadrupole-resonance studies of trivalent praseodymium in zero and weak static magnetic field* "

[14] L. E. Erickson, Phys. Rev. B42, 3789, (1990)

" *Optical-pumping effects on Raman-heterodyne-detected multipulse rf nuclear-spin-echo decay* "

[15] A. Szabo, T. Muramoto and R. Kaarli, Opt. Lett. 13, 1075, (1988)

" *Optical Raman heterodyne detection of ^{27}Al superhyperfine spectra in ruby* "

[16] A. Szabo, T. Muramoto and R. Kaarli, Phys. Rev. B42, 7769, (1990)

" *^{27}Al nuclear-spin dephasing in the ruby frozen core and Cr^{3+} spin-flip-time measurements* "

[17] K. Holliday, X.-F. He, P. T. H. Fisk and N. B. Manson, Opt. Lett. 15, 983, (1990)

" *Raman heterodyne detection of electron paramagnetic resonance* "

[18] N. B. Manson, X.-F. He and P. T. H. Fisk, Opt. Lett. 15, 1094, (1990)

" *Raman heterodyne detected electron-nuclear-double-resonance measurements of the nitrogen-vacancy centre in diamond* "

[19] P. T. H. Fisk, X.-F. He, K. Holliday and N. B. Manson, J. Lumin. 45, 26, (1990)

" *Anomalous lineshapes in Raman heterodyne detected EPR* "

[20] N. B. Manson, P. T. H. Fisk and X.-F. He, Appl. Magn. Reson. 3, 999, (1992)

" *Application of the Raman heterodyne technique for the detection of EPR and ENDOR* "

[21] X. -F. He, PhD Thesis, The Australian National University, Canberra, 1992

" *Raman heterodyne detected magnetic resonance of the nitrogen-vacancy centre in diamond* "

[22] C.B.Harris and W. G. Breiland, "*Coherent spectroscopy in electronically excited states*", in " *Laser and coherent spectroscopy* ", eds. J.I.Steinfeld, (Plenum, New York, 1978)

[23] K. Holliday, N. B. Manson, M. Glasbeek and E. van Oort, J. Phys. :Condens. Matter, 1, 7093, (1989)

" *Optical hole-bleaching by level anti-crossing and cross relaxation in the N-V centre in diamond* "

[24] X. -F. He, N. B. Manson and P. T. H. Fisk, Phys. Rev.B, 47, 8809, (1993)

" *Paramagnetic resonance of photoexcited N-V defects in diamond. I. level anti-crossing in the* ^3A *ground state* "

[25] B. C. Gerstein and C. R. Dybowski, " *Transient Techniques in NMR of Solids: An Introduction to Theory and Practice* ", (Academic, London, 1985)

Chapter 4

Coherent Transient Measurements Using the Raman Heterodyne Technique

4.1 Introduction

When a two-level quantum system is subjected to pulsed, coherent excitation, many interesting effects generally referred to as coherent transients can be observed in times short relative to the relaxation processes. The main interest in studying these effects lies in the fact that firstly, they exhibit very clearly the dynamics involved in the matter-radiation interaction, and thus can be used to obtain a deeper understanding of this interaction, and secondly, they provide spectroscopic information in the time domain which is complementary to that obtained in the frequency domain, from which many important parameters such as transition moments and dephasing times can be obtained. Thus, coherent transients have been extensively studied in the spectral range from magnetic transitions in the radio-frequency region to electric dipole transitions at optical frequencies [1-5].

Various coherent transients observed in the $I_z = |0\rangle \Leftrightarrow |-1\rangle$ ($S_z = 0$) 5.4 MHz NMR transition using the Raman heterodyne technique are described in this chapter including, nutation, free-induction-decay (FID), spin echo, spin-locking, rotary echo and delayed FID. The purpose of this chapter is to demonstrate the versatility of the Raman heterodyne technique. Due to the length limitation, only brief discussions in the Bloch vector model are presented.

4.2 Nutation: Measurement of Rabi frequency

Nutation [6,7] occurs when a strong, coherent field is suddenly applied to an ensemble of two-level systems at equilibrium. The two-level system undergoes alternate absorption and emission as the system is driven coherently between the ground and excited states. The magnitude of this oscillation decays on time scale when relaxation processes become significant. The nutation can be illustrated using the vector model shown in Fig.4-1 for resonant excitation. Initially the Bloch vector **M** lies anti-parallel to the z axis because the u and v components are zero and the ground state is more populated. When a resonant field is turned on, the field vector **F** points along the x axis and causes **M** to precess in the y-z plane at the Rabi flopping frequency.

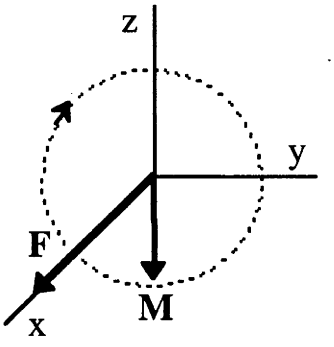

Figure 4-1. The nutation. The field vector **F** causes the Bloch vector **M** to precess in the y-z plane at Rabi frequency χ .

One of the nutation signals associated with the 5.4 MHz I_z=|0>⇔|-1> transition measured by the Raman heterodyne technique is shown in Fig.4-2. The nutation signal has an oscillation period of ~ 19.3 μsec which corresponds to a Rabi frequency of $\chi/2\pi$ ~ 51.8 kHz. In conventional NMR spectroscopy, the observation of nutation is often encumbered by the requirement of detecting the usually weak nutation signal in the presence of the strong rf excitation field. However, by using the Raman heterodyne technique, rather than trying to directly detect the signal at the rf frequency, as a beats signal the nutation can be conveniently observed.

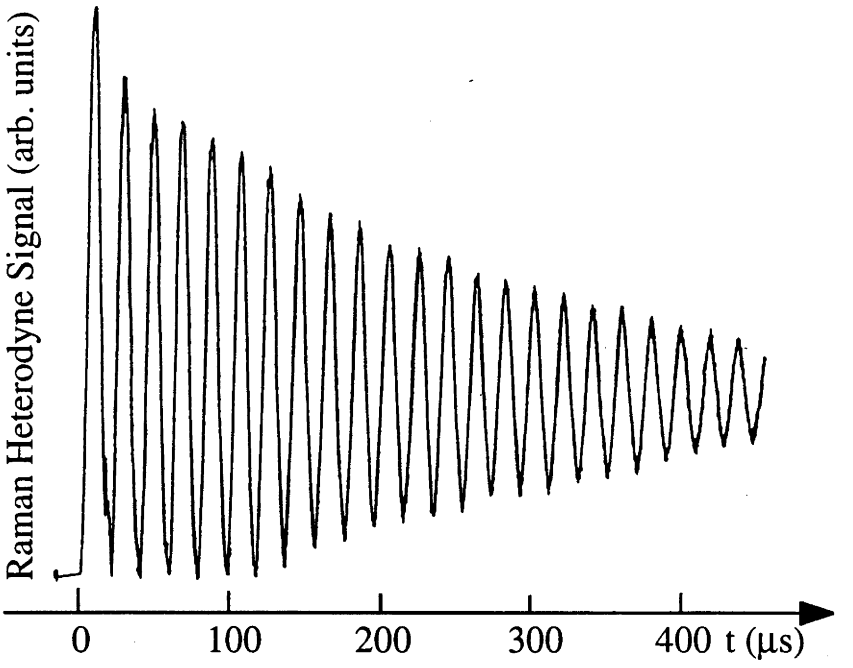

Figure 4-2. Nutation of the 5.4 MHz NMR transition measured using the Raman heterodyne technique.

For a resonant rf field the nutation frequency equals the Rabi frequency χ which is given by

$$\chi = \frac{\mu_{21}\,\mathbf{B}_{rf}}{\hbar}. \qquad (4.1)$$

Therefore, from nutation measurements the Rabi frequency χ can be obtained and the dipole transition moment μ_{21} can be calculated if the rf magnetic field strength $\mathbf{B}_{rf}$ is known. The lengths of the $\pi/2$ and π pulses, which are important experimental parameters for other type coherent transients measurements such as FID and spin echo, can be also determined.

Since the Bloch vector **M** precesses past both the y and z axes, both T_1 and T_2 contribute to its overall relaxation. Solving the Bloch equation, Eq.(1.22), the precise relaxation behaviour can be calculated. For a resonant

excitation the nutation magnitude decays exponentially with the time constant, T_n, given by [2,4-6]

$$\frac{1}{T_n} = \frac{1}{2}\left(\frac{1}{T_1} + \frac{1}{T_2}\right). \qquad (4.2)$$

Thus, from nutation experiments the relaxation times T_1 or T_2 can be deduced. In general, the observed nutation decays faster than for the ideal case due to the presence of inhomogeneity in either the static magnetic field or the rf field ($\delta\mathbf{B}$ or $\delta\mathbf{B}_{rf}$, respectively). The effect of inhomogeneity in the static magnetic field is that it causes different centres to have different resonant frequencies. This may be reduced to an insignificant level by making the rf field sufficiently large. As was discussed in Chapter 1, the field vector **F** lies in the x-z plane. The components along the x and z axis are given by the rf field Rabi frequency χ and detuning Δ, respectively. When the rf field is resonant with the centre of the transition, there is a detuning Δ between the rf field and the different centres within the inhomogeneous distribution. The magnitude of this detuning is $\Delta \sim \Gamma_{inh}$, where Γ_{inh} is the inhomogeneous linewidth of the transition. In the strong rf field limit, the x component χ is much larger than the z component Γ_{inh} arising from the static magnetic field inhomogeneity $\delta\mathbf{B}$. Therefore, the field vector **F** is effectively along the x axis for all centres within the inhomogeneous distribution and the effect of static magnetic field inhomogeneity is negligible. However, there is a practical limit to the strength of rf field since its inhomogeneity, $\delta\mathbf{B}_{rf}$, can become important and cause centres to have different precession frequencies. In what follows we will show that the rf field inhomogeneity can be eliminated by rotary echo or nutation echo measurement.

4.3 Rotary Echo or Nutation Echo: Measurement of T_n

We have seen that in the nutation measurement the effect of the static magnetic field inhomogeneity $\delta\mathbf{B}$ can be overcome by using a sufficiently strong rf field. However, for a sufficiently larger rf field the effect of the rf field inhomogeneity, $\delta\mathbf{B}_{rf}$, becomes significant. Solomon [8] first proposed a method called rotary echo method by which the effect of the rf field inhomogeneity can be eliminated. As is shown in Fig.4-3, when a resonant rf field is applied on an ensemble of two-level systems, the **M** vectors will precess in the y-z plane and, at time $t = \tau$, the angle of precession is $\theta = \chi\,\tau$. Due to the inhomogeneity in the rf field, the **M** vectors will fan out in the y-z plane resulting in a faster decay of nutation signal. If at $t = \tau$, we perform a 180° phase shift on the rf field so that $\mathbf{B}_{rf}$ is suddenly reversed. From then on, the **M** vectors will precess at the same rate as before, but in the opposite direction. Thus those centres that experienced the largest $\mathbf{B}_{rf}$ and hence have precessed the farthest before, now precess fastest in the opposite direction. Therefore, at $t = 2\tau$, the **M** vectors refocuses along the z axis and cause an echo. In this way, the effect of $\delta\mathbf{B}_{rf}$ is minimized which allows the spin relaxation effects including spin-spin relaxation and spin-lattice relaxation to be measured. The rotary echo decays with the time constant given by Eq.(4.2). The reason that the rotary echo is sometimes called nutation echo is obvious from the above discussion.

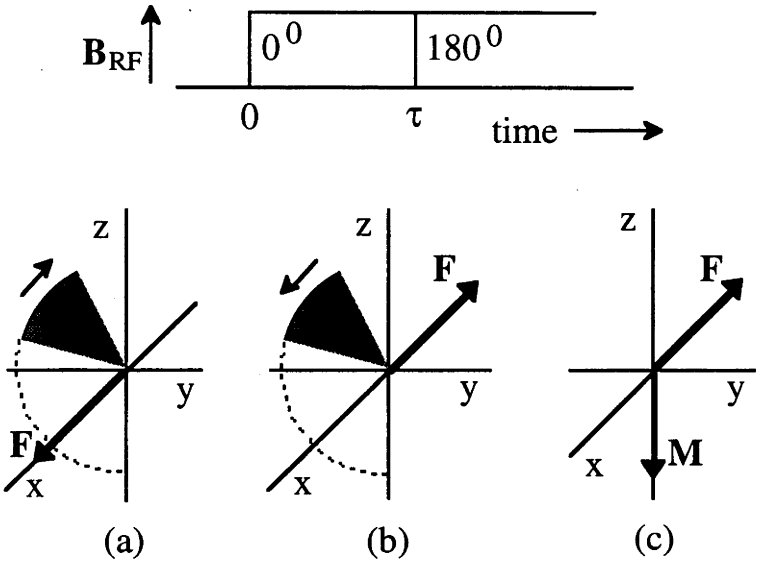

Figure 4-3. The rotary echo or nutation echo. (a) As the **F** is applied along the x axis, the **M** vectors precess in the y-z plane, some moving faster than others because of inhomogeneity in RF field. (b) Phase reversal of the **F** vector causes the **M** vectors to precess in the direction opposite that in (a). (c) The faster moving **M** vectors catch up to the slower moving **M** vectors to form an echo along the z axis.

Fig.4-4 shows a typical rotary echo observed in the 5.4 MHz transition using the Raman heterodyne technique. The nutation has an oscillation period of ~29 μsec corresponding to a Rabi frequency of $\chi/2\pi$ ~ 34.5 kHz. The magnitude of this oscillation would continue to decrease, but a π phase shift occurring at ~600 μsec results in a rotary echo at ~1200 μsec. It is worth noting that the observation of rotary echo indicates the presence of an inhomogeneity in the rf field. However, the relative small magnitude of the rotary echo implies that the rf field inhomogeneity is small in our experiments.

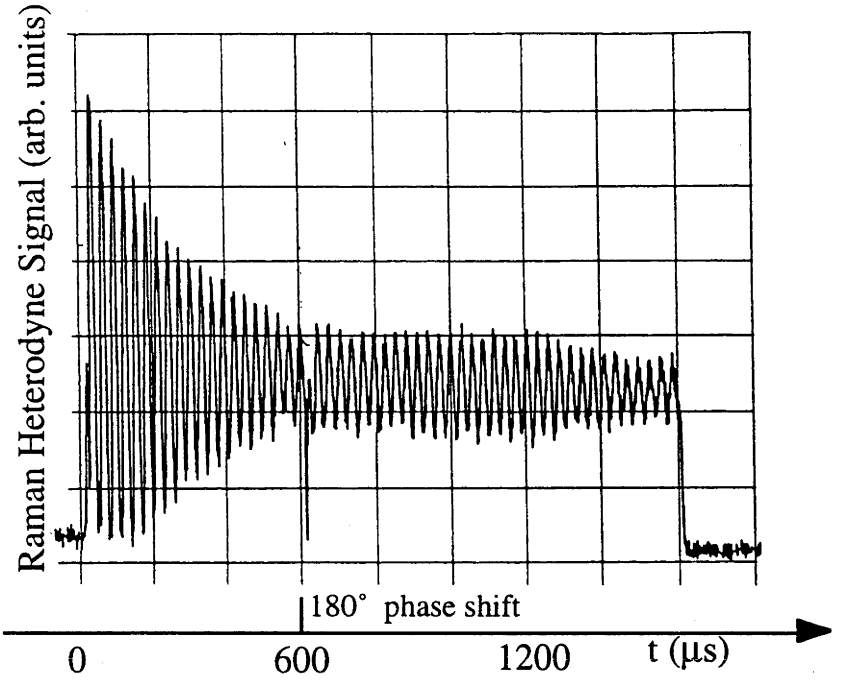

Figure 4-4. Rotaty echo of the 5.4 MHz NMR transition measured using the Raman heterodyne technique.

4.4 Free-Induction-Decay (FID): Measurement of T_2^*

FID [9,10] occurs after an ensemble of two-level systems at equilibrium are subjected to a pulsed excitation for a period of T so that $\chi T = \pi/2$. Fig.4-5 shows a typical experimental FID trace using a ~5.9 μsec $\pi/2$ pulse. The FID signal decays exponentially with a time constant of ~ 88 μsec corresponding to a linewidth of ~ 3.6 kHz.

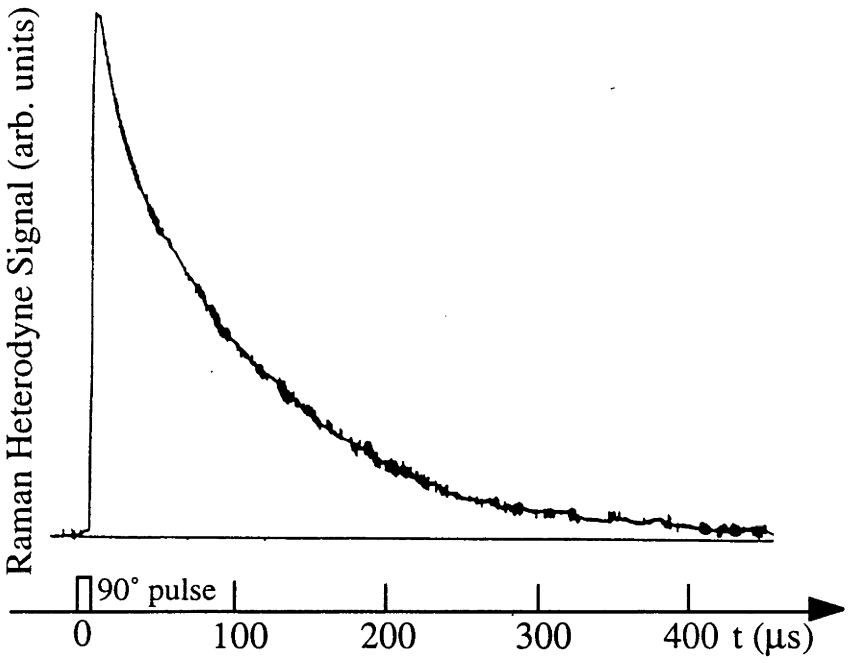

Figure 4-5. Free-Induction-Decay of the 5.4 MHz NMR transition measured using the Raman heterodyne technique.

In the vector model (see, Fig.4-6) the Bloch vector **M** corresponding to a two-level system at equilibrium lies along the z axis. If a strong resonant pulse ($\chi \gg \Gamma_{inh}$) is applied, the field vector **F** lies nearly along the x axis for all centres within the inhomogeneous distribution. Following the $\pi/2$ pulse, **M** lies along the y axis. As transverse relaxation occurs, the coherence decays. If a homogeneous broadened transition is studied then the field vector $\mathbf{F} = 0$ after the $\pi/2$ pulse and the coherence decays freely in a time of T_2 as predicted by the Bloch equation, Eq.(1.22). However, for an inhomogeneous broadened transition after the $\pi/2$ pulse the field vector $\mathbf{F} \neq 0$ due to the presence of inhomogeneity. The field vector **F** lies along the z axis and has a different magnitude for the different centres within the inhomogeneous distribution. In this case the Bloch vectors of different centres process in the x-y plane at different frequencies and as a consequence interfere destructively with each other. This results in a more rapidly decaying signal than in the homogeneous

case. Therefore, in general, the FID signal decays in a time T_2^* which includes contributions from both the pure coherence decay term T_2 and the inhomogeneity term due to both static magnetic field and crystal inhomogeneities.

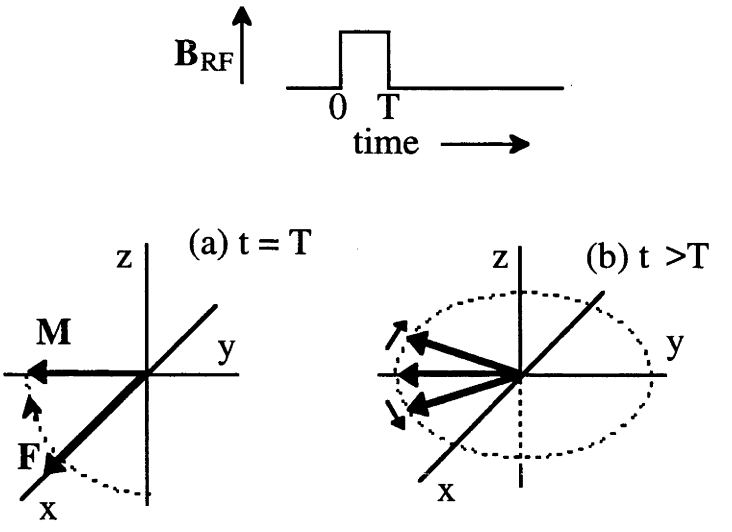

Figure 4-6. The free-induction-decay. (a) At the end of a π / 2 pulse along the x axis the **M** vectors lie along the y axis. (b) Dephasing occurs as the **M** vectors precess at differing rates in the x-y plane.

4.5 Spin Echo: Measurement of T_2

An echo occurs at time 2τ after an ensemble of two-level systems are excited by a $\pi/2$ pulse at time t = 0 and a following π pulse at time t = τ. This ingenious method for measuring T_2 was first proposed by Hahn [11] for magnetic transitions at rf frequencies and later extended to optical frequencies by Kurnit [12]. This method is important because it overcomes the inhomogeneous dephasing process discussed in the previous FID section and allows for the directly measurement of T_2 in the presence of inhomogeneities. The dephasing-rephasing echo process can be visualized using the vector model shown in Fig.4-7.

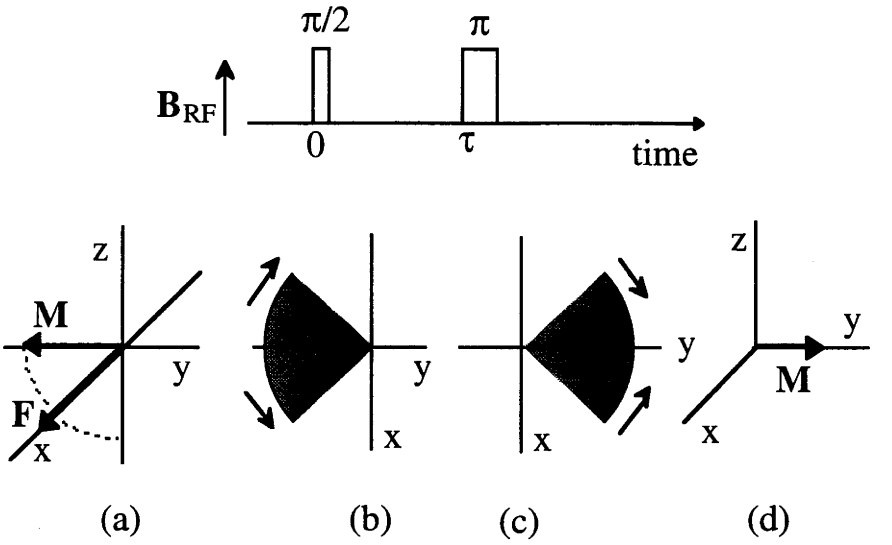

Figure 4-7. The spin echo. (a) A $\pi/2$ pulse along the x axis at t = 0 rotates the **M** vectors along the y axis. (b) Dephasing occurs as the **M** vectors faning out in the x-y plane due to the inhomogeneity. (c) A π pulse along the x axis at $t = \tau$ causes the **M** vectors to rotate 180^0 about the x axis. (d) At $t = 2\tau$ the faster moving **M** vectors catch up to the slower moving **M** vectors to form an echo.

Fig.4-8 shows a typical experimental trace of a spin echo observed in the 5.4 MHz transition using Raman heterodyne detection. The length of the $\pi/2$ and π pulses are ~ 3.3 and 6.6 μsec. The amplitude of the echo decays exponentially with the delay time τ and the transverse relaxation time T_2 can be obtained directly by measuring the echo amplitude as a function of the delay time τ. Fig.4-9 shows a typical experimental plot of the echo amplitude associated with the 5.4 MHz transition as a function of the delay times τ. The transverse relaxation time T_2 determined from the slope is found to be ~ 335 μsec corresponding to a homogeneous linewidth of Γ_h ~ 1 kHz.

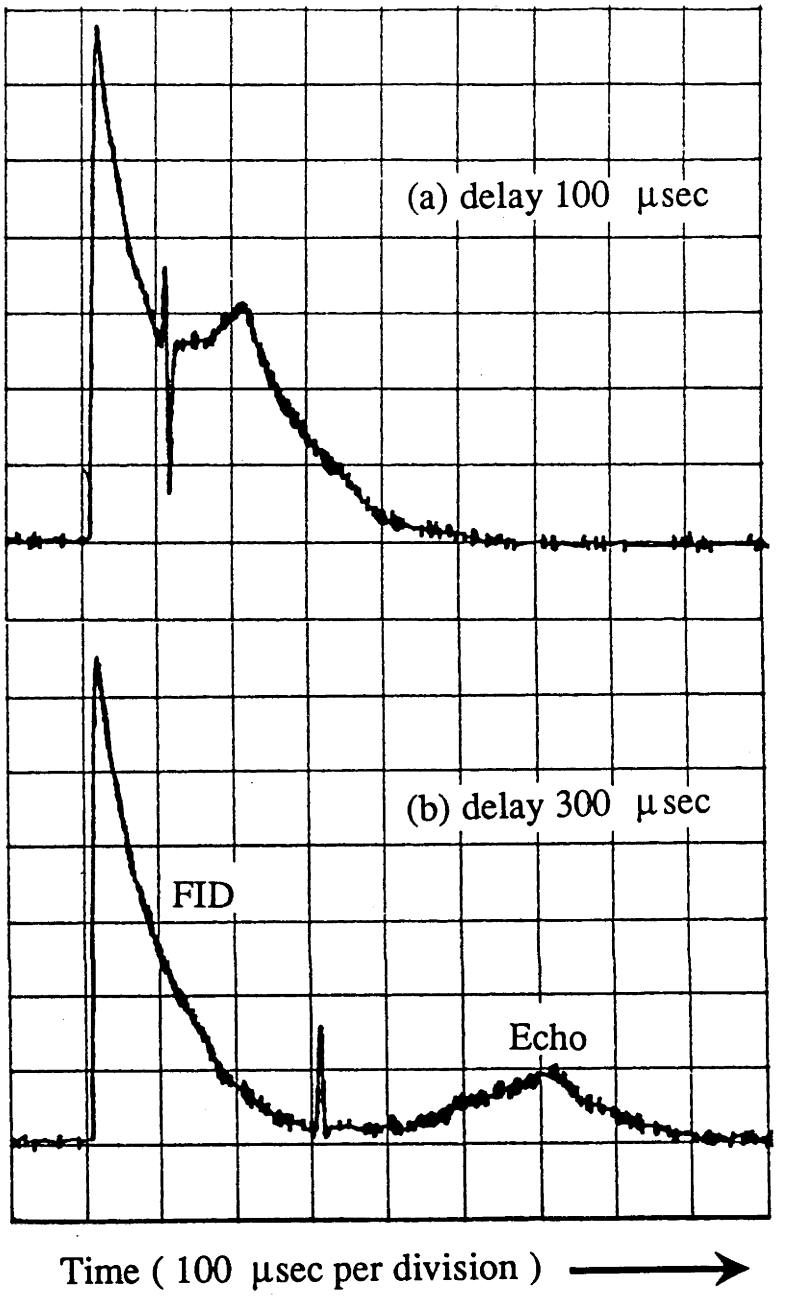

Figure 4-8. Spin echo associated with the 5.4 MHz transition observed using Raman heterodyne technique.

It is again worth noting that the observation of spin echo indicates the presence of the inhomogeneous broadening, but the long FID signal after the first $\pi/2$ pulse and the relative small magnitude of the spin echo implies the inhomogeneous broadening effect is small in our experiments.

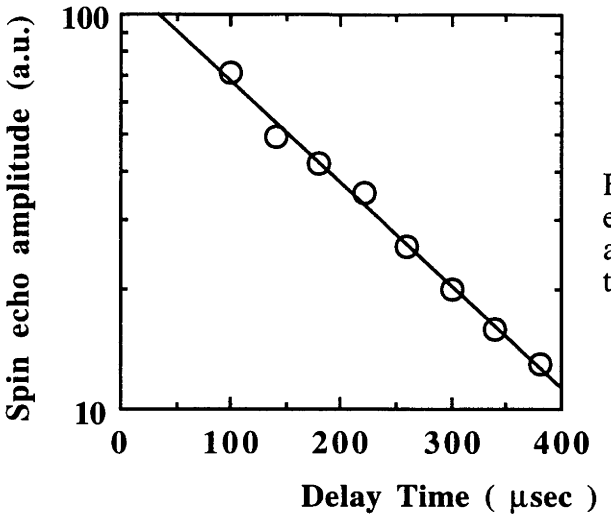

Figure 4-9. The spin echo amplitude as a function of delay time.

4.6 Delayed FID: Measurement of T_1

The longitudinal relaxation time, T_1, can be measured using the delayed FID or inversion-recovery method [2, 13,14]. This method uses a π, τ, $\pi/2$ sequence as shown in Fig.4-10. First a π pulse inverts the Bloch vector **M** along the z axis. After the π pulse longitudinal relaxation occurs, which causes the **M** vector to go from the value of M_0 through zero to its equilibrium value of $-M_0$. If at a time τ after the π pulse, a $\pi/2$ pulse is applied, **M** is rotated to the y axis and gives rise to a FID signal. The size of the FID signal is proportional to the magnitude of **M** at the time τ. Thus, by measuring the FID intensity as a function of delay τ the longitudinal relaxation time can be obtained.

The amplitude of the delayed FID signal $M(\tau)$ at time τ is given by

$$M(\tau) = M(0)\,[\,1 - 2\exp(-\frac{\tau}{T_1})\,]\,. \qquad (4.3)$$

Here M (0) is the amplitude of the normal FID signal of the system. T_1 can be determined from the slope of a plot of ln [M(0) - M(τ)] vs. τ. Fig.4-11 shows one of the experimental traces associated with the 5.4 MHz transition from which T_1 is found to be ~ 1280 μsec.

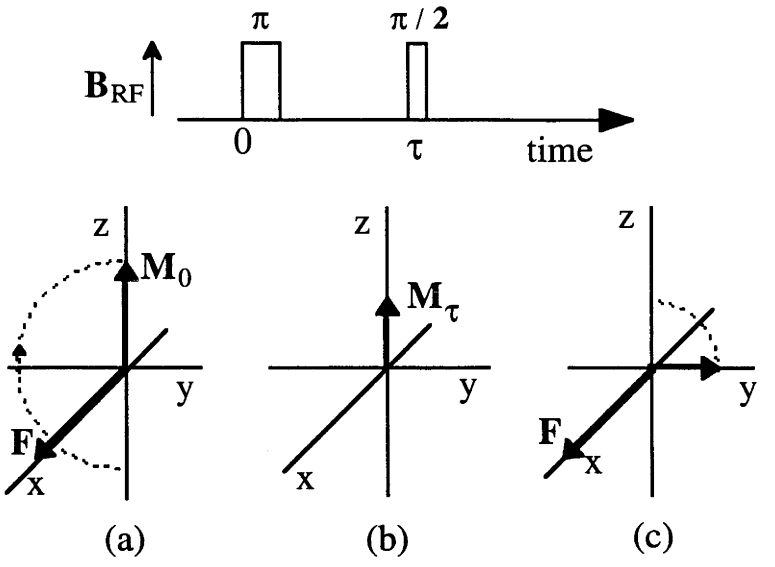

Figure 4-10. Determination of T_1 by π, τ, $\pi/2$ sequences. (a) the Bloch vector **M** is inverted by a π pulse along the x axis at t = 0. (b) **M** decays towards the equlibrium value. (c) At $t = \tau$, a $\pi/2$ pulse rotates **M** to the y axis and causes a FID signal whose amplitude is proportional to the value of **M** at time τ.

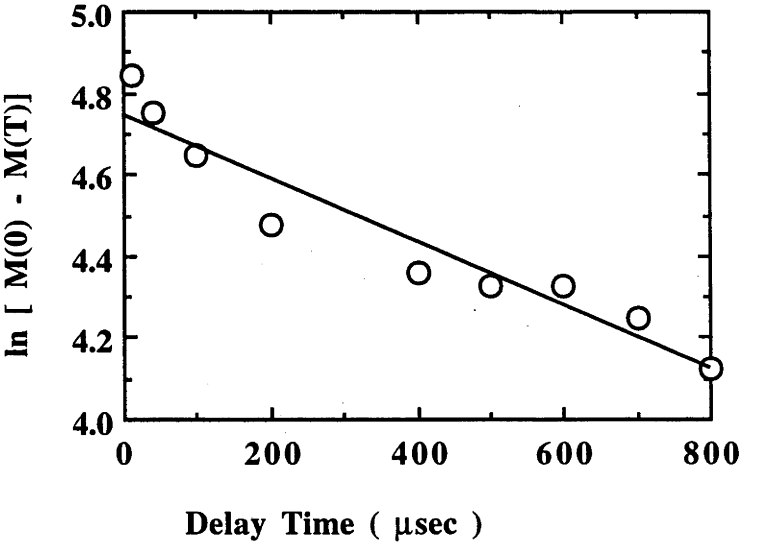

Figure 4-11. A plot of ln [M(0) - M(τ)] as a function of τ, where τ is the delay time between π and $\pi/2$ pulse.

4.7 Spin-Locking: Measurement of $T_{1\rho}$

Another ingenious method for eliminating the effect of the static magnetic field inhomogeneity is a technique called spin-locking [2,15] which can also be easily performed using the Raman heterodyne technique. The vector model describing the spin-locking process is shown in Fig.4-12. A $\pi/2$ pulse applied along the x axis rotates **M** to the y axis. The rf field phase is then immediately changed by $\pi/2$ so that **F** also lies along the y axis where it no longer exerts any torque on **M**.

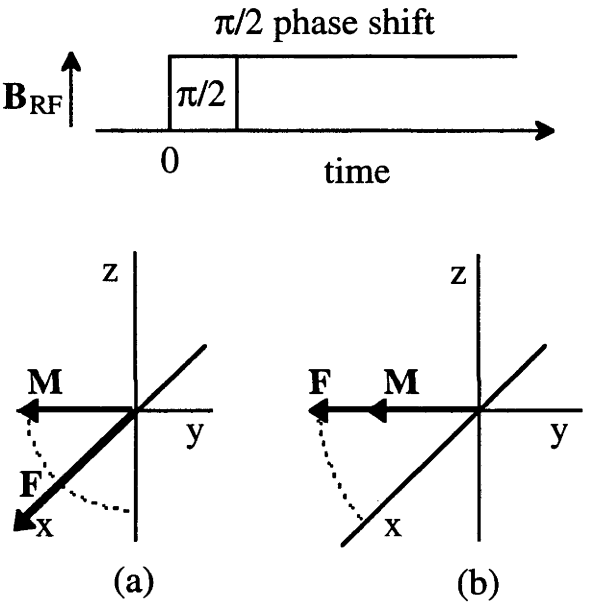

Figure 4-12. The spin locking. (a) A $\pi/2$ pulse applied along the x axis rotates the **M** vector along the y axis. (b) The phase of the RF field is then changed immediately by $\pi/2$ to bring the field vector **F** along the y axis also where it no longer exerts any torque on the **M** vector.

As discussed earlier, due to the inhomogeneity in static magnetic field, $\delta\mathbf{B}$, there will be a non-zero field vector **F** along the z-axis even in the absence of the rf field. After $\pi/2$ pulse, **M** would decay, both because of T_2 processes and because of $\delta\mathbf{B}$ effect. By applying an intense locking field along the y-axis,

the contribution of $\delta\mathbf{B}$ to the field vector **F** becomes negligible, hence the effect of $\delta\mathbf{B}$ is eliminated, and the spin is "locked" along the y-axis.

The relaxation of the **M** vector in the direction of the field vector **F** along the y axis is analogous to spin-lattice relaxation, and for this reason the relaxation is characterized by a time $T_{1\rho}$, which is called the "spin-lattice relaxation time in the rotating frame". Clearly $T_{1\rho}$ must also be closely related to T_2, because in the absence of a locking field, relaxation along the y axis is characterized by T_2. In fact, in liquids $T_{1\rho} = T_2$ and the spin-locking experiment provides an alternative and often convenient method for measuring T_2.

Fig.4-13 shows a typical spin-locking signal associated with the 5.4 MHz transition. Trace (a) shows a nutation signal observed when a constant phase resonant rf field is applied at t = 0. The nutation signal has a 2π period of ~ 20.4 μsec. When a 90° phase shift is introduced at time t = 5.1 μsec, corresponding to a $\pi/2$ pulse, the nutation stops and spin-locking occurs as shown in trace (b). The spin-locking signal is seen to decay exponentially with a time constant of $T_{1\rho}$.

In conventional NMR spectroscopy because it is difficult to detect the signal in the presence of the strong resonant rf field, the decay of the spin-locking is obtained by recording the FID signal intensities after the locking field is switched off as a function of locking period. However, using Raman heterodyne technique, the decay of the spin-locking can be measured directly.

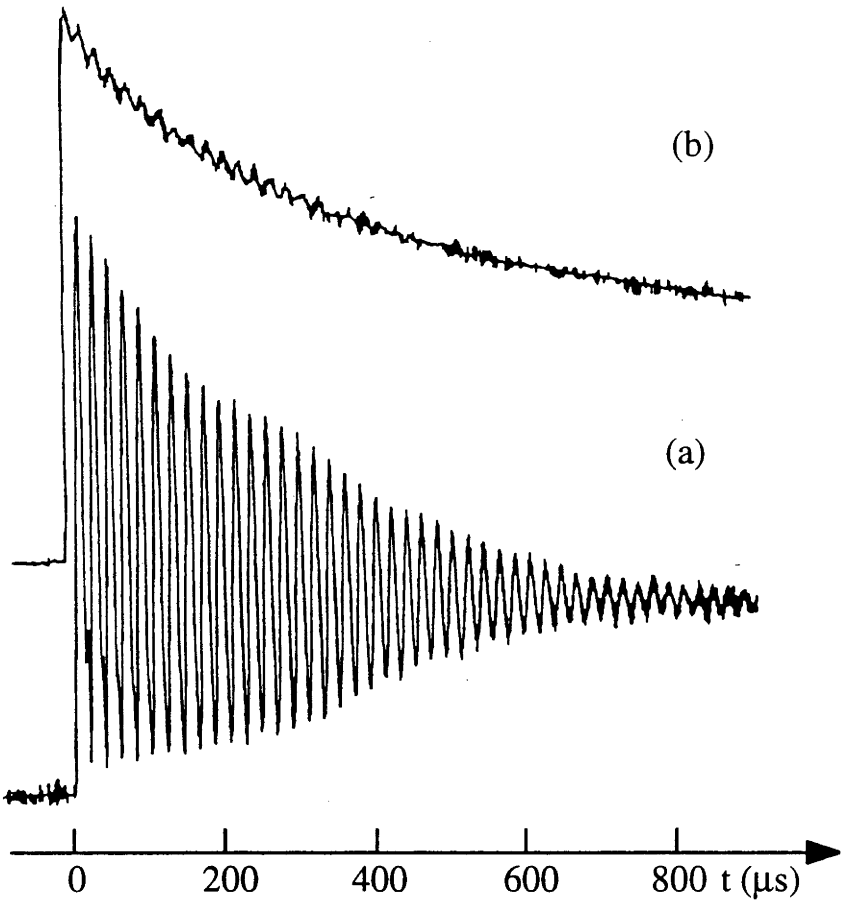

Figure 4-13. Nutation (a) and spin-locking (b) of the 5.4 MHz NMR transition measured using the Raman heterodyne technique.

4.8 The Significance of T_2 approaches T_1: Test of the Bloch Equation Using Spin-Locking Measurements

The Bloch equations [16,17], written as the two-level density matrix equations of motion or the classical torque equations, provide a simple and precise description of the resonance dynamics of two-level system interacting with electromagnetic field [1, 5]. Bloch's assumption of phenomenological damping parameters for the population relaxation time, T_1 (or diagonal, longitudinal, spin-lattice relaxation), and the coherence dephasing time, T_2 (or off-diagonal, transverse, spin-spin relaxation), introduced an element of simplicity in what is otherwise a complicated dynamics problem. It is implicitly

assumed that T_1 and T_2 in the Bloch equations are independent of driving field intensity.

Since the earliest studies of magnetic resonance [18,19], it is well-known that for the situation where $T_2 \sim T_1$ the Bloch equations are appropriate for all fields intensities, however, for the situation where $T_2 \ll T_1$, such as in most low temperature solids, the Bloch equations fail to account for the experimental observations in the strong field limit. Redfield [18] pointed out that for sufficiently strong rf fields, the T_2 spin-spin decay terms of the Bloch equations are partially forbidden because the spin system is unable to absorb the entire energy of the rf-induced nuclear magnetization. The T_2 is not a constant but depends on the field strength and at sufficiently strong fields $T_2 \rightarrow T_1$. Recently, in optical regime, experiments have shown that in the strong field limit the Bloch equations have to be modified [20,21]. For example, the Bloch equations incorrectly predicted a power broadened linewidth of $\chi\ (T_1/T_2)^{1/2}$. However, the experimental observations and the modified Bloch equations suggested a considerable slower power broadening behaviour, χ.[18, 20-22]. It can be seen that the deviation from the Bloch equations is significant only when T_1 value is considerably greater than T_2 value. For example, in the case of the $^1D_2 \Leftrightarrow {}^3H_4$ 592.5 nm optical transition of the $LaF_3:Pr^{3+}$ crystal [20], T_1 = 0.5 ms and T2 = 21.7 μs. This gives a value of $(T_1/T_2)^{1/2} \approx 5$ for the difference in the predicted power broadening behaviour between using the Bloch equations and using the modified Bloch equations. There are other examples showing more dramatical difference such as in an EPR transition of E' centre in silica, T_1 = 200 ms and T_2 = 115 μs [22] which gives $(T_1/T_2)^{1/2} \approx 40$.

Here we will give an illuminating example of testing the Bloch equation using spin-locking measurements. Consider the spin-locking experiment. With a $\pi/2$ pulse the Bloch vector **M** is rotated along the y axis. After the $\pi/2$ pulse

the field vector **F** is also along the y axis, hence, there is no interaction between the **M** and **F** vectors and **M** vector will undergo a free decay. From the Bloch equations, Eq.(1.22), we see that the **M** vector will decay to zero in time T_2. However, experimentally this prediction, derived from the Bloch equations, is found to be not correct for solids. Rather, in solids it is found that as long as the locking field is turned on and is sufficiently strong, the decay rate of **M** is much more like T_1 than a time T_2. The spin-locking decay time $T_{1\rho}$ is not a constant but lengthens with increasing field intensity.

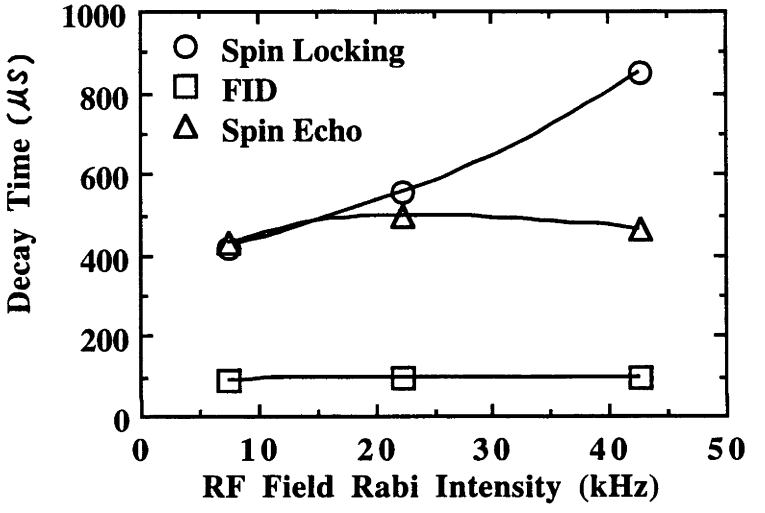

Figure 4-14. The dependence of $T_{1\rho}$, T_2, and T_2^* on the rf field intensity measured by spin-locking, spin echo and FID experiments.

Fig.4-14 shows the dependence of $T_{1\rho}$, T_2, and T_2^* on the rf field intensity measured by spin-locking, spin echo and FID experiments. The rf field Rabi intensity was determined by nutation measurement. It is seen at low rf field intensities that $T_{1\rho}$ is very close to T_2 which is in agreement with the prediction of the Bloch equations. However, $T_{1\rho}$ increases as the rf field intensity increases. The main conclusion from the experimental results shown in Fig.4-14 is that indeed the Bloch equations do not apply at the strong field limit. The other interesting observation is that the T_2 time measured by the spin echo

does not change with the rf field intensity because in spin echo measurement the rf field is only present for very short period and exerts no influence to the relaxation process.

Unlike in most solids where $T_2 \ll T_1$, the 5.4 MHz NMR transition studied in this thesis has a T_2 value close to T_1 value (see, Chapter 5). The difference in the power broadening predicted is only $(T_1/T_2)^{1/2} \approx 2$ (for $T_1 = 4$ T_2), even so, we were able to demonstrate the deviation from the Bloch equations using spin-locking measurements. However, it should be kept in mind that because the value of T_2 is close to that of T_1 the effect of this deviation is relatively small and negligible. Therefore, in the remainder of this thesis, the Bloch equations are applied without any modification in order to avoid extra complexities.

4.9 Conclusion

In this chapter it has been shown that the Raman heterodyne technique can be used to measure various coherent transients including nutation, FID, spin echo, delayed FID, spin-locking and rotary echo. From these measurements important parameters such as Rabi frequency, transition dipole moment, spin-lattice relaxation time and spin-spin relaxation time can be obtained.

I have shown that the deviation from the Bloch equations in the strong field limit. However, this deviation is small and negligible due to the fact that T_1 is only 3 - 4 times greater than T_2. Throughout the rest of this thesis the Bloch equations are used without modification for mathematic simplicity.

Finally, I would like to point out that the purpose of this chapter is to demonstrate the versatility of Raman heterodyne technique when applied to coherent transient measurement. As discussed in Chapter 2, the transition dipole moment and the relaxation rates depend strongly upon the experimental conditions such as crystal alignment and the static magnetic field magnitude. The experimental traces shown in this chapter for various coherent transients were chosen to clearly demonstrate the physical phenomena of interest with no attempt to systematically investigate the parameters which is the topic presented in Chapter 5.

References

[1] A. Abragam, *Principles of Nuclear Magnetism*, (Oxford, London, 1961)

[2] T. C. Farrar and E. D. Becker, *Pulsed and Fourier Transform NMR : Introduction to Theory and Methods*, (Academic, New York, 1971) .

[3] J. I. Steinfeld, ed., *Laser and Coherent Spectroscopy*, (Plenum, New York, 1978)

[4] R. G. Brewer, in R. Balian, S. Haroche and S. Liberman, eds., *Frontiers in Laser Spectroscopy*, (North-Holland Publishing Co., Amsterdam, 1977)

[5] L. Allen and J. H. Eberly, *Optical Resonance and Two-Level Atom*, (Dover, New York, 1978)

[6] H. C. Torrey, Phys. Rev. 76, 1059 (1949)

" *Transient Nutations in Nuclear Magnetic Resonance* "

[7] R. G. Brewer and R. L. Shoemaker, Phys. Rev. Lett, 27, 631, (1971)

" *Photon echo and optical nutation in molecules* "

[8] I. Solomon, Phys. Rev. Lett. 2, 301, (1959)

" *Rotary spin echoes* "

[9] E. L. Hahn, Phys. Rev., 77, 297, (1950)

" *Nuclear Induction due to Free Larmor Precession* "

[10] R. G. Brewer and R. L. Shoemaker, Phys. Rev. A, 6, 2001, (1972)

" *Optical Free Induction Decay* "

[11] E. L. Hahn, Phys. Rev. 80, 580, (1950)

" *Spin Echoes* "

[12] N. A. Kurnit, I. D. Abella and S. R. Hartman, Phys. Rev. Lett. 13, 567, (1964)

" *Observation of a photon echo*"

[13] E. Fukushima and S. B. W. Roeder, " Experimental Pulsed NMR: A nuts and bolts approach. ", (Addison-Wesley, Reading, Massachusetts, 1981)

[14] H. Y. Carr and E. M. Purcell, Phys. Rev. 94, 630, (1954)

" *Effects of diffusion on free precession in nuclear magnetic resonance experiments* '

[15] I. Solomon, C. R. Acad. Sci. 248, 92, (1959)

[16] F. Bloch, Phys. Rev. 70, 460, (1946)

" *Nuclear induction* "

[17] F. Bloch, W. W. Hansen and M. Packard, Phys. Rev. 70, 474, (1946)

" *The nuclear induction experiment* "

[18] A. G. Redfield, Phys. Rev. 98, 1787, (1955)

" *Nuclear magnetic resonance saturation and rotary saturation in solids* "

[19] C. P. Slichter and W. C. Holton, Phys. Rev. 122, 1701, (1961)

" *Adiabatic demagnetization in a rotating reference system* "

[20] R. G. DeVoe and R. G. Brewer, Phys. Rev. Lett. 50, 1269, (1983)

" *Experimental test of the optical Bloch equations for solids* "

[21] A. Schenzle, M. Mitsunaga, R. G. DeVoe and R. G. Brewer, Phys. Rev. A30, 325, (1984)

" *Microscopic theory of optical line narrowing of a coherently driven solid* "

[22] R. Boscaino and V. M. La Bella, Phys. Rev. A, 41, 5171, (1990)

" *Anomalous rate of free-induction-decay* "

Chapter 5

Characterization of NMR Transition at Level Anticrossing Region

5.1 Introduction

The characteristics of the NMR transitions of interest are significantly modified by the wave function mixing that depends strongly on the static magnetic field. Thus the characteristics of the NMR transition also have a strong dependence on the static magnetic field strength. The experimental characterization of the 5.4 MHz $I_z = |0\rangle \Leftrightarrow |-1\rangle$ transition is presented in this chapter. Also, various parameters including, transition dipole moment, longitudinal relaxation time T_1, transverse relaxation time T_2 and inhomogeneous linewidth are studied as a function of the static magnetic field strength.

5.2 Transition Strength as a Function of Magnetic Field

The transition strength or transition dipole moment can be determined by measuring the Rabi frequency associated with a known excitation intensity. The Rabi frequency can be determined directly from the nutation frequency (see, Chapter 4) or the Autler-Townes splitting (see, Chapter 8). In this chapter the Rabi frequency is obtained using the Autler-Townes splitting measurement.

By applying a rf field resonant with the 5.4 MHz transition, the 4.7 MHz transition is observed to be split into two components, the so-called Autler-Townes splitting [1], and the splitting equals the Rabi frequency associated with the 5.4 MHz transition. This Autler-Townes splitting, and

hence the Rabi frequency associated with the 5.4 MHz transition, is measured as a function of the static magnetic field strength and the result is shown in Fig.5-1. Likewise, when the rf field is resonant with the 4.7 MHz transition, the 5.4 MHz transition is split into two components and this splitting gives directly the Rabi frequency associated with the 4.7 MHz transition. A plot of the Rabi frequency of this transition vs. magnetic field strength is also shown in Fig.5-1.

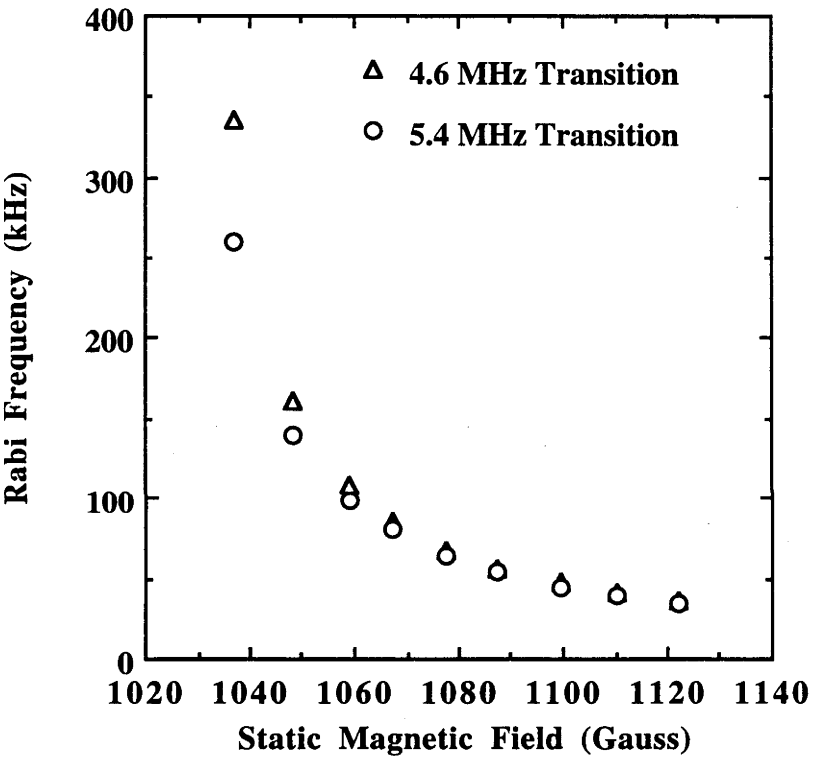

Figure 5-1. Rabi frequencies associated with 5.4 MHz (circle) and the 4.7 MHz (triangle) transitions as a function of static magnetic field strength measured by Autler-Townes splitting.

In the |Sz,Iz> representation, the magnetic dipole moment operator is given by [2],

$$\hat{\mathcal{H}} = \frac{\sqrt{2}}{4\pi i}$$

	|-1,-1>	|-1,0>	|-1,+1>	|0,-1>	|0,0>	|0,+1>
<-1,-1|	0	γ_n	0	$-\gamma$	0	0
<-1,0|	$-\gamma_n$	0	γ_n	0	$-\gamma$	0
<-1,+1|	0	$-\gamma_n$	0	0	0	$-\gamma$
<0,-1|	γ	0	0	0	γ_n	0
<0,0|	0	γ	0	$-\gamma_n$	0	γ_n
<0,+1|	0	0	γ	0	$-\gamma_n$	0

(5.1)

where γ and γ_n are the electronic and nuclear gyromagnetic ratio, respectively. The transition strength, $\mu_{SI} = \langle S_z, I_z | \hat{\mathcal{H}} | S_z', I_z' \rangle$, between any two levels of the ^3A state at various static magnetic field strengths and orientations can be calculated by using Eq.(5.1) and the wave functions of the spin Hamiltonian, Eq.(2.6). In usual circumstances, γ is much larger than γ_n ($\gamma/\gamma_n \sim 10^3$). Therefore, the EPR transition strength is much stronger than the NMR transition strength. In the level anticrossing region, however, the NMR transition strengths are substantially enhanced due to the wave function mixing. This gives rise to NMR signals that are comparable to those of EPR.

Using the wave functions with the first order correction, Eq.(2.10), the transition strengths of the 5.4 and 4.7 MHz transition were calculated as a function of the static magnetic field magnitude and were plotted in Fig.5-2 (solid lines). In the calculation the adjustable parameters are the rf field strength and the crystal orientation which are taken to be 2 Gauss and 0.5°, respectively.

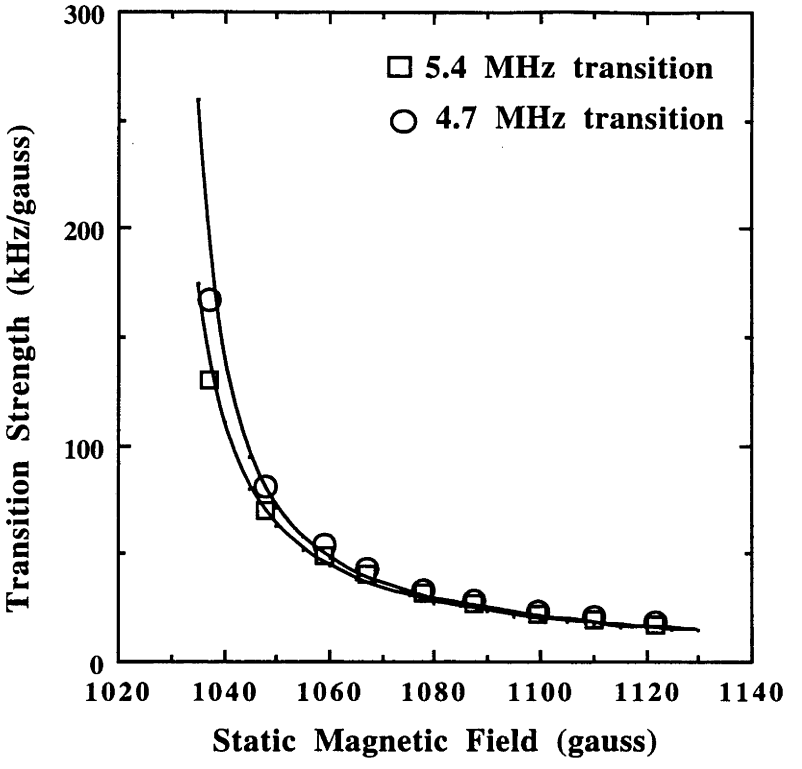

Figure 5-2. The transition dipole moments associated with the 5.4 MHz (circle) and the 4.7 MHz (triangle) transitions as a function of static magnetic field strength measured by Autler-Townes splitting. The calculated results are also shown for comparison in solid lines.

The transition strength can be obtained experimentally from the Rabi frequency measurement (see, Fig.5-1). The experimental transition strength as a function of the magnetic field strength is also shown in Fig.5-2. From the experiments the measured Rabi frequency is accurate to ~±2%, the static magnetic field magnitude to ~± 5% and the rf field strength to ~± 10%. Allowing the above experimental parameters to be adjustable, it is seen that the calculation is in good agreement with the experiments. These results confirm the main characteristic behaviour that, as the static magnetic field approaches the value associated with the level anticrossing, the transition dipole moment increases. This increase is associated with the increasing wave function mixing near level anticrossing. The transition dipole moment for the 5.4 (4.7) MHz

transition is increased by a factor of ~ 7.6 (9.3) as the magnetic field approaches the level anticrossing value from above (~ 1122 → ~ 1037 Gauss). Away from the anticrossing region, the 5.4 MHz and 4.7 MHz transitions have a similar transition strength as they are equivalent $\Delta I = \pm 1$ nuclear transitions, however, close to the anticrossing region the 4.7 MHz transition has a larger transition dipole moment. The typical magnetic field strength used in the experiments was ~ 1050-1070 Gauss. In this region the transition strength associated with the 5.4 MHz transition has a magnitude of ~ 40 - 70 kHz/Gauss which is about 120 - 210 times stronger than the normal nitrogen nuclear transition strength of 0.3 kHz/Gauss.

5.3 Relaxation time T_1 and T_2 as a Function of Magnetic Field

The longitudinal relaxation time T_1 (square) measured by delayed FID and the transverse relaxation time T_2 (circle) measured by spin echo associated with the 5.4 MHz $I_z=|0\rangle\Leftrightarrow|-1\rangle$ transition were measured as a function of the static magnetic field strength as shown in Fig.5-3.

Both T_1 and T_2 are found to decrease as the magnetic field magnitude approaches the level anticrossing region and the ratio between them remains nearly constant of $4<T_1/T_2<6$ as shown in Fig.5-4.

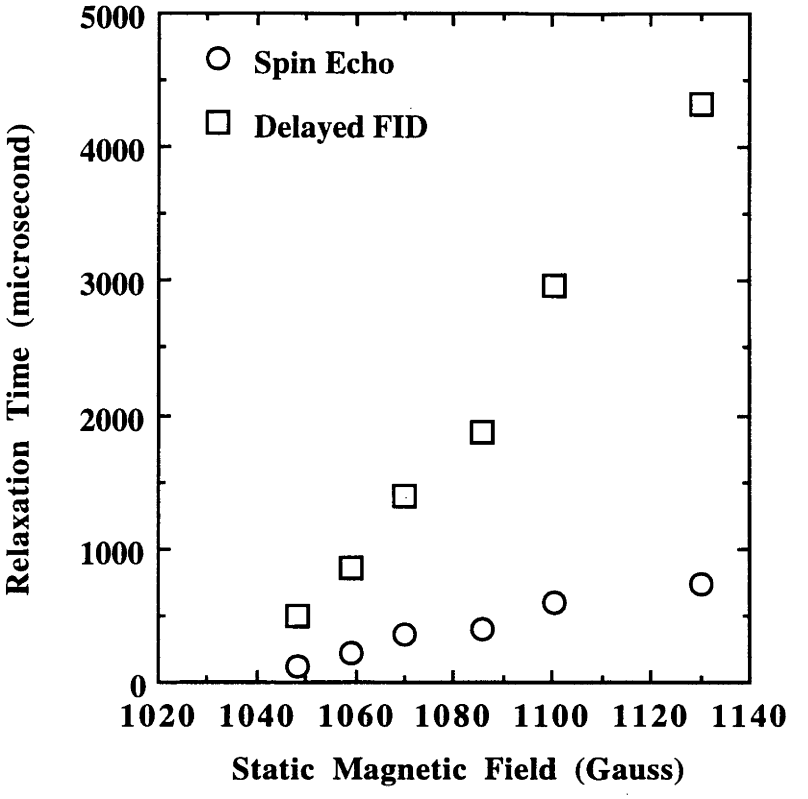

Figure 5-3. T_1 (square) and T_2 (circle) as a function of the static magnetic field strength.

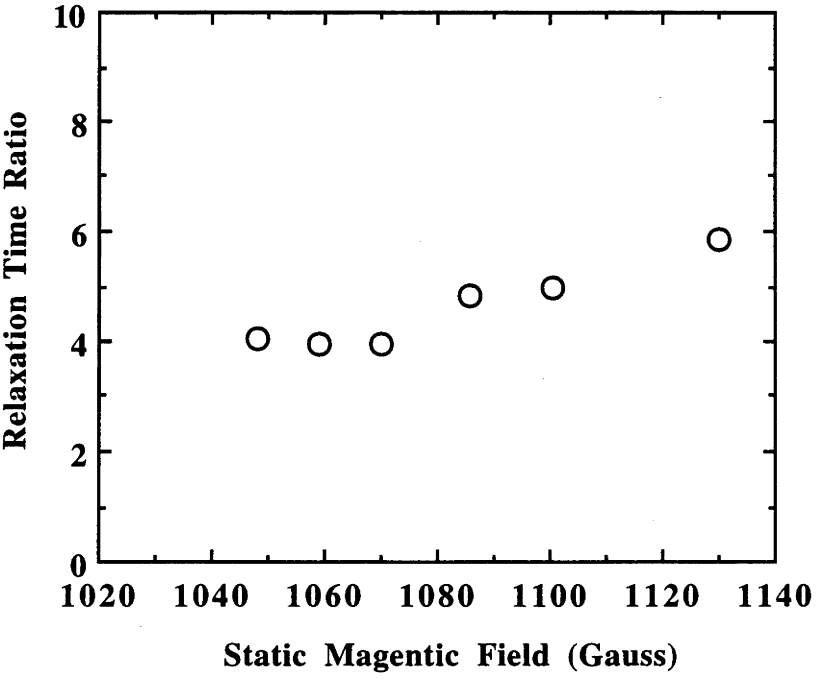

Figure 5-4. T_1/T_2 as a function of the static magnetic field strength.

It is well known that in many paramagnetic systems the dipole-dipole interaction is the dominant relaxation mechanism [3]. As was discussed in the previous section the transition dipole moment associated with the 5.4 MHz transition is enhanced by up to 2 orders of magnitude due to the wave function mixing. With such a large transition dipole moment, it is reasonable to assume that the relaxation processes occur mainly through dipole-dipole interactions. As the transition dipole moment increases as magnetic field strength approaches the level anticrossing value, the dipole-dipole interaction becomes stronger which leads to faster relaxation rates and hence short relaxation times.

The spin-spin relaxation involves energy conserving spin "flip-flops" of the neighbouring similar spins and hence is a resonant process, whereas the spin-lattice relaxation involves energy transfer from the spin system of interest to other energy reservoirs in the system. It is, thus, common in most solids that the spin-spin relaxation is faster than the spin-lattice relaxation. Therefore, it is common in solids for $T_2 \ll T_1$. In the case of the N-V centre, it is expected that the dominant mechanism for spin-lattice relaxation is the interaction between the nuclear and the electronic spins. Such a process is usually slow because the NMR and EPR transition frequencies differ by many orders of magnitude. However, in the case of the N-V centre, in the level anticrossing region the EPR frequency is less than 100 MHz. In this region, the spin-lattice relaxation rates are greatly enhanced and T_1 and T_2 are within one order of magnitude of each other as shown in Fig.5-3. It is expected that if the EPR and NMR transitions have the same frequencies then T_1 will equal T_2. When the static magnetic field magnitude is increased away from the level anticrossing region the EPR transition frequency becomes larger and thus the T_1/T_2 ratio increases slightly from ~ 4 to ~ 6.

5.4 Linewidth as a Function of Magnetic Field

The inhomogeneous linewidth Γ_{inh} of the 5.4 MHz Iz=|0>⇔|-1> transition was measured as a function of the static magnetic field strength using either cw (triangle and square) or pulsed (circle) methods as shown in Fig.5-5. In the cw measurement the absorption profile associated with the 5.4 MHz transition was obtained and the linewidth was measured. In the pulsed method the decay time T_2^* of a FID signal was obtained and the linewidth is deduced from $(\pi T_2^*)^{-1}$.

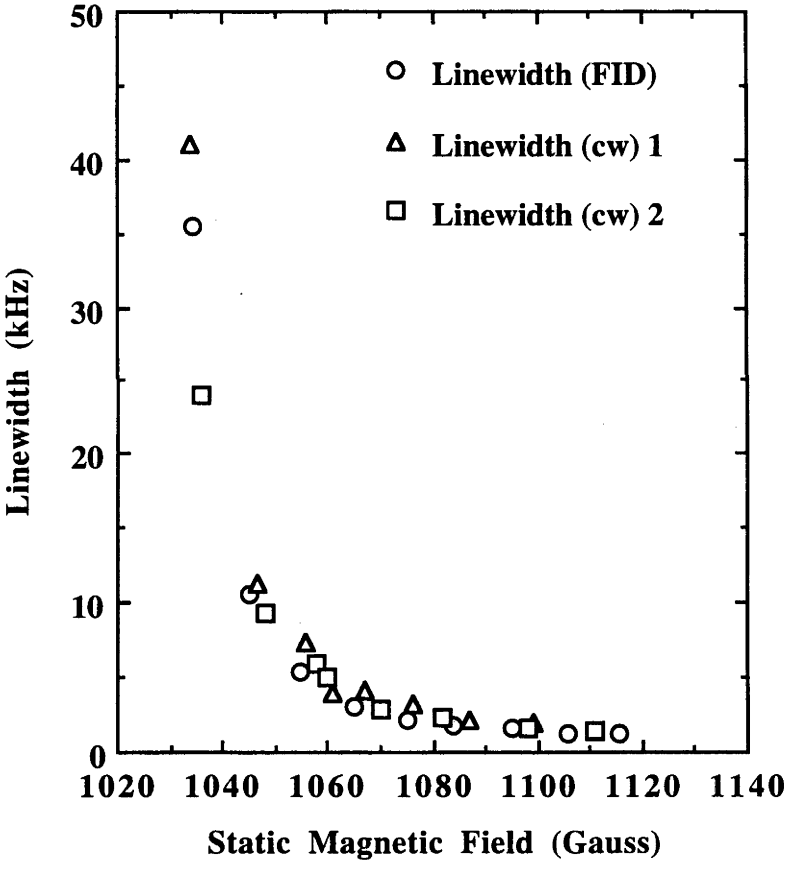

Figure 5-5. Inhomogeneous linewidth Γ_{inh} of the 5.4 MHz transition as a function of the static magnetic field strength.

It is seen from Fig.5-5 that the inhomogeneous linewidth Γ_{inh} obtained from cw and pulsed measurements are in good agreement and increases as the

static magnetic field strength nears the anticrossing region. To compare the inhomogeneous, Γ_{inh}, and homogeneous, Γ_{hom}, linewidth the decay time of FID, T_2^* (circle), and of spin echo, T_2 (square), are measured as a function of the static magnetic field strength as shown in Fig.5-6.

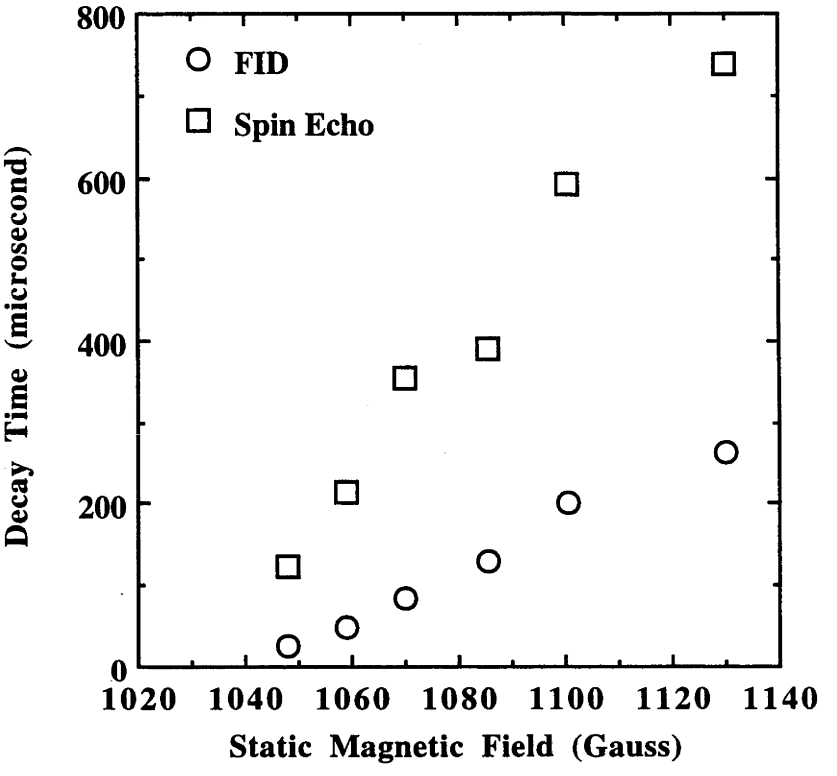

Figure 5-6. T_2^* (circle) and T_2 (square) as a function of the static magnetic field strength.

The inhomogeneous linewidth, Γ_{inh}, deduced from the FID measurement and the homogeneous linewidth, Γ_{hom}, deduced from the spin echo measurement is compared as shown in Fig.5-7.

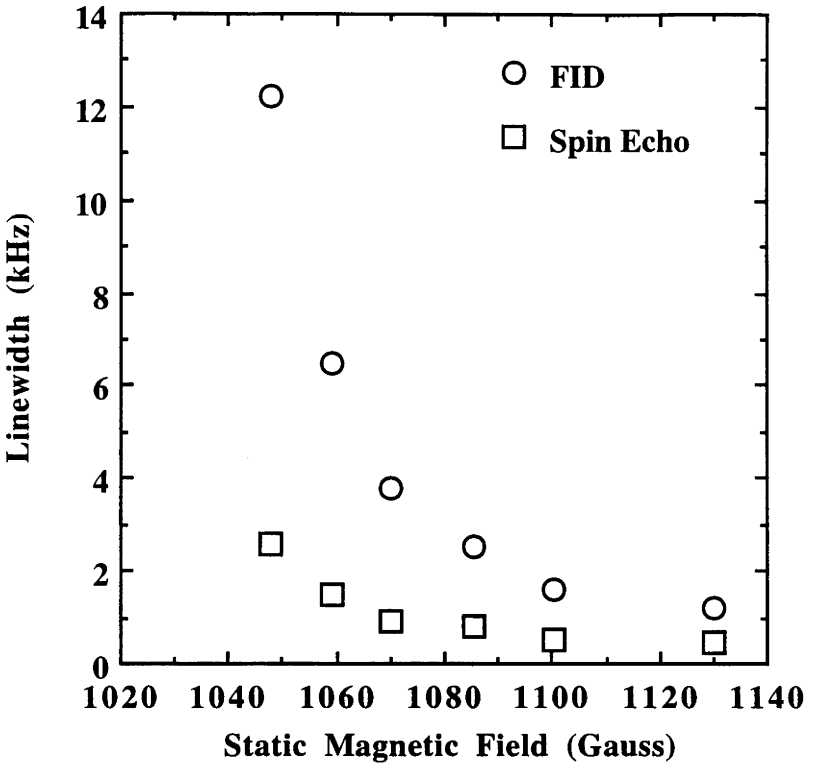

Figure 5-7. Inhomogeneous Γ_{inh} (circle) and homogeneous Γ_{hom} (square) linewidth as a function of the static magnetic field strength.

In solids the NMR transition is often inhomogeneously broadened due to either the inhomogeneity of the static magnetic field or the inhomogeneity of the lattice. The NMR transition of N-V centre in diamond studied is inhomogeneously broadened, but the effect of the inhomogeneous broadening is relatively small. Fig.5-8 shows the ratio of the inhomogeneous linewidth and the homogeneous linewidth as a function of the static magnetic field strength. It is seen that the ratio remains nearly constant of, $3<\Gamma_{inh}/\Gamma_{hom}<5$.

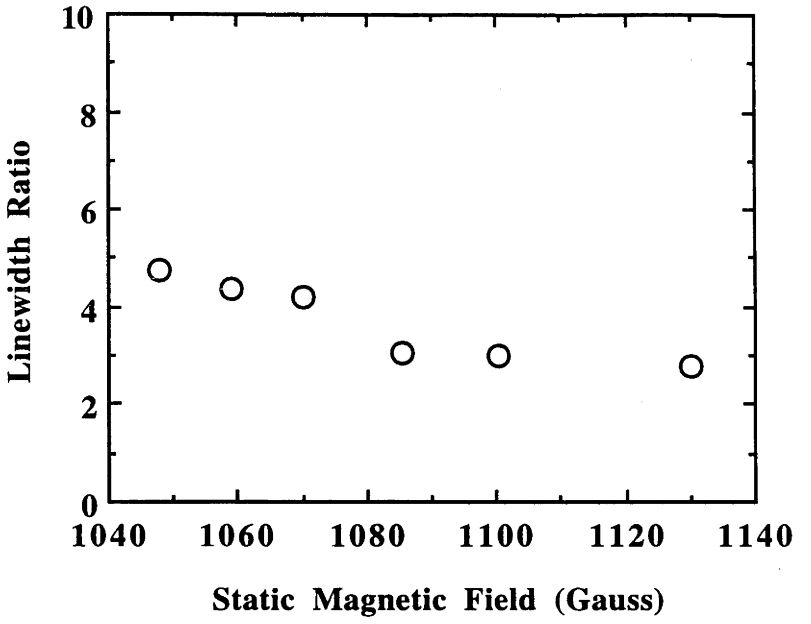

Figure 5-8. The ratio between the inhomogeneous linewidth and the homogeneous linewidth, $\Gamma_{inh}/\Gamma_{hom}$, as a function of the static magnetic field strength.

5.5 Conclusion

Various parameters associated with the 5.4 MHz $I_z = |0\rangle \Leftrightarrow |-1\rangle$ NMR transition were measured using the Raman heterodyne technique. The main purpose of this chapter was to demonstrate that the two-level system associated with the 5.4 MHz transition is a nearly ideal two-level system.

As was discussed in Chapter 1, an "ideal" two-level system is a system that exhibits no inhomogeneous broadening, $\Gamma_{inh} \Rightarrow \Gamma_{hom}$, and the transverse relaxation is limited by the longitudinal relaxation, $T_2 \Rightarrow T_1$. In the case of the 5.4 MHz transition it was shown that (i) inhomogeneous broadening is relatively small, $\Gamma_{inh} \approx 3 - 5\ \Gamma_{hom}$, and (ii) T_2 is of the same order of magnitude as T_1, $T_1 \approx 4 - 6\ T_2$. Both the ratios are considered small in contrast with a normal transition in the solid state where the ratios would be »100.

Furthermore, the transition strength is greatly enhanced due to the wave function mixing. Therefore, the 5.4 MHz transition in the N-V centre studied is very close to an "ideal" two-level system. This transition suits the overall purpose of this thesis which is to study the interaction between an ideal two-level system and electromagnetic fields.

References:

[1] S.H.Autler and C.H.Townes, Phys. Rev.,100, 703, (1955)

" *Stark effect in rapidly varying fields* "

[2] C. P. Poole and H. A. Farach, " *The Theory of Magnetic Resonance* ", (Wiley, NY, 1972)

[3] T. C. Farrar and E.D. Becker, " *Pulsed and Fourier Transform NMR* ", (Academic Press, New York, 1971)

Chapter 6

Absorption and Dispersion Profiles of a Strongly Driven Two-level System Probed by a Weak Field

As discussed earlier, in the level anticrossing region the $I_z=|0\rangle\Leftrightarrow|-1\rangle$ 5.4 MHz transition has the following characteristics: (i) the transition has a large transition strength, (ii) T_1 and T_2 are within one order of magnitude and (iii) there is only a small amount inhomogeneous broadening. With such a nearly ideal two-level system and the very sensitive Raman heterodyne technique, I have undertaken extensive experimental studies on the interaction between a two-level system and strong electromagnetic fields. This chapter deals with the situation where the strongly driven two-level system is probed by a weak field. The absorption and dispersion profiles of a weak field probing a driven two-level system are investigated at various pump field intensities and detunings using the Raman heterodyne technique. Sections of this chapter have been edited by the supervisor and published in Phys. Rev. A, June 1994.

6.1 Introduction

It is well known that a strong, resonant electromagnetic field can significantly modify the response of a two-level system. The simplest case is where the strongly driven two-level system is studied by a weak probe field and theoretical considerations of such a situation have been very thoroughly studied [1-7]. The experimental situation is surprisingly less satisfactory. Few systems behave as ideal two-level system. The experiments can be difficult, and there are restrictions on the profiles which can be measured. Hence, there have been few complete experimental investigations of the response of a strongly driven

two-level system probed by a weak field and there is considerable scope for further experimental work. This study was initiated to improve this situation.

Any transition energy is applicable and already the examples illustrating aspects of the changes caused by a strong driving field to the absorption, emission and dispersion profiles (including cases of two- and three-level systems) cover the radio-frequency [8,9], microwave [10], infrared [11] and the visible [12-15] wavelengths. There are practical restrictions associated with each wavelength region. In the visible, for example, it is not practical to obtain the dispersion profiles without elaborate interferometric measurements. However, in the radio-frequency regime it is straightforward to measure both the absorption and dispersion profiles and these are covered in this work.

The absorption spectrum of a weak field probing a driven two-level system has been calculated by Mollow [4] using a density matrix equations of motion formalism and this approach forms the basis of the calculation presented in this chapter. Indeed in his paper Mollow predicted dynamic Stark splitting and also pointed out that amplification was possible without inversion and these are topics of current interest. In 1974, Bonch-Bruevich *et al.* [8] reported the equivalent experimental measurements of the absorption and dispersion profiles of a driven two-level NMR transition of ^{113}Cd in a vapour. The experiment is consistent with theory but the profiles have been taken using point by point measurements and it is not possible to make a very detailed comparison with theory. In the optical regime there has only been one reported observation of the predicted weak probe absorption spectrum of a driven two-level atom by Wu *et al.* [14]. The signal to noise ratio in this case is excellent. The associated dispersion profiles, however, are not attempted. These papers represent the extent of the experimental investigations of the absorption and dispersion profiles of a driven two-level system probed by a weak field.

Experimentation is not a trivial matter. It is necessary to identify an appropriate two-level system and such systems are not common. Some of the current cases, for example, involve work on sodium $3^2S_{1/2} \Leftrightarrow 3^2P_{3/2}$ transitions chosen because of the ease of preparation, the large transition dipole moment and the convenient wavelength. The sodium system can behave as a two-level system especially when optical pumping technique is employed [15], but strictly, sodium is not a two-level system and certainly is not a simple two-level system. It is further desirable to have narrow spectral lines largely limited by the homogeneous linewidth (determined by transverse relaxation time T_2). In the case of atoms such as sodium the linewidth requirements are best met by adopting the more sophisticated but harder experimental techniques using collimated atomic beams or atom traps. The response of a driven two-level system to the weak probe field depends on the ratio of the relaxation rates [5,16]. For the purpose of observing dynamic Stark splitting, it is desirable to have the transverse relaxation time T_2 approaching the longitudinal relaxation time T_1. To approach this situation for atoms the amount of collision broadening must be limited. Finally it should be pointed out that by dealing with a strongly driven two-level system it is inevitable that population between the two levels will be nearly equal and, hence, the absorption of a weak probe field will be small and detection will require exceptional sensitivity. In light of the above factors it is, therefore, not surprising that there are so few experimental studies of the absorption and dispersion profiles of the strongly driven two-level system.

It has been shown in previous chapters that the NMR two-level system of the N-V centre in diamond which corresponds to the $I_z=|0\rangle \Leftrightarrow |-1\rangle$ 5.4 MHz transition is a nearly ideal two-level system and the magnetic transition can be detected by the very sensitive Raman heterodyne detection technique. In this chapter the experimental investigations on the absorption and dispersion profiles

of such a driven hyperfine transition probed by a weak field are reported for various pump field intensities and detunings.

6.2 Theory

6.2.1 Homogeneously Broadened Two-Level System

We consider a two-level system with a ground state |1> and an excited state |2> interacting with an arbitrary strong pump field at frequency ω and a weak probe field at frequency υ, as shown in Fig.6-1.

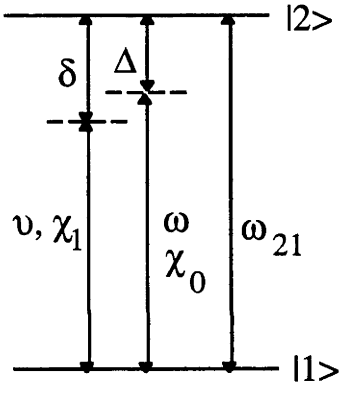

Figure 6-1. Pump-probe spectroscopy configuration in a two-level system. The strong pump field has frequency ω and detuning Δ. The weak probe field has frequency υ and detuning δ.

The rf magnetic field is given by

$$B_{rf}(t) = B_{pump} \cos \omega t + B_{probe} \cos \upsilon t . \qquad (6.1)$$

The density matrix equations of motion are given by (see, Chapter 1),

$$\frac{\partial \rho_{11}}{\partial t} = -\frac{i}{\hbar}(V_{12}\rho_{21} - V_{21}\rho_{12}) - \frac{\rho_{11} - \rho_{11}^{eq}}{T_1}, \qquad (6\text{-}2a)$$

$$\frac{\partial \rho_{22}}{\partial t} = \frac{i}{\hbar}(V_{12}\rho_{21} - V_{21}\rho_{12}) - \frac{\rho_{22} - \rho_{22}^{eq}}{T_1}, \qquad (6\text{-}2b)$$

$$\frac{\partial \rho_{21}}{\partial t} = -i\omega_{21}\rho_{21} + \frac{i}{\hbar}V_{21}(\rho_{22} - \rho_{11}) - \frac{\rho_{21}}{T_2} . \qquad (6\text{-}2c)$$

As introduced earlier T_1 and T_2 are the longitudinal and transverse relaxation times, respectively. ρ_{11}^{eq} and ρ_{22}^{eq} are the populations of state |1> and |2> without external field, respectively. In the rotating wave approximation the interaction energy, V_{21}, is given by

$$V_{21} = V_{12}^{*} = -\frac{1}{2}\mu_B B_{pump} e^{-i\omega t} - \frac{1}{2}\mu_B B_{probe} e^{-i\upsilon t}$$
$$= -\frac{1}{2}\hbar\chi_0 e^{-i\omega t} - \frac{1}{2}\hbar\chi_1 e^{-i\upsilon t}, \qquad (6.3)$$

where

$$\chi_0 = \frac{\mu_B B_{pump}}{\hbar} \quad \text{and} \quad \chi_1 = \frac{\mu_B B_{probe}}{\hbar} \qquad (6.4)$$

are the Rabi frequencies of pump and probe field, respectively.

The density matrix equations of motion, Eqs.(6.2), cannot be solved in closed form with an interaction in the form of Eq.(6.3). Mollow [4] deduced a first order solution by evaluating the weak probe field χ_1 to first order and the strong pump field χ_0 to all orders. The first order steady state solution of the coherence ρ_{21} has the form

$$\rho_{21} = \tilde{\rho}_{21}(\omega) e^{-i\omega t} + \tilde{\rho}_{21}(\upsilon) e^{-i\upsilon t} + \tilde{\rho}_{21}(2\omega - \upsilon) e^{-i(2\omega - \upsilon)t}, \qquad (6.5)$$

where the tilde denotes the slowly varying component of the density matrix element.

The physical consequences of the three terms in ρ_{21} in Eq.(6.5) are as follows: $\tilde{\rho}_{21}(\omega)$ and $\tilde{\rho}_{21}(\upsilon)$ give rise to the response of the two-level system to the pump and probe fields, respectively. The third term $\tilde{\rho}_{21}(2\omega-\upsilon)$ represents a "wave-mixing" process. The weak probe field absorption and dispersion

profiles are given by imaginary part and real part of $\tilde{\rho}_{21}(\upsilon)$, respectively, which can be written as

$$\tilde{\rho}_{21}(\upsilon) = -i\frac{\chi_1}{2}\frac{w^{dc}}{F(i\delta)}\left[\left(\frac{1}{T_2} - i\delta + i2\Delta\right)\left(\frac{1}{T_1} - i\delta + i\Delta\right) + \frac{i(\delta-\Delta)\frac{\chi_0^2}{2}}{\frac{1}{T_2} + i\Delta}\right], \tag{6.6}$$

where $F(i\delta)$ is the cubic function

$$F(i\delta) = \left(\frac{1}{T_2} - i\delta\right)\left(\frac{1}{T_2} - i\delta + i2\Delta\right)\left(\frac{1}{T_1} - i\delta + i\Delta\right) + \chi_0^2\left(\frac{1}{T_2} - i\delta + i\Delta\right), \tag{6.7}$$

where $\Delta = \omega - \omega_{21}$ and $\delta = \upsilon - \omega_{21}$ are the pump and probe field detuning, respectively. w^{dc} is the steady state population inversion induced by the pump field alone,

$$w^{dc} = \frac{(\rho_{22}^{eq} - \rho_{11}^{eq})(1 + T_2^2\Delta^2)}{1 + T_2^2\Delta^2 + \chi_0^2 T_1 T_2}. \tag{6.8}$$

To obtain the theoretical absorption and dispersion lineshape we plotted $\mathrm{Im}\tilde{\rho}_{21}(\upsilon)$ (for absorption) and $\mathrm{Re}\tilde{\rho}_{21}(\upsilon)$ (for dispersion) as a function of probe field detuning, δ, with a given pump field detuning, Δ, and Rabi intensity, χ_0, as shown in Figs.6-2 and 6-3 (dashed line) for on- and off-resonance pumping, respectively. The traces are calculated using the relaxation times $T_1 = 360\ \mu s$ and $T_2 = 120\ \mu s$ and to highlight the structures of the profiles the traces are scaled to maintain the overall size of the features. Because the solution Eq.(6.6) scales linearly with $\rho_{22}^{eq} - \rho_{11}^{eq}$ we assume, without loss of generality, that $\rho_{11}^{eq} = 0.7$, $\rho_{22}^{eq} = 0.3$ and $\rho_{22}^{eq} - \rho_{11}^{eq} = -0.4$.

6.2.2 Inhomogeneously Broadened Two-Level System

The present two-level system has a small amount of inhomogeneous broadening (see, Chapters 4 and 5). This is taken into account by integrating over the inhomogeneous distribution.

$$< \tilde{\rho}_{21} (\upsilon) > = \int_{-\infty}^{+\infty} D (\Delta_{21}) \tilde{\rho}_{21} (\upsilon, \Delta_{21}) d\Delta_{21} , \qquad (6.9)$$

where $\Delta_{21}=\omega_{21}-\omega_{21c}$ is the detuning of ω_{21}, which is the atomic frequency of a specific sub-group two-level system, with respect to ω_{21c}, which is the central atomic frequency of the inhomogeneous distribution; and D (Δ_{21}) is the distribution function of atomic resonant frequencies, and is assumed as Gaussian profile:

$$D (\Delta_{21}) = \frac{1}{\sigma \sqrt{\pi}} e^{-(\frac{\Delta_{21}}{\sigma})^2} , \qquad (6.10)$$

where σ is the half width at the 1/e point of the inhomogeneous distribution function. The dispersion response is then proportional to

$$\text{Dispersion} - I_s (0^0) \propto \text{Re} < \tilde{\rho}_{21} > , \qquad (6.11)$$

The absorption response is proportional to

$$\text{Absorption} - I_s (90^0) \propto \text{Im} < \tilde{\rho}_{21} > . \qquad (6.12)$$

The integration is carried out numerically by substituting Eqs.(6.6) and (6.10) into Eq.(6.9). The results are shown in Figs.6-2 and 6-3 (solid line) with σ = 4 kHz for on- and off-resonance pumping, respectively. For a small amount of inhomogeneous broadening such as in the present study, the integration over the inhomogeneous line results in profiles of the same form as for the homogeneous line but with features of increased linewidth. There are

other changes, for example, for on-resonance pumping at low Rabi intensities the sharp features in absorptive profiles for homogeneously broadened two-level system becomes a "hole" for inhomogeneously broadened two-level system. At high Rabi intensities the inhomogeneity enhances the absorption and reduces the gain (negative absorption).

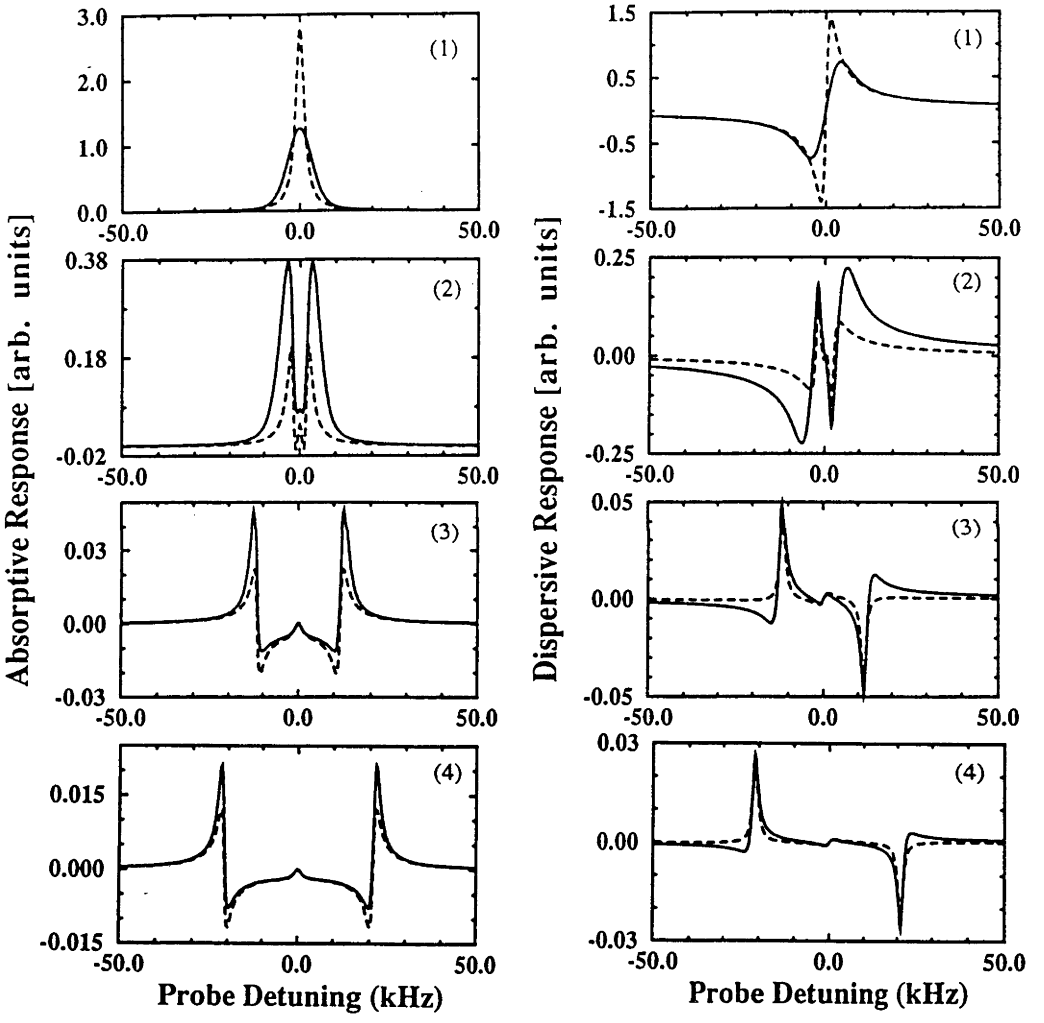

Figure.6-2. Calculated weak probe absorption (left) and dispersion (right) profiles at resonant pumping for homogeneously (dashed line) and inhomogeneously (solid line) broadened two-level system. Traces (1), (2), (3) and (4) for pump intensities of 0.0, 2.1, 11.8 and 21.0 kHz.

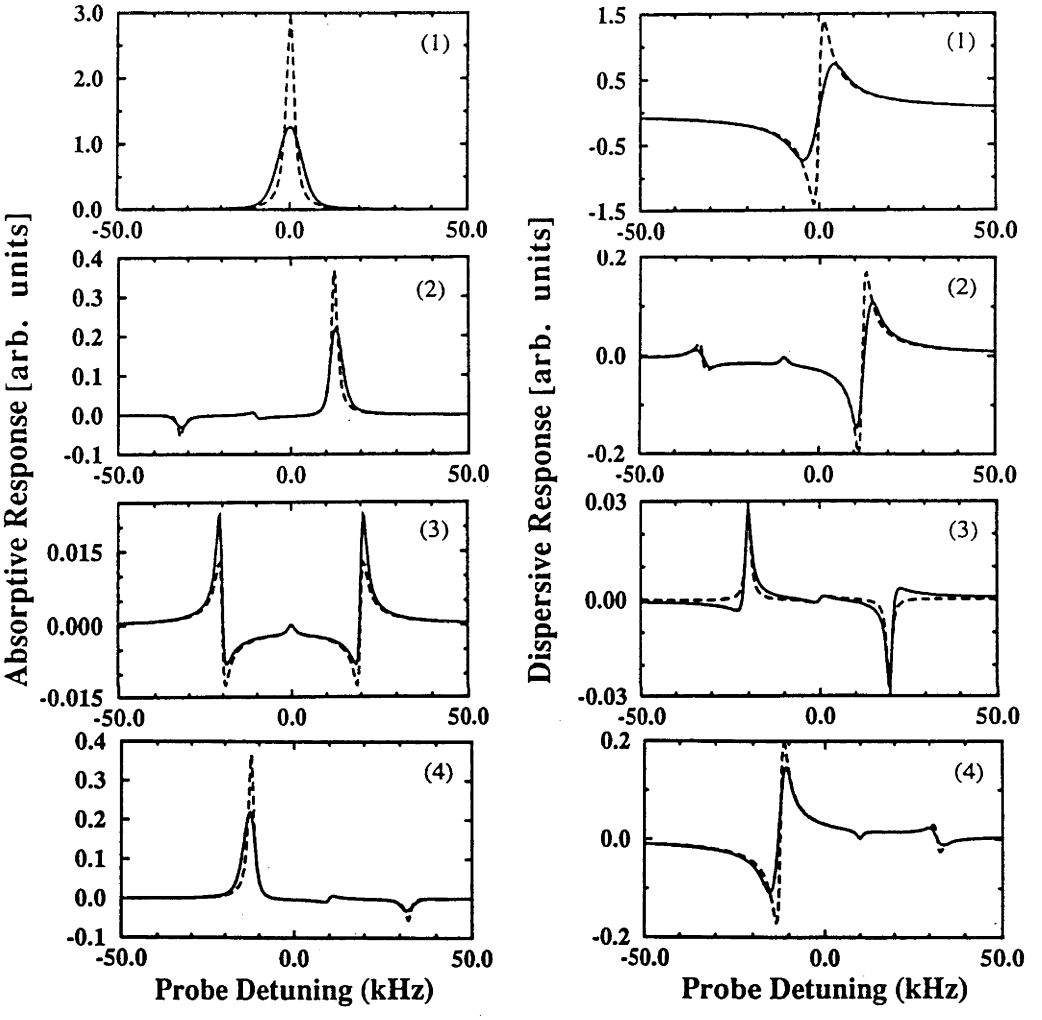

Figure 6-3. Calculated weak probe absorption (left) and dispersion (right) profiles dependence on pump detunings Δ with fixed pump Rabi intensity of 40 kHz for homogeneously (dashed line) and inhomogeneously (solid line) broadened two-level system. Trace (1) for zero pump intensity, (2) Δ = - 20 kHz, (3) zero detuning and (4) Δ = 20 kHz.

6.3 Experimental Results

6.3.1 On-Resonance Pumping

The experimental absorptive I_S (90°) and dispersive I_S (0°) profiles of Raman heterodyne signal are shown in Figs.6-4 (a) and 6-5 (a), respectively. The top trace (1) in Fig.6-4 (a) gives the absorption profile in the absence of the pump field, and the following traces (2) - (6) give the absorption profiles for increasing intensity of the resonant pump field at 5.4 MHz. The experimental traces are scaled to highlight the spectral features. The weaker signal gives rise to the deteriorating signal to noise ratio due to saturation. The absorption signal totally changes its characteristic shape between low and high pump field intensities. At the higher pump intensities two dispersion-like profiles separated by two times the Rabi frequency are the prominent features and it is also interesting to note that between these two features the signal is predominantly negative absorption or gain. Fig.6-5 (a) shows the corresponding behaviour of the dispersion profile. The dispersion signal likewise decreases (although not so rapidly as in absorption) with pump intensity and develops into positive and negative absorptive-like profiles separated by two times the Rabi frequency at the higher pump intensities. There is, therefore, a total change-over from absorptive to dispersive profiles between the high and low pump field limits and the in-phase and out-of-phase signals interchange their lineshapes. The splitting of the features into two components is caused by the interaction of the magnetic dipole moment and the magnetic component of the electromagnetic field and is, hence, an ac Zeeman or dynamic Zeeman effect. Owing to the parallels with other regions of the electromagnetic spectrum where the splitting is caused by the interaction of the electric dipole moment and the electric component of the radiation this splitting is also termed as ac or dynamic "Stark" splitting.

In both the absorption and dispersion experimental traces there is a weak feature to higher energy which is not well understood [see, Figs.6-4 (a) and 6-5 (a)]. That the signal is more obvious at the higher pump powers indicates that it is not saturated and hence, must be associated with a totally different transition. The feature is not of great significance to the present work.

For the theoretical absorption and dispersion profiles calculated from Eq.(6.9) and shown in Figs.6-4(b) and 6-5(b) the Rabi frequencies χ_0 are determined by first measuring the largest doublet separation (21 kHz) of experimental traces (6) in Fig.6-4(a) or 6-5(a) and then deduced from rf power attenuation used for the other traces as 2.1, 3.74, 6.64 and 11.8 kHz for traces (2), (3), (4) and (5) in Figs.6-4(b) and 6-5(b). The theoretical calculation then gives very good agreement with experiment and confirms the various characteristic behaviours, such as the signal amplification, the splitting by the Rabi frequency and the interchange between absorptive and dispersive profiles. The only feature not reliably established experimentally is the weak feature at the pump field frequency. This feature is masked by the pick-up from the strong pump field and there is no attempt to investigate this feature further. The pick-up signal itself is used as a frequency mark in the experiments.

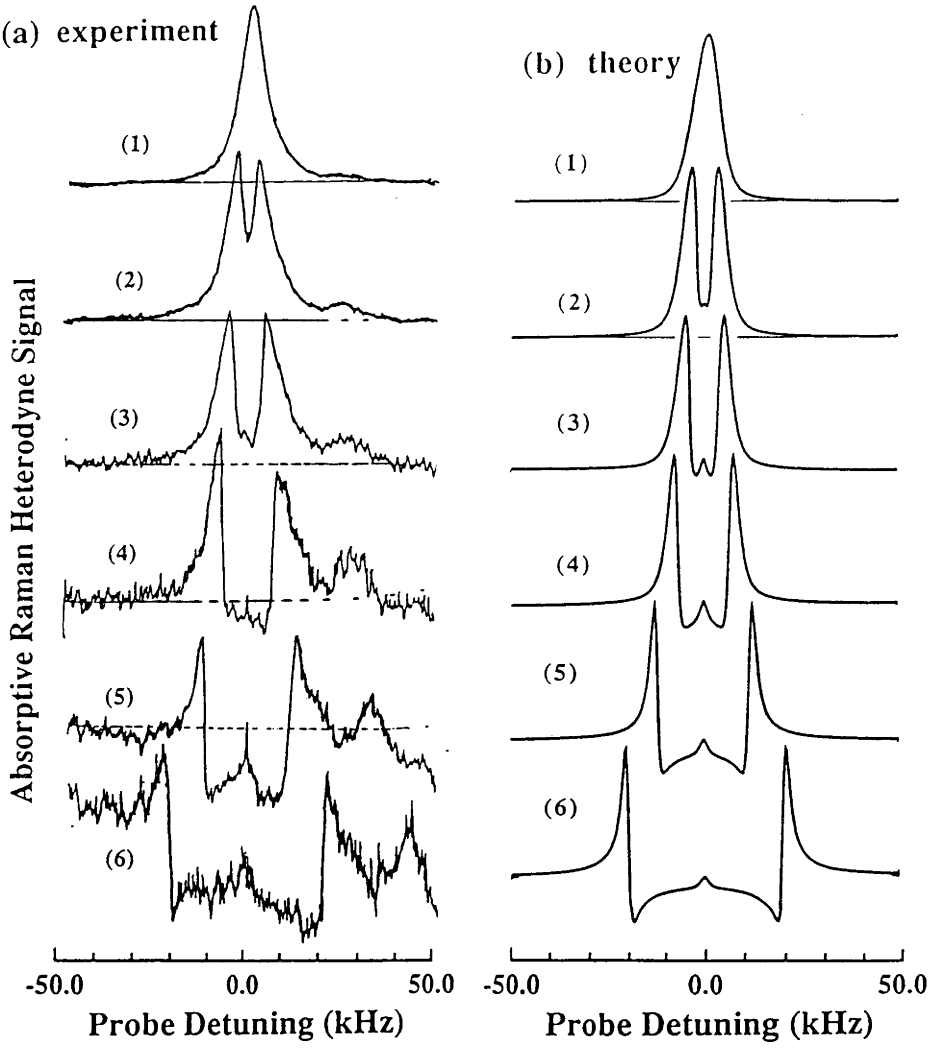

Figure 6-4. Measured (a) and calculated (b) absorption profiles dependence on pump field intensities for resonant pumping. For experimental traces, curve (1) zero pump field, (2) pump intensity 0 dB, I=1.0, (3) 5 dB, I=3.16, (4) 10 dB, I=10.0, (5) 15 dB, I=31.6, (6) 20 dB, I=100.0. The theoretical absorption profiles roughly corresponding to measured profiles with parameter of T_1 = 360, T_2 = 120 μs are calculated from Eq.(6.9). The pump Rabi intensities used in the theoretical traces are (1) 0, (2) 2.1, (3) 3.74, (4) 6.64, (5) 11.8, and (6) 21.0 kHz.

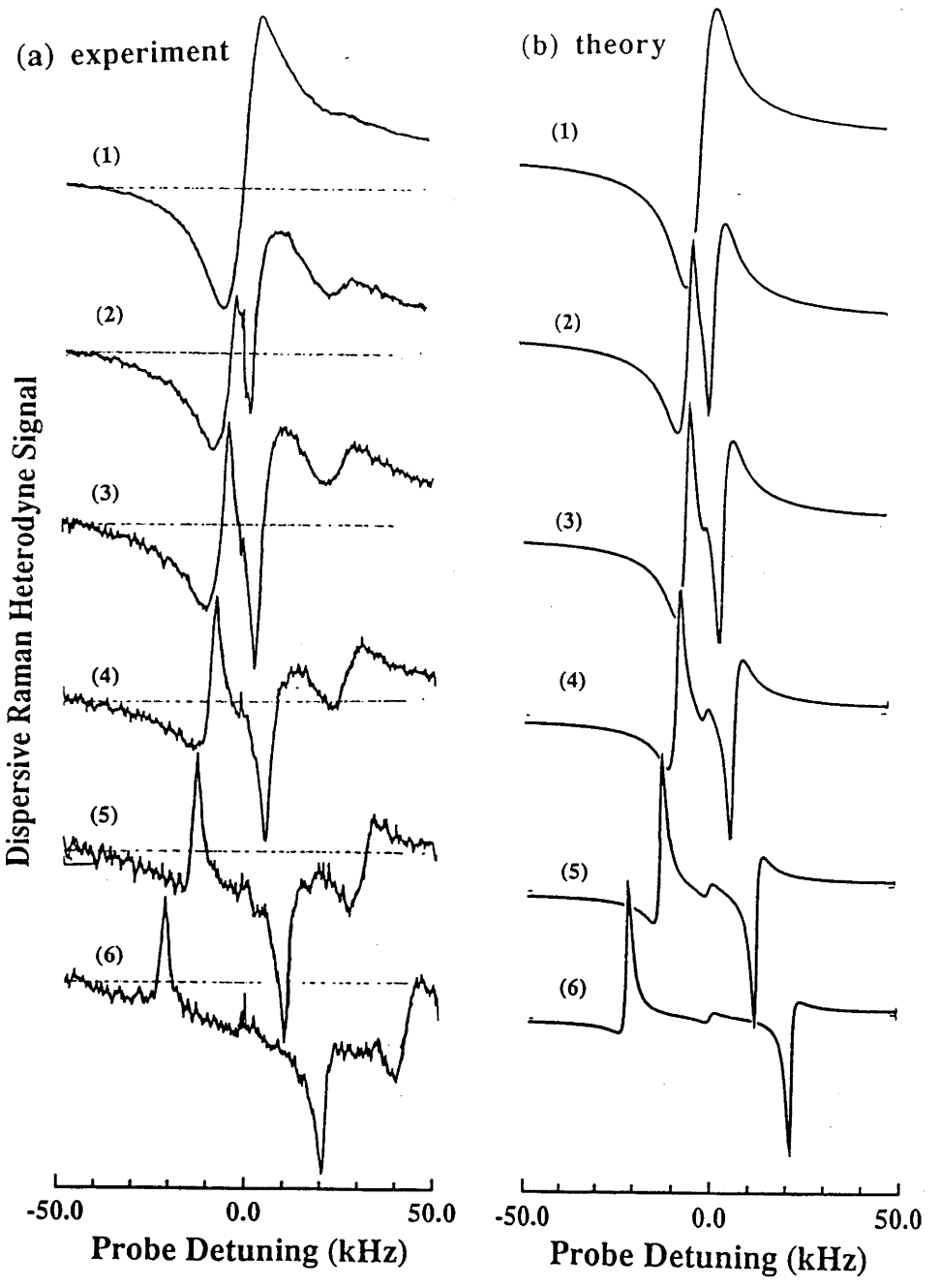

Figure 6-5. Measured (a) and calculated (b) dispersion profiles dependence on pump intensities for resonant pumping. The pump intensities are same with Fig.6-4 for corresponding traces. The parameters used in theoretical traces are same with Fig.6-4.

6.3.2 Off-Resonance Pumping

Fig.6-6 shows the experimental absorption profiles associated with a fixed rf pump intensity but with negative, zero and positive detunings. The top trace (1) is that obtained in the absence of the pump field whereas the central trace (4) is that for zero detuning or on-resonance pump (Rabi intensity $\chi_0 \sim 55$ kHz) and is equivalent to that given in the previous section. The other four traces (2), (3), (5) and (6) in Fig.6-6 are for detunings of -40, -22, 22 and 35 kHz, respectively. It is very noticeable that whereas in the resonant case the signals are very weak the situation changes as soon as the pump frequency is off-resonance. There are both positive and negative signals that are significantly above the noise level. Hence there are prominent amplification signals for both negative and positive pump field detunings. The positive and negative signals themselves are equally displaced from the pump field frequency with separation of the general Rabi frequency: $\Omega = [\ \chi_0^2 + \Delta^2\ ]^{1/2}$. The experimental dispersion traces for a resonant Rabi intensity of $\chi_0 \sim 55$ kHz are shown in Fig.6-7 with detunings of (2) -40, (3) -12, (4) 0, (5) 40 and (6) 125 kHz. Although there is no attempt to fit the experimental traces in detail the overall correspondence between experiments (Figs.6-6 and 6-7) and theory (Fig.6-3) is excellent.

The characteristic lineshapes presented in the experimental results are again worth noting. For the off-resonance situation the dispersion signal displays two dispersive features throughout. In general one strong and one weak with the two signals always of opposite sign. Correspondingly the absorption spectra consist of two absorptive features throughout although one is positive and one is negative (amplification). It is the on-resonance case that gives the anomalous lineshapes, where the dispersion signal exhibits absorption-like profile and the absorption dispersion-like profile. The individual components then always satisfy the Kramers-Kronig relationship.

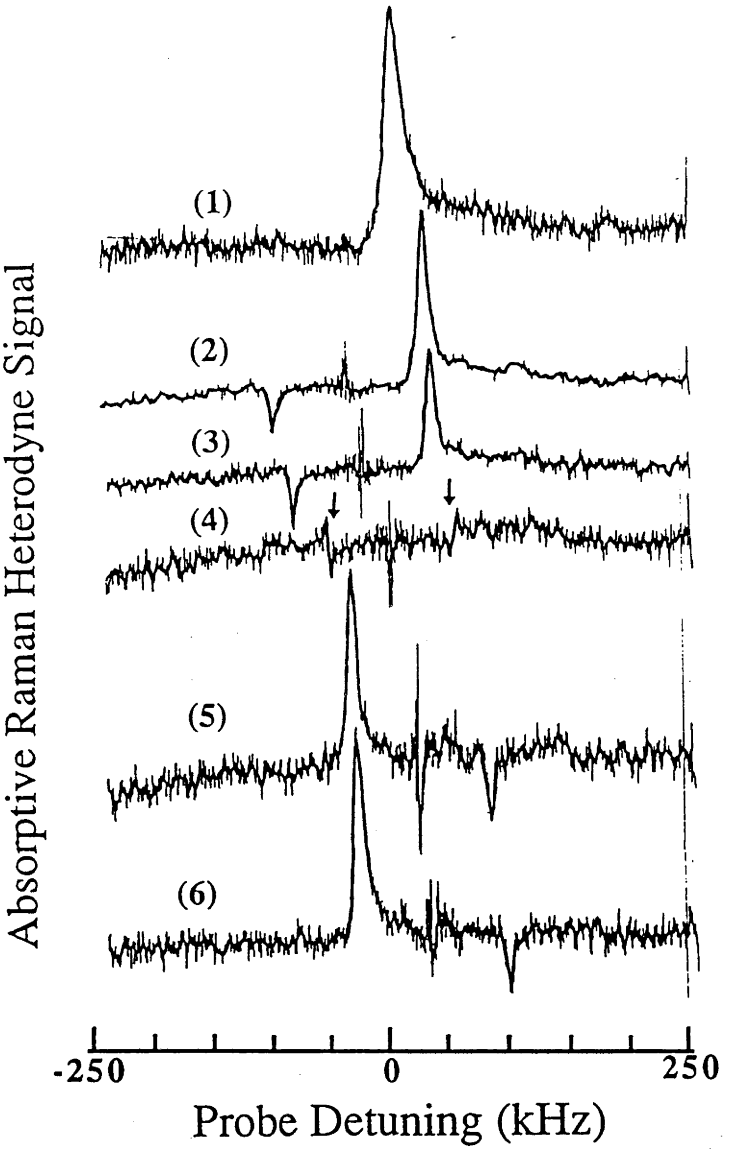

Figure 6-6. Experimental absorption profiles dependence on pump detunings Δ with fixed pump Rabi intensity of χ_0~ 55 kHz. Trace (1) zero pump field, and traces (2), (3), (4), (5) and (6) are for detunings of Δ ~ -40, ~ -22, 0, ~ 22 and ~ 35 kHz, respectively. The two arrows in trace (4) are used to indicate two dispersion-like profile which is very weak for resonant pump field.

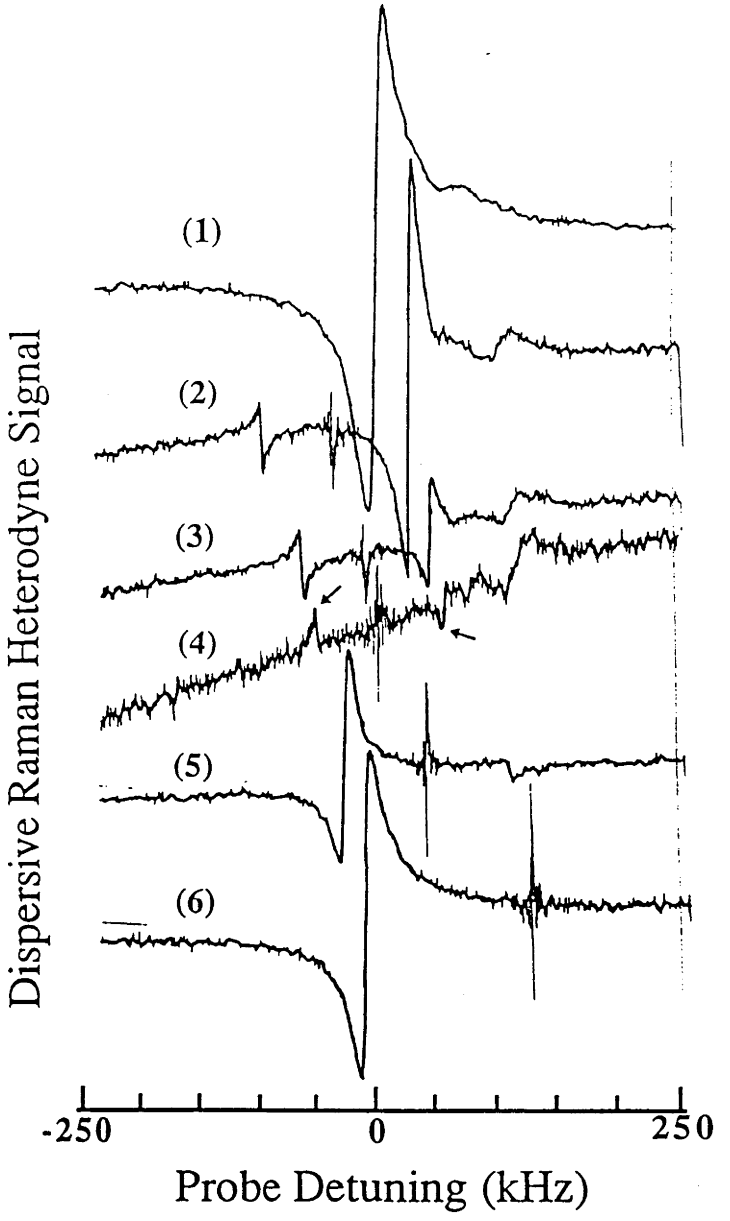

Figure 6-7. Experimental dispersion profiles dependence on pump detunings Δ with fixed Rabi pump intensity of $\chi_0 \sim 55$ kHz. Trace (1) zero pump field, and traces (2), (3), (4), (5) and (6) are for detunings of $\Delta \sim -40, \sim -12, 0, \sim 40$ and ~ 125 kHz, respectively. The two arrows in trace (4) are used to indicate two absorption-like profile which is very weak for resonant pump field.

The measured doublet splitting caused by a fixed pump field intensity is plotted for various values of the detunings Δ as shown in Fig.6-8 and it is readily confirmed that the splittings correspond to the general Rabi frequency given by $\Omega = [\chi_0^2 + \Delta^2]^{1/2}$ which is also plotted for comparison.

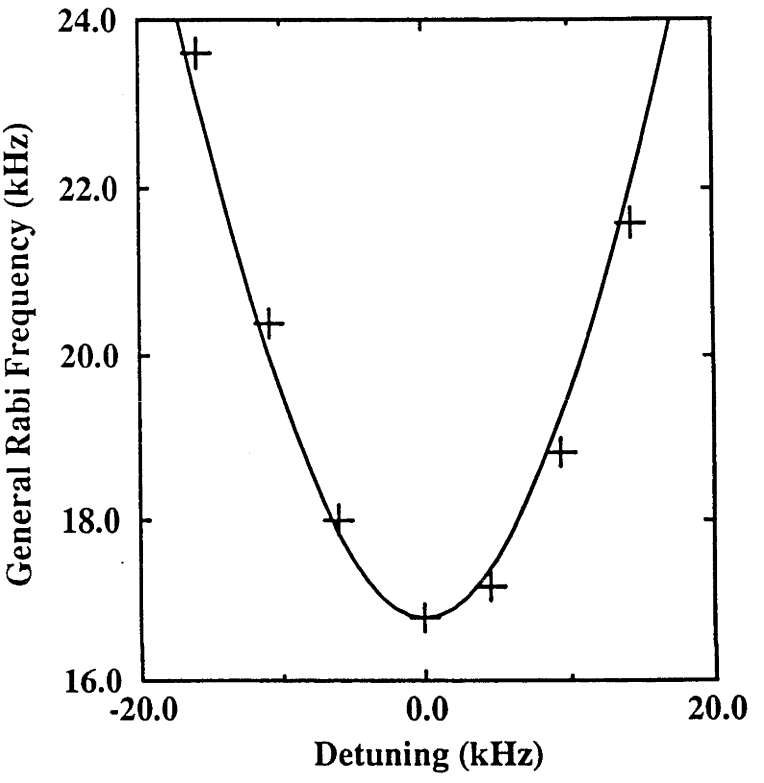

Figure 6-8. The measured general Rabi frequency Ω as a function of detuning Δ compared with theoretical dependence (solid line) $\Omega = [\chi_0^2 + \Delta^2]^{1/2}$ with measured value of $\chi_0 = 16.8$ kHz.

The absolute positions of the dynamic "Stark" doublet in the absorption or dispersion profiles are as follows:

$$\omega + \Omega = \omega_{21} + \Delta + \Omega = \omega_{21} + \Delta + [\chi_0^2 + \Delta^2]^{1/2}, \qquad (6.13a)$$

$$\omega - \Omega = \omega_{21} + \Delta - \Omega = \omega_{21} + \Delta - [\chi_0^2 + \Delta^2]^{1/2}, \qquad (6.13b)$$

and, therefore, the frequency shift from ω_{21} are:

$$\Delta + [\chi_0^2 + \Delta^2]^{1/2}, \tag{6.14a}$$

$$\Delta - [\chi_0^2 + \Delta^2]^{1/2}, \tag{6.14b}$$

Fig.6-9 shows the measured position of the dynamic "Stark" split features as a function of pump field detuning as well as the above theoretical curves of Eqs.(6.14a) and (6.14b).

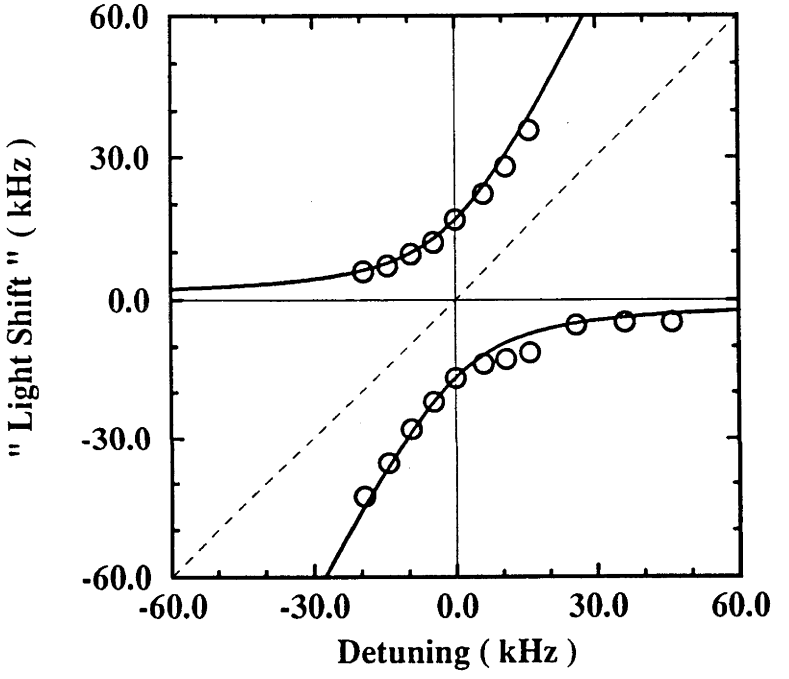

Figure 6-9. Measured dynamic "Stark" doublet frequency shift as a function of detuning Δ compared with theoretical dependence (solid line) calculated from Eqs.(6.14) with measured χ_0= 16.8 kHz.

When a strong pump field is tuned from the low frequency or negative detuning side toward resonance the absorption feature which lies close to the resonance frequency is decreased in size and displaced to higher frequency. Under the same condition the negative absorption signal or amplification peak at frequency below the pump frequency develops from zero strength, goes

through a maximum, then decreases again as the on-resonance situation is approached. At resonance the signal is both weak and has a dispersion-like profile. As the pump field is continued to be tuned to higher frequency and tuned away from resonance, the positive component of the dispersion-like feature at frequency below pump frequency gains intensity and gives an absorption peak. The feature increases in size and moves asymptotically toward the unperturbed two-level resonant frequency. As the overall behaviour is symmetric for positive and negative detunings the other dynamic "Stark" split component becomes an amplification feature. Throughout the doublets are always symmetrically displaced from pump field frequency with separation of general Rabi frequency Ω.

At very large detunings the extreme component has negligible intensity whereas the absorption feature will be only slightly shifted from the resonance position in the absence of the pump field. This shift is the so called "light shift" observed in earlier experiment by Liao et al [17].

6.4 Discussions

6.4.1 Physical Origin of Amplification Without Population Inversion

Signal gain is observed in both on-resonance and off-resonance pumping even though the characteristics of the signals are very different. For resonant pumping the gain occurs over a range of frequencies but the gain is weak. For off-resonance the gain only occurs at more restrict frequency range but is much larger. It is interesting to understand the origin of this gain as it is not possible to obtain population inversion in a two-level system in the steady state limit.

The observed amplification can be interpreted as a three-photon process in which energy is transferred from pump to probe field via the nonlinear response of the strongly driven two-level system [5,14]. The three features (Fig.6-10a) that are observed in the absorption spectrum with off-resonance pumping can be interpreted in either the bare-atom picture (Fig.6-10b) or the dressed-atom picture (Fig.6-10c). In the bare-atom picture, the strong off-resonance pump field causes a shift of the atomic energy levels, the so called light shift, to give the absorption peak at $\omega'_{21}=\omega+\Omega$. The weak dispersion-like feature at ω is due to the resonance induced at the pump field frequency. The three-photon process, in which two pump field photons at frequency ω is absorbed and a photon with frequency $2\omega-\omega'_{21}=\omega-\Omega$ is stimulated, is the physical origin of amplification at $\omega - \Omega$.

An alternative account of the amplification without inversion can be given using the dressed-atom approach [18-21]. In the dressed-atom picture, the three spectral features are due to transitions indicated in Fig.6-10c. The central transition at ω to is due to the transition $|A,n\rangle \Leftrightarrow |A, n-1\rangle$ and $|B,n\rangle \Leftrightarrow |B, n-1\rangle$ and the transitions will have little strength as the populations are equal. The transition $|A,n\rangle \Leftrightarrow |B,n-1\rangle$ at $\omega + \Omega$ is absorptive as the lower population is greater. The remaining component at $\omega - \Omega$ due to the transition between $|B,n\rangle \Leftrightarrow |A,n-1\rangle$ corresponds to the transition with amplification, since the upper level in this case is more populated. Therefore, the off-resonance pumping gain can be contributed to population inversion occurred in dressed-atom picture. With on-resonance pumping all the populations are equal and all signals approach zero intensity. This is in agreement with experiments (see, Figs.6-6 and 6-7) as it is very noticeable that the on-resonance pump signals are very much weaker than off-resonance pump signals. It is also interesting to note that the amplification observed in on-resonance pumping situation occurs without inversion in either bare- or dressed-atom state.

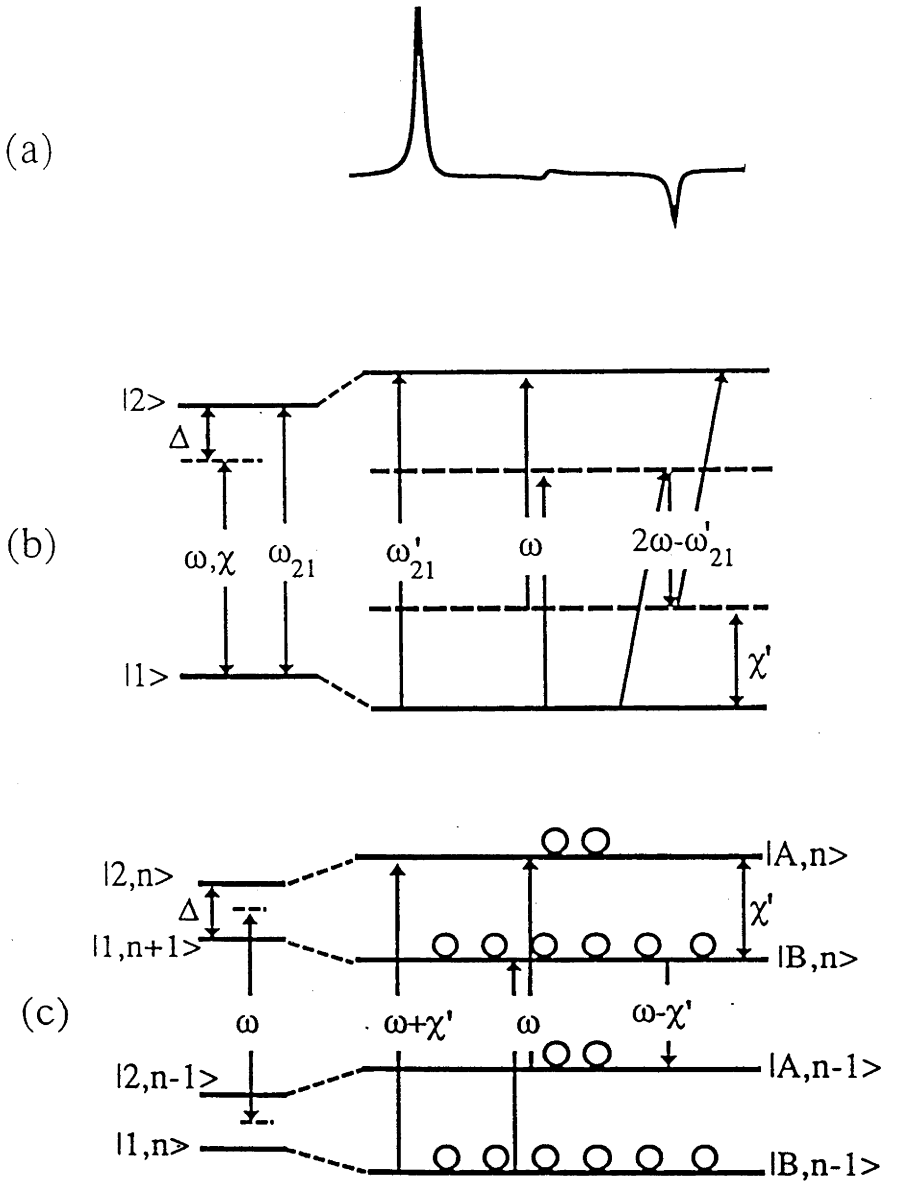

Figure 6-10. Schematic illustrating the processes for amplification without inversion. (a) Absorption profile of a weak probe showing amplification for off-resonance pumping. (b) The energy levels in bare-atom picture where the probe is amplified by a three-photon process involving absorption of two pump photons ω and a stimulated emission at $2\omega - \omega'_{21}$. (c) The energy levels and populations in dressed-atom picture. The dots schematically represent the populations. The probe is amplified at frequency $\omega - \Omega$ due to the population inversion between the dressed states.

6.4.2 High Refraction Index With No Absorption

It has been pointed out theoretically that with a driven two-level system it is possible to obtain a large value of refractive index at the frequency where there is no absorption [22]. This is observed for resonant pumping as shown in Fig.6-11. The absorption response consists of two dispersion-like profiles displaced by the Rabi frequency and, hence, each component has a value of zero at line centre of the doublets. At the same frequency the absorption-like dispersion response (refractive index) has a maximum. This is in accordance with theory and corresponds to the situation proposed in reference [22].

6.5 Conclusion

There has been considerable recent interest in achieving amplification without inversion mainly directed for application in the visible or ultra-violet regions for obtaining new laser wavelengths. The conditions required are hard to achieve and there have been few examples of successful observations [23,24]. The value, then, of the present experiments is that they give a very clear demonstration of the fundamental principle behind such schemes in the simplest possible case. The origin of the amplification can be understood from the above theoretical considerations and then the way of achieving the best situations is confirmed by experiment. For example, it has been seen that gain can be achieved over a wide range with on-resonance pumping but much larger responses are obtained over more restricted frequency range by using off-resonance pumping. This is apparent in the calculations and demonstrated experimentally. This chapter present studies employ a two-level system, a strong pump and a weak probe. More dramatic situations are obtained with higher probe intensities and this will be presented in the following chapter.

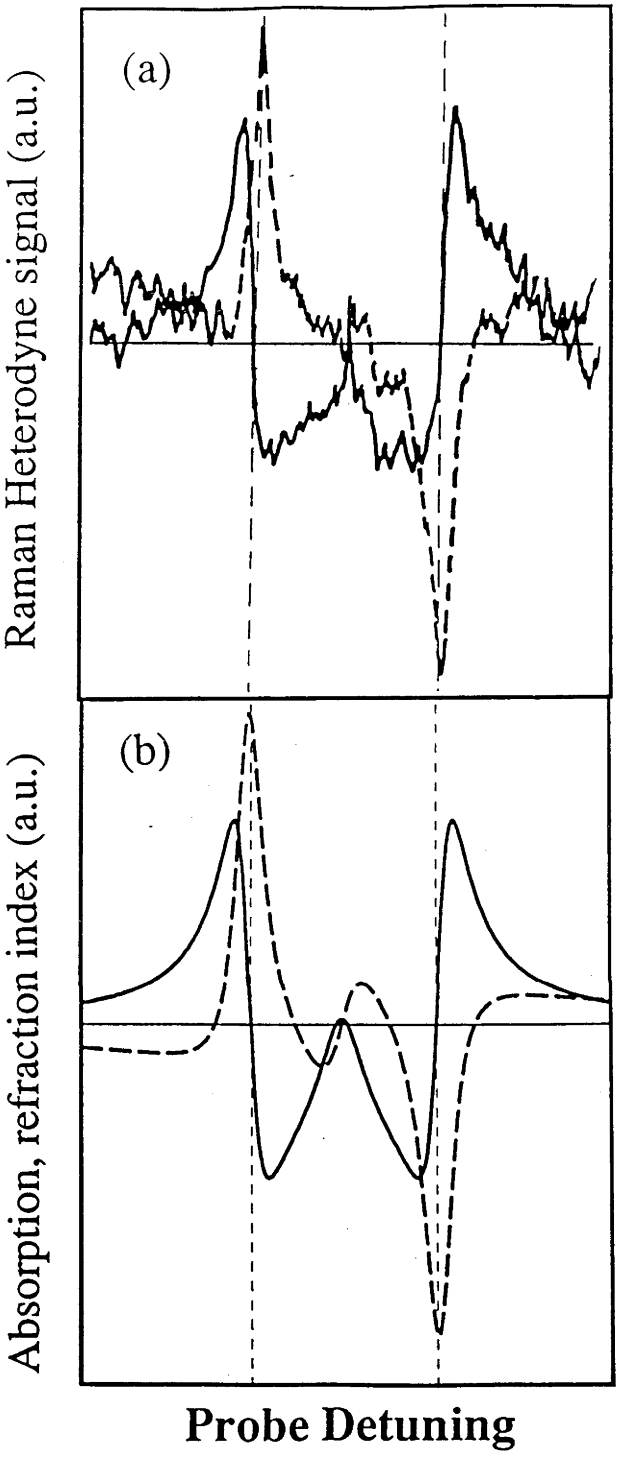

Figure 6-11. Schematic showing large refraction index at the frequencies with zero absorption. Traces (a) and (b) are the experimental and theoretical profiles, respectively. The solid line is the absorption and dashed line dispersion. The frequencies of zero absorption at $\delta = \pm \chi_0$ coincide with the maximum of refraction index.

In summary with a well characterized two-level system in the radio-frequency range which can be very sensitively probed by a coherent optical technique we have studied the changes in weak probe field absorption and dispersion profiles caused by a strong driving field. Various physical phenomenon common to any wavelength region are very clearly illustrated such as dynamic "Stark" splitting, high refraction index with zero absorption and amplification without population inversion. A density matrix treatment gives a very satisfactory account of all the experimental observations. The response of a two-level system to a strong driving field is well established and even contained in many text books [see, for example, Ref.7]. In this sense the present studies are not original. However, the experimental traces clearly illustrate the phenomena in a wide range of experimental parameters and for this reason the observations are of considerable value.

References

[1] E.T.Jaynes and F.W.Cummings, Proc. IEEE, 51, 89 (1963)

" *Comparison of quantum and semiclassical radiation theories with application to the beam maser* "

[2] N.Bloembergen and Y.R.Shen, Phys.Rev. 133, A37 (1964)

" *Quantum-theoretical comparison of nonlinear susceptibilities in parametric media, lasers, and Raman lasers* "

[3] B.R.Mollow, Phys. Rev., 188, 1969 (1969)

" *Power spectrum of light scattered by two-level systems* "

[4] B.R.Mollow, Phys. Rev.A 5, 2217 (1972)

" *Stimulated emission and absorption near resonance for driven systems* "

[5] R.W.Boyd, M.G.Raymer, P.Narum, and D.J.Harter, Phys.Rev.A24, 411 (1981)

" *Four-wave parametric interactions in a strongly driven two-level system* "

[6] for a review paper see. P.L.Knight and P.W.Milonni, Phys. Rep. 66, 21 (1980)

" *The Rabi frequency in optical spectra* "

[7] also see, L.Allen and J.Eberly, " *Optical resonance and two-level atoms* ", (Dover, New York, 1987)

P. Meystre and M.Sargent III, " *Elements of Quantum Optics* ", (Springer-Verlag, Berlin-New York, 1991)

R.W.Boyd, " *Nonlinear optics* " , (Academic Press Inc, 1992)

[8] A.M.Bonch-Bruevich, V.A.Khodovoi, and N.A.Chigir, Sov. Phys. JETP, 40, 1027, (1975)

" *Changes in the absorption spectrum and of dispersion of a two-level system in a rotating monochromatic radiation field* "

[9] X.He, P.T.H.Fisk, and N.B.Manson, J. Appl. Phys.,72, 211 (1992)

" *Autler-Townes effect of the photoexcited diamond nitrogen-vacancy centre in its triplet ground state* "

[10] S.H.Autler and C.H.Townes, Phys. Rev.,100, 703, (1955)

" *Stark effect in rapidly varying fields* "

[11] Ph.Cahuzac and R.Vetter, Phys.Rev.A14, 270, (1976)

"*Observation of the Autler-Townes effect on infrared laser transitions of xenon*"

[12] F.Schuda, C.R.Stroud Jr., and M.Hercher, J. Phys. B, 7, L198 (1974)

" *Observation of the resonant Stark effect at optical frequencies* "

[13] F.Y.Wu, R.E.Grove, and S.Ezekiel, Phys.Rev.Lett. 35, 1426 (1975)

" *Investigation of the spectrum of resonance fluorescence induced by a monochromatic field* "

[14] F.Y.Wu, S.Ezekiel, M.Ducloy and B.R.Mollow, Phys. Rev. Lett., 38, 1077 (1977)

" *Observation of amplification in a strongly driven two-level atomic system at optical frequencies* "

[15] R.E.Grove, F.Y.Wu, and S.Ezekiel, Phys. Rev. A 15, 227 (1977)
" *Measurement of the spectrum of resonance fluorescence from a two-level atom in an intense monochromatic field* "
[16] L.W.Hillman, R.B.Boyd, J.Krasinsky and C.R.Stroud,Jr. Opt. Commun. 45, 416 (1983)
" *Observation of a spectral hole due to population oscillations in a homogoneously broadened optical absorption line* "
[17] P.F.Liao and J.E.Bjorkholm, Phys. Rev. Lett., 34, 1 (1975)
" *Direct observation of atomic energy level shifts in two-photon absorption two-laser three-level Na experiment* "
[18] C.Cohen-Tannoudji and S.Reynaud, J. Phys. B, 10, 345 (1977)
" *Dressed-atom description of resonance fluorescence and absorption spectra of a multi-level atom in an intense laser beam* "
[19] C.Cohen-Tannoudji and S.Reynaud, J. Phys. B, 10, 365 (1977)
" *Modification of resonance Raman scattering in very intense laser fields* "
[20] C.Cohen-Tannoudji and S.Reynaud, J. Phys.B, 10, 2311 (1977)
" *Simultaneous saturation of two atomic transitions sharing a common level* "
[21] C. Cohen-Tannoudji and S. Reynaud, *Multiphoton Processes*,
Eds. J.H.Eberly and P.Lambropoulos, (Wiley, New York, 1977)
[22] A.D.Wilson-Gordon and H.Friedmann, Opt. Commun. 94, 238 (1992)
" *Enhanced index of refraction: a comparison between two- and three-level systems* "
[23] J.Gao, C. Guo, X. Guo, G. Jin, P. Wang, J. Zhao, H. Zhang, Y. Jiang, D. Wang, and D. Jiang, Opt. Commun. 93, 323 (1992)
" *Observation of light amplification without population inversion in sodium* "
[24] W.E.van der Veer, R. J. J. van Diest, A. Donszelmann and
H. B. van Linden van den Heuvell, Phys.Rev.Lett.,70, 3243 (1993)
" *Experimental demonstration of light amplification without population inversion* "

Chapter 7

Absorption and Dispersion Profiles of a Strongly Driven Two-level System Probed by a Strong Field

In chapter 6 we studied the response of a driven two-level system when probed by a weak field. In this chapter we extend the study to the case where the probe field is also strong.

7.1 Introduction

The nonlinear behaviour of a two-level system interacting with a single coherent electromagnetic field has been investigated extensively and examples include power broadening, saturation, Rabi nutation and Rabi sidebands in the resonance fluorescence spectrum [1-5]. Interesting effects have been also obtained when the driven two-level system is probed by a weak field. This situation has been investigated both theoretically and experimentally [6-10] and was the subject presented in Chapter 6. In the weak probe limit the probe field interacts linearly with the strongly driven two-level system and calculation accurate to first order of the probe field is adequate. Various interesting effects such as dynamic Stark splitting and gain without inversion have been predicted theoretically and illustrated experimentally (see, Chapter 6).

An obvious and intriguing generalization of the weak probe case is that where the probe field is also strong and interacts nonlinearly with the driven two-level system. There have been a number of theoretical calculations and some experimental investigations of this situation [11-20]. The first experimental investigation is that of Bonch-Bruevich *et al.* [12] who in 1979 reported on an investigation of the strong probe absorption spectrum of a driven

NMR two-level system in cadmium atomic vapour. In this case the pumping was restricted to the resonance frequency and the dispersion profile was not measured. Later Papademetriou *et al.* [20] reported an experiment in the optical frequency region using a sodium atomic beam with both on- and off-resonance pumping. However, their data were restricted to the case where the pump and probe intensities are equal, equivalent to a fully amplitude modulated laser beam. Signals were detected in excitation by monitoring the fluorescence and the strong dependence on the pump detuning was not apparent. The remarkable feature of these experimental traces is the multiphoton resonances at subharmonics of the Rabi frequency. When absorptive response is detected, interesting two-photon amplification without inversion has been observed for off-resonance pumping in barium atomic beam [19]. The resonance fluorescence of a two-level system driven by two strong fields has also been investigated [21-23]. The general feature is again characterized by multi-peak profiles.

Despite the extensive studies on the subject our understanding of a two-level system driven by two strong fields is by no means complete due to complexity in theoretical treatments and difficulties in experimental measurements. For example, although the absorption and dispersion are closely related, the dispersion response of a driven two-level system probed by a strong field has not been studied, and without experimental data there has been no motivation for the theoretical calculation of the dispersion response.

In this chapter, we report on the experimental studies of both absorptive and dispersive responses of a strongly driven two-level system when probed by a strong field. As in Chapter 6 the experiments were carried out using the I_z=|0>⇔|-1> 5.4 MHz transition and the magnetic transition was detected by the very sensitive Raman heterodyne technique. The profiles of absorption and

dispersion are recorded and shown to be in good agreement with those expected for an ideal two-level system. The motivation of such experimental studies lies in the fact that they provide a successful testing grounds for the theory of matter-radiation interaction, as the experiments can be directly compared with the calculations as well as a number of practical applications in laser physics and high resolution spectroscopy.

7.2 Theory

There have been a number of published theoretical analysis [11, 13, 15-17] treating a two-level system interacting with two strong fields. The present treatment is based on the analysis of Friedmann *et al.* [17]. Fig.7-1 shows a two-level system with a ground state, |1>, and an excited state, |2>, interacting with a pump field ω_1 and a probe field ω_2.

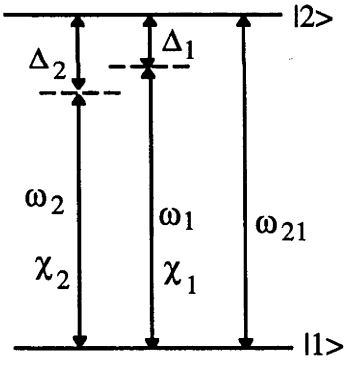

Figure 7-1. A two-level system interacting with pump field ω_1 and probe field ω_2.

The rf magnetic field is given by

$$\mathbf{B_{rf}}\,(t) = \mathbf{B_{pump}}\, cos\ \omega_1 t + \mathbf{B_{probe}}\, cos\ \omega_2 t\ . \qquad (7.1)$$

The density matrix equation of motion can be written in the rotating wave approximation as (see, Chapter 1),

$$\frac{\partial \rho_{12}}{\partial t} = i\omega_{21}\rho_{12} - \frac{\rho_{12}}{T_2} + i(V_1 + V_2 e^{i\delta t})e^{i\omega_1 t}(\rho_{22} - \rho_{11}), \tag{7.2a}$$

$$\frac{\partial W}{\partial t} = -2i(V_1 + V_2 e^{i\delta t})e^{i\omega_1 t}\rho_{21} + 2i(V_1 + V_2 e^{-i\delta t})e^{-i\omega_1 t}\rho_{12} - \frac{W}{T_1} + \frac{W^{eq}}{T_1}, \tag{7.2b}$$

$$W = \rho_{22} - \rho_{11}. \tag{7.2c}$$

Here (i) $\delta = \omega_2 - \omega_1$ is the pump-probe detuning, (ii) T_1 and T_2 are the longitudinal and transverse relaxation time, respectively, (iii) ω_{21} is the two-level system transition frequency, and (iv) W^{eq} is the population inversion without external field. Since the solution of Eq.(7.2) scales linearly with W^{eq} we assume, without loss of generality, that $W^{eq}=-1$. Finally, V_1 and V_2 are related to the Rabi intensity of pump and probe field χ_1 and χ_2, respectively, which are defined as

$$\chi_1 \equiv 2V_1 = \frac{\mu_B B_{pump}}{\hbar} \quad \text{and} \quad \chi_2 \equiv 2V_2 = \frac{\mu_B B_{probe}}{\hbar}. \tag{7.3}$$

According to Floquet theorem [24] the steady state solution of Eq.(7.2) can be written in the form

$$\rho_{12} = \sum_n \tilde{\rho}_{12}(n\delta - \omega_1)e^{-i(n\delta-\omega_1)t} = \sum_n a_{-n} e^{-i(n\delta-\omega_1)t} = \sum_n a_n e^{i(n\delta+\omega_1)t}, \tag{7.4a}$$

$$W = \sum_n W^{n\delta} e^{-in\delta t} = \sum_n d_{-n} e^{-in\delta t}. \tag{7.4b}$$

By substituting Eq.(7.4) into Eq.(7.2), we obtain a set of recurrence relations between the Floquet coefficients which can be solved in terms of continued fractions. The absorptive and dispersive responses [17] are proportional to the imaginary and real parts of

$$\tilde{\rho}_{21}(\omega_2) = a_1^* = -\frac{V_2 + V_1 Z_1^*}{\Delta_2 - i/T_2}\, d_0 . \tag{7.5}$$

where

$$d_0 = -\frac{i}{T_1}\left(P_0 - 2\,i\,\mathrm{Im}\,R_0 V_1 V_2 Z_1\right)^{-1}, \tag{7.6a}$$

$$Z_n = \frac{U_n V_1 V_2}{1 - \dfrac{S_n V_1^2 V_2^2}{1 - \cdots}}, \qquad U_n = \frac{Q_n}{P_n}, \qquad S_n = \frac{R_n}{P_n} U_{n+1}, \tag{7.6b}$$

$$P_n = -n\delta + \frac{i}{T_1} - 4\left(n\delta - \frac{i}{T_2}\right)\left[\frac{V_1^2}{\Delta_1^2 - \left(n\delta - i/T_2\right)^2} + \frac{V_2^2}{\Delta_2^2 - \left(n\delta - i/T_2\right)^2}\right], \tag{7.6c}$$

$$Q_n = \frac{2\left[(2n-1)\delta - \dfrac{2i}{T_2}\right]}{\left(\Delta_1 - n\delta + 1/T_2\right)\left(\Delta_2 + n\delta - 1/T_2\right)}, \tag{7.6d}$$

$$R_n = \frac{2\left[(2n+1)\delta - \dfrac{2i}{T_2}\right]}{\left(\Delta_1 + n\delta - 1/T_2\right)\left(\Delta_2 - n\delta + 1/T_2\right)}, \tag{7.6e}$$

where $\Delta_1=\omega_{21}-\omega_1$ and $\Delta_2=\omega_{21}-\omega_2$ are the pump and probe detunings, respectively.

The above calculations are for a homogeneously broadened two-level system. The inhomogeneous broadening effect can be treated by integrating the above solutions over the inhomogeneous broadening distribution. However, the two-level system studied in this work has only a small amount of inhomogeneous broadening (see, Chapter 5). It has been shown that such a small amount of inhomogeneous broadening only gives minor modification to the calculation provided the pump Rabi frequency is substantially larger than the transition linewidth (see, Chapter 6). For the majority of this chapter both pump and probe fields satisfy this condition. Therefore, the extra complexity of including inhomogeneous broadening is not merited. Nothing is lost from the understanding of the physical phenomenon and the calculated absorption and dispersion profiles where inhomogeneous broadening is neglected will be shown still give excellent agreement with experiment.

7.3 Numerical Calculations and Discussions

7.3.1 On-Resonance Pumping

This section presents the calculation results of absorption, dispersion and amplitude response for the case where the pump field is on-resonance with the two-level system, $\Delta_1=0$, and the parameters used are $T_1=3T_2$ and pumping Rabi frequency $\chi_1 T_2=20$.

The absorption response $\mathrm{Im}\tilde{\rho}_{21}(\omega_2)$ is shown in Fig.7-2 for various probe Rabi intensities χ_2, covering three ranges: (A) $\chi_2<\chi_1$, (B) $\chi_2\sim\chi_1$ and (C) $\chi>\chi_1$. In the weak probe limits ($\chi_2 T_2=0.1$) the characteristic of the absorption profiles includes the dynamic Stark splitting with two separated dispersion-like profiles. This is in agreement with earlier first order calculation and has been observed experimentally (see, Chapter 6). As the probe intensity increases, the

dynamic Stark doublet becomes broadened and shifted towards larger separation. In addition new resonances appear between the two primary peaks and converge towards the centre of the line. The positions of the new peaks are approximately described by χ/n, where n is an integer and χ is the total Rabi frequency determined by both pump and probe intensities.

Fig.7-3 shows the corresponding dispersion traces Re $\tilde{\rho}_{21}(\omega_2)$ as a function of pump-probe detuning δ for equivalent probe intensities of Fig.7-2 again in the three ranges: (A) $\chi_2<\chi_1$, (B) $\chi_2\sim\chi_1$, and (C) $\chi_2>\chi_1$.The weak probe dispersion profile shows dynamic Stark splitting with two separated absorption-like profiles of opposite signs and is in agreement with the previous first order calculation and experiment (see, Chapter 6). As for absorption, at high probe intensities multiphoton resonances appear in the dispersion traces.

The amplitude of the signal is equivalent to measuring the module of the $\tilde{\rho}_{21}$ and $|\tilde{\rho}_{21}|$ is plotted as a function of pump-probe detuning δ as shown in Fig.7-4 for the three ranges (A) $\chi_2<\chi_1$, (B) $\chi_2\sim\chi_1$ and (C) $\chi_2>\chi_1$. For high probe intensities the multiphoton resonance in absorption and dispersion response are again very clearly visible in the amplitude response.

The multi-peak structures arises from the multiphoton processes. For example, it can be seen from Eq.(7-4) that the steady-state observables contain terms oscillating at frequencies $\omega_1 \pm n\,\delta$ (n = 0, 1, 2, ...). The amplitude of the oscillations has a maximum when the Rabi frequency is a multiple of the beating frequencies δ, hence, the origin of the term "subharmonic transition". For a specific n-th order resonance it is a 2n-1 (or 2n+1) photon process involving n probe field photons and n-1 (or n+1) pump field photons depending on detuning of the probe from the pump field.

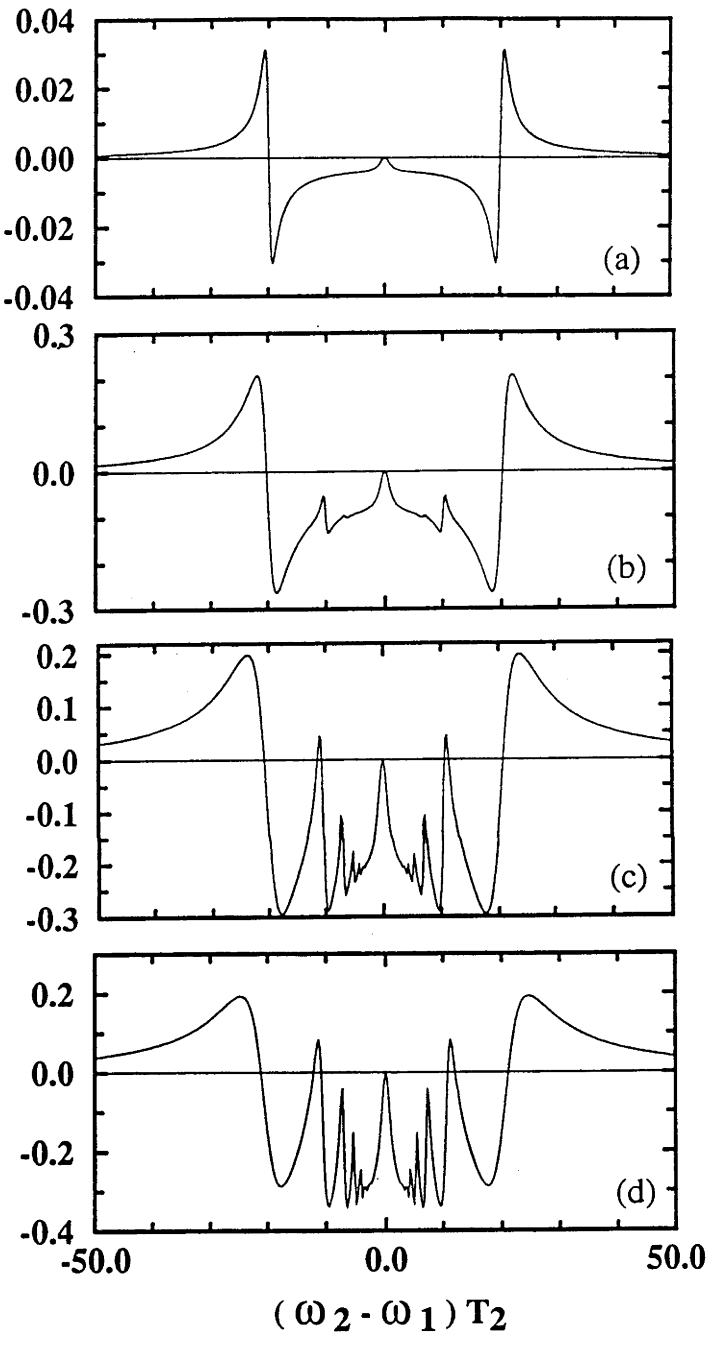

Figure 7-2 (A). Calculated absorption profiles for resonant pumping. The pump Rabi frequency is $\chi_1 T_2 = 20$. The probe Rabi frequencies are: $\chi_2 T_2 = 0.2$, 4, 8 and 10 for traces (a), (b), (c) and (d).

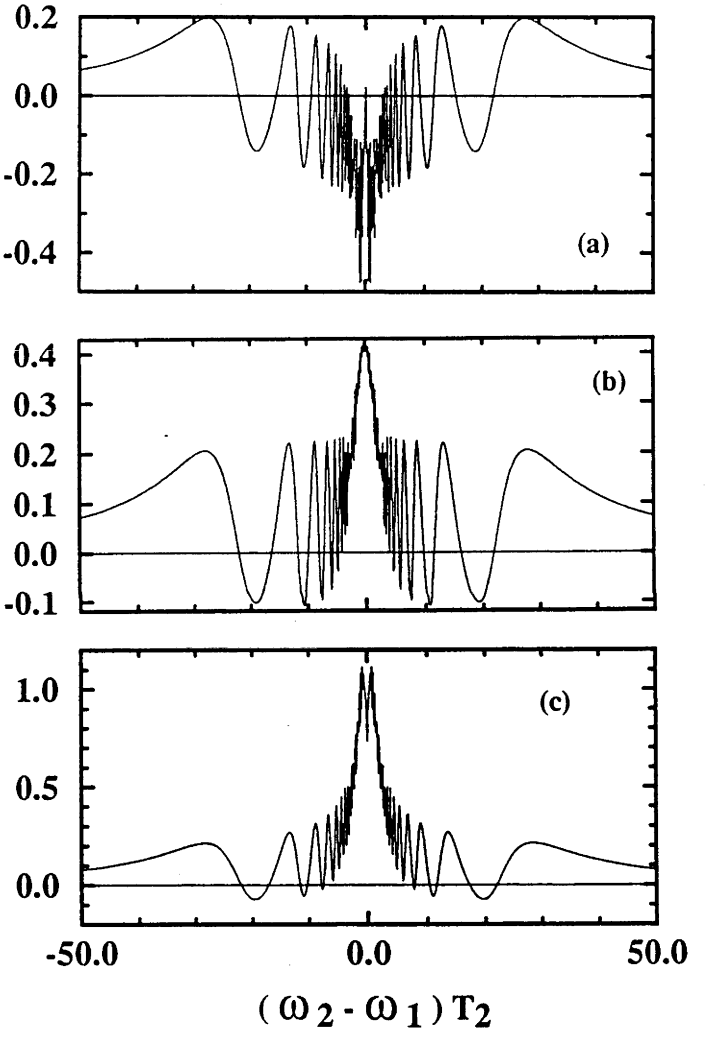

Figure 7-2 (B). Calculated absorption profiles for resonant pumping. The pump Rabi frequency is $\chi_1 T_2 = 20$. The probe Rabi frequencies are: $\chi_2 T_2 = 18$, 20, and 22 for traces (a), (b) and (c).

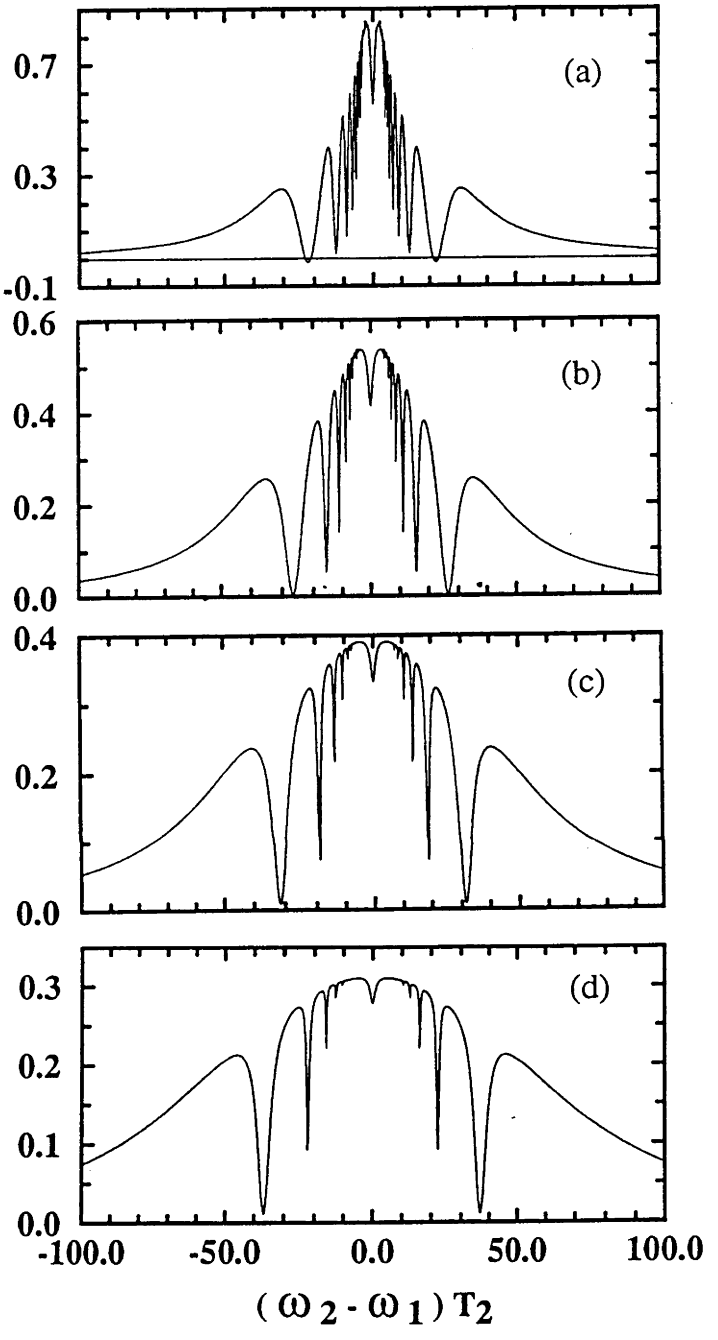

Figure 7-2 (C). Calculated absorption profiles for resonant pumping. The pump Rabi frequency is $\chi_1 T_2 = 20$. The probe Rabi frequencies are: $\chi_2 T_2 = 30$, 40, 50, and 60 for traces (a), (b), (c) and (d).

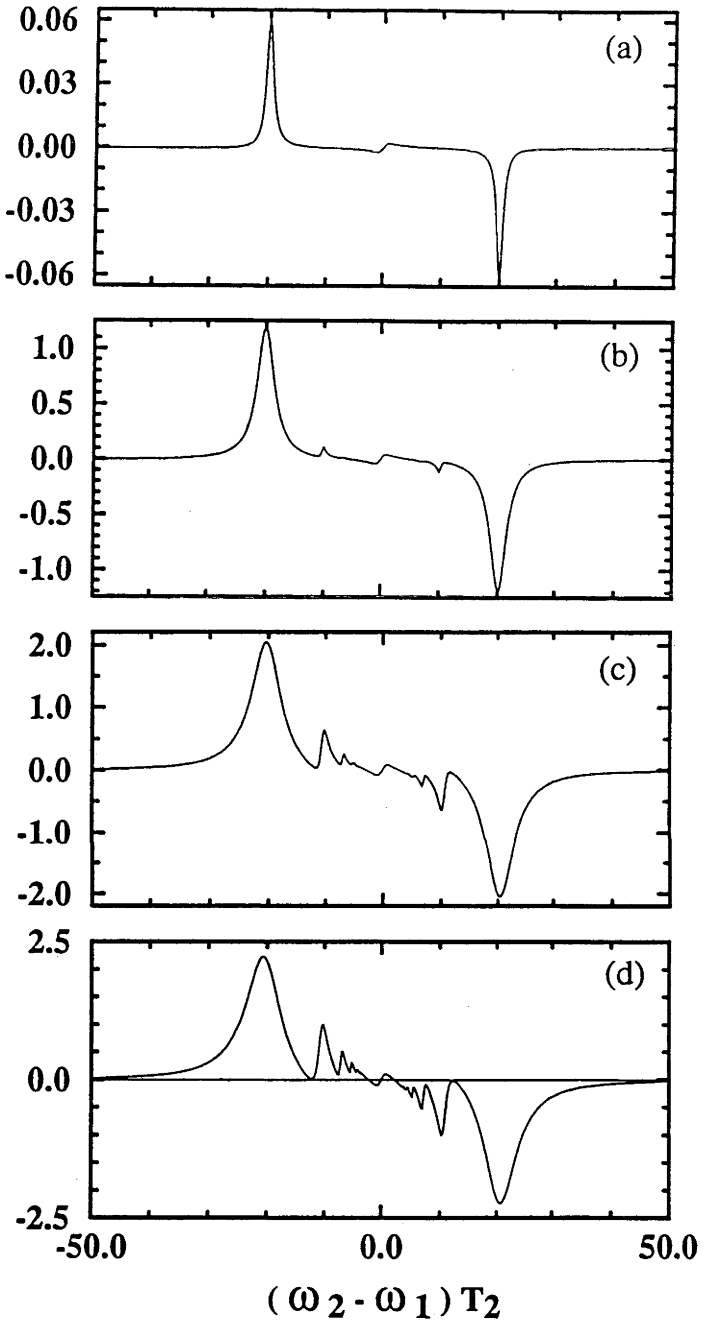

Figure 7-3 (A). Calculated dispersion profiles for resonant pumping. The pump Rabi frequency is $\chi_1 T_2 = 20$. The probe Rabi frequencies are: $\chi_2 T_2 = 0.2$, 4, 8 and 10 for traces (a), (b), (c) and (d).

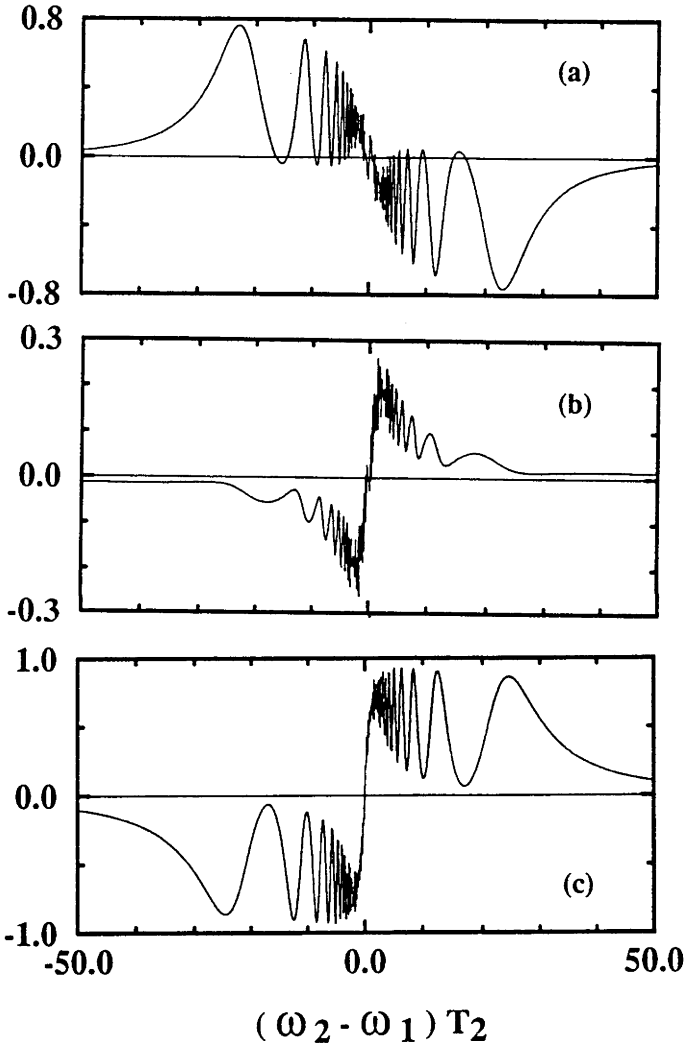

Figure 7-3 (B). Calculated dispersion profiles for resonant pumping. The pump Rabi frequency is $\chi_1 T_2 = 20$. The probe Rabi frequencies are: $\chi_2 T_2 = 18$, 20, and 22 for traces (a), (b) and (c).

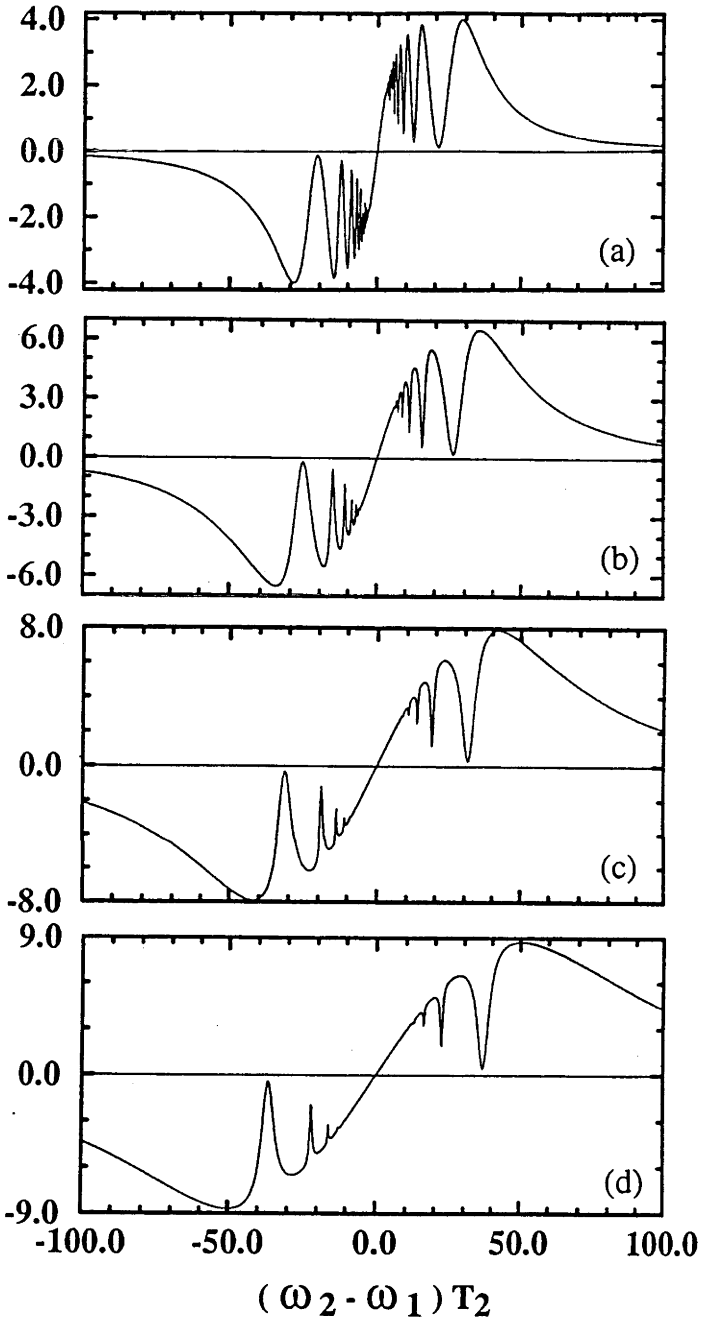

Figure 7-3 (C). Calculated dispersion profiles for resonant pumping. The pump Rabi frequency is $\chi_1 T_2 = 20$. The probe Rabi frequencies are: $\chi_2 T_2 = 30$, 40, 50, and 60 for traces (a), (b), (c) and (d).

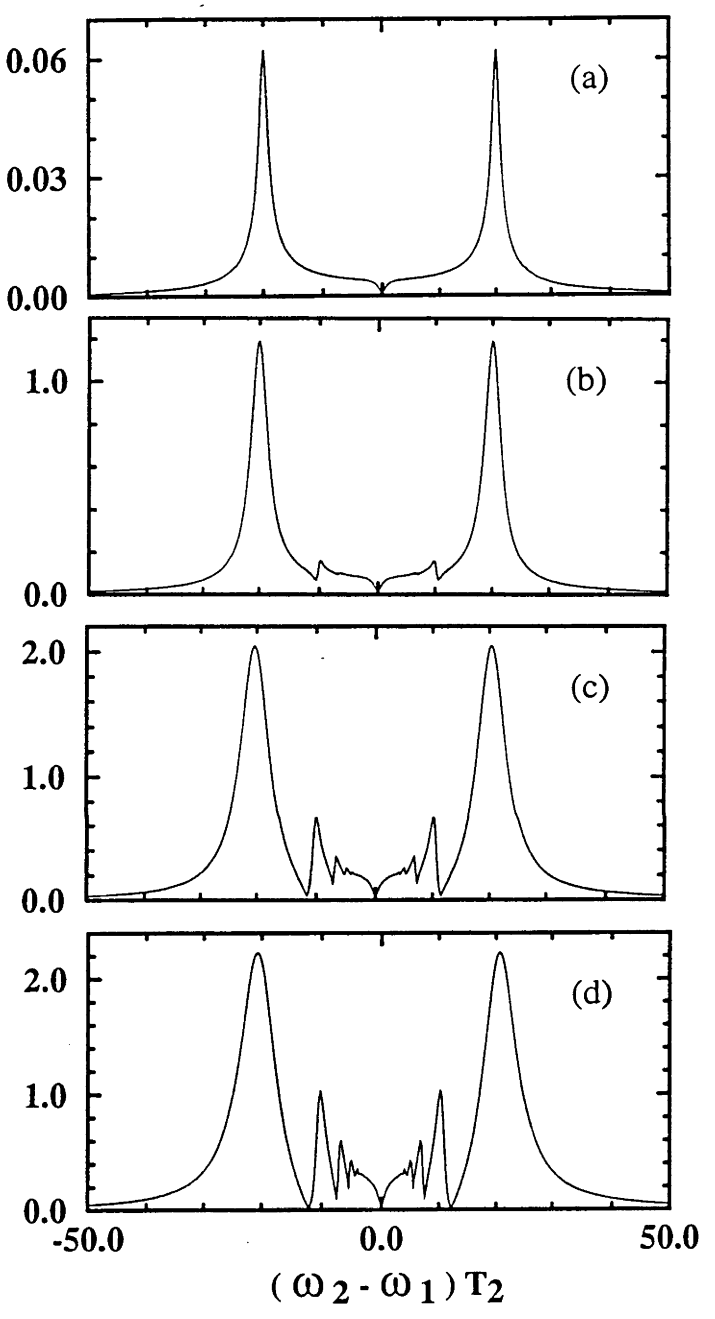

Figure 7-4 (A). Calculated amplitude profiles for resonant pumping. The pump Rabi frequency is $\chi_1 T_2 = 20$. The probe Rabi frequencies are: $\chi_2 T_2 = 0.2$, 4, 8 and 10 for traces (a), (b), (c) and (d).

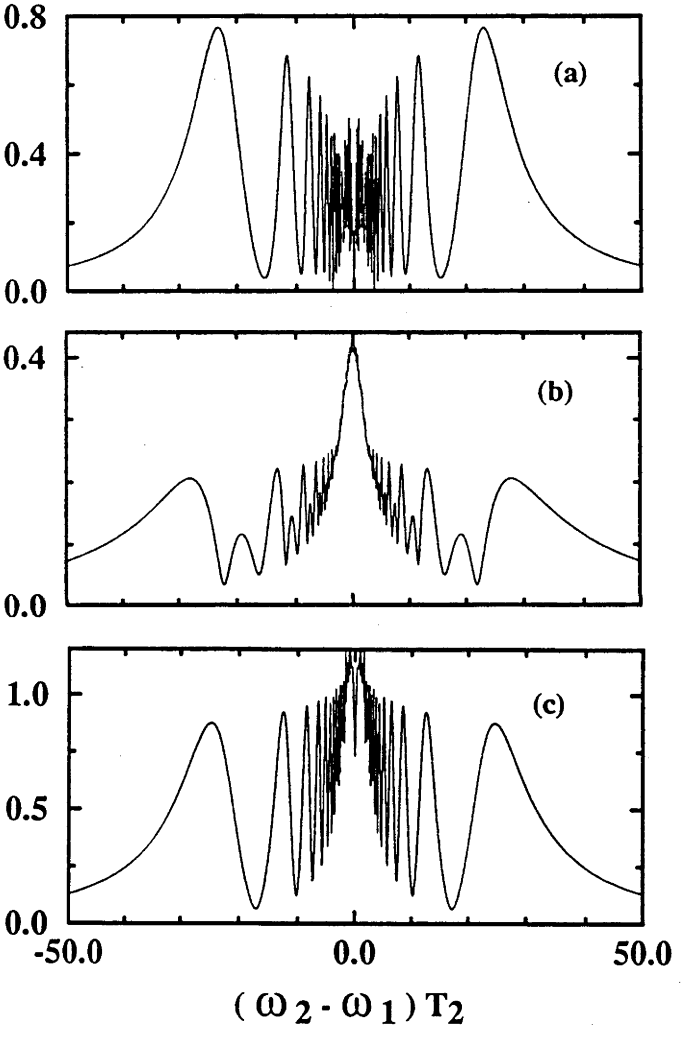

Figure 7-4 (B). Calculated amplitude profiles for resonant pumping. The pump Rabi frequency is $\chi_1 T_2 = 20$. The probe Rabi frequencies are: $\chi_2 T_2 = 18$, 20, and 22 for traces (a), (b) and (c).

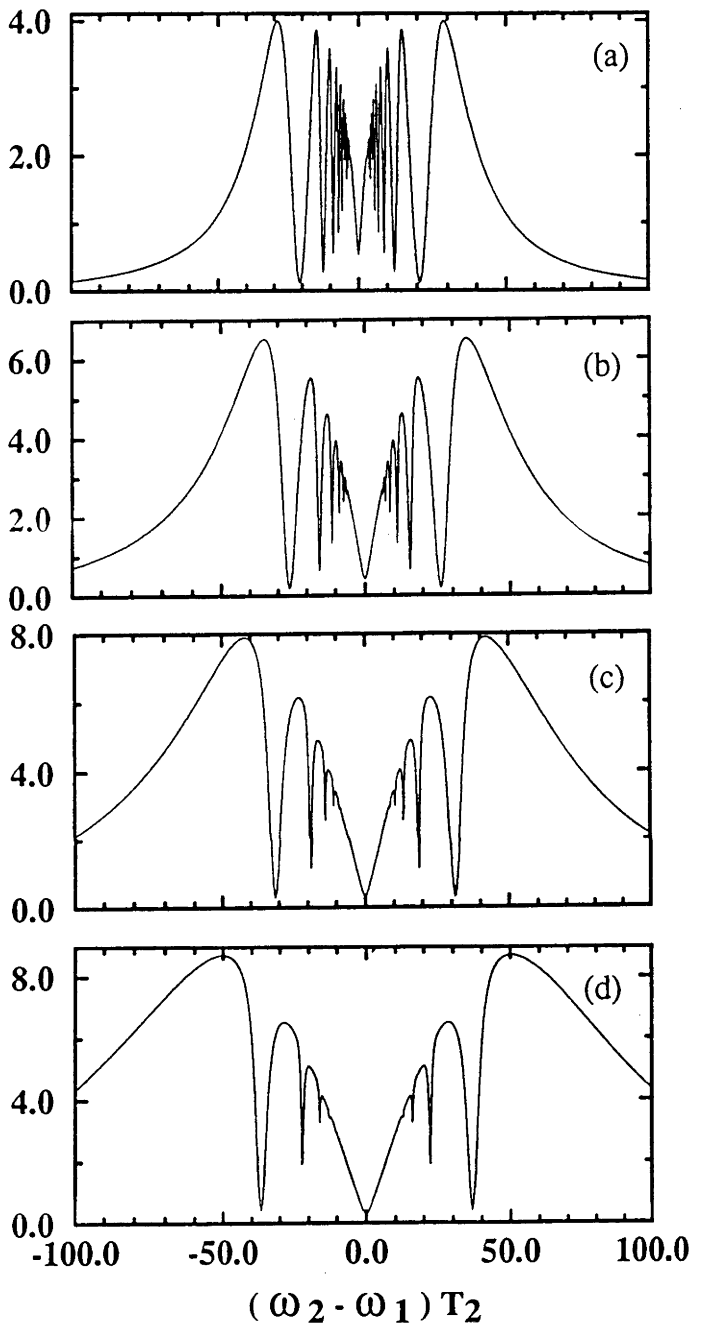

Figure 7-4 (C). Calculated amplitude profiles for resonant pumping. The pump Rabi frequency is $\chi_1 T_2 = 20$. The probe Rabi frequencies are: $\chi_2 T_2 = 30$, 40, 50, and 60 for traces (a), (b), (c) and (d).

The physical origin of the oscillation maximum occurring at the subharmonics of the Rabi frequency can be visualized in the dressed-state picture [25] as shown in Fig.7-5. The dressed-state is the eigenstate of a two-level atom "dressed" by pumping field. The peaks of the probe field correspond to the transitions between the dressed-states. At low probe intensity the main feature is two components corresponding to the transitions between adjacent dressed-state pairs which involve a single photon process. As probe intensity increases, the higher order interaction terms cause a broadening, a shift the single photon transitions and an introduction of multiphoton transitions between non-adjacent dressed-state pairs. Obviously the maximum amplitude of the oscillation occurring at χ/n is the manifestation of a resonant n-photon transition. At low probe intensity the probe field probes the driven two-level system but does not perturb it. Hence the dynamic Stark doublet splitting is twice of the pump field Rabi frequency and the total Rabi frequency χ is determined solely by the pump field: $\chi = \chi_1$. For strong probe field χ is a function of both pump and probe intensities: χ_1 and χ_2 in the form $\chi = [\chi_1^2 + \chi_2^2]^{1/2}$[15]. It is also interesting to note that in bare-atom state picture the resonance of order n corresponds to a 2n-1 (or 2n+1) photons process involving n probe photons and n-1 (or n+1) pump photons, while in dressed-atom state description it corresponds to a n photon process as the pumping field has already been taken into account in constructing the dressed-state.

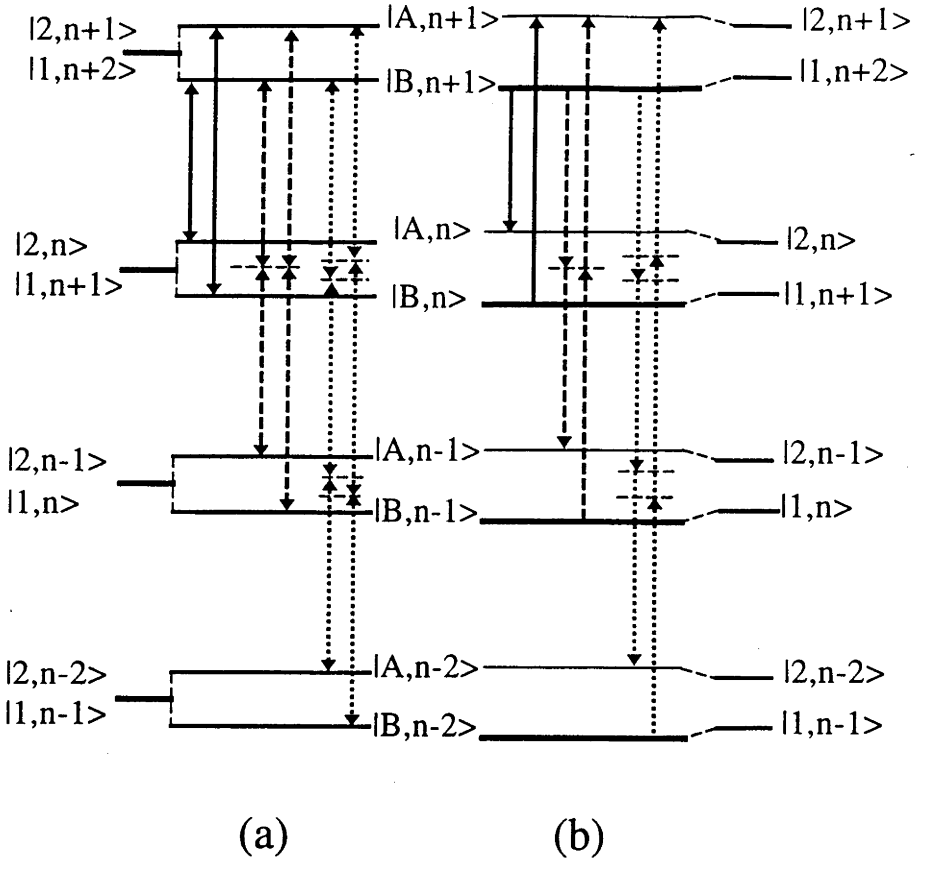

Figure 7-5. Schematic of energy levels and populations in dressed state for resonant (a) and off resonant pumping (b). The one photon transitions are those between adjacent dressed state levels |A,n> to |B,n+1> or |B,n> to |A,n+1> (solid line). The long dashed line represents two-photon transitions and the short dashed line three-photon transitions. For off resonant pumping (b) the solid, long dashed and short dashed line represent 1, 2 and 3-photon absorption (arrow up) and amplification (arrow down).

In the above discussion the dressed state is formed by considering only the pump field. The various spectral components are viewed as arising from the transitions between these dressed state and the interaction of dressed state and the probe field has not been incorporated in such a simple dressed state picture. It is observed that only when probe intensity ≤ pump intensity so that the dressed state levels are not significantly disturbed by the probe field, the

multiphoton resonances occur at the subharmonics of Rabi frequency, χ/n. When the probe field is sufficiently strong the multiphoton transitions do not obey the "subharmonic of Rabi frequency" rule which indicates the dressed state levels are modified by the strong probe field. The simple dressed state picture adopted here does not reflect this modification, however, the strict calculation using density matrix formalism does show such a behaviour [see, Figs.7-2(C), 7-3(C) and 7-4(c)].

It is worthwhile to note that the order of multiphoton processes has a maximum when the pump and probe field intensities are close or equal. As the n-th order resonance is actually a $2n\pm1$ photons process involving n probe photons and $n\pm1$ pump photons. Therefore, it is a natural consequence that a n-th order resonance is most probable when probe and pump field intensity are close. A further interesting observation is that the overall lineshapes are dominated by the stronger field. This is clearly demonstrated in the dispersion profiles in Fig.7-3. When the probe field is weaker than pump field as in (A) $\chi_2<\chi_1$ the dispersion profiles consist of absorption-like multi-peak profiles. On the other hand when $\chi_2>\chi_1$ the dispersive response has a power-broadened dispersion profile dominated by strong probe field with multiple dips produced by the pump field.

7.3.2 Off-Resonant Pumping

This section presents the computational results for the case where the pump field is off-resonance with the two-level system $\Delta_1 \neq 0$ and the parameters used are $T_1=3T_2$, $\chi_1T_2=36$ and $\Delta_1T_2=18$.

The calculated probe absorption profiles are shown in Fig.7-6 for various probe intensities. For weak probe situation [χ_2T_2 =0.2, in Fig.7-6(a)],

the main characteristic is the dynamic Stark splitting consisting of an absorption and a negative absorption (amplification). This is in agreement with the previous first order calculation and experiments (see, Chapter 6). As the probe intensity increases, the dynamic Stark doublet becomes power broadened and multiphoton absorption (amplification) peaks appear. At high probe intensity as in Fig.7-6(d) the central component at pump frequency also becomes a significant feature with a dispersion-like profile and will be discussed in experimental section.

The corresponding calculated probe dispersion profiles are shown in Fig.7-7 for equivalent probe intensities as for Fig.7-6. The weak probe results are again in agreement with first order calculation and previous experiments (see, Chapter 6). At high probe intensities multiphoton transitions occur and the central component at pump frequency as in absorption response becomes a significant feature but with an absorption-like profile.

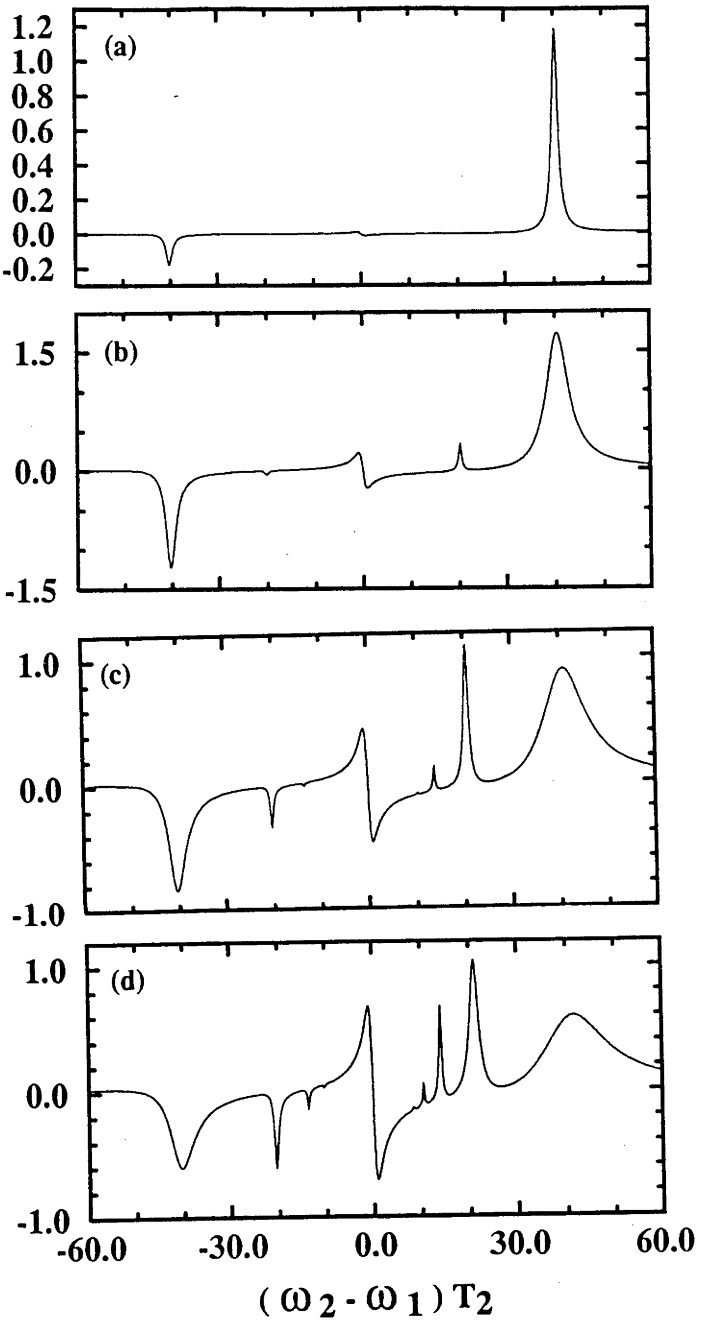

Figure 7-6. Calculated absorption profiles for off-resonant pumping. The pump Rabi frequency is $\chi_1 T_2 = 36$ and detuning $\Delta_1 T_2 = 18$. The probe Rabi frequencies are: $\chi_2 T_2 = 0.2$, 4, 6 and 8 for traces (a), (b), (c) and (d).

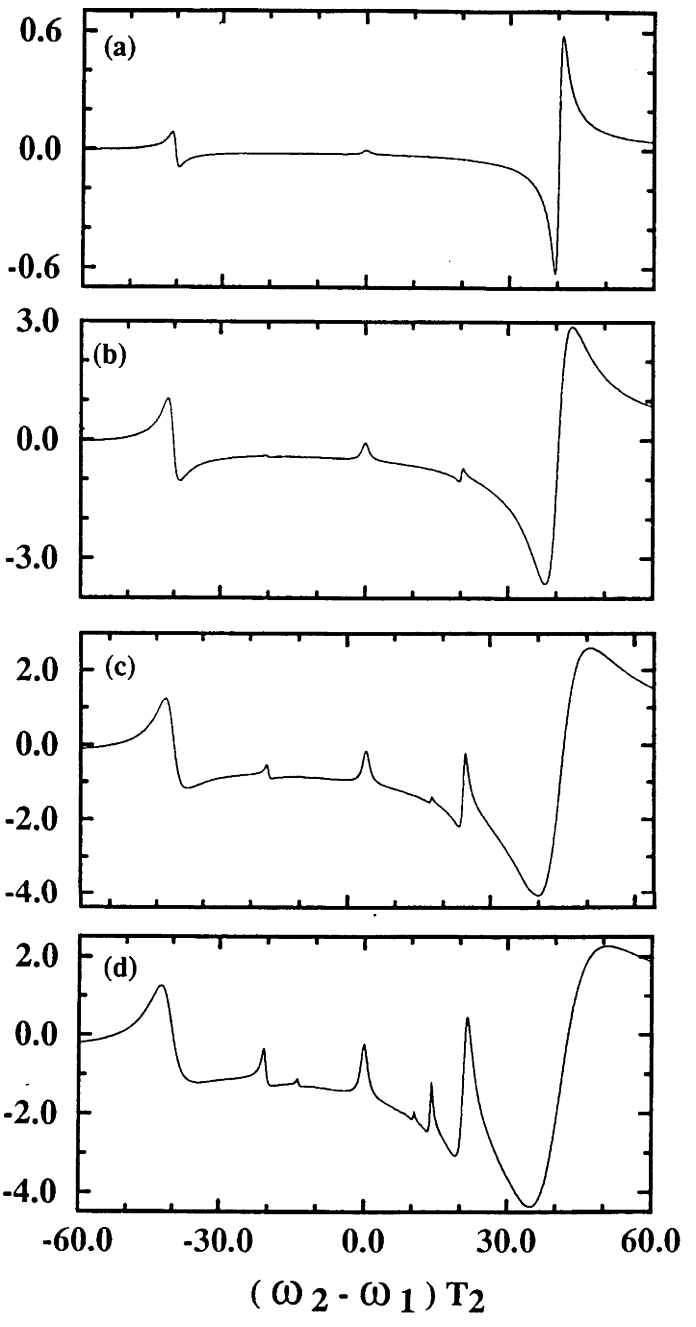

Figure 7-7. Calculated dispersion profiles for off-resonant pumping. The pump Rabi frequency is $\chi_1 T_2 = 36$ and detuning $\Delta_1 T_2 = 18$. The probe Rabi frequencies are: $\chi_2 T_2 = 0.2$, 4, 6 and 8 for traces (a), (b), (c) and (d).

7.4 Experimental Results and Discussions

7.4.1 On-Resonance Pumping

The experimental results for the on-resonance pumping case (Δ_1=0, ω_{21}=ω_1=5.4 MHz) is illustrated in this section. The pump field has a Rabi frequency of χ_1=21 kHz which is determined from a dynamic Stark splitting of 42 kHz measured using weak probe.

The experimental absorptive and dispersive profiles are shown in Figs.7-8 and 7-9, respectively, for various probe field intensities. Traces (a) in Figs.7-8 and 7-9 give the weak probe absorption and dispersion profiles, respectively. The following traces (b)-(d) in Figs.7-8 and 7-9 give the absorption and dispersion profiles, respectively, for increasing probe intensities. The strong fields tend to equalise the population of the two-level system and the resultant response particularly the absorption response is weak, hence results in the poor signal to noise ratio at large field intensity. The dispersion response saturates more slowly than the absorption response the signal quality of dispersion response is better.

Figs.7-10 shown the experimental dispersion response for increasing probe intensities showing the gradually change-over of the dispersion profiles. It can be seen that the experiments are in excellent agreement with the theory.

The measured strong probe amplitude profiles of the driven two-level system are shown in Fig.7-11. The profiles reflect the features of both absorption and dispersion whereas with different saturation behaviour of these two responses the dispersion profile dominate at the larger probe field intensities.

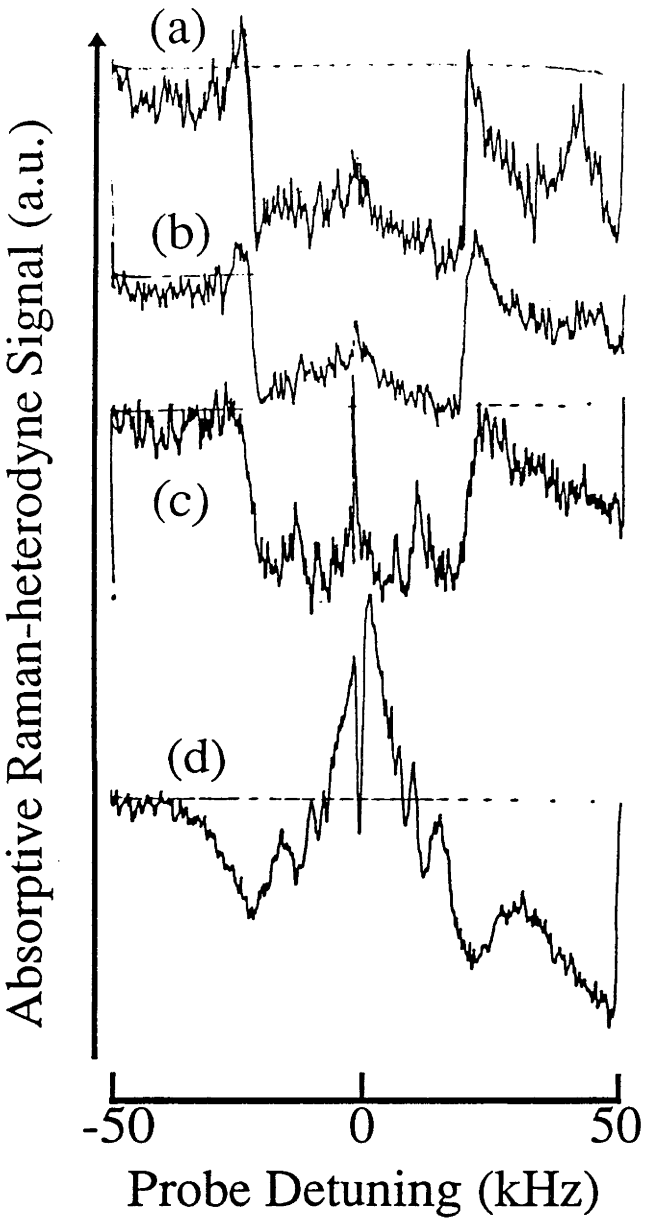

Figure 7-8. Measured absorption profiles for resonant pumping. The pump Rabi frequency is $\chi_1 = 21$ kHz. The probe intensities are: 0, 10, 20, and 30 dB for traces (a), (b), (c) and (d).

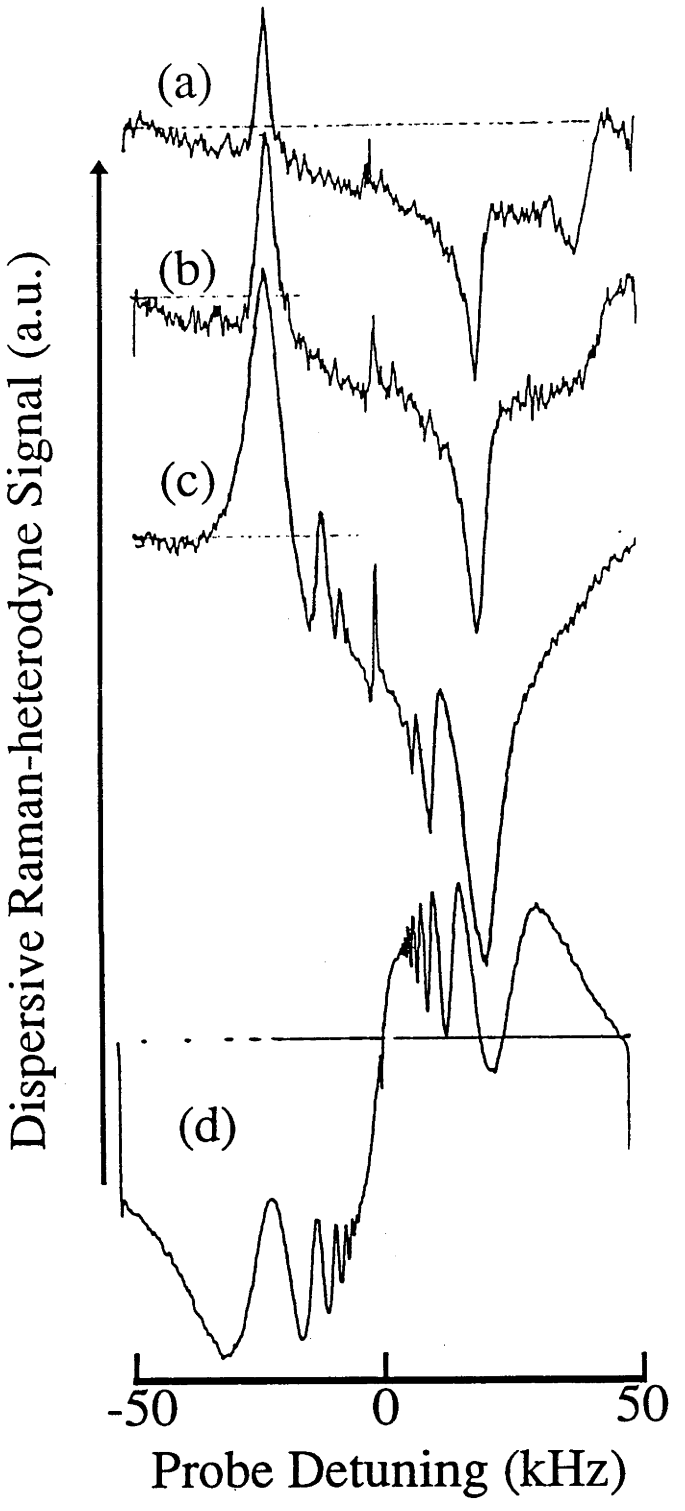

Figure 7-9. Measured dispersion profiles for resonant pumping. The pump Rabi frequency is $\chi_1 = 21$ kHz. The probe intensities are: 0, 10, 20, and 30 dB for traces (a), (b), (c) and (d).

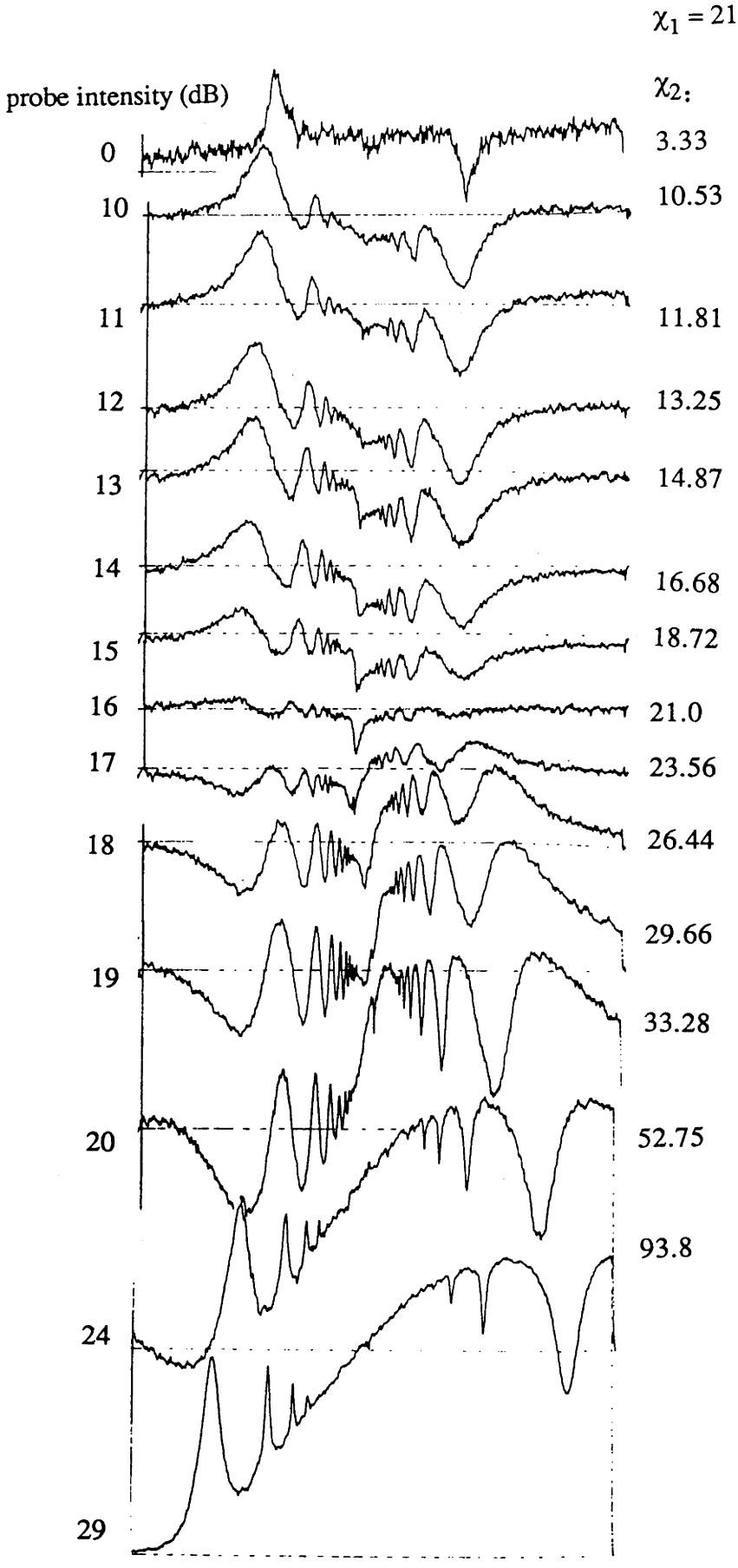

Figure 7-10. Measured dispersion profiles for resonant pumping.

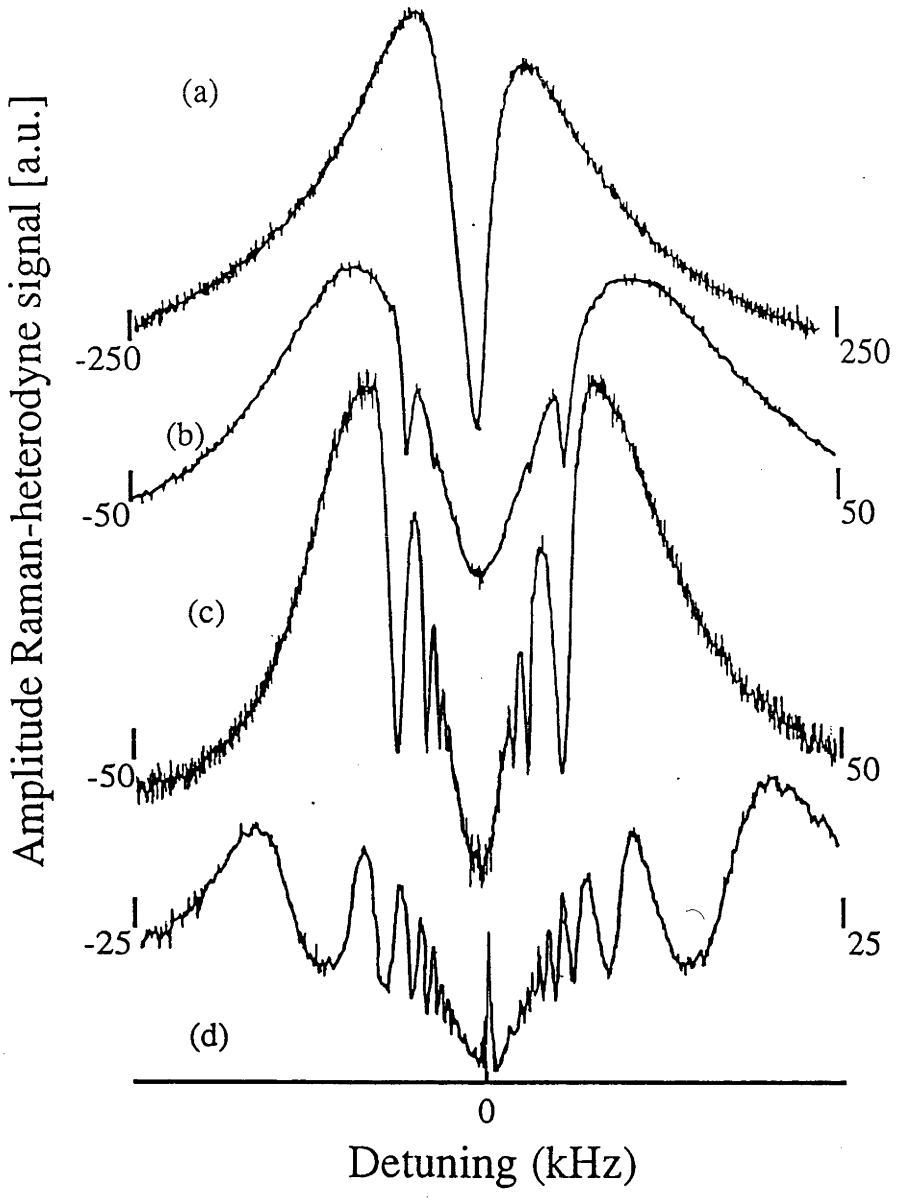

Figure 7-11. Measured amplitude profiles for a strong probe field with a fixed intensity and a resonant pumping field with increasing intensities. Trace (a) gives a power broadened amplitude profile without pumping. Traces (b), (c) and (d) give the amplitude profiles with a resonant pumping field of Rabi frequencies 4.5, 8 and 11 kHz, respectively.

The experimental results confirm the characteristic features of the theoretical calculations presented in previous section. As the probe intensity is increased the sharp feature observed at low probe intensity are power broadened and shifted to larger separation. New resonances occur at positions of χ/n and χ varies from χ_1 at low probe intensity to larger magnitudes at high probe intensities.

Fig.7-12 shows an enlarged section of trace (d) in Fig.7-9 and has up to 11-th order resonance clearly distinguished. In the inserted of Fig.7-12 the multiphoton resonances positions are plotted as a function of n along with the expression of χ/n fitted with χ=32 kHz. From this measured value for χ and χ_1=21 kHz determined from weak probe field splitting an estimate of χ_2 = 24 kHz is obtained using the above expression for χ for the probe intensity of 30 dB. This value which has $\chi_1<\chi_2$ is further supported by the change in the lineshape compared to lower probe intensities as predicted by theoretical calculation.

Another remarkable feature is the dependence of linewidth of n-photon resonances on order n. The data are taken from either on-resonance pumping dispersive response (Fig.7-9) or off-resonance pumping absorptive response to be shown later in Fig.7-14. In both case the multiphoton transitions are characterized by absorption-like profiles and the linewidth can be reliably determined from the spectra. Our results, then, show unambiguously that the n-photon resonances linewidth varies as function of $1/n^2$. The typical results of normalized n-photon resonances linewidth as a function of n are shown in Fig.7-13, where data in circles and stars are taken from the high and low frequency side resonances of Fig.7-9 and the data in up and down triangles from the multiphoton absorption and amplification side of Fig.7-14, respectively. A plot of $1/n^2$ is also shown in Fig.7-13 (solid line) for

comparison. From the theoretical treatment given in previous section it is not practical to derive an explicit expression for the n-photon resonances linewidth dependence upon n, nevertheless, by inspecting the theoretical profiles shown in Figs.7-2 and 7-3 it is found that the linewidth variation in the calculated profiles shows a dependence close to $1/n^2$.

Our result of n-photon resonances linewidth dependence upon n is clearly in contradiction with that reported by Bonch-Bruevich *et al.* [12], in which the n-photon resonances linewidth was claimed to decrease approximately as a function of 1/n. In [12] the authors did not state explicitly how the n-photon resonances linewidth was obtained but it can be assumed that their data are taken from the on-resonance pumping absorption response as that is the only data presented in their paper. This procedure has the difficult that in on-resonance pumping the multiphoton resonance in absorption response is characterized by dispersion-like feature and at high probe intensity are power broadened, overlapped and distorted. It is possible then that large measurement error can be attributed to poorly defined linewidths and hence erroneous conclusion. Further support of the $1/n^2$ dependence comes from data presented in Papademetriou et al's paper [20]. Their data clearly shows a dependence far from 1/n and very close to $1/n^2$.

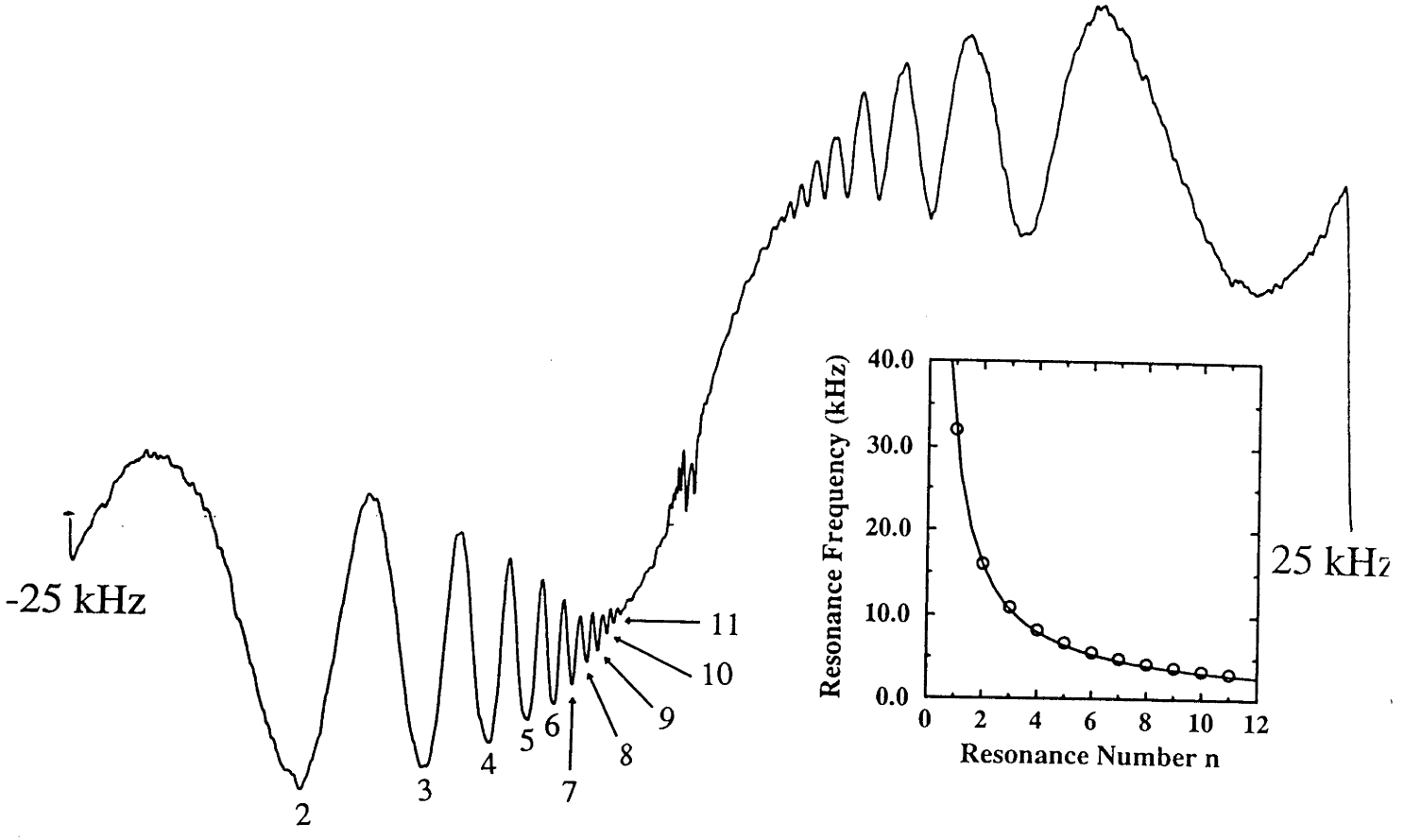

Figure 7-12. An enlarged dispersion profile of trace (d) in Fig.7-9 showing up to 11-th order transitions.

The inserted figure shows the multiphoton resonances positions as a function of n with a plot of 1/n for comparison.

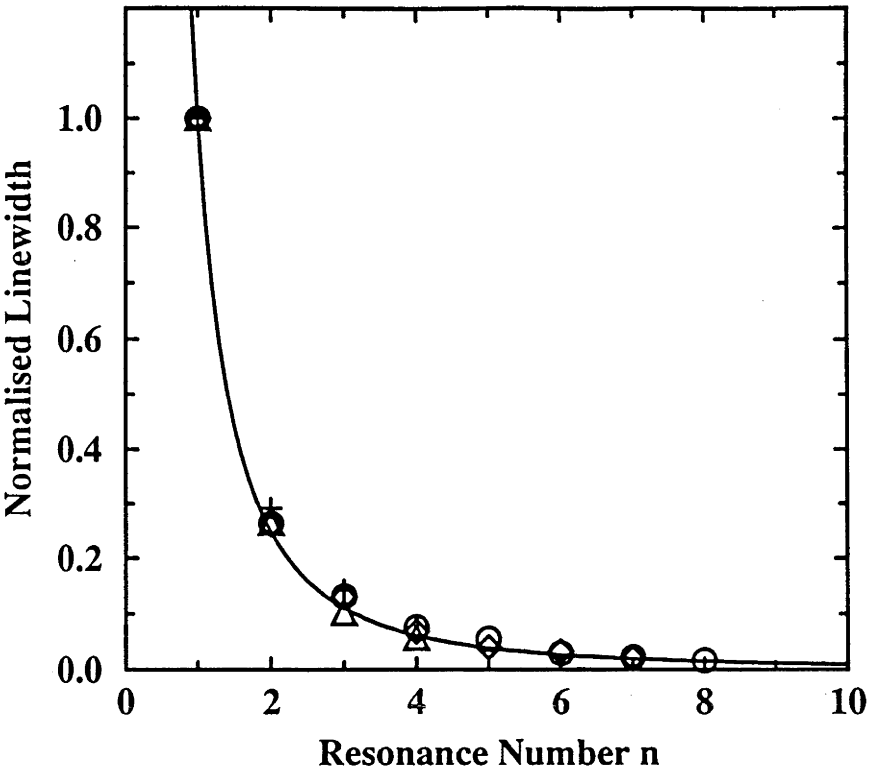

Figure 7-13. Measured linewidth of multiphoton transition as a function of n with a plot of $1/n^2$ for comparison.

7.4.2 Off-Resonance Pumping

This section presents the experimental results for the case where the pump field is off-resonance: $\Delta_1 \neq 0$. In the experiment the pump field has a negative detuning of Δ_1=-18 kHz and a Rabi frequency χ_1 = 36 kHz which gives a generalised Rabi frequency of $\chi = [\chi_1^2 + \Delta_1^2]^{1/2}$ = 40.3 kHz and results in a dynamic Stark splitting of 81 kHz.

The measured absorption and dispersion profiles are shown in Figs.7-14 and 7-15, respectively, for various probe intensities. At weak probe intensity [Fig7-14(a)] the absorption profile consists of an absorption and a negative-absorption (amplification) peak separated by the generalised Rabi frequency

from the pump field frequency. This is in agreement with the first order calculation and previous observations (see, Chapter 6). As the probe intensity increases, the dynamic Stark doublets become broadened and new absorption and amplification peaks appear [Fig.7-14(b)-(d)]. The dispersion responses behaviour is similar. In both absorption and dispersion the positions of multiphoton resonances again can be described by the empirical formula χ/n and their linewidth by $1/n^2$ (Fig.7-13) as discussed above. Up to n=4 resonance in absorption and n=3 resonance in amplification are observed for off-resonance pumping [Fig.7-14(f)] and equivalent features seen in dispersion [Fig.7-15(f)]. These experimental profiles (Figs.7-14 and 7-15) can be seen to be in good agreement with the calculations given in Figs.7-6 and 7-7 indicating that the system behaves remarkably closely to that expected for an ideal two-level system.

The theory predicts a feature at about the pump field frequency, while so far there has not been a demonstrative experimental observation as the signal in the pump frequency is usually weak and emerged in pick-up signal due to the presence of strong pump field. For high probe intensity this feature is broader and stronger such that it can be easily distinguished from the pick-up as shown in Figs.7-14 and 7-15. The central feature has a dispersion-like profile in the absorption response and an absorption-like profile in the dispersion response. Part of the absorption response consequently corresponds to gain and this is treated below.

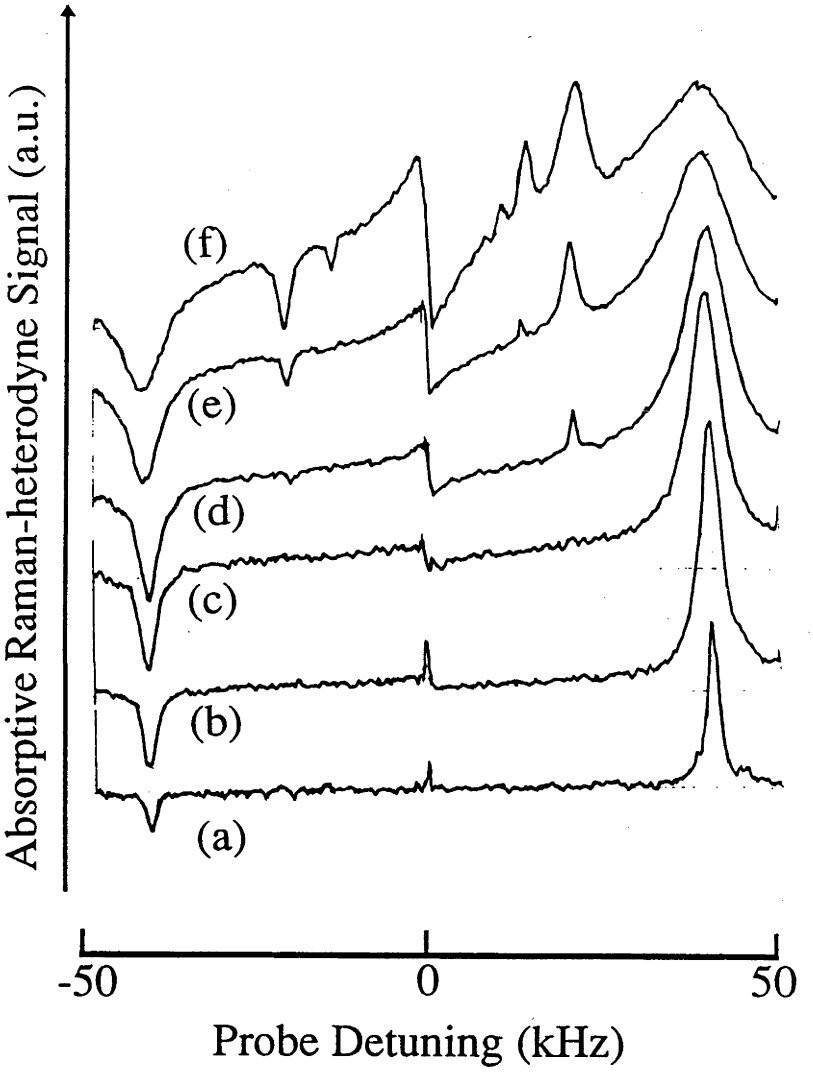

Figure 7-14. Measured absorption profiles for off-resonant pumping. The pump Rabi frequency is $\chi_1 = 36$ kHz and detuning $\Delta_1 = 18$ kHz. The probe field intensities are: 0, 10, 20, 25, 30 and 35 dB for traces (a), (b), (c), (d), (e) and (f).

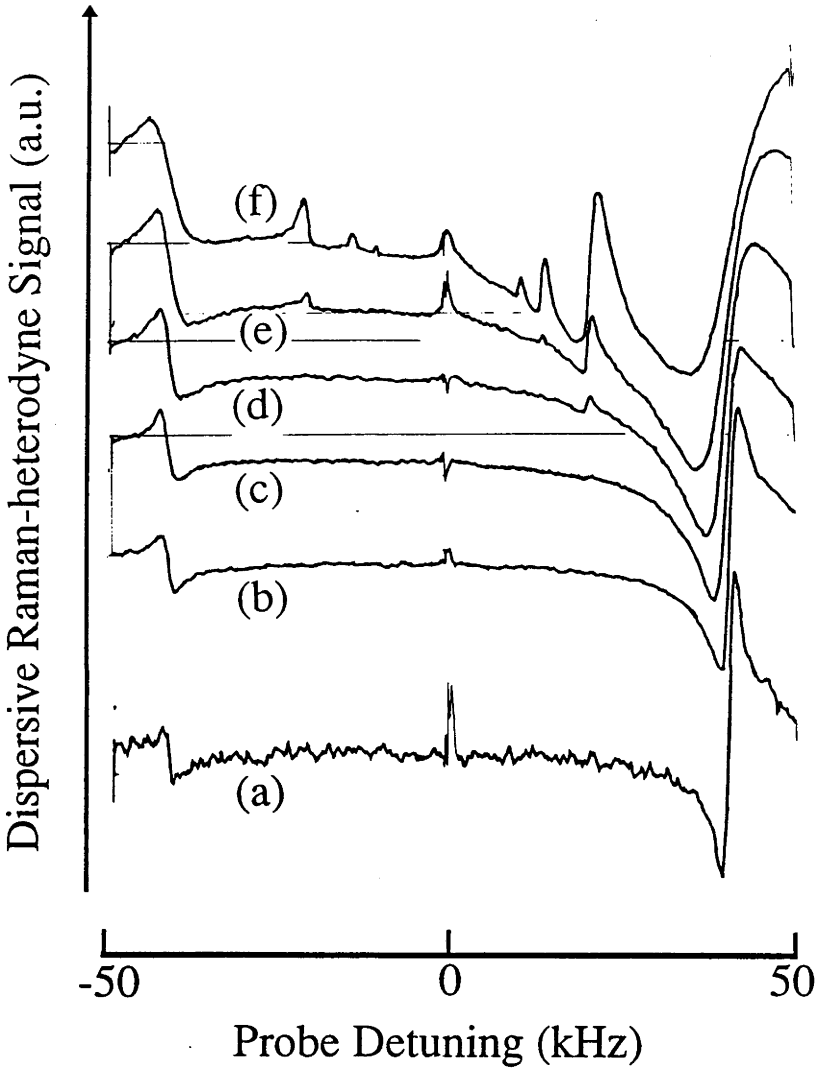

Figure 7-15. Measured dispersion profiles for off-resonant pumping. The pump Rabi frequency is $\chi_1 = 36$ kHz and detuning $\Delta_1 = 18$ kHz. The probe field intensities are: 0, 10, 20, 25, 30 and 35 dB for traces (a), (b), (c), (d), (e) and (f).

To achieve amplification the stimulated emission are to be stronger than the absorption and thus it is usually required to achieve a population inversion between the amplification transition. It is well known that in steady state limit it is not possible to achieve population inversion in a two-level system and, thus, the amplification observed in strongly driven two-level system is referred to as amplification without population inversion. There are two state basis used in the studies of atom interacting with strong radiation: the bare-state basis, which is the eigenstate of the isolated atomic system, and the dressed-state basis, which is the eigenstate of the coupled atom plus radiation field system. It is also found that amplification without inversion can be fell under one of the two cases. The first case is that the amplification can be attributed to a hidden inversion. In this case, one may found that although there is no inversion in one state basis (often the bare-state basis), there is an inversion in the other state basis (often the dressed-state basis). The second is the true non-inversion case where the amplification takes place without inversion either in bare- or dressed-state basis.

In bare-atom state picture the one-photon amplification without inversion in a strongly driven two-level system can be attributed to energy transfer from pump to probe field via a stimulated three-photon process [8,9, also see, Chapter 6], in which two pump photons are absorbed and a photon of probe frequency is stimulated. Likewise the two- and three-photon gain can be understood as due to a stimulated five- and seven-photon process, respectively, by which the probe field is amplified at the expense of pump field.

An alternative description of multiphoton amplification can be provided by the dressed-state picture [Fig.7-5(b)][19,25]. For a negative detuned pump field, the $|B,n\rangle$ levels are more populated than the $|A,n\rangle$ levels. The transition between the dressed-state $|A,n+m\rangle \Leftrightarrow |B,n\rangle$ (m=1,2,3,...) corresponds to an absorptive m-photon transition. A m-photon gain process arises from the

transition between population inverted dressed-state $|B,n+m\rangle \Leftrightarrow |A,n\rangle$ (m=1,2,3,...).

From above discussion it is seen that the population inversion in dressed-state is found to be responsible for the one-, two- and three-photon amplification although there is no population inversion in the bare-state. Then it is interesting to note that the central component at pump field frequency has a dispersion-like profile feature consisting of an absorption and an amplification parts and this component is due to transitions between $|A,n+m\rangle \Leftrightarrow |A,n\rangle$ or $|B,n+m\rangle \Leftrightarrow |B,n\rangle$ (m=1,2,3, ...). It is clear that this is a true amplification without population inversion process because the population inversion does not occur in either bare- or dressed-atom state.

7.5 Conclusions

The absorption and dispersion profiles of a strongly driven two-level system when probed by a strong field have been presented including the first case where the dispersion profiles have been reported. The two-level system is approximately homogeneously broadened and the linewidth of the transition approaches that set by the radiative limit. The system is then close to the simplest possible two-level system and it is shown that the experimental traces make excellent comparison with those calculated from density matrix equations of motion for a simple two-level system.

The prominent feature has been shown to be the appearance of multiphoton resonance peaks. The position and linewidth of these multiphoton transition are investigated: a χ/n dependence of the peak position and a $1/n^2$ of the peak linewidth. The other notable feature is the observation of gain without inversion. Given that the current observations are associated with a rf transition

the utilisation of the gain in unlikely to have much practical implication, but gain without inversion does have promising possibilities in other spectral regions and the illustration of the phenomenon itself is of considerable interest. Significantly the illustrations are the clearest to date. Two-photon gain has been observed in a barium atomic beam in the optical region [19] whereas up to three-photon gain without inversion is reported in this work.

The origin of the gain in the driven two-level system has been discussed and it is shown that there are two kinds of amplification without inversion depending on the pump detuning. For on-resonance pumping the amplification can be classified as true amplification without inversion and it occurs over a range of frequency given by the twice the pump Rabi frequency but the gain is relatively small. For off-resonance pumping both kinds of amplification without inversion are present. The gain experienced by probe field when the probe frequency is detuned from pump field by Rabi frequency or its subharmonic frequency, giving the one-, two- and three-photon gain, is due to population inversion within the dressed-state basis, while the gain near the pump frequency occurs without population inversion in either bare- or dressed-state basis. With off-resonance pumping it is shown that the gain occur in a restricted range but are more substantial than that achieved with on-resonance pumping.

References

[1] A. Abragam, *Principles of Nuclear Magnetism*, (Clarendon Press, Oxford, 1961)

[2] L. Allen and J. H. Eberly, *Optical Resonance and Two Level Atoms*, (Dover, NY., 1987)

[3] P.L.Knight and P.W.Milonni, " *The Rabi frequency in optical spectra*" Phys. Rep. 66, pp 21-107 (1980)

[4] B. R. Mollow, " *Theory of intensity dependent resonance light scattering and resonance fluorescence* " in Progress in Optics, Vol. 19, 1, E. Wolf ed. (North-Holland, Amsterdam, 1981)

[5] See, also,

B.W.Shore, *The theory of coherent atomic excitation*, Vol I and II, (Wiley, Now York, 1990)

P. Meystre and M.Sargent III, *Elements of Quantum Optics*, (Springer-Verlag, Berlin-New York, 1991)

R.W.Boyd, *Nonlinear optics*, (Academic Press Inc, 1992)

[6] B. R. Mollow, Phys. Rev. A5, 2217, (1972)

" *Stimulated emission and absorption near resonance for driven systems* "

[7] A. M. Bonch-Bruevich, V. A. Khodovoi, and N. A. Chigir, Sov. Phys. JETP, 40, 1027, (1975)

" *Changes in the absorption spectrum and of dispersion of a two-level system in a rotating monochromatic radiation field* "

[8] F. Y. Wu, S. Ezekiel, M. Ducloy, and B. R. Mollow, Phys. Rev. Lett., 38, 1077, (1977)

" *Observation of amplification in a strongly driven two-level atomic system at optical frequencies* "

[9] R. W. Boyd, M. G. Raymer, P. Narum, and D. J. Harter, Phys. Rev. A24, 411, (1981)

" *Four-wave parametric interactions in a strongly driven two-level system* "

[10] A.D. Wilson-Gordon, and H. Friedmann, Opt. Commun., 94, 238, (1992)

" *Enhanced index of refraction: a comparison between two- and three-level systems* "

[11] S. Feneuille, M -G. Schweighofer, and G. Oliver, J. Phys. B9, 2003, (1976)

" *Response of a two-level system to a narrow-band light excitation completely modulated in amplitude.* "

[12] A. M. Bonch-Bruevich, T. A. Vartanyan, and N. A. Chigir, Sov. Phys. JETP, 50 (5), 901, (1979)

" *Subradiative structure in the absorption spectrum of a two-level system in a biharmonic radiation field* "

[13] N. Tsukada, J. Phys. Soc. Japn., 46, 1280 (1979)

" *Saturation effects of a two-level system in two RF field* "

[14] P. Thomann, J. Phys. B13, 1111, (1980)

" *Optical resonances in a strong modulated laser beams* "

[15] G.I.Toptygina and E. E. Fradkin, Sov. Phys. JETP, 55 (2), 246, (1982)

" *Theory of subradiative absorption structure in the interaction between two intense waves in a nonlinear medium* "

[16] G.S.Agarwal and N.Nayak, J. Opt. Soc. Am. B1, 164, (1984)

" *Multiphoton processes in two-level atoms in two intense pump beams* "

[17] H.Friedmann and A.D.Wilson-Gordon, Phys. Rev. A36, 1333, (1987)

" *Dispersion profiles of the absorptive response of a two-level system interacting with two intense fields* "

[18] S. Chakmakjian, K. Koch, and C. R. Stroud, Jr., J. Opt. Am. B5, 2015, (1988)

" *Observation of resonances at subharmonics of the Rabi frequency in the saturated absorption of a 100% amplitude-modulated laser beam* "

[19] Y. Zhu, Q. Wu, S. Morin, and T. W. Mossberg, Phys. Rev. Lett. 65, 1200, (1990)

" *Observation of a two-photon gain feature in the strong-probe absorption spectrum of driven two-level atoms* "

[20] S. Papademetriou, S. Chakmakjian, and C. R. Stroud, Jr., J. Opt. Am. B9, 1182, (1992)

" *Optical subharmonic Rabi resonances* "

[21] H. Freedhoff and Z. Chen, Phys. Rev. A41, 6013, (1990)

" *Resonance fluorescence of a two-level atom in a strong bichromatic field* "

[22] Z. Ficek and H. S. Freedhoff, Phys. Rev. A48, 3092, (1993)

" *Resonance-fluorescence and absorption spectra of a two-level atom driven by a strong bichromatic field* "

[23] Yifu Zhu, Qilin Wu, A. Lezama, D. J. Gauthier, and T. W. Mossberg, Phys. Rev. A41, 6574 (1992)

" *Resonance fluorescence of two-level atoms under strong bichromatic excitation* "

[24] S. Shu, Adv. At. Mol. Phys. 21, 197 (1985)

" *Recent developments in semiclassical Floquet theories for intense-field multiphoton processes* "

[25] C.Cohen-Tannoudji, Jacques Dupont-Roc and G.Grynberg

Atom-Photon Interactions: Basic Processes and Applications (Wiley, New York, 1992)

Chapter 8

Absorption and Dispersion Profiles of a Strongly Driven Transition: Three-level System with a Strong Probe

In the previous two chapters the weak (Chapter 6) and strong (Chapter 7) probe response of a driven two-level system are investigated for the case where the pump and probe fields interact with the same transition. In this chapter we extend the study to the case where the pump and probe fields interact with different transitions sharing one common level.

8.1 Introduction

Previously, we have reported experimental investigations of the absorption and dispersion responses of a strongly driven two-level system when probed by a weak (Chapter 6) and strong (Chapter 7) field, where both pump and probe fields interact with the same $I_z = |0\rangle \Leftrightarrow |-1\rangle$ transition at 5.4 MHz. The dynamic "Stark" splitting, multiphoton transitions and amplification without inversion have been observed. These two levels are part of a nuclear spin triplet, and when the $I_z = |1\rangle$ state is included the two-level system is extended to a three-level system. Such a three-level system interacting with two fields for weak probe case has also been studied previously, where the $I_z=|0\rangle\Leftrightarrow|1\rangle$ transition at 4.7 MHz is driven by a strong pump field and the $I_z=|0\rangle\Leftrightarrow|-1\rangle$ transition at 5.4 MHz is probed by a weak field, and the Autler-Townes splitting has been observed [1].

The splitting of an energy level by a strong driving field, known as dynamic Stark splitting or Autler-Townes effect [2], is the manifestation of

the interaction of monochromatic electromagnetic fields with matter and has been studied by many researchers [1-21] both theoretically and experimentally. Such experimental studies provide important and fundamental information about the nature of radiation-matter interactions and can be compared directly with theoretical calculations. However, in most earlier studies the situations are restricted to the weak probe limit where the probe field power is kept sufficiently low that the interaction is linear and needs only to be treated to first order. For the strong probe case there have been only two reported investigations [9, 13]. Gray *et al.* [9] reported the first observation of the power broadened Autler-Townes profiles in a sodium atomic beam as a three-level system. More recently Fisk *et al.* [13] presented a systematic investigation of power broadened Autler-Townes profiles in a barium atomic beam as a three-level system. The sodium or barium atoms systems are interesting systems, but they are not simple three-level systems due to hyperfine structure and the presence of isotopes. In both experiments the profiles were obtained by monitoring the fluorescence induced by the probe field which is directly related to diagonal term of the density matrix or the population of the fluorescent level [9,13]. There have been no reported investigations of the absorption and dispersion profiles of a strongly driven transition in a three-level system configuration.

This chapter reports the experimental investigations of the power broadened Autler-Townes effect. The absorption, dispersion and amplitude profiles of a strongly driven transition are measured in a three-level system configuration with the probe field intensity varying from weak to strong. The three-level system consists of the hyperfine levels: $I_z = |0\rangle, |+1\rangle$ and $|-1\rangle$, in which the $I_z=|0\rangle \Leftrightarrow |1\rangle$ 4.7 MHz transition is strongly driven by a pump field and the $I_z=|0\rangle \Leftrightarrow |-1\rangle$ 5.4 MHz transition is scanned by a probe field.

8.2 Theory

A three-level system interacting with two near-resonant fields is shown in Fig.8-1. The three-level system has energy levels $E_1 < E_2 < E_3$, corresponding to the three states |1>, |2>, |3>.

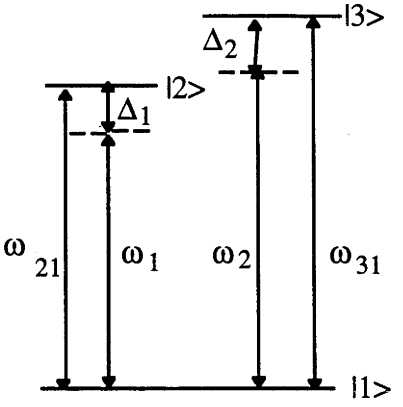

Figure 8-1. Three-level system interacting with two fields.

The system interacts with two near-resonant fields of frequencies ω_1 and ω_2 and the rf magnetic field has the form

$$\mathbf{B_{rf}}(t)=\mathbf{B}_1\cos\omega_1 t + \mathbf{B}_2\cos\omega_2 t. \qquad (8.1)$$

When the field ω_1 (ω_2) interacts only with the |1>⇔|2> (|1>⇔|3>) transition the interaction Hamiltonian, H_I, can be written as

$$H_I = \begin{bmatrix} 0 & -2\hbar V_1\cos\omega_1 t & -2\hbar V_2\cos\omega_2 t \\ -2\hbar V_1\cos\omega_1 t & 0 & 0 \\ -2\hbar V_2\cos\omega_2 t & 0 & 0 \end{bmatrix} \qquad (8.2)$$

where we have introduced the notations V_1 and V_2 which are related to the Rabi frequencies χ_1 and χ_2 of pump and probe field, respectively

$$\chi_1 \equiv 2V_1 = \frac{\mu_{21}\mathbf{B}_1}{\hbar}, \text{ and } \chi_2 \equiv 2V_2 = \frac{\mu_{31}\mathbf{B}_2}{\hbar}. \qquad (8.3)$$

We use the following transformations to remove the rapidly oscillating factors of the off-diagonal elements

$$\rho_{31} = \tilde{\rho}_{31} e^{-i\omega_2 t}, \tag{8.4a}$$

$$\rho_{21} = \tilde{\rho}_{21} e^{-i\omega_1 t}, \tag{8.4b}$$

$$\rho_{32} = \tilde{\rho}_{32} e^{-i(\omega_2 - \omega_1)t}. \tag{8.4c}$$

The transition frequencies ω_{ij} and detunings Δ_1, Δ_2 are defined

$$\hbar\,\omega_{ij} = E_i - E_j, \tag{8.5a}$$

$$\Delta_1 = \omega_{21} - \omega_1, \tag{8.5b}$$

$$\Delta_2 = \omega_{31} - \omega_2, \tag{8.5c}$$

$$\Delta = \Delta_1 - \Delta_2. \tag{8.5d}$$

The equations of motion of the density matrix in the rotating wave approximation are given by (Chapter 1),

$$\frac{\partial \rho_{11}}{\partial t} = i V_1 (\tilde{\rho}_{21} - \tilde{\rho}_{12}) + i V_2 (\tilde{\rho}_{31} - \tilde{\rho}_{13}) - \frac{\rho_{11} - \rho_{11}^{eq}}{T_1}, \tag{8.6a}$$

$$\frac{\partial \rho_{22}}{\partial t} = - i V_1 (\tilde{\rho}_{21} - \tilde{\rho}_{12}) - \frac{\rho_{22} - \rho_{22}^{eq}}{T_1}, \tag{8.6b}$$

$$\frac{\partial \rho_{33}}{\partial t} = - i V_2 (\tilde{\rho}_{31} - \tilde{\rho}_{13}) - \frac{\rho_{33} - \rho_{33}^{eq}}{T_1}, \tag{8.6c}$$

$$\frac{\partial \tilde{\rho}_{31}}{\partial t} = - (\frac{1}{T_2} + i \Delta_2) \tilde{\rho}_{31} - i V_1 \tilde{\rho}_{32} - i V_2 (\rho_{33} - \rho_{11}), \tag{8.6d}$$

$$\frac{\partial \tilde{\rho}_{32}}{\partial t} = - (\frac{1}{T_2} - i \Delta) \tilde{\rho}_{32} - i V_1 \tilde{\rho}_{31} + i V_2 \tilde{\rho}_{12}, \tag{8.6e}$$

$$\frac{\partial \tilde{\rho}_{21}}{\partial t} = - (\frac{1}{T_2} + i \Delta_1) \tilde{\rho}_{21} - i V_1 (\rho_{22} - \rho_{11}) - i V_2 \tilde{\rho}_{23}. \tag{8.6f}$$

where ρ_{ii}^{eq} is the population of level $|i\rangle$ in the absence of the external field and is assumed that $\rho_{11}^{eq} = 0.5$, $\rho_{22}^{eq} = 0.3$, $\rho_{33}^{eq} = 0.2$.

The three-level system is formed by the hyperfine levels of the nitrogen nuclear spin I=1 and the two fields drive the $\Delta I=\pm 1$ transitions. These two transitions are equivalent and will have, at least to first order, the same longitudinal and transverse relaxation times. The relaxation times have been measured for the $I_z=|0\rangle \Leftrightarrow |-1\rangle$ transition at 5.4 MHz. The values are T_1 = 1.2 ms and T_2 = 0.4 ms which are used in the theoretical calculation. The relaxation times associated with the $\Delta I=2$ magnetic dipole forbidden transition of $I_z=|1\rangle \Leftrightarrow |-1\rangle$ at 0.7 MHz may have different magnitude as those associated with the allowed $\Delta I=\pm 1$ transitions. However, our

calculation has shown that the moderate modifications of these values have negligible effect on the overall lineshape, and therefore, the same values are used in the calculations.

Under the steady state limit Eq.(8.6) can be solved analytically by setting the time derivatives equal to zero. With lengthy algebraic manipulation the solutions are found to be of the form

$$\rho_{22} = \rho_{22}^{eq} + 2\,T_1\,V_1\,\mathrm{Im}\,\tilde{\rho}_{21}\,, \tag{8.7a}$$

$$\rho_{33} = \rho_{33}^{eq} + 2\,T_1\,V_2\,\mathrm{Im}\,\tilde{\rho}_{31}\,, \tag{8.7b}$$

$$\tilde{\rho}_{31} = \mathrm{Re}\,\tilde{\rho}_{31} + i\,\mathrm{Im}\,\tilde{\rho}_{31}\,, \tag{8.7c}$$

$$\tilde{\rho}_{21} = \mathrm{Re}\,\tilde{\rho}_{21} + i\,\mathrm{Im}\,\tilde{\rho}_{21}\,, \tag{8.7d}$$

$$\tilde{\rho}_{32} = \mathrm{Re}\,\tilde{\rho}_{32} + i\,\mathrm{Im}\,\tilde{\rho}_{32}\,. \tag{8.7e}$$

and

$$\mathrm{Im}\,\tilde{\rho}_{31} = \frac{w_1\,V_2\,(\rho_{11}^{eq} - \rho_{33}^{eq}) - y_1\,V_1\,(\rho_{11}^{eq} - \rho_{22}^{eq})}{x_1\,w_1 - y_1\,z_1}\,, \tag{8.8a}$$

$$\mathrm{Im}\,\tilde{\rho}_{21} = \frac{x_1\,V_1\,(\rho_{11}^{eq} - \rho_{22}^{eq}) - z_1\,V_2\,(\rho_{11}^{eq} - \rho_{33}^{eq})}{x_1\,w_1 - y_1\,z_1}\,, \tag{8.8b}$$

$$\mathrm{Im}\,\tilde{\rho}_{32} = x\,\mathrm{Im}\,\tilde{\rho}_{21} + y\,\mathrm{Im}\,\tilde{\rho}_{31}\,, \tag{8.8c}$$

$$\mathrm{Re}\,\tilde{\rho}_{32} = z\,\mathrm{Im}\,\tilde{\rho}_{21} + w\,\mathrm{Im}\,\tilde{\rho}_{31}\,, \tag{8.8d}$$

$$\mathrm{Re}\,\tilde{\rho}_{31} = \Delta_2\,T_2\,\mathrm{Im}\,\tilde{\rho}_{31} + V_1\,T_2\,\mathrm{Im}\,\tilde{\rho}_{32}\,, \tag{8.8e}$$

$$\mathrm{Re}\,\tilde{\rho}_{21} = \Delta_1\,T_2\,\mathrm{Im}\,\tilde{\rho}_{21} - V_2\,T_2\,\mathrm{Im}\,\tilde{\rho}_{32}\,. \tag{8.8f}$$

where we have defined the following quantities,

$$x = (2\Delta_1 - \Delta_2) \frac{V_2}{D}, \tag{8.9a}$$

$$y = (\Delta_1 - 2\Delta_2) \frac{V_1}{D}, \tag{8.9b}$$

$$z = [1 + T_2^2 (V_1^2 + V_2^2 - \Delta\Delta_1)] \frac{V_2}{DT_2}, \tag{8.9c}$$

$$w = [1 + T_2^2 (V_1^2 + V_2^2 + \Delta\Delta_2)] \frac{V_1}{DT_2}, \tag{8.9d}$$

$$D = \frac{1}{T_2^2} + V_1^2 + V_2^2 + \Delta^2, \tag{8.9e}$$

$$x_1 = \frac{1}{T_2} + 4 V_2^2 T_1 + V_1 w + \Delta_2 T_2 (\Delta_2 + V_1 y), \tag{8.9f}$$

$$y_1 = V_1 (z + x T_2 \Delta_2 + 2 T_1 V_2), \tag{8.9g}$$

$$z_1 = V_2 (w - y T_2 \Delta_1 + 2 T_1 V_1), \tag{8.9h}$$

$$w_1 = \frac{1}{T_2} + 4 V_1^2 T_1 + V_2 z + \Delta_1 T_2 (\Delta_1 - V_2 x). \tag{8.9i}$$

The absorptive and dispersive responses of the fields ω_1 and ω_2 are proportional to the imaginary and real parts of the off-diagonal density matrix terms $\tilde{\rho}_{21}$ and $\tilde{\rho}_{31}$, respectively. Since the above solutions are correct to all orders of both fields, there is no difference between the pump and probe fields. In the experiment the frequency of field ω_1 is held fixed resonant with the 4.7 MHz transition while the frequency of field ω_2 is scanned through the 5.4 MHz transition. In such a situation the field ω_1 is called pump field and the field ω_2 probe field. The theoretical absorptive and dispersive probe profiles are obtained by plotting Im $\tilde{\rho}_{31}$ and Re $\tilde{\rho}_{31}$ as a function of the probe detuning Δ_2. The amplitude signal corresponds to the

magnitude of $|\tilde{\rho}_{31}|=[(Im\tilde{\rho}_{31})^2 + (Re\tilde{\rho}_{31})^2]^{1/2}$. The results of these calculations are given in Figs. 8-2, 8-4 and 8-5 for a specific pump field intensity and a range of probe field intensities matching experimental conditions. For these calculations the value of T_1=1.2 ms and T_2=0.4 ms determined experimentally were used. As also noted in the previous chapters the transitions exhibit only a small amount of inhomogeneous broadening while the Rabi frequency are larger than the inhomogeneous linewidth, therefore the inhomogeneous broadening effect is neglected.

8.3 Results and discussions

A series of experimental absorptive profiles of the 5.4 MHz I_z=|0>⇔|-1> transition with increasing probe field intensities are shown in Fig.8-2(a). The traces in dashed line are those in the absence of the pump field and represent the absorption profile of the transition probed by a single field. The traces in solid line give the equivalent responses when there is a pump field applied resonant with the 4.7 MHz I_z=|0>⇔|1> transition with a Rabi frequency of χ_1 = 32 kHz. The probe field intensities used were 0, 10, 20, 25, 30, and 35 dB, respectively. At the "weak probe" limit (0 dB) the absorption line has a linewidth of ~ 2.4 kHz and shows the well known symmetric Autler-Townes splitting under resonant pumping. As the probe field intensity increases, it interacts nonlinearly with the three-level system. Power broadening and saturation of the Autler-Townes doublet is observed, as shown in Fig.8-2(a).

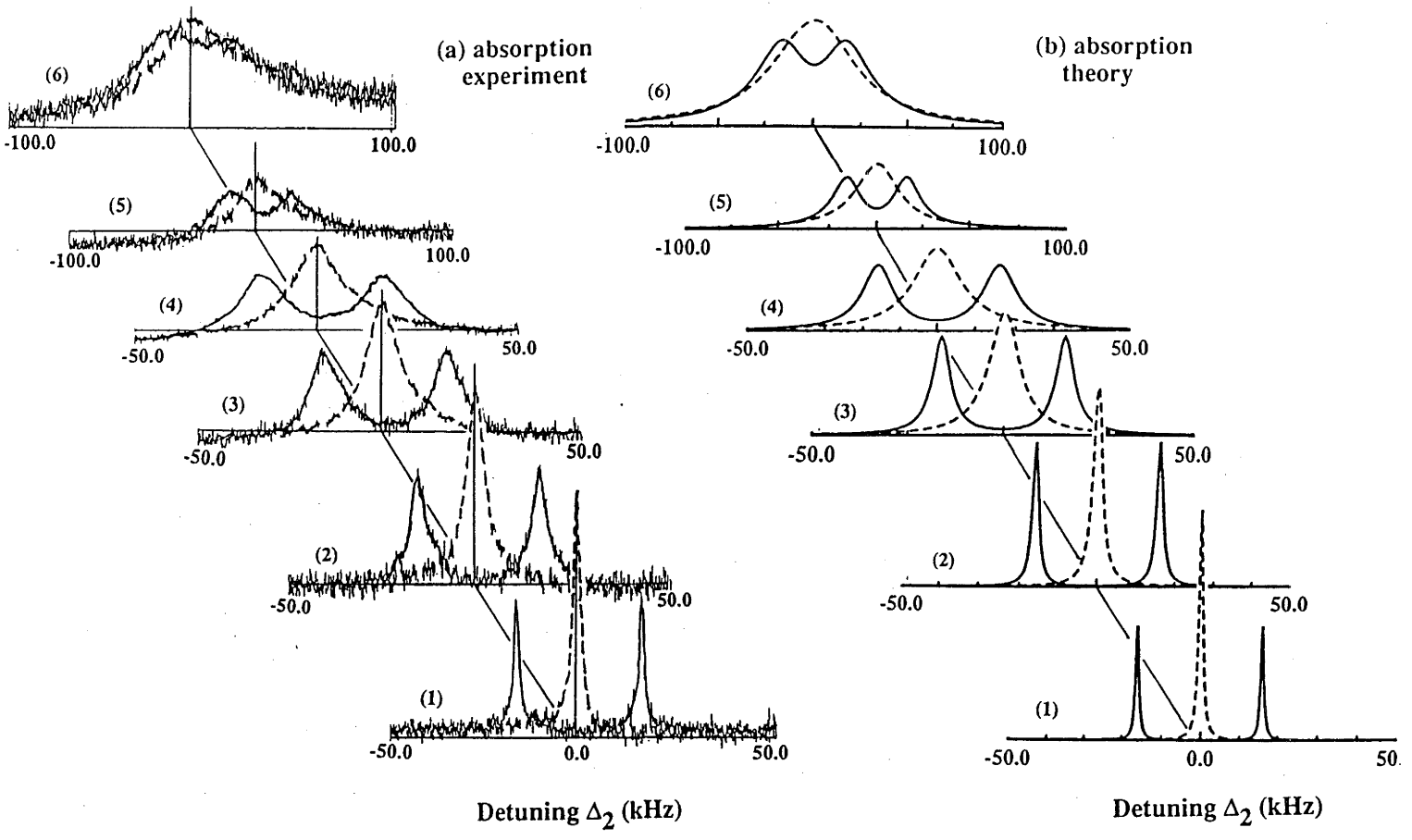

Figure 8-2. Measured (a) and calculated (b) absorption profiles. Solid line: resonant pumping, Rabi frequency 32 kHz. Dashed line: zero pumping. The experimental probe intensities are: (1) 0, (2) 10, (3) 20, (4) 25, (5) 30, and (6) 35 dB, respectively. The parameters used in the calculation are: pump Rabi intensity 32 kHz, probe Rabi intensities: (1) 0.26, (2) 0.82, (3) 2.6, (4) 4.62, (5) 8.22, and (6) 14.62 kHz.

The power broadening behaviour of the Autler-Townes doublet (in triangles) is shown in Fig.8-3. The power broadening behaviour of the 5.4 MHz transition itself (in circles) is also shown in Fig.8-3. It is seen that the power broadening behaviour of the Autler-Townes doublet is similar to that of the original transition. The interesting observation is that the power broadening for both cases in the high power limit is slower than that predicted by the Bloch equation consistent with observations in other system [22]. This aspect is out of scope of this thesis and will not be investigated further.

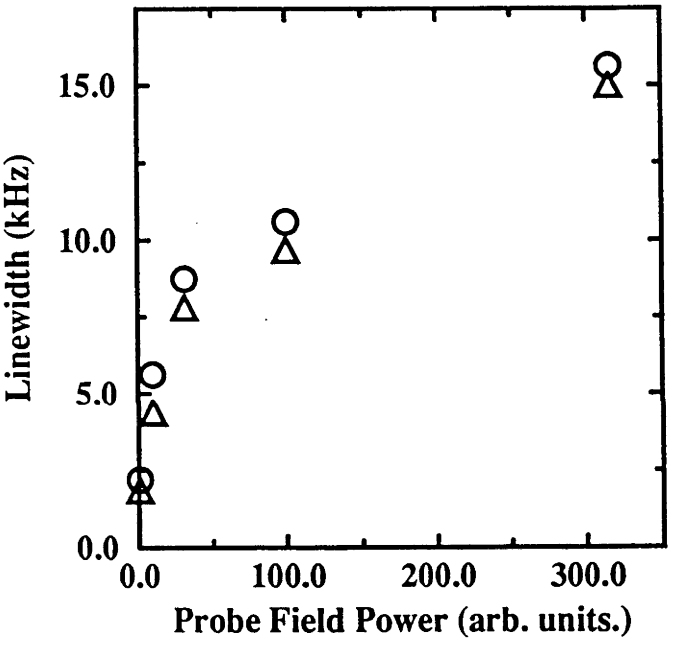

Figure 8-3. Linewidth of Autler-Townes doublet (△) and the 5.4 MHz transition (○) dependence on probe intensity.

The equivalent theoretical absorptive profiles for a pump Rabi frequency of 32 kHz calculated by plotting $\mathrm{Im}\tilde{\rho}_{31}$ as a function of detuning Δ_2 are shown in Fig.8-2(b). The pump field ω_1 is on-resonance with the $|1\rangle \Leftrightarrow |2\rangle$ transition ($\Delta_1 = 0$). The Rabi intensities of the probe power used in the calculation are χ_2 = 0.26, 0.82, 2.6, 4.62, 8.22 and 14.62 kHz corresponding to the probe powers 0, 10, 20, 25, 30 and 35 dB, respectively, in the experimental traces of Fig.8-2(a). In the experiments the

rf field intensity could be obtained by measuring the current in the rf coil. However, it is more appropriate to use the experimental itself as the pump Rabi frequency can be obtained from the Autler-Townes splitting of the 5.4 MHz transition. The probe Rabi intensity can be obtained from the splitting of 4.7 MHz transition or from the power broadening. Such a procedure is followed at one power level and the Rabi intensities at other power levels are obtained by scaling from the known relationship $\chi_2 \propto (\text{power})^{1/2}$. The theoretical calculation gives very good agreement with experiment.

Fig.8-4(a) shows the experimental dispersive profiles of the 5.4 MHz $I_z=|0\rangle\Leftrightarrow|-1\rangle$ transition of increasing probe field intensity without (dashed line) and with a driving field (solid line). The experimental parameters are the same as those for Fig.8-2, i.e., the pump field is resonant with the 4.7 MHz $I_z=|0\rangle\Leftrightarrow|1\rangle$ transition with a fixed Rabi frequency of χ_1= 32 kHz. Likewise the probe field intensities used were 0, 10, 20, 30, 35 and 40 dB. It can be seen that the inner parts of the two components of the dispersive doublet which are close to the resonance frequency have opposite phase, as the probe field intensity increases the doublet becomes power broadened and two components interfere destructively with each other. The dispersion profiles continue to grow in size for the probe power used in our experiments.

The theoretical dispersive profiles calculated from $\mathrm{Re}\tilde{\rho}_{31}$ as a function of probe detuning Δ_2 are shown in Fig.8-4(b). The parameters are the same as those used for absorptive profiles calculation shown in Fig.8-2(b). The theoretical calculations give very good agreement with experiment and confirm the various characteristic behaviours, such as power broadening and destructive interference.

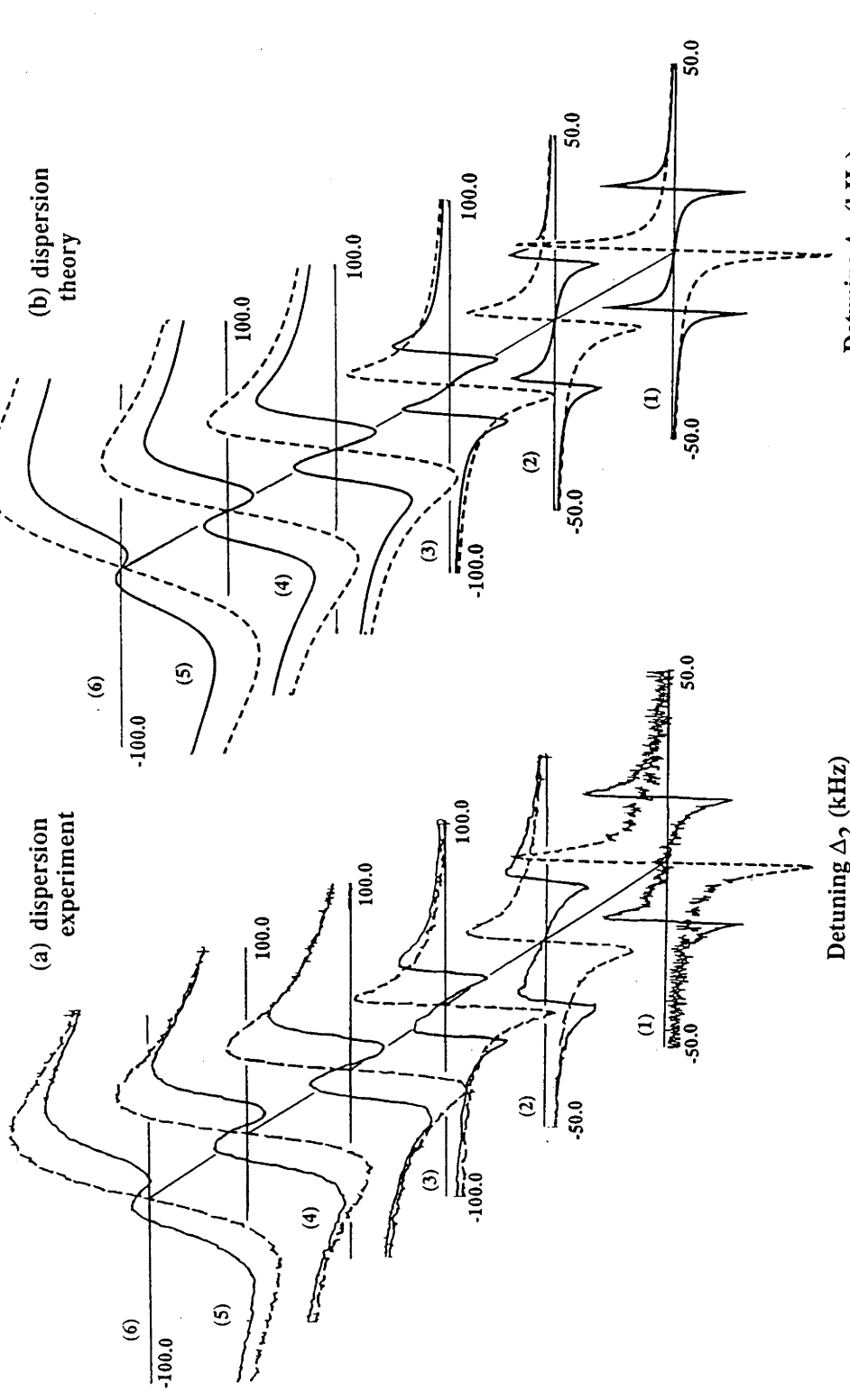

Figure 8-4. Measured (a) and calculated (b) dispersion profiles. The parameters are same as in Fig.8-2 for corresponding traces.

The profiles obtained using amplitude detection for increasing probe field intensity are shown in Fig.8-5. In this case a higher pump Rabi intensity of 60 kHz is used. The pump field is on-resonance with the 4.7 MHz I_z=|0>⇔|1> transition. As before the solid (dashed) lines are with (without) a pump field. The probe intensities used in experiments are 0, 10, 20, 30, and 40 dB. The probe Rabi frequencies used in theoretical calculation are χ_2 = 0.2, 0.632, 2, 6.32, and 20 kHz, respectively. It can be seen that the amplitude profile becomes power broadened and finally develops into an anomalous lineshape with a "hole" in the line centre of each component. There is a slightly asymmetry in the experimental traces due to a background from the power broadened EPR signal, but allowing for this, it can be seen that the calculated profiles are in good agreement with the experimental profiles.

The amplitude signal is the vector sum of absorptive and dispersive components. Since the absorptive response saturates much faster than the dispersive response, the power broadened dispersive response dominates the amplitude signal at higher probe power. This is illustrated more clearly in Fig.8-6 where the calculated absorptive, dispersive and amplitude response are superimposed (a) along with a measured amplitude profile for comparison (b). As phase information is lost in amplitude detection, the negative part of the dispersive response is folded up and results in a rather unusual lineshape with a "hole" in the line centre of each component.

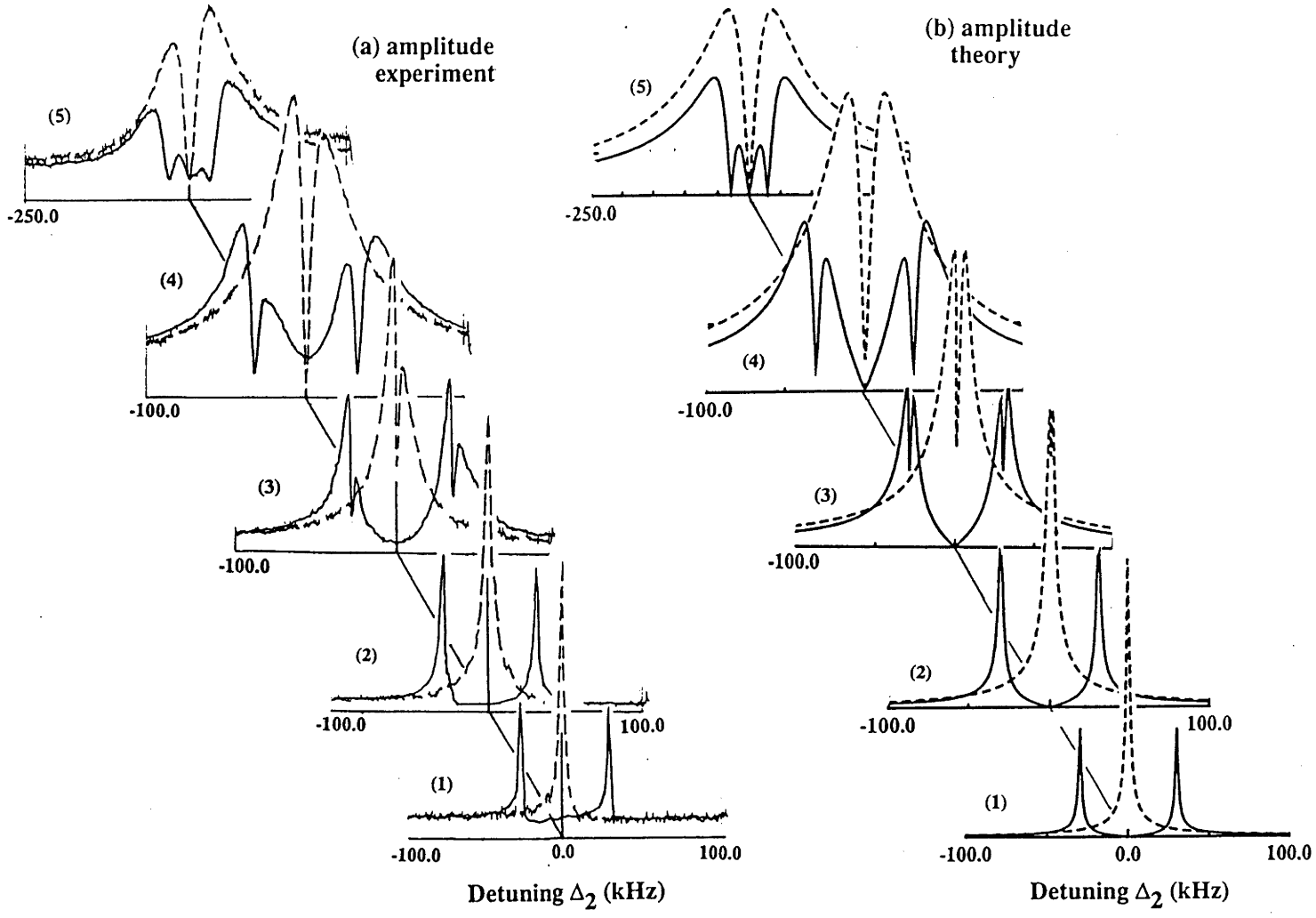

Figure 8-5. Measured (a) and calculated (b) amplitude profiles. Solid line: resonant pumping, Rabi frequency 60 kHz. Dashed line: zero pumping. The experimental probe intensities are: (1) 0, (2) 10, (3) 20, (4) 30, and (5) 40 dB, respectively. The parameters used in the calculation are: pump Rabi intensity 60 kHz, probe Rabi intensities: (1) 0.2, (2) 0.63, (3) 2.0, (4) 6.32, and (5) 20.0 kHz.

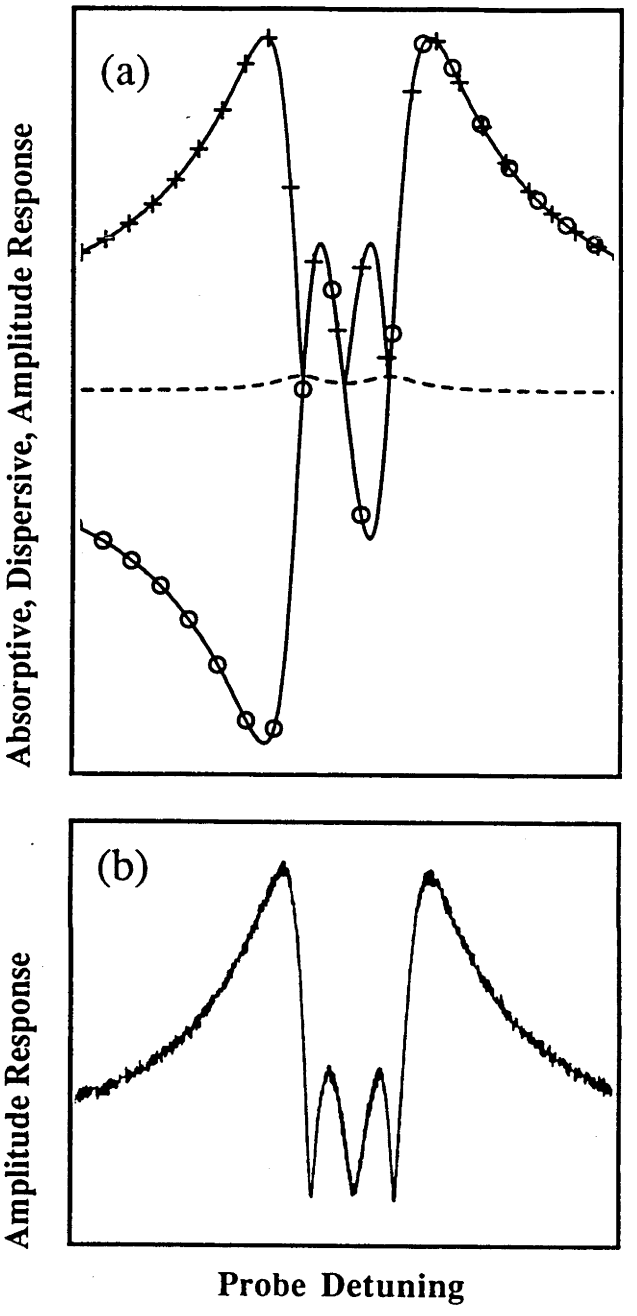

Figure 8-6. Schematic (a) showing absorptive (dashed line), dispersive (solid line with squares) and amplitude (solid line with pluses) profiles for high probe field intensity. The different nonlinear behaviour of the absorptive and dispersive responses leads to the anomalous amplitude profiles. The experimental amplitude profiles (b) is also shown for comparison

8.4 Conclusions

The power broadened Autler-Townes doublet profiles in a three-level system subjected to two near-resonant strong electromagnetic fields have been investigated both experimentally and theoretically. The main characteristic noted is that (i) in absorption response the features broadened and saturated but add constructively, (ii) in dispersion response the features broadened and add destructively and (iii) in amplitude response anomalous lineshape is observed due to the different saturation behaviour of the absorption and dispersion response in the high power limit. All features are satisfactorily accounted for by a density matrix treatment for a simple three-level system. The derivation of the density matrix equation of motion for the three-level system can be found in many text books [23] and the exact analytical solution for the Lamda-shaped three-level system has been derived by Brewer et al [14]. The exact analytical solution for a V-shape three-level system presented in this chapter is derived for the first time.

References

[1] X-F.He, P.T.H.Fisk, and N.B.Manson, J.Appl.Phys.71, 211, (1992)
" *Autler-Townes effect of the photoexcited diamond nitrogen-vacancy centre in its triplet ground state* "

[2] S. H. Autler and C. H. Townes, Phys. Rev., 100, 703, (1955)
" *Stark effect in rapidly varying fields* "

[3] A.Schabert, R.Keil, and P. E. Toschek, Opt. Commun. 13, 265 (1975)
" *Dependence on light amplitude of the dynamic Stark splitting of an optical line* "

[4] A. Schabert, R. Keil, and P. E. Toschek, Appl. Phys. 6, 181 (1975)

" *Dynamic Stark effect of an optical line observed by cross-saturated absorption* "

[5] C. Delsart and J. -C. Keller, J. Phys. B9, 2769 (1976)

" *Observation of the optical Autler-Townes splitting in neon gas with a cascade level scheme* "

[6] Ph. Cahuzac and R. Vetter, Phys. Rev. A14, 270 (1976)

" *Observation of the Autler-Townes effect on infrared laser transition of xenon* "

[7] J.L.Picque and J.Pinard, J.Phys. B9, L77 (1976)

" *Direct observation of the Autler-Townes effect in the optical range* "

[8] J. E. Bjorkholm and P. F. Liao, Opt. Commun. 21, 132 (1977)

" *AC Stark splitting of two-photon spectra* "

[9] H.R.Gray and C.R.Stroud, Jr. Opt. Commun., 25, 359 (1978)

" *Autler-Townes effect in double optical resonance* "

[10] C. Delsart and J -C. Keller, J. Phy. B13, 241, (1980)

" *Effect of Zeeman degeneracy on optical dynamic Stark splitting* "

[11] P.R.Hemmer, B.W.Peuse, F.Y.Wu, J.E.Thomas, and S.Ezekiel, Opt. Lett, 6, 531 (1981)

" *Precision atomic-beam studies of atom-field interactions* "

[12] P. T. H. Fisk, H. -A. Bachor and R. J. Sandeman, Phys. Rev., A33, 2418, (1986)

" *Investigation of the dynamic Stark effect in a J=0 -> 1 -> 0 three-level system. I. Experiment* "

[13] P. T. H. Fisk, H. -A. Bachor and R. J. Sandeman, Phys. Rev., A34, 4762, (1986)

" *Investigation of the dynamic Stark effect in a J=0 -> 1 -> 0 three-level system. III. The "strong-probe" case* "

[14] R. G. Brewer and E. L. Hahn, Phys. Rev. A11, 1641 (1975)

" *Coherent two-photon processes: transient and steady-state cases* "

[15] S. Feneuille and M. -G. Schweighofer, J. Physique, 36, 781, (1975)
" *Conditions for the observation of the Autler-Townes effect in a two step resonance experiment* "
[16] R.M.Whitley and C.R.Stroud, Jr. Phys. Rev. A14, 1498, (1976)
" *Double optical resonance* "
[17] W.A.McClean and S. Swain, J. Phys. B10, L143, (1977)
" *The theory of the optical Autler-Townes effect in sodium* "
[18] C. Cohen-Tannoudji and S. Reynaud, J. Phys. B10, 345, (1977)
" *Dressed-atom description of resonance fluorescence and absorption spectra of a multi-level atom in an intense laser beam* "
[19] C. Cohen-Tannoudji and S. Reynaud, J. Phys. B10, 2311, (1977)
"*Simultaneous saturation of two atomic transitions sharing a common level*"
[20] P. R. Berman and R. Salomaa, Phys. Rev. A25, 2667, (1982)
" *Comparison between dressed-atom and bare-atom pictures in laser spectroscopy* "
[21] P. T. H. Fisk, H. -A. Bachor and R. J. Sandeman, Phys. Rev., A33, 2424, (1986)
" *Investigation of the dynamic Stark effect in a J=0 -> 1 -> 0 three-level system. II. Theoretical description* "
[22] R.G.DeVoe and R.G.Brewer, Phys. Rev. Lett. 50, 1269 (1983)
" *Experimental test of the optical Bloch equations for solids* "
[23] for example, see,
M. Sargent III, M. O. Scully and W. E. Lamb, Jr.,
Laser Physics, (Addison-Wesley, London, 1974)
P. Meystre and M. Sargent III,
Elements of Quantum Optics, (Springer-Verlag, Berlin, 1991)

Chapter 9

Absorption and Dispersion profiles of a Transition Driven by Two Strong Fields: "Dressing" the Dressed States

9.1 Introduction

Our understanding of nature has continuously been deepened by the healthy loop: the more we study the more we know, and the more we know the more we study. The study of the interaction of a two-level system and electromagnetic fields is no exception. The simplest situation is when a two-level system is irradiated by a single monochromatic field. This is the topic presented in the chapters 4 and 5 where coherent transients are reported. The interaction of a two-level system and a single monochromatic field can be studied by a separate probe field. In this case, the simpler situation is to investigate this interaction by probing a separate transition from one of the driven two levels to a third level, in which the well-known Autler-Townes doublets profiles can be observed (Chapters 8). For such a situation it is possible to derive an exact analytical steady state solution even at the strong probe field limit (Chapter 8), as the pump and probe fields couple different transitions and hence there is no beating terms. In addition the signal is relatively large as the probed transition is not saturated by the strong pump field. The situation, where the probe field interacts with the same two-level system transition as the pump field, has also been studied for both weak (Chapter 6) and strong (Chapter 7) probe field cases. In this case, the investigations are more difficult because (i), theoretically, as the pump and probe fields drive the same transition, there will be many beating terms and hence there is no simple analytical solution to the problem, and (ii),

experimentally, the signal is much more weaker than the situation when a third level is involved due to saturation.

A question naturally arises of how the absorption and dispersion profiles of a two-level system are modified by the presence of two strong near-resonant monochromatic fields? As in the case of single pump field, it is expected that the situation will be simpler if the probe field couples a separate transition which has a common level with the driven transition and this is the situation studied in this chapter. There have only been a few theoretical considerations [1-3] whereas the only experimental observation is claimed by a Russian group [1] where the $6^3P_1 \Leftrightarrow 6^3D_1$ transition (553.587 nm) of the barium atom was strongly driven by two strong light fields and the $6^3P_1 \Leftrightarrow 6^3D_2$ transition (551.95 nm) was probed by a weak field. Their work indicated that the weak probe absorption profile consists of a multi-peak feature. But the spectrum was recorded using photographic plates, it was not practical to obtain the spectral profiles.

In this chapter we report the experimental results for a V-shaped three-level system as shown in Fig.9-1, where the $|1\rangle \Leftrightarrow |2\rangle$ transition is driven by two strong monochromatic fields and the absorption and dispersion profiles are measured with a weak field probing the adjacent $|1\rangle \Leftrightarrow |3\rangle$ transition. The results presented in this chapter is, I believe, the first experimental observation of this kind. The theoretical calculation using the continued fraction formalism accurate to the first order of weak probe field will be outlined. However, detailed numerical calculation will not be carried out due to the time limitation. Discussions in terms of the dressed state are also presented. It is shown that using the dressed state picture the resonance peak positions can be conveniently predicted for some special cases of the pump intensities and detunings.

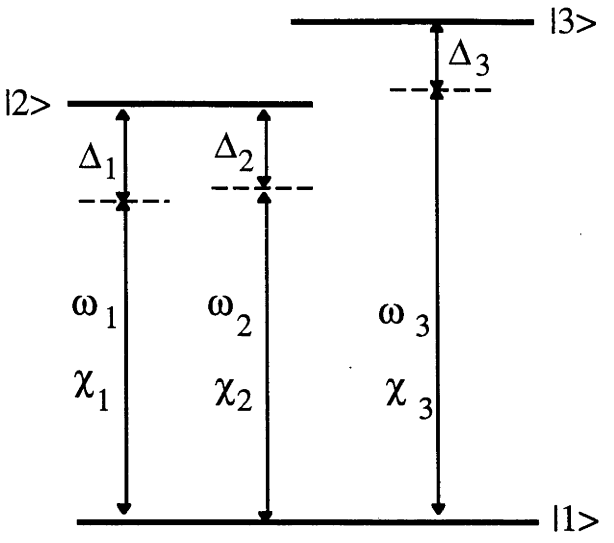

Figure 9-1. Three-level system interacting with two strong pump fields and a weak probe field. The $|1\rangle \Leftrightarrow |2\rangle$ transition is driven by two strong monochromatic fields at frequencies ω_1 and ω_2, with Rabi intensities of χ_1 and χ_2 and detuning Δ_1 and Δ_2, respectively. The $|1\rangle \Leftrightarrow |3\rangle$ transition is probed by a weak field at frequency ω_3 .

9.2 Outline of Theory

9.2.1 Density Matrix Equations of Motion Formalism

Consider a three-level system interacting with two strong pump fields and one weak probe field as shown in Fig.9-1. The three-level system has energy levels $E_1 < E_2 < E_3$ corresponding to the three states $|1\rangle$, $|2\rangle$, $|3\rangle$. The rf field has the form

$$\mathbf{B}_{rf}(t) = \mathbf{B}_1 \cos \omega_1 t + \mathbf{B}_2 \cos \omega_2 t + \mathbf{B}_3 \cos \omega_3 t \,. \qquad (9.1)$$

The Rabi frequencies χ_1, χ_2 and detunings Δ_1, Δ_2 of the two pump fields are defined by

$$\chi_1 = \frac{\mu_{12}\,\mathbf{B}_1}{\hbar}\ ,\ \chi_2 = \frac{\mu_{12}\,\mathbf{B}_2}{\hbar} \quad \text{and} \quad \Delta_1 = \omega_{21} - \omega_1\ ,\ \ \Delta_2 = \omega_{21} - \omega_2\ . \tag{9.2}$$

Similarly the Rabi frequency χ_3 and detuning Δ_3 of the probe field are defined by

$$\chi_3 = \frac{\mu_{31}\,\mathbf{B}_3}{\hbar} \quad \text{and} \quad \Delta_3 = \omega_{31} - \omega_3\ . \tag{9.3}$$

The density matrix equation of motion can be written as (Chapter 8)

$$\dot{\rho}_{11} = -\frac{i}{\hbar}\left(V_{12}\rho_{21} - V_{21}\rho_{12} + V_{13}\rho_{31} - V_{31}\rho_{13}\right) - \frac{\rho_{11} - \rho_{11}^{eq}}{T_1}\ , \tag{9.4a}$$

$$\dot{\rho}_{22} = \frac{i}{\hbar}\left(V_{12}\rho_{21} - V_{21}\rho_{12}\right) - \frac{\rho_{22} - \rho_{22}^{eq}}{T_1}\ , \tag{9.4b}$$

$$\dot{\rho}_{33} = \frac{i}{\hbar}\left(V_{13}\rho_{31} - V_{31}\rho_{13}\right) - \frac{\rho_{33} - \rho_{33}^{eq}}{T_1}\ , \tag{9.4c}$$

$$\dot{\rho}_{31} = -i\,\omega_{31}\rho_{31} + \frac{i}{\hbar}V_{31}\left(\rho_{33} - \rho_{11}\right) + \frac{i}{\hbar}V_{21}\rho_{32} - \frac{\rho_{31}}{T_2}\ , \tag{9.4d}$$

$$\dot{\rho}_{21} = -i\,\omega_{21}\rho_{21} + \frac{i}{\hbar}V_{21}\left(\rho_{22} - \rho_{11}\right) + \frac{i}{\hbar}V_{31}\rho_{23} - \frac{\rho_{21}}{T_2}\ , \tag{9.4e}$$

$$\dot{\rho}_{32} = -i\,\omega_{32}\rho_{32} - \frac{i}{\hbar}V_{31}\rho_{12} + \frac{i}{\hbar}V_{12}\rho_{31} - \frac{\rho_{32}}{T_{21}}\ . \tag{9.4f}$$

With the rotating-wave-approximation the interaction terms can be written as

$$V_{21} = V_{12}^{*} = -\frac{\hbar\chi_1}{2}\,e^{-i\omega_1 t} - \frac{\hbar\chi_2}{2}\,e^{-i\omega_2 t}\ , \tag{9.5a}$$

$$V_{31} = V_{13}^{*} = -\frac{\hbar\chi_3}{2}\,e^{-i\omega_3 t}\ . \tag{9.5b}$$

In order to calculate the absorption and dispersion responses of the $|1\rangle \Leftrightarrow |3\rangle$ transition probed by a weak field, it is necessary to solve the above density matrix equations of motion, Eqs.(9.4), in the steady state limit.

The absorption and dispersion responses associated with the $|1\rangle \Leftrightarrow |3\rangle$ transition are given by the imaginary and real part of the off-diagonal matrix element, $\rho_{31}(\omega_3)$, respectively. In the weak probe field limit: $\chi_3 \ll \chi_1, \chi_2$, Eqs.(9.4) can be solved in two steps: (1) solving the equations in the zeroth order of the weak probe field at $\chi_3 = 0$, the reduced equations describing the two-level system interacting with two strong driving fields can be solved using the continued fraction formalism (Chapter 7), (2) calculating the off-diagonal density matrix element ρ_{31} to first order of χ_3 by using the previously obtained zeroth order solutions. The solutions of these equations using this procedure is suggested for future work. In what follows the dressed state description is presented with which, for some particular cases, the multipeak positions can be conveniently predicted.

9.2.2 Dressed States Formalism

9.2.2.1 Equal Pump Rabi Frequencies $\chi_1 = \chi_2$ case

As discussed in Chapter 1, although the dressed states model does not provide mathematical simplification for calculating the spectral profiles, it does give a clear and simple physical picture in which the spectral components can be viewed as arising from the transitions between the dressed states. In the experimental configuration discussed in this chapter, the $|1\rangle \Leftrightarrow |2\rangle$ transition is driven by two strong monochromatic fields and the $|1\rangle \Leftrightarrow |3\rangle$ transition is probed by a weak field. The two strong fields can be treated as dressing fields and the dressed states can be derived by solving the total Hamiltonian of the

two-level system + two dressing fields. Various components in the weak probe responses can be viewed as arising from the transitions between the dressed states.

The total Hamiltonian for the two-level system: $|1\rangle$ and $|2\rangle$, interacting with two strong monochromatic fields: ω_1 and ω_1, is given by

$$H = H_0 + H_{AF} = H_A + H_F + H_{AF}, \tag{9.6}$$

where H_0 is the non-interacting atom + field Hamiltonian and consists of the Hamiltonian for the two-level system, H_A, and Hamiltonian for the fields, H_F, which are given by

$$H_A = \hbar\omega_{21} |2\rangle\langle 2|, \tag{9.7a}$$

$$H_F = \hbar\, \omega_1\, a_1^+ a_1 + \hbar\, \omega_2\, a_2^+ a_2 . \tag{9.7b}$$

The atom-field interaction Hamiltonian, H_{AF}, is given by (in the rotating-wave-approximation)

$$H_{AF} = \hbar \sum_{i=1}^{2} \frac{\chi_i}{2} (a_i^+ |1\rangle\langle 2| + a_i |2\rangle\langle 1|). \tag{9.8}$$

The undressed states of the non-interacting atom + field Hamiltonian $H_0 = H_A + H_F$ are just direct products of atomic states: $|1\rangle$ and $|2\rangle$, with photon number states: $|n_1\rangle$ and $|n_2\rangle$, where n_1 and n_2 represent the photon occupation numbers of the field modes at the two frequencies, ω_1 and ω_2, respectively. They can be written as $|1, n_1, n_2\rangle$ or $|2, n_1, n_2\rangle$. These product states group into manifolds, each corresponding to a particular value of $n_1 + n_2 \equiv N$. Using the products states $|1, n_1, n_2\rangle$ or $|2, n_1, n_2\rangle$ as basis states and setting the zero of energy at that of $|1, n_1, n_2\rangle$, $\hbar(n_1\, \omega_1 + n_2\, \omega_2)$ and adopting the notions of Ficek et al [4]

$$\delta_1 = \Delta_1 = \omega_{21} - \omega_1,\ \delta_2 = -\Delta_2 = \omega_2 - \omega_{21}\,, \tag{9.9a}$$

$$2\,\delta = \delta_1 + \delta_2,\ \omega_s = (\,\omega_1 + \omega_2\,)/2,\ \Delta = \omega_{21} - \omega_s. \tag{9.9b}$$

The matrix which represents the Hamiltonian given by Eq. (9.6) in the manifold N+1 is an infinite tri-diagonal matrix and given by [4]

$$H = \hbar \begin{bmatrix} \cdot & & & & & & \\ & \cdot & & & & & \\ \frac{\chi_1}{2} & (2\delta+\Delta) & \frac{\chi_2}{2} & & & & \\ & \frac{\chi_2}{2} & \delta & \frac{\chi_1}{2} & & & \\ & & \frac{\chi_1}{2} & \Delta & \frac{\chi_2}{2} & & \\ & & & \frac{\chi_2}{2} & -\delta & \frac{\chi_1}{2} & \\ & & & & \frac{\chi_1}{2} & -(2\delta-\Delta) & \frac{\chi_2}{2} \\ & & & & & \cdot & \\ & & & & & & \cdot \end{bmatrix} \tag{9.10}$$

For the general situation the above matrix has no simple solutions [4]. However, if the two pump fields have equal Rabi intensities, $\chi_1 = \chi_2 = \chi$, and are symmetrically detuned, $\Delta = 0$, i.e., $\delta_1 = \delta_2 = \delta$, (or in our notation $\Delta_1 = -\Delta_2$), the above matrix can be solved exactly and has the following eigenvalues or dressed states energies [5]

$$\lambda = m\,\delta \qquad m = 0, \pm 1, \pm 2, \ldots\,. \tag{9.11}$$

Using above solution as the zero order solution, a perturbative solution with a first order correction to the eigenvalue $\lambda = m\,\delta$ have been derived for two special cases [4]. These two special cases are (i) the two pump fields are of equal Rabi intensity $\chi_1 = \chi_2 = \chi$, but can have arbitrary detunings, (ii) the two pump fields are symmetrically placed about ω_{21} so that $\Delta = 0$, or $\Delta_1 = -\Delta_2$, but can have unequal Rabi frequencies. In this chapter, only the first situation is

discussed. When two pump fields have equal Rabi intensity, the dressed state energies with a first order correction are given by [4]

$$\lambda = m\,\delta + \frac{\Delta}{2} - (-1)^m \frac{\Delta}{2} J_o\left(\frac{-2\chi}{\delta}\right) \qquad (9.12)$$

where $J_0(x)$ is the Bessel function of zero order. These values will be compared with experiments.

9.2.2.2 Special Detuning Case: $\Delta_1 = 0$, $\Delta_2 = \pm\chi_1$ and $\chi_2 < \chi_1$

The dressed state formalism discussed in the previous section treats the two dressing fields equivalently and the Hamiltonian of the two-level atom + two dressing fields can be written in the form of an infinite tri-diagonal matrix. In what follows a different approach is introduced, which sometimes provides a simpler answer to the problem. It is applicable for the case where (1), two pump fields have unequal Rabi intensities and (2), their detunings satisfy some special conditions. In this approach we first construct the dressed state by considering the stronger driving field only, and then the resulting dressed state is dressed again by the weaker driving field. The weaker driving field is treated as a "weak perturbation" to the dressed state by neglecting the non-resonant interaction.

Consider the situation shown in Fig.9-2, where the stronger pump field, ω_1, is resonant with the two-level system: $\Delta_1 = 0$, and has a Rabi frequency χ_1, the weaker pump field, ω_2, has a Rabi frequency $\chi_2 < \chi_1$, and the detuning: $\Delta_2 = \pm\chi_1$. The dressed states incorporating the two-level system and the resonant pump field, ω_1, can be written as (Chapter 1)

$$|A, n_1\rangle = \frac{1}{\sqrt{2}}(|2, n_1\rangle + |1, n_1 + 1\rangle), \tag{9.13a}$$

$$|B, n_1\rangle = \frac{1}{\sqrt{2}}(-|2, n_1\rangle + |1, n_1 + 1\rangle). \tag{9.13b}$$

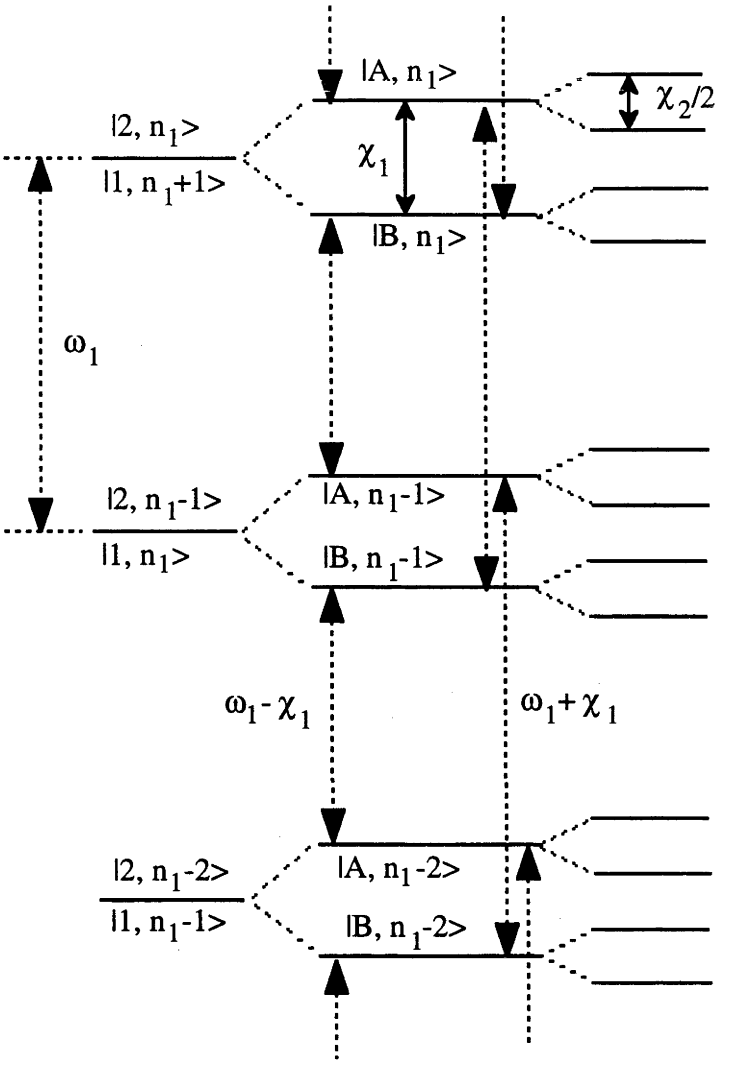

Figure. 9-2. " Dressing " the dressed states.

The splitting between the dressed state doublet $|A, n_1\rangle$ and $|B, n_1\rangle$ is given by the Rabi frequency χ_1. The dipole transition matrix elements between the dressed states are given by

$$\mu_{BA} = \langle B, n_1 - 1|\mu|A, n_1\rangle = \frac{1}{2}\langle 1, n_1|\mu|2, n_1\rangle = \frac{1}{2}\mu_{12}, \tag{9.14a}$$

$$\mu_{AB} = \langle A, n_1 - 1|\mu|B, n_1\rangle = -\frac{1}{2}\langle 1, n_1|\mu|2, n_1\rangle = -\frac{1}{2}\mu_{12}. \tag{9.14b}$$

If a weaker pump field has a frequency of $\omega_2 = \omega_1+\chi_1$, in the dressed state picture it is resonant with the $|B, n_1-1\rangle \Leftrightarrow |A, n_1\rangle$ transition. As a consequence of the periodic property of the dressed states this weaker pump field is also resonant with $|B, n_1-1-m\rangle \Leftrightarrow |A, n_1-m\rangle$ (m: integer) transitions. If the weaker pump field is sufficiently weak, the off-resonant interaction between other dressed state transitions, such as $|A,n_1-1\rangle \Leftrightarrow A,n_1\rangle$ or $|B,n_1-1\rangle \Leftrightarrow |B,n_1\rangle$ transitions, is then negligible and the only interaction needed to be considered is the resonant interaction between the $|B,n_1-1\rangle \Leftrightarrow |A,n_1\rangle$ transition. Introducing the following notations

$|A, n_1\rangle \, | \, n_2\rangle = |A, n_1, n_2\rangle$, and $|B, n_1-1\rangle \, | \, n_2+1\rangle = |B, n_1-1, n_2+1\rangle$,

It is obvious that they form a degenerate doublet. By taking the interaction of the dressed states and weaker pump field into account, the degenerate doublet splits and the final dressed states $|a, n_1, n_2\rangle$ and $|b, n_1, n_2\rangle$ can be written as

$$| a, n_1, n_2 \rangle = \frac{1}{\sqrt{2}} (|A, n_1, n_2 \rangle + |B, n_1 - 1, n_2 + 1 \rangle) , \tag{9.15a}$$

$$| b, n_1, n_2 \rangle = \frac{1}{\sqrt{2}} (- |A, n_1, n_2 \rangle + |B, n_1 - 1, n_2 + 1 \rangle) . \tag{9.15b}$$

The adjacent dressed states $|a, n_1, n_2\rangle$ and $|b, n_1, n_2\rangle$ are separated by the dressed state Rabi frequency χ_{BA} which is given by

$$\chi_{BA} = \frac{\mu_{BA} \mathbf{B}_2}{\hbar} = \frac{1}{2} \frac{\mu_{12} \mathbf{B}_2}{\hbar} = \frac{1}{2} \chi_2 \tag{9.16}$$

where χ_2 is the weaker pump field Rabi frequency as defined in Eq. (9.2) and $\mu_{BA} = \mu_{12} / 2$ [see, Eq. (9.14)] has been used.

When a weaker pump field has a frequency of $\omega_2=\omega_1-\chi_1$, in the dressed state picture it is resonant with the $|B,n_1-m\rangle \Leftrightarrow |A,n_1-1-m\rangle$ (m: integer) transitions. Similar results can therefore be derived as for the $\omega_2=\omega_1+\chi_1$ case. The dressed state Rabi frequency χ_{AB} is given by

$$\chi_{AB} = \frac{\mu_{AB}\mathbf{B}_2}{\hbar} = \frac{1}{2}\frac{\mu_{12}\mathbf{B}_2}{\hbar} = \frac{1}{2}\chi_2 \quad . \tag{9.17}$$

From the above discussions the following conclusions can be drawn, (i) the spectral profile is characterized by a four peak structure when probed through a third level as shown in Fig.9-2, and (ii) the dressed state Rabi frequencies χ_{AB}, χ_{BA} are half of the bare state Rabi frequency χ_2 and hence the splitting of the dressed state by the weaker pump field is half of the splitting of the bare state. These will be examined by experiments.

9.3 Experimental Results and Discussions

In this section the experimental results are presented. In the measurements, the two pump fields are applied on the I_z=|0>⇔|1> 4.7 MHz transition and their Rabi intensities are determined by measuring the Autler-Townes splitting of the I_z=|0>⇔|-1> 5.4 MHz transition. The probe field scans through the I_z=|0>⇔|-1> 5.4 MHz transition and its intensity is kept sufficient low to avoid causing power broadening (Chapter 8).

9.3.1 Special Detuning Case: $\Delta_1 = 0$, $\Delta_2 = \pm \chi_1$ and $\chi_2 < \chi_1$

The measured absorptive profile of the normal Autler-Townes doublet with only a single pump field is shown in Fig.9-3. Trace (a) is the absorption profile of 5.4 MHz transition in the absence of a pump field. Trace (b) is obtained when only the stronger pump field, ω_1, is applied with a Rabi intensity χ_1 = 120 kHz. Trace (c) is obtained when only the weaker pump field, ω_2, is applied with a Rabi intensity χ_2 = 40 kHz. The corresponding measured dispersive profiles are shown in Fig.9-4. It can be seen that the profiles are those of the well-known Autler-Townes doublets whose characteristic is, for

resonant pumping, two peaks symmetrically located about the two-level system transition frequency and separated by the pump field Rabi frequency (Chapter 8).

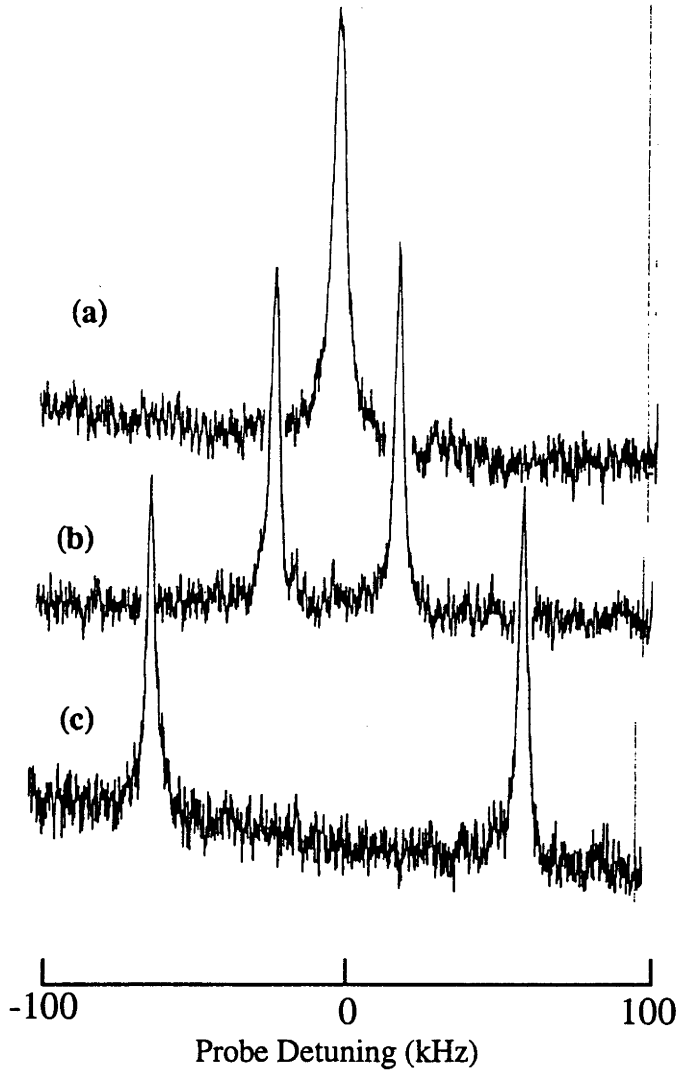

Figure 9-3. Measured absorptive Autler-Townes profiles of the 5.4 MHz transition. The pump field is on-resonance with the 4.7 MHz transition and has a Rabi frequency of (a) zero, (b) 40 and (c) 120 kHz.

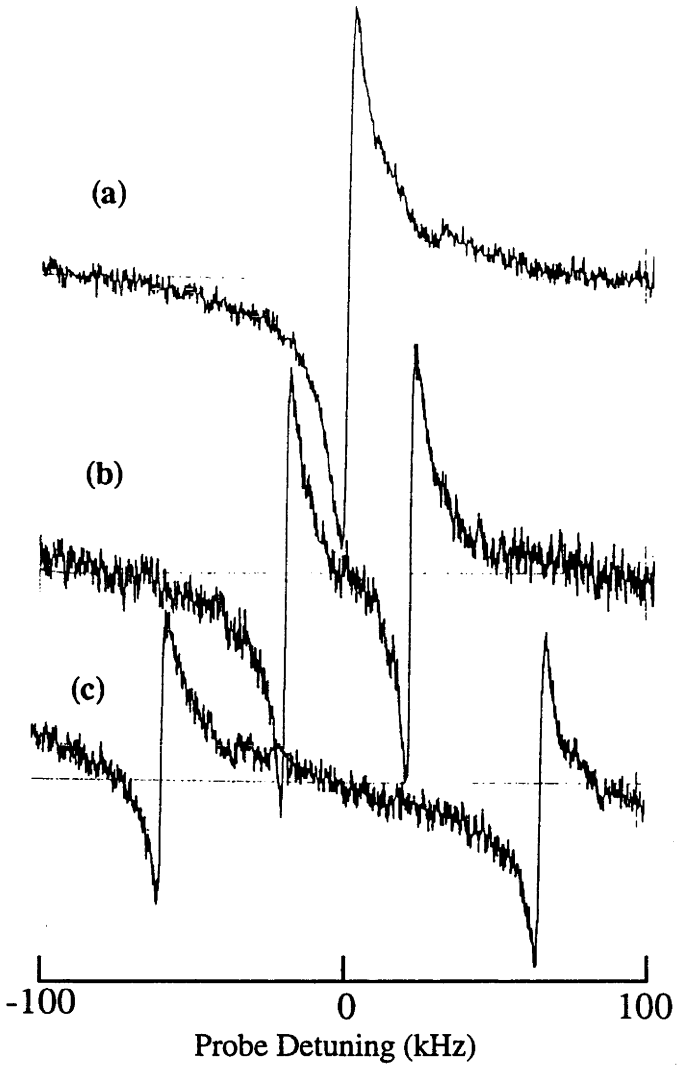

Figure 9-4. Measured dispersive Autler-Townes profiles of the 5.4 MHz transition. The pump field is on-resonance with the 4.7 MHz transition and has a Rabi frequency of (a) zero, (b) 40 and (c) 120 kHz.

When the two pump fields are applied simultaneously, the resulting absorption (a) and dispersion (b) profiles are shown in Fig.9-5 for the situation where the stronger pump field detuning $\Delta_1 = 0$ and the weaker pump field is detuned by $\Delta_2 = \chi_1$. For the situation where the stronger pump field detuning $\Delta_1 = 0$ and the weaker pump field is detuned by $\Delta_2 = -\chi_1$, the corresponding absorption (a) and dispersion (b) profiles are shown in Fig.9-6. It is seen that both of the absorption and dispersion profiles indeed show a four peak structure

as predicted by the theory given in section 9.2.2.2. The observed profiles consist of two doublets symmetrically located about the 5.4 MHz transition and separated by ~ 120 kHz which corresponds to the stronger pump field Rabi frequency χ_1. The splitting of the neighbouring peaks within each doublet is ~ 20 kHz which is half of the weaker pump field Rabi frequency χ_2 = 40 kHz. The four peak structure can be viewed as arising from the fact that the weaker pump field further splits each of the Autler-Townes components related to the stronger pump field.

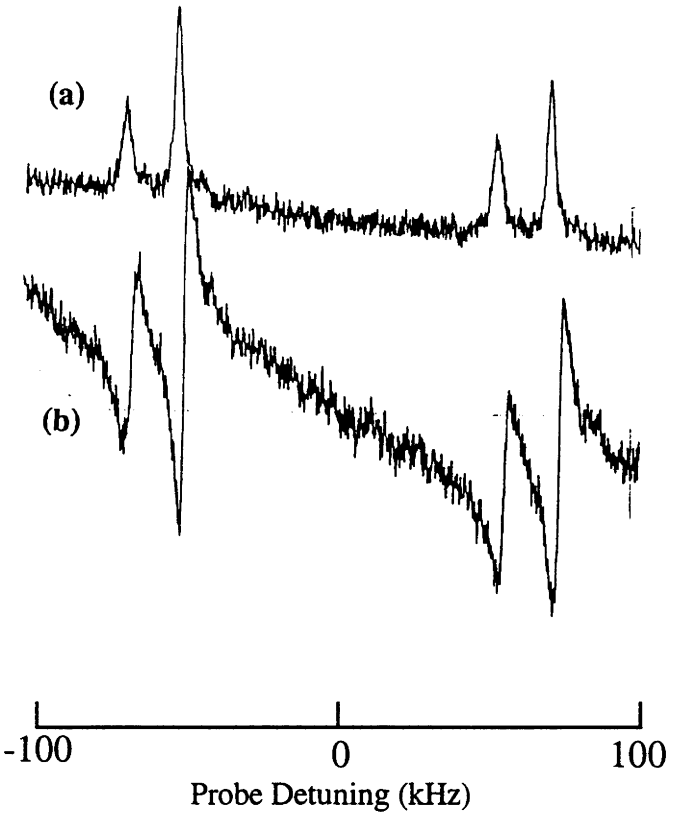

Figure 9-5. Measured absorptive (a) and dispersive (b) Autler-Townes profiles of the 5.4 MHz transition. The stronger pump field is resonant with the 4.7 MHz transition. The weaker pump field is positively detuned by an amount equal to the Rabi frequency of the stronger pump field.

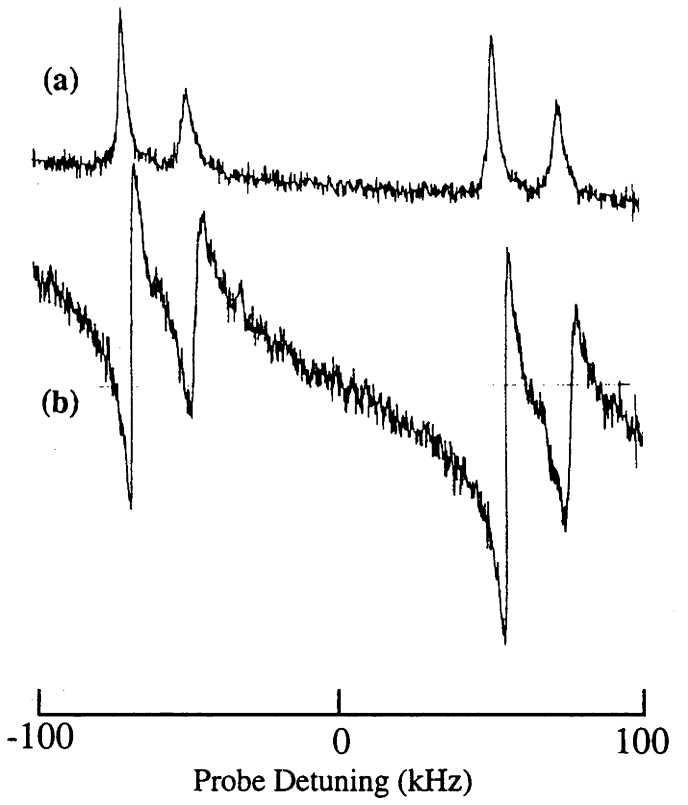

Figure 9-6. Measured absorptive (a) and dispersive (b) Autler-Townes profiles of the 5.4 MHz transition. The stronger pump field is resonant with the 4.7 MHz transition. The weaker pump field is negatively detuned by an amount equal to the Rabi frequency of the stronger pump field.

Keeping the stronger pump field Rabi intensity χ_1 and detuning $\Delta_1 = 0$ fixed, the ratios χ_{AB} / χ_2 , χ_{BA} / χ_2, where χ_2 is the weaker pump field Rabi frequency as defined before and χ_{AB}, χ_{AB} are the dressed state Rabi frequencies, are investigated as a function of the weaker pump field intensity and shown in Fig.9-7. The measured ratios can be seen to be close to 1/2 which is in good agreement with theory. In this measurement, the weaker field intensity is always smaller than the stronger field intensity.

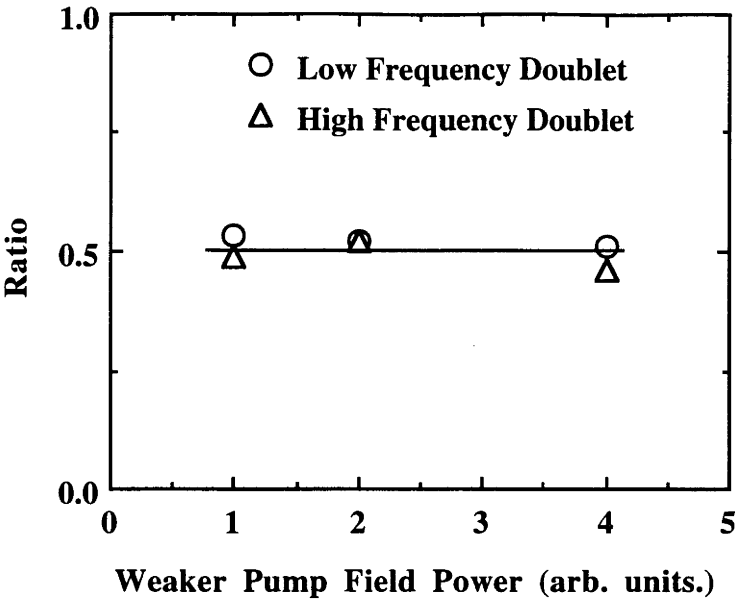

Figure 9-7. The Ratios of dressed state Rabi frequency and the bare state Rabi frequency as a function of weaker pump field power. The solid line is the value of 1/2 predicted by the theory.

It is found that the above mentioned appearance of the simple four peak structure and the ratio = 1/2 is only applicable to the situation that (i) the weaker pump field is indeed weaker than the stronger pump field: $\chi_2 < \chi_1$, and (ii) the weaker pump field is detuned to $\Delta_2 = \pm \chi_1$.

For example, Fig.9-8 shows the measured absorptive (a) and dispersive (b) profiles when both of the stronger and weaker pump fields are resonant with the 4.7 MHz transition, i.e. $\Delta_1 = \Delta_2 = 0$, which does not satisfy the condition $\Delta_2 = \pm\chi_1$. It is seen that the spectrum has a complicated multipeak structure. There are two broad bands of ~ 37 kHz width which is close to the weaker field Rabi intensity χ_2 = 40 kHz and each band is a multi-peak feature. The separation between the centres of two multi-peak bands is about 120 kHz which is equal to the stronger field Rabi intensity χ_1 = 120 kHz.

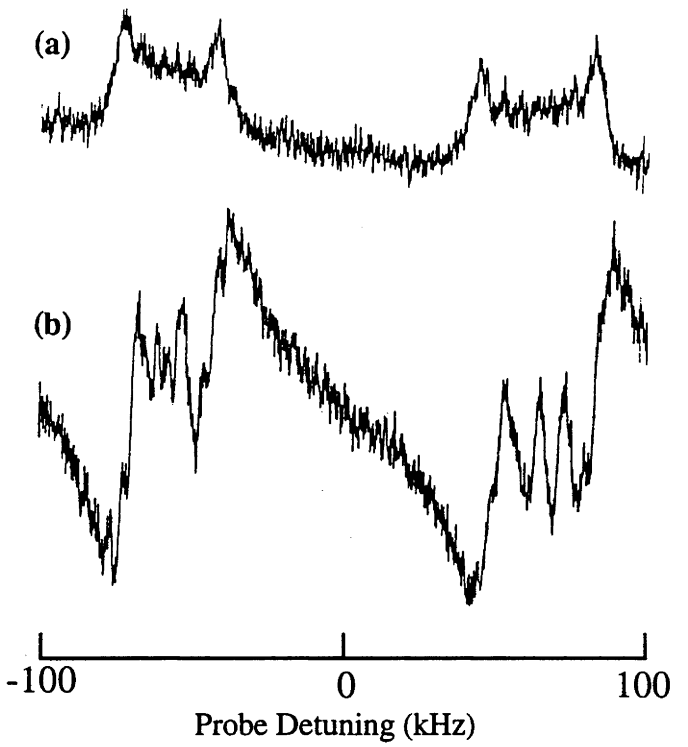

Figure 9-8. Measured absorptive (a) and dispersive (b) Autler-Townes profiles of the 5.4 MHz transition. Both of the two pump fields are resonant with the 4.7 MHz transition and have a Rabi frequencies of 120 and 40 kHz, respectively.

When the two pump fields have the same intensity $\chi_2 = \chi_1$, which does not satisfy the condition $\chi_2 < \chi_1$, the observed profiles have also a different characteristic. However, in this case the dressed state formalism developed by Ficek *et al.* [4] becomes applicable and this is discussed in next section.

9.3.2 Equal Pump Rabi Frequencies $\chi_1 = \chi_2$ case

Fig.9-9 shows the absorption profiles obtained for the situation when the two pump fields have the same Rabi frequency $\chi=\chi_1=\chi_2=60$ kHz and one is resonant with the 4.7 MHz transition, $\Delta_1=0$, while the other is detuned by (a) $\Delta_2=\chi=60$ kHz and (b) $\Delta_2=-\chi=-60$ kHz. It is seen that the predominant feature is

a three peaks structure with an additional weak feature indicated by the arrow. Fig.9-10 shows the dispersion profile for the situation where $\chi=\chi_1=\chi_2=60$ kHz, $\Delta_1=0$ and $\Delta_2=\chi=60$ kHz. Similarly three strong dispersive peaks are the main feature but again a fourth weak feature is present. When the probe field intensity is increased, the signal to noise ratio is improved and more peaks are observed as shown in Fig.9-11(a).

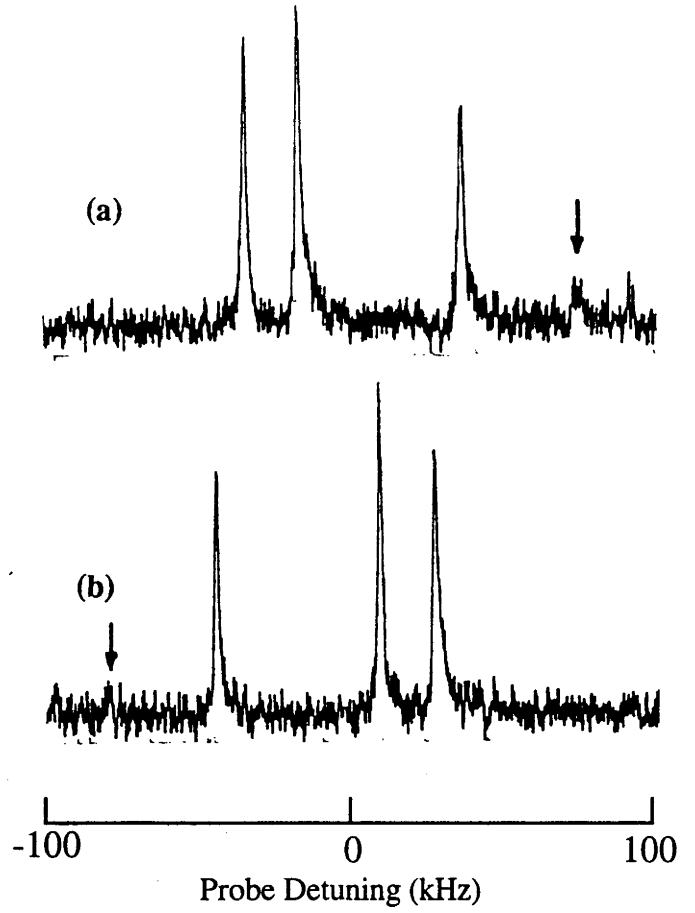

Figure 9-9. Measured absorptive Autler-Townes profiles of the 5.4 MHz transition for $\chi = \chi_1 = \chi_2 = 60$ kHz, $\Delta_1 = 0$, and (a) $\Delta_2 = \chi = 60$ kHz, (b) $\Delta_2 = -\chi = -60$ kHz, respectively.

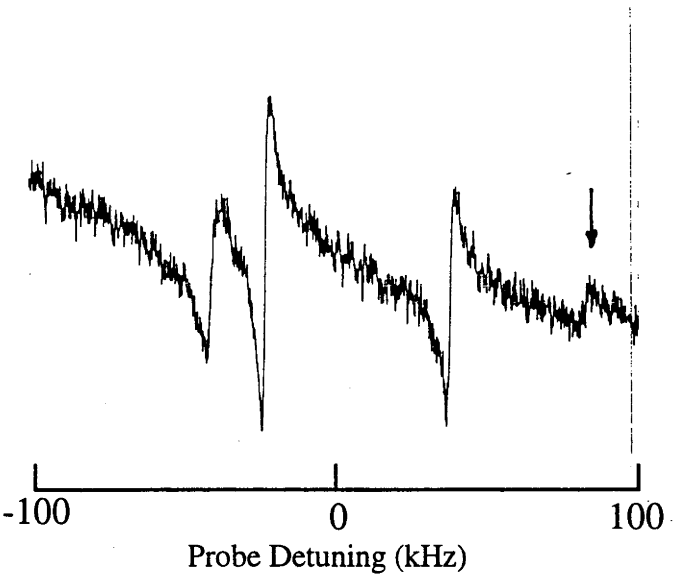

Figure 9-10. Measured disperstive Autler-Townes profiles of the 5.4 MHz transition for $\chi = \chi_1 = \chi_2 = 60$ kHz, $\Delta_1 = 0$, and $\Delta_2 = \chi = 60$ kHz.

In the situations discussed here, the second pump field (the detuned one) is of the same intensity as the first pump field (the resonant one), the non-resonant interaction becomes significant, therefore, the simple approach used in the section 9.2.2.2 is not applicable. However, for this particular situation $\chi_1=\chi_2$ the positions of the multipeaks can be calculated using the theory developed by Ficke *et al.* [4] which is outlined in the section 9.2.2.1. Substituting the above experimental parameters: $\chi_1 = \chi_2 = 60$ kHz, $\Delta_1 = 0$, and $\Delta_2 = \pm 60$ kHz, into Eq. (9.11), the eigenvalues are found to be

$$\lambda_0 = \pm 21, \lambda_1 = \mp 21, \lambda_{-1} = \pm 39, \lambda_2 = \mp 39, \lambda_{-2} = \pm 81,$$
$$\lambda_3 = \mp 81, \lambda_{-3} = \pm 99, \lambda_4 = \mp 99 \text{ kHz}, \quad \text{for } \Delta_2 = \pm\chi = \pm 60 \text{ kHz}. \tag{9.18}$$

The positions of the spectral components calculated by Eq.(9.18) is shown in Fig.9-11(b), it is seen that the theory is in good agreement with the experiment.

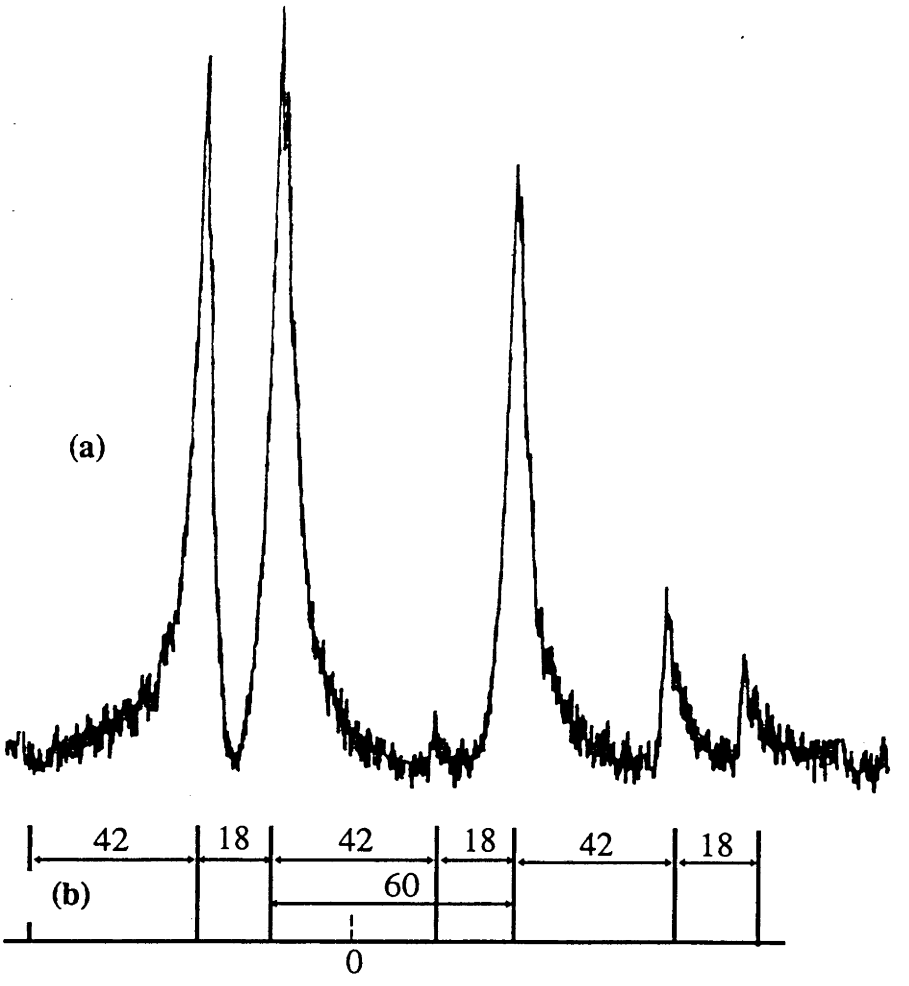

Figure 9-11. (a) Measured Autler-Townes profiles of the 5.4 MHz transition for $\chi = \chi_1 = \chi_2 = 60$ kHz, $\Delta_1 = 0$, and $\Delta_2 = \chi = 60$ kHz. (b) Calculated spectral positions using the theory developed in Ref.4.

It is also worth noting that it is only at these particular situations that the profile shows a relative simple structure and the positions can be predicted. In general with arbitrary detunings and intensities the profiles have a complicated multipeak structures. For example, Fig.9-12 shows the spectrum for the following experimental parameters: $\chi_1 = 60$ kHz, $\Delta_1 = 0$, $\chi_2 = 30$ kHz and (a) $\Delta_2 = 10$ kHz and (b) $\Delta_2 = -10$ kHz. There is no simple way in calculating the peak positions for the general case, and a complete solution of either Eqs. (9.4) or (9.10) is needed. This is out of the scope of this thesis and will not discussed further.

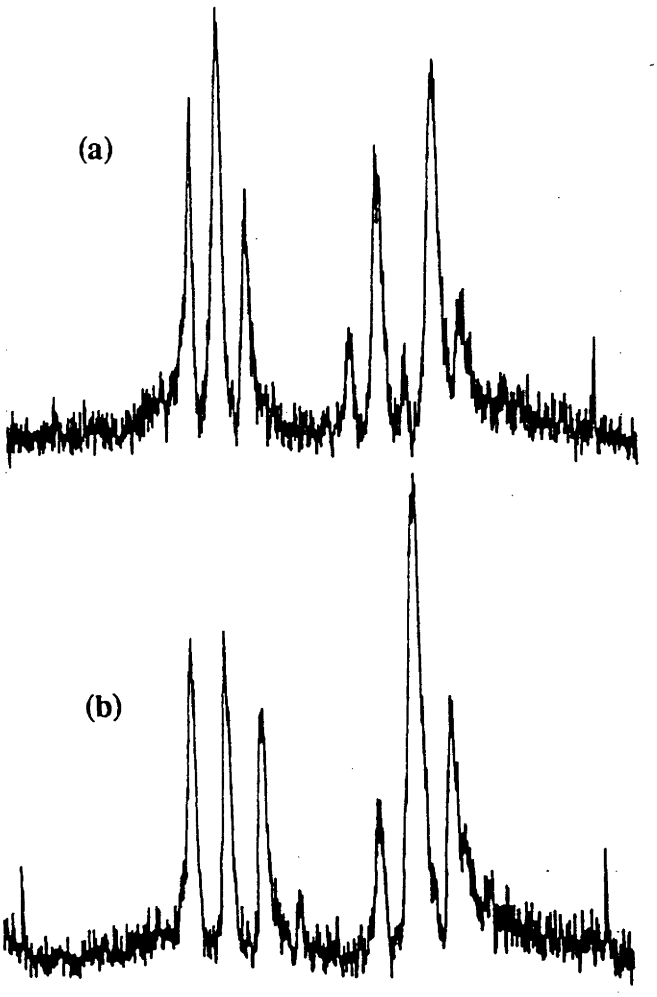

Figure 10-12. Measured Autler-Townes profiles of the 5.4 MHz transition for $\chi_1 = 60$, $\chi_2 = 30$ kHz, $\Delta_1 = 0$, and (a) $\Delta_2 = 10$, (b) $\Delta_2 = -10$kHz.

9.4 Conclusions

In this chapter, the absorption and dispersion profiles are presented, for the first time, in a V-shaped three-level system where one transition is strongly driven by two monochromatic fields and the profiles are obtained by probing the adjacent transition with a weak field. It is shown that, in general, the measured profile is characterized by a complicated multipeak structure. However, for some particular experimental situations, the positions of the

multipeaks can be readily predicted by either the formalism developed by Ficke *et al.* [4] or by the approach developed here. An outline of theoretical calculation is also presented which will facilitate further theoretical work to fully calculate the profiles for the general case.

References:

[1] L. S. Gaida and S. A. Pulkin, Opt. Spektrosk. 67, 761, (1989) [Opt. Spectrosc. 64, 446, (1989)].

" *Three-level atomic system in a strongly resonant bichromatic light field and a weak probe field at an adjacent transition* "

[2] L. F. Vitushkin, S. V. Lazaryuk, S. A. Pulkin and G. I. Toptygina, Opt. Spektrosk. 73, 880, (1992) [Opt. Spectrosc. 73, 526, (1992)].

" *Double resonance spectroscopy in strong biharmonic and weak probe fields* "

[3] M. Z. Smirnov, J. Opt. Soc. Am. B, 9, 2171, (1992)

" *Coherent effects in a three-level gas medium on exposure to a strong bichromatic pumping field and a weak probe wave* "

[4] Z. Ficek and H. S. Freedhoff, Phys. Rev. A 48, 3092, (1993)

" *Resonance-fluorescence and absorption spectra of a two-level atom driven by a strong bichromatic field* "

[5] H. Freedhoff and Zhidang Chen, Phys. Rev. A 41, 6013, (1990)

" *Resonance fluorescence of a two-level atom in a strong bichromatic field* "

Chapter 10

Nutation in Dressed States and Nutation by Dynamic "Stark" Switching

10.1 Introduction

Nutation occurs when a strong, coherent field is suddenly applied to an ensemble of two-level quantum-mechanical systems. It manifests the dynamic process occurring in matter-radiation interaction and hence, has been studied extensively [1,2]. This chapter reports the observation of a new type of nutation by extending the common configuration of a two-level system interacting with a single pulsed field to that of a three-level system interacting simultaneously with a cw and a pulsed field.

The energy levels involved are shown in Fig.10-1(a) where a probe field of ω_2 and Rabi frequency χ_{13} drives the $|1\rangle \Leftrightarrow |3\rangle$ transition and a pump field of ω_1 and Rabi frequency χ_{12} drives the $|1\rangle \Leftrightarrow |2\rangle$ transition. Nutation was observed in the $|1\rangle \Leftrightarrow |3\rangle$ transition for two situations (i) cw pump + pulsed probe and (ii) pulsed pump + cw probe. Quantum beats superimposed on the nutation signal were also observed. In the bare atom state picture the observed nutation is a complicated process involving the coherence ρ_{12} and ρ_{13} driven by the pump and the probe field at the $|1\rangle \Leftrightarrow |2\rangle$ and $1\rangle \Leftrightarrow |3\rangle$ transition, respectively. However, the dressed state picture [3] provides a simple physical picture in which the $|1\rangle \Leftrightarrow |2\rangle$ transition and the pump field ω_1 are treated as a global "atom+field" system. The nutation occurs when the probe field is suddenly applied in resonance with the dressed states (the eigenstates of the "atom+field" system). The nutation frequency is determined by the dressed states transition strength. For the cw pump + pulsed probe case the dressed

states are in the steady state and the observed nutation is referred as to nutation in dressed states. For the pulsed pump + cw probe case, nutation occurs when the dressed states transition is brought into resonance with the cw probe field by the dynamic "Stark" effect induced by the pulsed pump field, thus, it is referred as to nutation by dynamic "Stark" switching in analogy to optical nutation experiments [4].

10.2 Theoretical Background

Consider a three-level system interacting with a pump field ω_1 and a probe field ω_2 as shown in Fig.10-1(a). The definitions of the various parameters are not repeated here as they are in consistent with the previous chapters.

The interactions between the pump field and the $|1\rangle \Leftrightarrow |2\rangle$ transition and the probe field and the $|1\rangle \Leftrightarrow |3\rangle$ transition are characterized by their corresponding Rabi frequencies which are given by

$$\chi_{12} = \frac{\mu_{12} B_1}{\hbar}, \quad \text{and} \quad \chi_{13} = \frac{\mu_{13} B_2}{\hbar}. \tag{10.1}$$

B_1 and B_2 are the strength of pump and probe fields, respectively and μ_{12} and μ_{13} are the magnetic dipole moment of the $|1\rangle \Leftrightarrow |2\rangle$ and $|1\rangle \Leftrightarrow |3\rangle$ transition in bare atom states, respectively. It is assumed that the pump and probe field satisfy the quasi-resonance conditions, i.e, the pump field ω_1 only interacts with the $|1\rangle \Leftrightarrow |2\rangle$ transition and the probe field ω_2 only interacts with the $|1\rangle \Leftrightarrow |3\rangle$ transition.

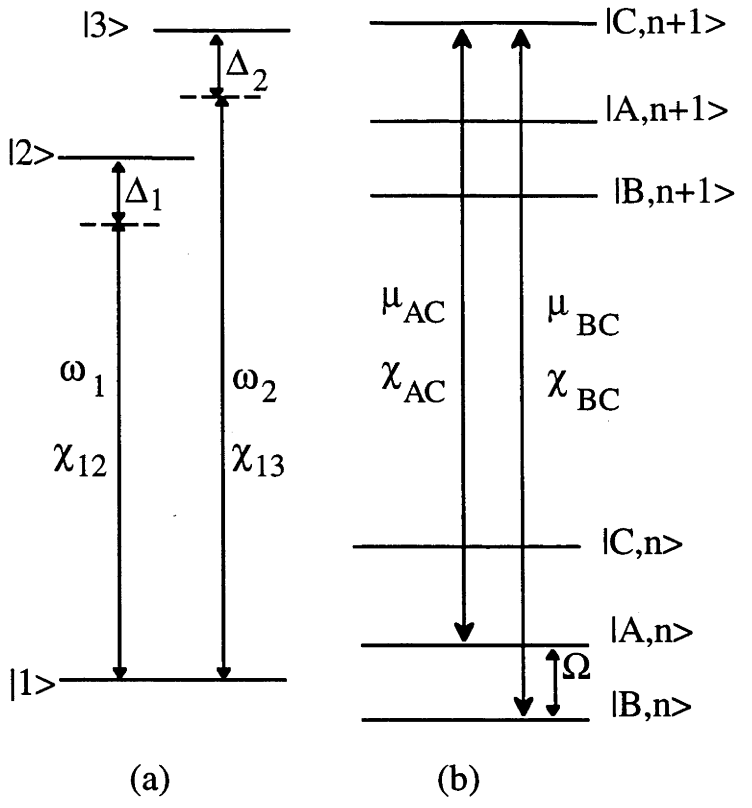

Figure 10-1. A three-level system interacting with a pump field ω_1 and a probe field ω_2 (a). Dressed states levels when the pump field is considered as a dressing field (b).

Consider the pump field ω_1 as the dressing field. The resulting dressed states can be written as (see, Chapter 1)

$$|A, n\rangle = \cos\theta\, |2, n\rangle + \sin\theta\, |1, n+1\rangle , \qquad (10.2a)$$

$$|B, n\rangle = -\sin\theta\, |2, n\rangle + \cos\theta\, |1, n+1\rangle , \qquad (10.2b)$$

$$|C, n\rangle = |3, n\rangle , \qquad (10.2c)$$

where θ is characterized by the Rabi frequency and detuning of the pump field and is given by

$$\tan 2\theta = \chi_{12} / \Delta_1, \qquad (10.3a)$$

$$\sin\theta = \frac{1}{\sqrt{2}}\left[1 - \frac{\Delta_1}{(\chi_{12}^2 + \Delta_1^2)^{1/2}}\right]^{1/2}, \qquad (10.3b)$$

$$\cos\theta = \frac{1}{\sqrt{2}}\left[1 + \frac{\Delta_1}{(\chi_{12}^2 + \Delta_1^2)^{1/2}}\right]^{1/2}. \qquad (10.3c)$$

The splitting between |A, n> and |B, n> is $\hbar\Omega$ where Ω is the generalized Rabi frequency given by

$$\Omega = \sqrt{\Delta_1^2 + \chi_{12}^2}\ . \qquad (10.4)$$

The resulting dressed states are shown in Fig.10-1(b). The Autler-Townes doublet arises from the transition between |C, n+1>⇔|A, n> and |C, n+1>⇔|B, n> in the dressed states picture. The dipole transition moments μ_{ij} between the dressed states are given by

$$\mu_{AC} = <C, n+1|\mu|A, n> = \mu_{13}\sin\theta\ , \qquad (10.5a)$$

$$\mu_{BC} = <C, n+1|\mu|B, n> = \mu_{13}\cos\theta. \qquad (10.5b)$$

The dressed states Rabi frequencies are given by

$$\chi_{AC} = B_2\,\mu_{AC}/\hbar = B_2\,\mu_{13}\sin\theta/\hbar = \chi_{13}\sin\theta, \qquad (10.6a)$$

$$\chi_{BC} = B_2\,\mu_{BC}/\hbar = B_2\,\mu_{13}\cos\theta/\hbar = \chi_{13}\cos\theta. \qquad (10.6b)$$

In the experiments χ_{AC} and χ_{BC} are determined from the nutation frequency. It is obvious from the above discussion that: (i) when the dressing Rabi intensity χ_{12} and probe Rabi intensity χ_{13} are held fixed the dependence of the ratio of χ_{AC}/χ_{13} and χ_{BC}/χ_{13} on the pump detuning Δ_1 is a $\sin\theta$ and $\cos\theta$ function, respectively, (ii) with a resonant pump field (Δ_1=0) and fixed probe Rabi frequency $\sin\theta = \cos\theta = 2^{-1/2} = 0.707$, the ratios χ_{AC}/χ_{13} and χ_{BC}/χ_{13} are $2^{-1/2} = 0.707$ and do not changed with pump Rabi frequency. These topics are studied experimentally.

10.3 Experimental Results and Discussions

10.3.1 cw Pump and Pulsed Probe: Nutation in Dressed State

The three-level system consists of the I_z = |0>, |1> and |-1> hyperfine levels. The I_z= |0>⇔|1> transition [corresponding to the |1>⇔|2> transition in Fig.10-1(a)] at 4.7 MHz is driven by a pump field and the nutation is observed at the I_z= |0>⇔|-1> transition [corresponding to the |1>⇔|3> transition in Fig.10-1(a)] at 5.4 MHz which is coupled by a probe field.

Fig.10-2 shows the nutation signal observed for the cw pump + pulsed probe case. Trace (a) shows the nutation signal when a probe field resonant with the I_z = |0>⇔|-1> 5.4 MHz transition is switched on at t=0 in the absence of a pump field. Trace (b) shows the nutation signal observed when there is a pump field (Rabi frequency χ_{12}=60 kHz) applied resonant with the I_z=|0>⇔|1> 4.7 MHz transition and the probe field applied resonant the |C, n+1>⇔|A, n> transition (frequency = ω_{13} - χ_{12}/2, where ω_{13} = 5.4 MHz). Two traces were taken using the same probe field intensity. Similar nutation was also observed when the pulsed probe field is resonant with the |C, n+1>⇔|B, n> transition. It is seen that both cases exhibit transient nutation after the probe field is switched on. The nutation shown in Fig.10-2(a) is a normal nutation observed in bare atom states with a Rabi nutation frequency of χ_{13} = 9.17 kHz whereas the nutation shown in Fig.10-2(b) is a nutation in dressed states with a Rabi nutation frequency of χ_{AC} = 6.37 kHz (for the |C, n+1>⇔|B, n> transition the observed Rabi nutation frequency is χ_{BC} = 6.49 kHz). The ratio between dressed states and bare states Rabi nutation frequency χ_{AC} / χ_{13} (χ_{BC} / χ_{13}) is 0.695 (0.708) which is in excellent agreement with the theoretical value of

$0.707 = 2^{-1/2}$ for the resonant pumping. There are also quantum beats corresponding to the 60 kHz pump Rabi frequency χ_{12} superimposed in the nutation signal shown in Fig.10-2(b) which are not resolved due to the time scale used in the experiments. To demonstrate quantum beats the pump Rabi intensity χ_{12} was reduced to 30 kHz to yield an Autler-Townes splitting of 30 kHz. The nutation observed when pulsed probe is resonant with $|C, n+1\rangle \Leftrightarrow |B, n\rangle$ transition is shown in the Fig.10-2 insert which clearly reveals the quantum beats at 30.8 kHz. This is in good agreement with the 30 kHz splitting measured by steady state Autler-Townes spectrum in the frequency domain.

Fig.10-3 shows the dressed states Rabi nutation frequency χ_{AC} and χ_{BC} as a function of pump detuning Δ_1 with fixed pump and probe intensities: χ_{12} = 80 kHz and χ_{13} = 8.83 kHz. Eqs. 2a and 2b are also plotted in Fig.10-3 for comparison. The only parameter used in Eqs. 2a and 2b was χ_{13} = 8.83 kHz which can be determined from experiment. As can be seen the experiments are in excellent agreement with the theory calculations.

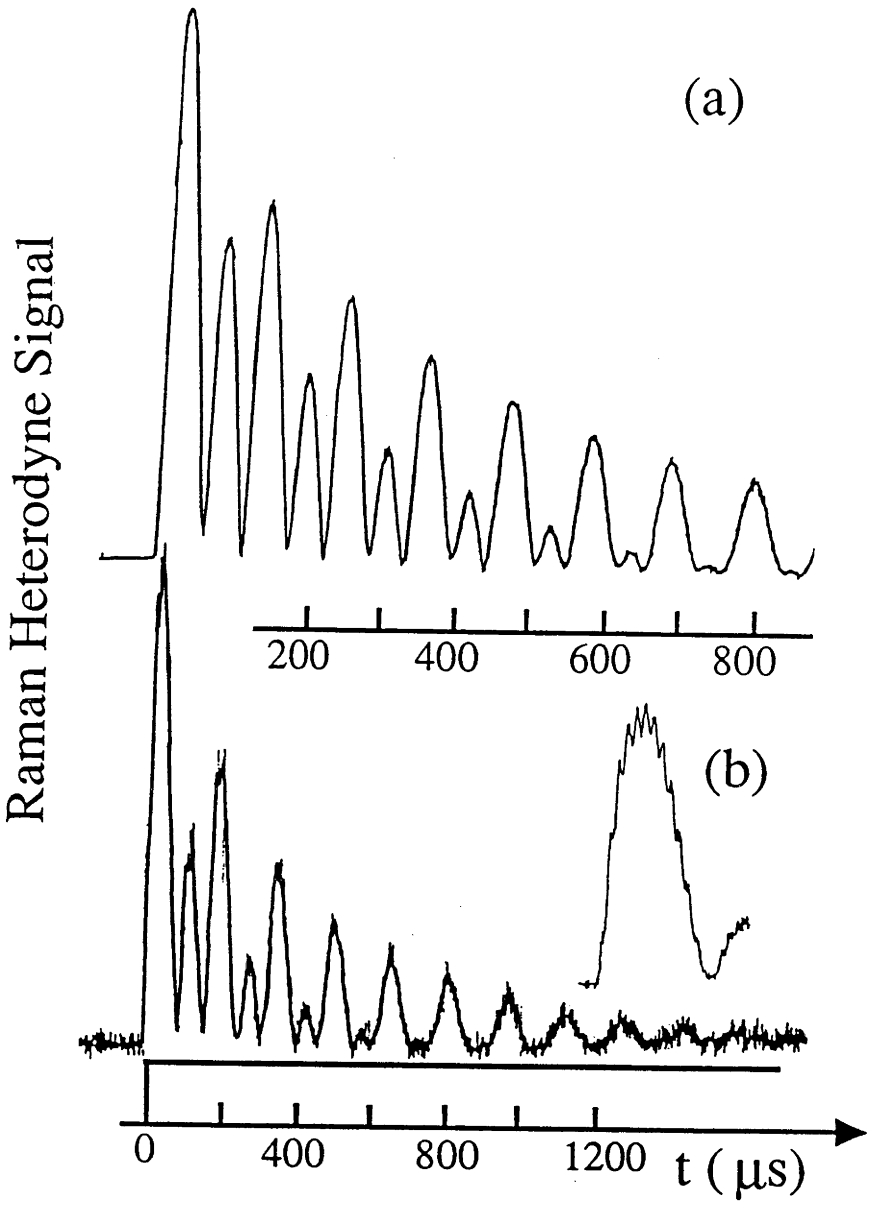

Fig.10-2. (a) Nutation in bare atom state transition. A pulsed probe field was resonant with the I_z=|0>⇔|-1> 5.4 MHz transition. (b) Nutation in dressed state transition. A cw pump field of Rabi frequency 60 kHz was resonant with the I_z=|0>⇔|1> 4.7 MHz transition. A pulsed probe field was resonant with the |C,n+1>⇔|A,n> transition. Similar nutation was observed when the pulsed probe field was resonant with |C,n+1>⇔|B,n> transition. The insert shows the beats superimposed on the nutation signal when the pump Rabi frequency is reduced to 30 kHz, the beats frequency was 30.8 kHz.

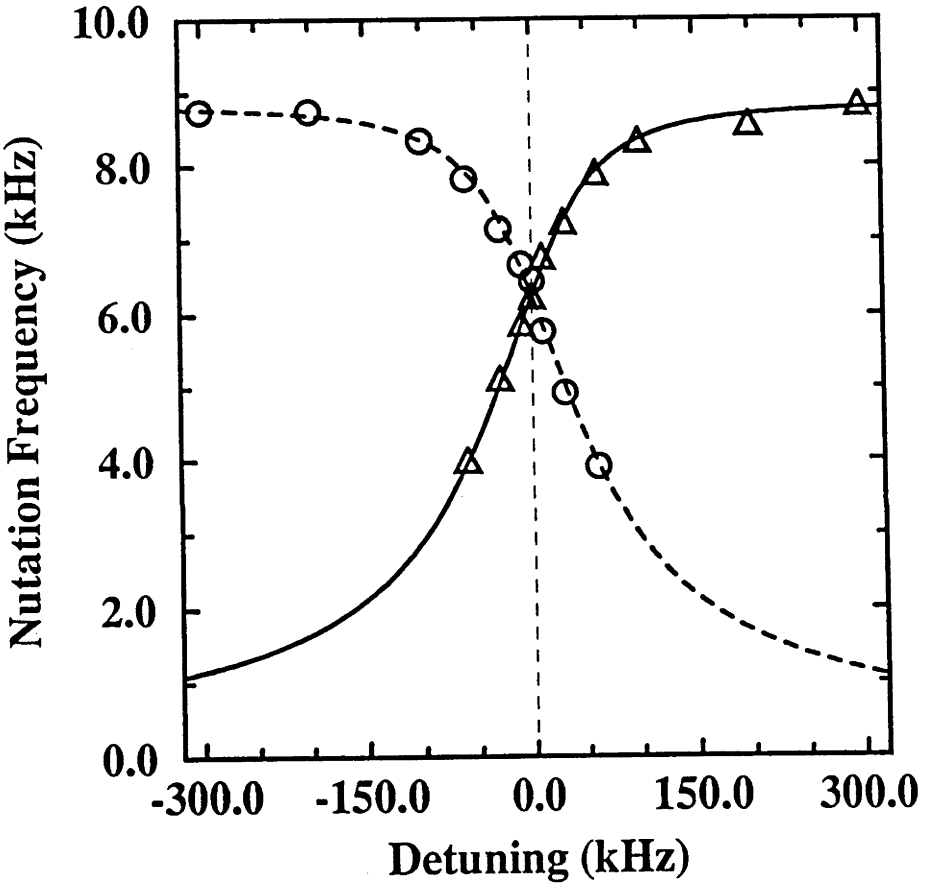

Fig.10-3. Dressed states Rabi nutation frequencies χ_{AC} (circle) and χ_{BC} (triangle) as a function of the cw pump detuning Δ_1. The pump Rabi frequency is 80 kHz. The dashed (solid) trace is a theoretical plot of Eq. 2a (2b) with χ_{13} = 8.83 kHz and χ_{12} = 80 kHz which are determined from experiment.

Fig.10-4 shows the ratios between the dressed states nutation frequencies and the bare atom state nutation frequency χ_{AC}/χ_{13} and χ_{BC}/χ_{13} as a function of the pump Rabi frequency. In the experiments the pump field frequency was resonant with the $I_z=|0\rangle\Leftrightarrow|1\rangle$ 4.7 MHz transition. It can be seen that the measured ratios are very close to the theoretical value of $2^{-1/2} = 0.707$ and do not change with the pump Rabi frequency. This is in good agreement with the theory because for resonant pumping the wave function mixing does not depend upon the pump field intensity. It is also worth noting that at higher pump intensity the ratios deviates from the theoretical value 0.707. The most possible origin of this deviation is because of the off-resonant interaction between the $I_z=|0\rangle\Leftrightarrow|-1\rangle$ transition at 5.4 MHz and the pump field which is neglected within the quasi-resonant assumption. It is assumed in our discussion that the pump field only interacts with the $I_z=|0\rangle\Leftrightarrow|1\rangle$ transition at 4.7 MHz. The energy separation between the $I_z = |1\rangle$ and $I_z = |-1\rangle$ levels is 700 kHz. When the pump Rabi frequency is much smaller than 700 kHz, the off-resonant interaction between the 5.4 MHz transition and the pump field is negligible. However, when the value of the pump Rabi frequency is comparable to the energy separation of 700 kHz, this off-resonant interaction becomes significant and the lowest order theory [5] is no longer exact.

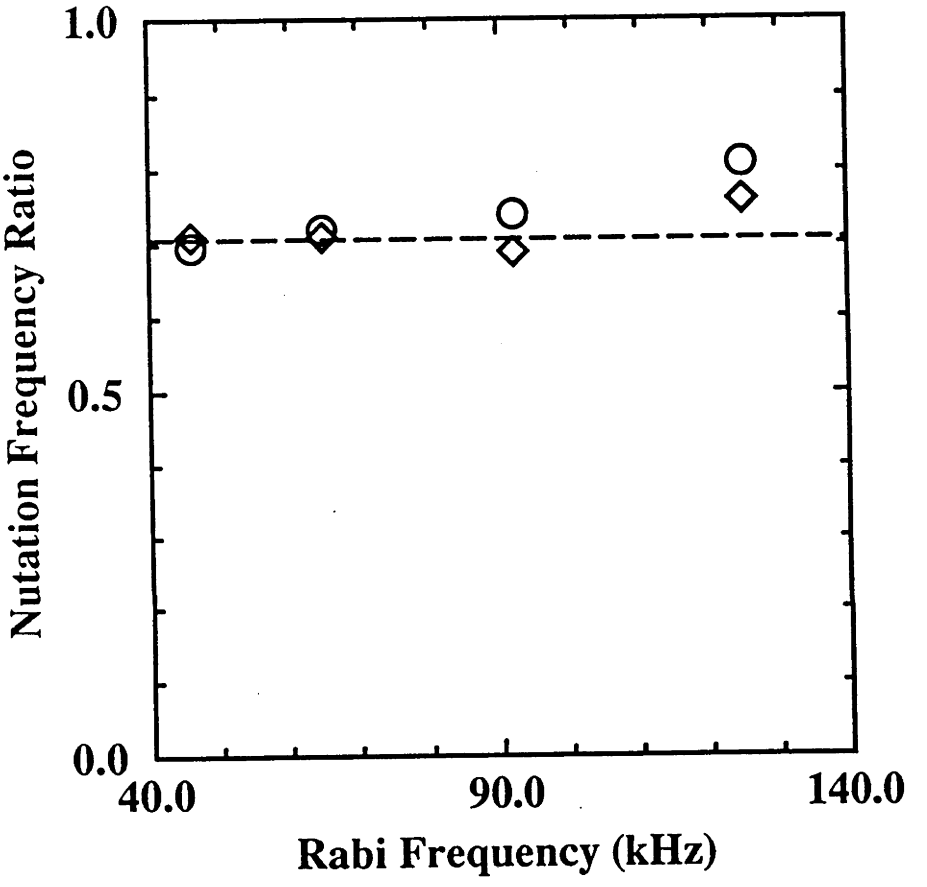

Fig.10-4. Ratios between dressed states nutation frequency and bare atom state nutation frequency χ_{AC}/χ_{13} (circles) and χ_{BC}/χ_{13} (diamonds) as a function of pump Rabi frequency. The cw pump field was resonant with the 4.7 MHz transition. The dashed line represents the theoretical value of $2^{-1/2} = 0.707$.

10.3.2 Pulsed Pump and cw Probe: Nutation by Dynamic "Stark" Switching

Fig.10-5 shows the nutation observed for the pulsed pump + cw probe case. The pulsed pump field was resonant with the I_z = |0> ⇔|1> 4.7 MHz transition and the cw probe field was resonant with one of the Autler-Townes components |C, n+1>⇔|A, n> transition whose position can be determined from the steady state Autler-Townes spectrum measurement. Similar nutation was observed when the |C, n+1>⇔|B, n> transition was probed. There are also quantum beats superimposed on the nutation signal corresponding to the Autler-Townes splitting. Nutation in optical frequency has been observed using the well-known technique: Stark switching method developed by R.G.Brewer *et al* [4]. In this method an atomic transition is suddenly brought into resonant with a cw laser field by the static Stark effect induced by a pulsed DC electrical field. In our experiments the transition is suddenly brought into resonant with a cw probe field by the dynamic "Stark" effect using a pulsed pump field. In this sense we refer to our method as nutation by dynamic "Stark" switching. The quantum beat reported in this paper also has a close analogue: Raman beats at optical wavelengths [6]. Again a pulsed DC electrical field was used to Stark-split a degenerate level and quantum beats occur at the frequency of the degenerate level Stark splitting due to the coherence prepared before the DC Stark pulse. However, there are fundamental differences between the two methods and hence the two observations. In the DC Stark switching method the atomic levels are shifted in energy due to the static Stark effect but the eigenstates have not been changed and are still in one of the bare atom eigenstates. Thus the Rabi nutation frequency corresponds to the bare atom state Rabi frequency. On the other hand, in the dynamic "Stark" switching method the atomic states being shifted are no longer bare atom eigenstates but are a superposition of the bare atom states and thus the Rabi nutation frequency is no

longer the bared state Rabi frequency. The Raman beats at optical wavelengths [6] rely on the coherence prepared in the period when the levels are degenerate while in our case the coherence occurs because of the intrinsic property of the dressed states.

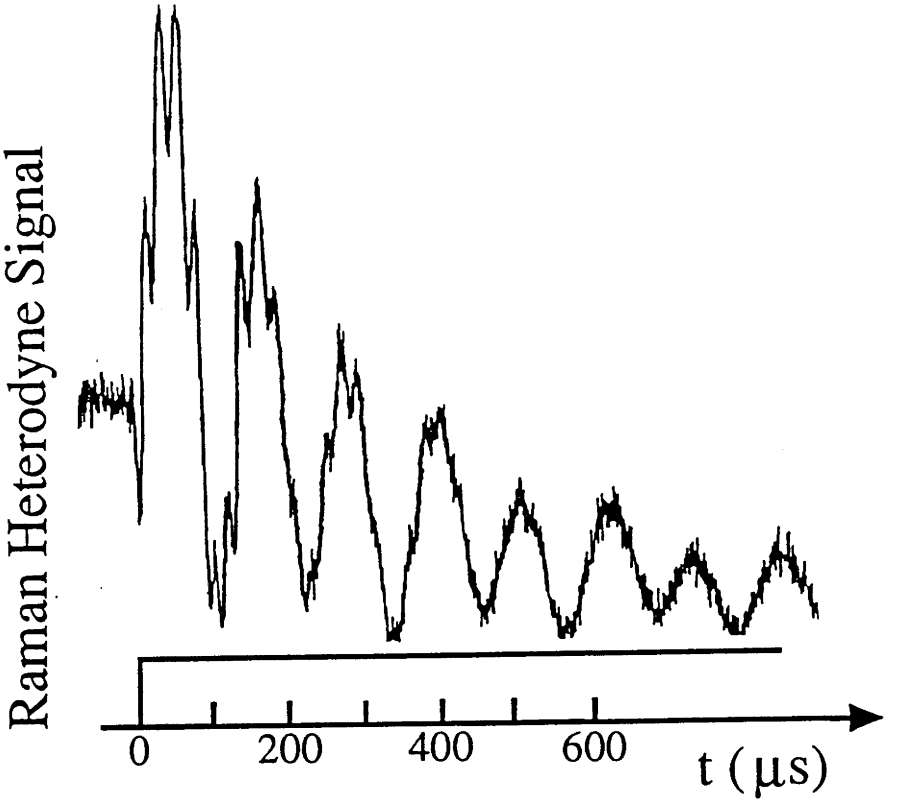

Fig.10-5. Nutation by dynamic "Stark" switching. A cw probe field was resonant with the |C,n+1>⇔|A,n> transition. Nutation was observed when the pump field which has a Rabi frequency 39 kHz and is resonant with the 4.7 MHz transition was switched on. Quantum beats is also observed. Similar nutation was also observed when the |C,n+1>⇔|B,n> transition was probed.

10.3.3 Observation of the Spin-locking and Anomalous Beats

When the pulsed field has a constant phase the nutations are similar for the two situations. However, when a 90^0 phase shift of the pulsed field is introduced after the pulsed field has been switched on for a $\pi/2$ period, the observed transient behaviour differs dramatically depending on which field is pulsed as shown in Fig.10-6. When the probe field is pulsed spin-locking was observed for the |C, n+1>⇔|A, n> transition as shown in Fig.10-6(a). The nutation is prohibited by the locking field and the signal exhibits exponential decay with a time constant of approximately 340 μsec. The beating superimposed on the spin-locking signal has a frequency of 39 kHz which is in good agreement with the Autler-Townes splitting of 39 kHz measured in the frequency domain. Fig.10-6(b) shows the "anomalous" strong beats when the pump field is pulsed and the cw probe field is resonant with the |C, n+1>⇔|A, n> transition. The nutation is totally concealed by the strong beats which again corresponds to the Autler-Townes splitting of 39 kHz. The results demonstrate that the transient process can be influenced strongly by the initial condition of the dressed state [7,8]. A fully analysis and calculations of the response is beyond the scope of this thesis.

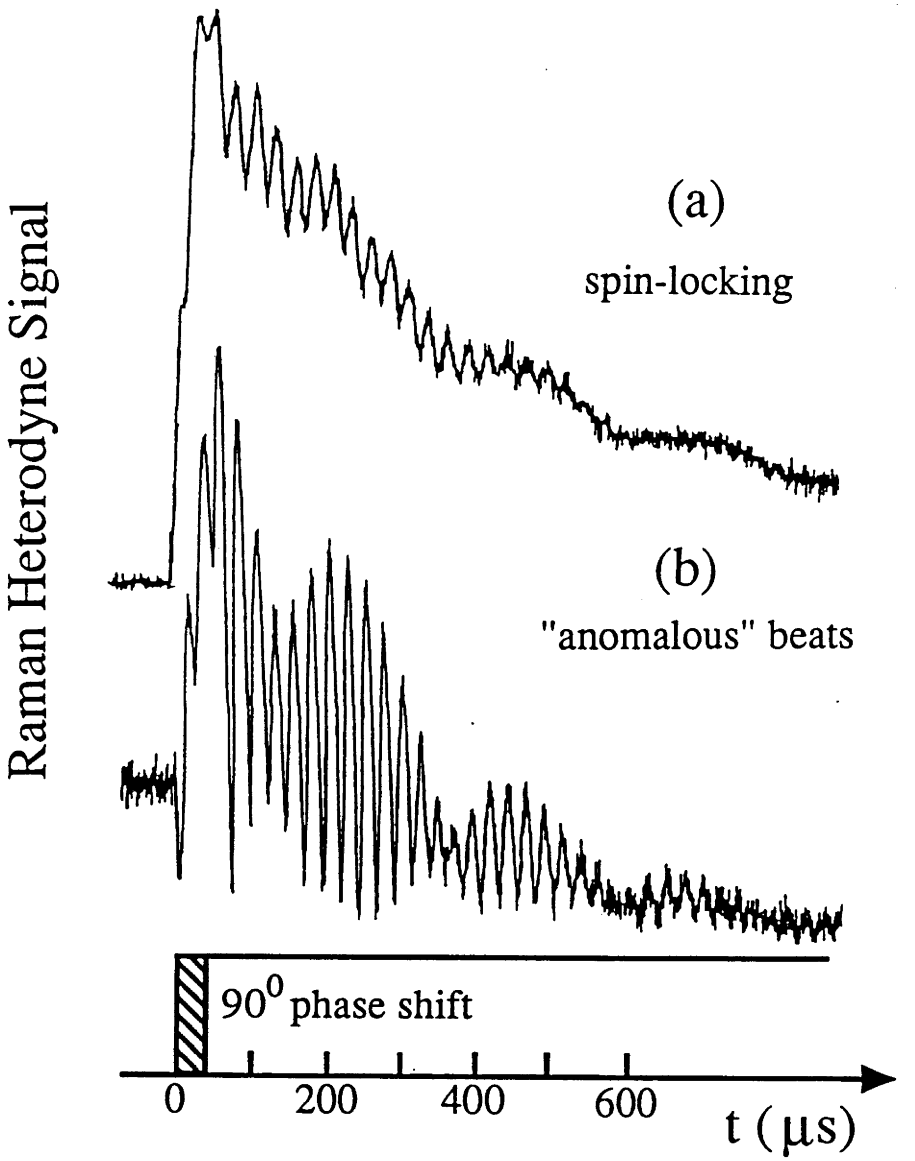

Fig.10-6. Spin-locking (a) and "Anomalous" strong beats (b). In (a) the probe field was pulsed and its phase was shifted by 90^0 after a $\pi/2$ period. The cw resonant pump field was resonant with the I_z=|0>⇔|1> 4.7 MHz transition. In (b) the pump field was pulsed and its phase was shifted by 90^0 after a $\pi/2$ period. The cw probe field was resonant with the |C,n+1>⇔|A,n> transition.

10.4 Summary

In summary, we report the first experimental observation of nutation in dressed states for (i) a cw pump + a pulsed probe field and (ii) a pulsed pump + a cw probe field in a three-level system. The Rabi frequency of the dressed states can be readily determined by nutation measurement and the experimental results are in good agreement with the simple consideration based on the dressed states theory. Spin-locking is also observed for the first time. The anomalous strong beats demonstrate that the transient behaviour can be influenced dramatically by the dressed states initial condition. Fully understanding of the interesting strong oscillation challenges further experimental and theoretical studies which are in progress .

References

[1] A. Abragam, *Principles of Nuclear Magnetism*, (Oxford, 1961)

[2] L.Allen and J.Eberly, *Optical resonance and two-level atoms*, (Dover, N. Y., 1987)

[3] C. Cohen-Tannoudji, J.Dupont-Roc and G.Grynberg, *Atom-Photon Interactions*, (Wiley, N. Y., 1992)

[4] R.G.Brewer and R.L.Shoemaker, Phys. Rev. Lett, 27, 631, (1971)

" *Photon echo and nutation in molecules* "

[5] C. Cohen-Tannoudji and S. Reynaud, J. Phys. B10, 365, (1977)

" *Modification of resonance Raman scattering in very intense laser fields* "

[6] R.G.Brewer and E.L.Hahn, Phys. Rev. A, 11, 1641, (1975)

" Coherent two-photon process: transient and steady state cases "

[7] N. Lu, P.R.Berman, A.G.Yodh, Y.S.Bai and T.W.Mossberg, Phys. Rev. A33, 3956, (1986)

"*Time-dependent Spectrum of Resonance Fluorescence for Atoms Prepared in Pure Dressed States*"

[8] Y.S.Bai, T.W.Mossberg, N.Lu and P.R.Berman, Phys. Rev. Lett. 57, 1692, (1986)

" *Transient Suppression of the Autler-Townes Doublet*"

Chapter 11

Summary

The 5.4 MHz hyperfine transition within the electronic ground state of the nitrogen-vacancy centre in diamond is studied using the Raman heterodyne detection technique.

Using a single field a variety of coherent transients associated with the 5.4 MHz transition have been observed. The results show that the hyperfine transition is very close to an ideal two-level transition. It has an enhanced transition strength, small inhomogeneous broadening and a transverse relaxation time T_2 within the same order as the longitudinal relaxation time T_1.

The main topic of the thesis is the investigation of the steady state properties of this two-level transition interacting with two fields using the pump-probe method. For the weak probe case, I have presented a systematic study of absorption and dispersion profiles of a driven two-level system including the best experimental traces of dispersion profiles. This studies are then extended to strong probe and in this case the dispersion response is reported for the first time. There are several observations of significance including features which correspond to up to 11th subharmonic of the Rabi frequency and gain features which correspond to two types of gain without inversion. The response of a three-level system is also studied and the power broadening of the Autler-Townes effect in absorption, dispersion and amplitude responses has been investigated for the first time.

The experimental results utilizing three cw fields are also reported. The two strong fields are applied to the two-level transition and their effects are

studied by measuring a transition to the third level with a third field. The results show that dressed states can be dressed. These again are the first observations of this type.

The transient behaviour of the two-level system interacting with two driving fields has also been studied. The results are discussed in terms of coherent transients in dressed states. A variety of coherent transients in dressed states have been observed, including nutation, spin echo, free-induction-decay, delayed FID, spin-locking. From these measurements many important parameters associated with the dressed states such as transition strength, T_1 and T_2 have been obtained. In this thesis only the results of nutation associated with dressed states are presented.

Finally I would like to point out that the present study only represents the tip of an iceberg and leaves much more to be explored. Although the studies of a two-level system are already extensive, they are still limited as usually the experimentation is difficult and there is no motivation for calculating the response of a system if it is unlikely to realize the experimental observation. We have identify a close to ideal two-level system and the experimental technique is very flexible which can be easily extended to very complex situations. In the course of this study, in addition to the results presented in this thesis, many interesting investigations have been contemplated and often preliminary results obtained. They will certainly stimulate corresponding theoretical calculations. For example, the observation of coherent transients associated with dressed states is in fact a totally new topic. There are other interesting experiments waiting to be carried out, which will consequently lead to a better understanding of phenomena associated with matter-radiation interaction.